



HAL
open science

Experimental study of liquid films on the structured packing elements of distillation columns

Manasa Srinivas Iyer Periyapattana

► **To cite this version:**

Manasa Srinivas Iyer Periyapattana. Experimental study of liquid films on the structured packing elements of distillation columns. Chemical and Process Engineering. Université Paris-Saclay, 2021. English. NNT : 2021UPAST121 . tel-03592838

HAL Id: tel-03592838

<https://theses.hal.science/tel-03592838v1>

Submitted on 1 Mar 2022

HAL is a multi-disciplinary open access archive for the deposit and dissemination of scientific research documents, whether they are published or not. The documents may come from teaching and research institutions in France or abroad, or from public or private research centers.

L'archive ouverte pluridisciplinaire **HAL**, est destinée au dépôt et à la diffusion de documents scientifiques de niveau recherche, publiés ou non, émanant des établissements d'enseignement et de recherche français ou étrangers, des laboratoires publics ou privés.

Experimental study of liquid films on the
structured packing elements of distillation
columns

Thèse de doctorat de l'université Paris-Saclay

École doctorale n°579 – Sciences mécaniques et énergétiques,
matériaux et géosciences (SMEMAG)
Spécialité de doctorat : Génie des Procédés
Unité de recherche : Université Paris-Saclay, CentraleSupélec,
Laboratoire de Génie des Procédés et Matériaux, 91190, Gif-sur-Yvette, France
Référent : CentraleSupélec

**Thèse présentée et soutenue à Paris-Saclay,
le 7/12/2021, par**

Manasa PERIYAPATTANA

Composition du Jury

Benoît SCHEID Professeur, Université Libre de Bruxelles	Président
Michel MEYER Professeur, ENSIACET	Rapporteur
Huai-Zhi LI Professeur, ENSIC	Rapporteur
Sophie MERGUI Maître de Conférence, Sorbonne Université	Examinatrice

Direction de la thèse

Hervé DUVAL Professeur, CentraleSupélec	Directeur de thèse
Laurent ZIMMER Chercheur CNRS, EM2C	Co-encadrant
Mikael WATTIAU Ingénieur R&D, Air Liquide	Tuteur en entreprise

Abstract (English and French)

Title: Experimental study of liquid films on the structured packing elements of distillation columns

Keywords: structured packing, perforation, liquid curtain, rivulet spreading, dean vortices, 3D 3C PTV

Abstract: Perforations assist in redistributing the liquid film on the complex surface of corrugated and perforated metallic sheets of structured packing, used in distillation columns. Depending on the inertial, gravitational, viscous, and capillary contributions, falling liquid film undergoes different modes of transition (rim, jet, drops, or liquid curtain) in the perforation, promoting the exchange of liquid between two faces.

Our objective is to examine the hydrodynamics of these modes. We constructed an experimental setup to study the modes of transition and liquid film repartition. A simplified geometry, yet pertinent, is considered to characterize the role of perforations in corrugated and perforated packings. The basic configuration consists of a falling liquid film on a vertical aluminium plate. The feed rate can be controlled either on one or both sides.

The modes of transition depend on the geometry of the perforation and the physical properties of the liquid. The curtain mode, when liquid fully fills the perforation, is associated with profound modifications of the flow pattern. In addition, it exhibits strong hysteresis and presents stationary capillary waves. In actual distillation columns, the same phenomenon is expected to favour liquid distribution. We experimentally studied the onset of liquid curtain formation for a wide range of parameters. Based on a force balance, a criterion of curtain formation is proposed.

The liquid leaking through a perforation flows like a rivulet, spreading along the length of the plate. At first, we experimentally investigated the efficiency of liquid transfer through holes for

various parameters (spacing, number of holes, and diameter) and modes of transition. A recurrence model is proposed, which suitably predicts the transfer flow rate downstream any given row of perforations.

The rivulet spanwise profile has a Gaussian shape, with a thickness peak height decaying in the streamwise direction. The rivulets from a row of perforations spread in the streamwise and spanwise directions, merge into a continuous wavy film, and eventually level to a flat film. The merging distance from the perforation and the characteristic length of the leveling scale as a power of the perforation spacing.

In curtain mode, liquid films on perforated plates exhibit capillary waves and recirculation zones, highly influencing mass transfer. To further investigate the film flow structure, we adopted a new optical technique of Lagrangian Particle Tracking Velocimetry with the notion of defocus. This technique is based on the measurement of the defocused sizes of particles. Since this size is a function of the distance from the focal plane, it is thus possible to determine the position of particles in three dimensions. The measurement technique is validated by measuring the velocity of the liquid film on a flat aluminum plate. Optical distortions from the reflective surface of aluminum were kept to a minimum by using fluorescent particles. The recirculating structures in the liquid curtain are analysed and quantified using a probability density maps of the negative velocity and particle tracking from the supported film to the suspended film ("twin films"). We also used Dynamic Mode Decomposition to examine the spatial modes within the curtain.

Title: Étude expérimentale des écoulements liquides dans un garnissage de distillation

Mots clés : garnissage structuré, perforation, nappe ou rideau liquide, étalement ruisselet, tourbillon de Dean, 3D 3C PTV

Résumé : Les perforations favorisent la redistribution du film liquide sur la surface complexe des garnissages structurés du type ondulés-croisés utilisés dans les colonnes de distillation. En fonction des contributions inertielle, gravitaire, visqueuse, et capillaire, l'écoulement révèle différents modes de franchissement des perforations, en bourrelet, en jet, en gouttes ou en nappe (ou rideau) liquide. Ces modes influent sur l'échange de liquide entre les deux faces.

Notre objectif est d'examiner l'hydrodynamique des différents mécanismes de transfert de la phase liquide d'une surface de garnissage à l'autre. Pour ce faire, nous avons construit un dispositif expérimental afin d'étudier les modes de transition et d'étalement du film liquide. Une géométrie simplifiée, mais pertinente, est étudiée pour la caractérisation du rôle des perforations dans les garnissages ondulés et perforés. Notre configuration de base sera un écoulement de film tombant le long d'une feuille d'aluminium verticale. La plaque pourra être alimentée sur une ou deux faces.

Les modes de transition varient en fonction de la géométrie de la perforation et des propriétés physiques du liquide. Lorsque la nappe liquide remplit la perforation, le régime d'écoulement est profondément modifié. En outre, ce mode de franchissement présente une forte hystérésis et des ondes capillaires stationnaires. Dans les colonnes de distillation industrielle, on s'attend à ce que ce même phénomène favorise la distribution du liquide. Dans cet esprit, nous avons étudié les critères de formation de la nappe liquide pour une large gamme de paramètres. Ensuite, à partir des données expérimentales, nous avons établi un modèle mathématique simple, basé sur un calcul d'équilibre des forces, qui fournit un critère de formation de la nappe.

Le liquide transféré à travers des perforations

s'écoule comme un ruisselet se répartissant sur toute la longueur de la plaque. Nous avons d'abord étudié expérimentalement l'efficacité du transfert de liquide à travers des trous pour différents paramètres (l'espacement, le nombre de trous et le diamètre) et différents modes de franchissement des perforations. Un modèle de récurrence a été proposé pour prédire le débit transféré en aval d'une rangée de perforations et ce, quelle que soit la rangée.

Le profil dans la largeur du ruisselet a la forme d'une distribution gaussienne dont le pic décroît dans le sens de l'écoulement. Les ruisselets qui s'écoulent d'une rangée de perforations s'étalent dans les directions longitudinale et transversale de la plaque, ils fusionnent en un film ondulé continu qui relaxe en aval en une surface plane. La distance nécessaire pour que les ruisselets fusionnent et la longueur caractéristique du nivellement de la surface du film varient en loi de puissance avec l'espacement des perforations.

La nappe liquide sur la plaque perforée présente des ondes capillaires et des zones de recirculation, qui influencent fortement le transfert de masse. Pour caractériser la structure de l'écoulement, on adopte une technique de mesure de vitesse 3D par suivi de particules, basée sur le principe de défocalisation. La taille apparente d'une particule étant fonction de sa distance au plan focal, il est ainsi possible de connaître sa position en trois dimensions. Une première validation de cette technique a été réalisée en mesurant la vitesse du film liquide sur une plaque plane d'aluminium. Grâce à l'utilisation de particules fluorescentes, les distorsions optiques dues à la surface réfléchissante de l'aluminium ont été réduites.

La nappe liquide a été caractérisée à l'aide de cartes de densité de probabilité des vitesses négatives et du suivi de particules du film supporté au film suspendu (« twin films »). Nous avons également appliqué la décomposition en modes dynamiques pour examiner des modes spatiaux au sein de la nappe liquide.

Acknowledgements

Yet another chapter of my life has come to an end. I must acknowledge that it was a long, challenging journey. In the last three years, I have received incredible support from many people, and I would like to extend my gratitude with all my heart.

First and foremost, I am profoundly grateful to my supervisor, Prof. Hervé Duval, for allowing me to conduct a Ph.D. study under his supervision. He constantly supported me with his invaluable advice and devoted his time to numerous discussions. I have always found that I could approach for him any help. I would like to mention his immense knowledge and years of experience, which led our work towards a valuable contribution. I would also like to thank him for reviewing and correcting my manuscript and articles. For these reasons and many others, I will be forever indebted to him. Also, I would like to mention his pleasant nature, quick wit, and particularly humoristic nature, which kept the work environment positive.

I would also like to thank my co-supervisor, Dr. Laurent Zimmer, for his enormous assistance in the experimentation work of Particle Tracking Velocimetry. Due to his collaboration and expertise in experimentation and image processing, I was able to test novel experimental techniques and add originality to our work. My special thanks to him for assisting me in completing the experiments and correcting a part of my manuscript when the world was paused during the pandemic outbreak.

I would like to express my immense gratitude to Mikael Wattiau for his support on the scientific front and administrative aspect on the industrial side. He helped me valorize my study among the scientific community at Air Liquide. I am also grateful to Jacopo Siewert, Mikael Wattiau, and John Pachon-Morales for dedicating their valuable time on reviewing scientific articles. I would also like to express my special thanks to Joel Casalinho, who guided me in designing and constructing the test bench. I really appreciate his reasoning and foreseeing skills which made the test bench functional. I wholeheartedly appreciate his dedication and support.

I would also like to thank François Puel and Patrick Perré, director and ex-director of the Laboratoire Génie des Procédés et Matériaux (LGPM), for supporting me in conducting my thesis. I really appreciate their efforts in organizing intellectual events like seminars and also fun-filled events like Christmas lunch, barbeque, etc., to create a healthy environment within the laboratory.

I am also grateful to Prof. Marie Laurence Giorgi for sharing the frequency detection Matlab code and valuable hints for measuring the contact angle.

I would like to convey my thanks to Nathalie Ruscassier for helping me with roughness measurements. My special thanks to Sebastien Gautier and Frederic Léssage for having helped me prepare the test samples and assisting me with the necessary materials and 3D impressions. I want to convey my thanks to Jamila El-Bekri for her assistance in using measurement instruments.

I want to thank Helene Santigny, Vincent Butin, Corinne Roussel, Yoland Bisson for their support in maintaining the lab.

I want to convey my thanks to Sandra Julien-Anchier and Elisabeth Dos Santos Lobo for their assistance in administrative aspects. My special thanks to the ex and current director of SMeMAG, Prof. Benoît Goyeau, and Prof. Benoît Fiorina for their support.

I express my gratitude to Association Nationale de la Recherche et de la Technologie ANRT (CONVENTION CIFRE No 2017/1472) and Air Liquide for having funded my PhD.

I convey my special thanks to all the jury members for having accepted to be part of the jury and for their interest in my work. My sincere thanks to Dr. Benoit Scheid for having accepted to be the president of the jury. Thanks to Michel Meyer and Huai-Zhi Li for reviewing and commenting on my manuscript. Finally, thanks to Sophie Mergui for having accepted to be the examiner of the jury.

I would also like to thank all my colleagues and friends (Yuanyuan, Marie-Adelaide, John, Julia, Magali, Clarisse, Yong, Yan, Sufang, Andrea, Najib, Benham, Mathilde) for sharing this journey with me. I have learned and discovered many things (culture, food) from this diverse group of friends. My special thanks to Yuanyuan for supporting me morally during challenging times. I am going to miss the fun times I shared with her during these three years.

I want to thank the sports team of Centralesupelec (Frédéric Fargues, Alexis Jardin and Xavier Pujos) for having me discover my love for sports activity.

Finally, I would like to express my enormous gratitude for the love and blessings of my family. I would also like to thank my life partner and his parents for constantly supporting me and encouraging me since I arrived in France.

No words can express my appreciation and gratitude for the support I have received from all the people during these years. Without their support and belief, I would not have reached this milestone today.

General preamble

The work described in this thesis manuscript was carried out at the laboratory LGPM (Laboratoire de Génie des Procédés et Matériaux), belonging to CentraleSupélec (Université Paris-Saclay).

The manuscript is based on two publications and a manuscript, which make up chapters 4, 5 and 6, with some additional unpublished information also included. The contents of the publications were unchanged except for the section, figure, table and equation numbers and the corresponding references to these in the text (the numbering was adapted to follow the manuscript format).

The publication references are the following:

- Iyer M, Duval H, Casalinho J, Seiwert J, Wattiau M. Experimental study of a liquid film flowing over a perforation. 2021;(March). (doi:10.1002/aic.17363)
- Iyer M, Duval H, Casalinho J, Seiwert J, Wattiau M, Pachon J, Zimmer L, A comprehensive study of the liquid transfer from the front to the back of a perforated sheet, accepted AIChE journal (date: 10/02/2022).
- Iyer M, Duval H, Casalinho J, Morales J P, Seiwert J, Wattiau M, Zimmer L, Visualization of Recirculation Zones Over a Perforated Plate: An Optical Flow Technique for Characterization of Fluid Dynamics in Structured Packing. *Submitted* (Conference article <http://www.da2022.org/>).

This work was also presented during oral presentations at one international conference and one national conference, which are the following:

- 12th European Congress of Chemical Engineering, Fluid mechanics and transport phenomena, ECCE 2019, 15th to 19th September, Florence, Italy.
Manasa IYER, Hervé DUVAL, Joel CASALINHO, Jacopo SEIWERT, Mikael WATTIAU, “Confined liquid distribution in structured packings: Study of liquid films around a perforated topography”
- Société Française de Génie des Procédés SFGP 2019, 15th to 17th October 2019, Nantes, Manasa IYER, Hervé DUVAL, Joel CASALINHO, Jacopo SEIWERT, Mikael WATTIAU, France, “Confined liquid distribution in structured packings: Study of liquid films around a perforated topography”

Contents

Table of Contents

Abstract (English and French).....	3
Acknowledgements.....	5
General preamble.....	10
Contents.....	10
List of abbreviations and acronyms	1
Nomenclature.....	3
Introduction	8
1. Bibliographic review	12
1.1. Air distillation	12
1.1.1. Need of air distillation.....	12
1.1.2. Air separation challenges.....	13
1.1.3. Safety and reliability in design and operation	14
1.2. Theory and working of ASU	15
1.2.1. Working principle and operation of ASU	15
1.2.2. Vapour-liquid equilibrium and mass balance	17
1.3. Column internals	17
1.3.1. Counter-current gas flow in the column	17
1.3.1. Tray contactors.....	19
1.3.2. Random packings	20
1.3.3. Structured packing.....	21
1.4. Mechanism of liquid redistribution	32
1.4.1. Introduction	32
1.4.2. Liquid redistribution at packing scale	33
1.4.3. Redistribution at liquid film scale.....	36
1.5. Evaluation of the measurement techniques: State of art	45
1.6. Conclusion and objectives.....	49
2. Materials and Methods.....	53
2.1 Mechanisms of transition, liquid transfer and distribution	53
2.1.1. Description of Experimental set-up	53
2.1.2. Preliminary tests.....	58
2.1.3. Parameters of experiments.....	59
2.1.4. Physical properties of test liquids	63

2.1.5.	Measurement techniques	66
2.2	3D 3C Particle Tracking Velocimetry for the investigation of liquid films	75
2.2.1.	Description of the optical setup	75
2.2.2.	Parameters of experiments	77
2.2.3.	Measurement techniques	77
2.3	Experimental protocol.....	80
2.4	Conclusions and Perspectives	82
3.	Experimental study of a liquid film flowing over a perforation	83
1.	Introduction	83
2.	Problem description	86
3.	Experimental setup	88
3.1.	Materials	88
3.2.	Experimental setup	89
3.3.	Experimental protocol	91
4.	Flow modes over a perforation.....	92
4.1.	Far below the curtain transition	92
4.2.	Prior to the curtain transition.....	94
4.3.	Curtain transition and just beyond	97
4.4.	Hysteresis	99
5.	Parametric study.....	100
5.1.	Influence of perforation dimensions.....	100
5.2.	Influence of the flow rate ratio $Q2/Q1$	101
5.3.	Influence of liquid type	102
6.	Discussion	103
6.1.	Model for curtain transition.....	103
6.2.	Liquid behavior within and around the perforation in curtain mode	106
7.	Conclusion	109
8.	Supplementary Material	111
4	A comprehensive study of the liquid transfer from the front to the back of a vertical perforated sheet	120
1.	Introduction	120
2.	Problem description	125
3.	Experimental set-up	127
4.	Results.....	131

4.1.	Single perforation.....	131
4.2.	Spanwise row of perforations	134
4.3.	Staggered array of perforations	137
5.	Discussion	140
5.1	Transferred volume flow rate per perforation (in the curtain mode).....	141
5.2	Rivulet spreading	142
5.3	Rivulet merging and film leveling	146
5.4	Flow balancing between the front and the back of the plate	148
6.	Conclusion	149
7.	Supplementary Material	152
5	3D 3C PTV and optical flow applied to wall bounded and suspended liquid films	171
1.	Introduction	172
2.	Methodology.....	177
2.1.	Principle of PTV.....	177
2.2.	Principle of defocus.....	177
2.3.	Annular aperture technique.....	178
2.4.	Velocity measurements	179
2.5.	Locating the particles in 3D space.....	180
2.6.	Association of particles between two images	180
3.	Experimental procedure	181
4.	Quality assessment of the experimental data: Film on vertical flat plate	181
4.1.	Axial velocity (ux) distribution in liquid film on flat plate	182
4.2.	Relation between apparent size (di) of the particle and film thickness (δ)..	184
4.3.	Partial conclusion.....	186
5.	Applicability of the 3D PTV on the liquid curtain	188
5.1.	Recirculation zones prior to curtain mode	189
5.2.	Recirculation zones in inertial and hysteretic curtain mode.....	190
5.3.	Axial velocity (ux) on perforated plate.....	193
5.4.	Probability density distribution of negative velocity	194
5.5.	Tracking.....	196
5.6.	Flow characteristics through DMD post processing.....	198
6.	Discussion	199
6.1.	Vortex structures in liquid curtain on a perforated plate.....	199
6.2.	DMD spatial modes.....	200

7. Conclusions.....	202
8. Supplementary Material	204
6 Conclusions and Perspectives	209
Appendix 1 : Construction of McCabe-Thiele diagram	213
Appendix 2: CAD model of the test bench.....	216
Appendix 3 : Complementary information related to test setup construction.....	217
1.1. Evolution of distributor	217
1.2. Roughness measurements	218
1.3. Preparation of aqueous glycerol mixture	219
1.4. Particles selection and Annual aperture	219
Appendix 4 : Model derivation predicting curtain Reynolds number (Re_{cr})	222
Appendix 5 : Theoretical expression for length scale of onset of rivulet merging	224
Appendix 6 : Dynamic Mode Decomposition	226
Bibliography	228
List of Figures	240
List of tables.....	246
French summary (résumé français).....	247

List of abbreviations and acronyms

2D	Two-dimensional
3D	Three-dimensional
3C	Three-component
ASU	Air separation unit
CAD	Computer-aided design
CCD	Charge-coupled device
CCI	Confocal chromatic imaging
CCS	Confocal chromatic sensor
CFD	Computational fluid dynamics
CMOS	Complementary Metal-Oxide-Semiconductor
CT	Computed tomography
FB	Force balance
FFT	Fast Fourier Transform
fps	Frames per second
HETP	Height equivalent theoretical plate
HP	High pressure
HTU	Height of transfer unit
HWA	Hot wire anemometry
LCD	Liquid crystal display
LDA	Laser Doppler anemometry
LDR	Level detection and recording
LED	Light-emitting diode
LP	Low pressure
MW	Mega watt
NCP	Needle contact probe
Nd: YAG	Nd:Y ₃ Al ₅ O ₁₂
NTU	Number of transfer units
PDA	Photochromic Dye Activation
PIV	Particle image velocimetry
PLA	Poly lactide

PLIF	Planar Laser Induced Fluorescent
PMMA RhB	Poly methyl methacrylate Rodamine B
POD	Proper Orthogonal Decomposition
PTV	Particle tracking velocimetry
PVC	Poly(vinyl chloride)
PSA	Pressure swing adsorption
VPSA	Vacuum pressure swing adsorption
VLE	Vapour Liquid Equilibrium
μ -SPIV	Stereoscopic micro particle image velocimetry

Nomenclature

A	Absorbance
a_e	Effective interfacial area (m^2/m^3)
a_p	Specific area (m^2/m^3)
B	Width of test plate (m)
b_c	Distance between 2 peaks of corrugations (m)
C_s, C_{in}, C_{out}	Saturated concentration of gas, concentration of gas at the film inlet, dissolved concentration (moles)
C_G, C_L	Capacity factor (m/s)
C_t	Correction for time or kinetic energy correction
c_{var}	Velocity of the varicose waves (m/s)
d	Diameter of perforation (m)
D	Diffusion coefficient in liquid phase (m^2/s)
d_H	Hydraulic diameter (m)
d_i	Apparent size of the tracer particle (m)
d_p	Particle diameter (m)
d_R	Rim diameter (m)
$\frac{dP}{dZ}$	Pressure drop (Pa/m)
f	Frequency (Hz)
F_G	Kinetic factor of gas ($\text{Pa}^{0.5}$)
F_c	Kinetic factor of gas at holdup ($\text{Pa}^{0.5}$)
g	Acceleration due to gravity (m/s^2)
h	Curtain half-thickness (m)
h_c	Height of corrugations (m)
h_L	Holdup
h_p	Height of the wave peak (m)
h_s	Height of structured packing bed (m)
I	Intensity of transmitted image (counts)
I_0	Light intensity of reference image (counts)
k_L	Mass transfer coefficient in liquid phase
k_v	Viscosimeter constant
k	Wave number, index

L	Length of test plate (m)
l_a	Length scale associated with the curved channel cross-section (m)
l_c	Capillary length (m)
l_v	Visco-gravitational length (m)
\mathcal{L}	Characteristic length of the relaxation (m)
m	Standard deviation of normal distribution
N	Number of perforations
p	Slope
$q_L, {}^1q$	Supply flowrate (m ³ /s)
q_b	Liquid volume flow rate on the back of the plate (m ³ /s)
$Q_L, {}^1Q$	Supply volume flow rate per unit width W (m ³ /m h, m ³ /m s, m ³ /m min)
Q_b	Volume flow rate per unit width (m ³ /m min)
Q_f	Flowmeter reading (L.s ⁻¹)
Q_m	Measured flow rate (L.s ⁻¹)
Q_1, Q_2	Front and back side flow rate per unit width (m ³ /m min)
Q_{cr}	Curtain Reynolds number (m ³ /m min)
Q_{th}	Threshold flow rate (m ³ /m h)
R_1	Radius of the curvature of curved rim (m)
Ra	Roughness (m)
s	Spacing (m)
S	Spread factor (m)
t	Plate thickness (m)
t_v	Time in viscosity measurements (s)
u_G	Vapour superficial velocity (m/s)
u_L	Liquid superficial velocity (m/s)
u_{th}	Theoretical mean flat film velocity (m/S)
u_x	Axial velocity (m/s)
u_y	Transverse velocity (m/s)

u_w	Wave phase velocity
V	Local attenuation of the signal
w	Width of the film (m)
w_a	width of the array (m)
2x	Molar fraction in liquid phase
$x^\#$	Rescaled streamwise position (m)
x_e	Highest measuring point within the curtain (m)
2y	Molar fraction in vapour phase
y_c	Spanwise peak position (m)
Z	Packing height (m)
Z_i	Packing height at i position (m)

¹ Volume flowrate in liquid phase in chapter 2, 3, 4 and 5

² x and y are coordinates unless otherwise specified as molar fractions

Dimensionless numbers

Bo	Bond number $\left(\frac{g(\rho_L - \rho_G)\delta^2}{\sigma}\right)$
Ca	Capillary number $\left(\frac{\mu u_{th}}{\sigma}\right)$
De	Dean number $\left(Re \sqrt{\frac{d_R}{R_1}}\right)$
Ga	Galileo number
Ka	Kapitza number $\left(\frac{\sigma}{\rho(g \sin \alpha)^{1/3} \nu^{4/3}}\right)$
N_λ	Dimensionless wave separation $\left(\lambda \left(\frac{g}{\nu^2}\right)^{1/3}\right)$
N_{uw}	Dimensionless wave celerity $(u_w / (\nu g)^{1/3})$
N_{hp}	Dimensionless wave peak $(h_p (g / \nu)^{1/3})$
N_f	Dimensionless frequency $\left(\frac{f}{(\nu^{-1} g^2)^{1/3}}\right)$
Re_g	Gas Reynolds number
Re_L	Liquid film Reynolds number $\left(\frac{\rho Q}{\mu}\right)$
Re_{cr}	Curtain Reynolds number $\left(\frac{\rho Q_{cr}}{\mu}\right)$
Sc	Schmidt number $\left(\frac{\nu}{D}\right)$
Sh_g	Sherwood number $\left(\frac{k_L L}{D}\right)$
St	Stokes number $\left(\frac{\tau_p}{\tau_\kappa}\right)$
We	Weber number $\left(\frac{\rho Q^2}{h \sigma}\right)$
X	Overflow number (Q_t / Q)

Greek letters

α	Inclination of corrugation to horizontal (degree or rad)
β	Crimp / folding angle (degree or rad)
δ	Film thickness (m)
δ_c	Maximum rivulet film thickness (m)

$\delta_c^\#$	Rescaled maximum rivulet film thickness (m)
δ_{Nu}	Nusselt film thickness (m)
δ_∞	Film thickness far from perforation or Flat film thickness (m)
ε	Dimensionless perturbation amplitude of the film thickness
ω	Dimensionless frequency of the neutral disturbance
λ	Critical Taylor wavelength (m)
μ	Dynamic viscosity (Pa.s)
μ_L	Dynamic viscosity of liquid (Pa.s)
ν	Kinematic viscosity (m^2/s)
φ	Phase angle (rad)
ρ	Density (kg/m^3)
ρ_G	Density of the vapour (kg/m^3)
ρ_L	Density of the liquid (kg/m^3)
σ_{sv}	Interfacial tension between vapour/solid (N/m)
σ_{sl}	Interfacial tension between vapour/liquid (N/m)
τ_p	Response time of the particles (s)
τ_κ	Kolmogorov time scale (s)
θ	Dynamic contact angle (rad or deg)
θ_r	Receding contact angle (deg)
θ_a	Advancing contact angle (deg)

Introduction

Air Separation Units (ASU) are major industrial systems allowing the industrial production of oxygen, nitrogen and argon from air. The history of such systems started with the first successful liquefaction of air by Polish scientists Zygmunt Florenty Wróblewski and Karol Olszewski in 1883. Soon after, Carl Paul Gottfried Linde, in 1899, developed a dual pressure cycle that produced up to 50 L/hr of liquefied air. Linde commercialised the process for the first time and developed the technique of distilling liquid air to produce oxygen and nitrogen. Around the same time, Georges Claude proposed a more efficient expansion engine (see **Figure 1**) to reach cryogenic temperatures. Claude liquefied air by allowing a fraction of high-pressure air in a Joule-Thompson cycle to expand and cool in a reciprocating engine before returning it to the low-pressure side of a heat exchanger. The process adopted by Claude increased the efficiency of the liquefaction of air and permitted the use of lower pressures. Therefore, the production of oxygen by air separation through cryogenic distillation became much cheaper than by chemical means. Georges Claude collaborated with Paul Delorme, a visionary entrepreneur, to create « Air Liquide », one of today's world-leading supplier of industrial gases and services for industry.

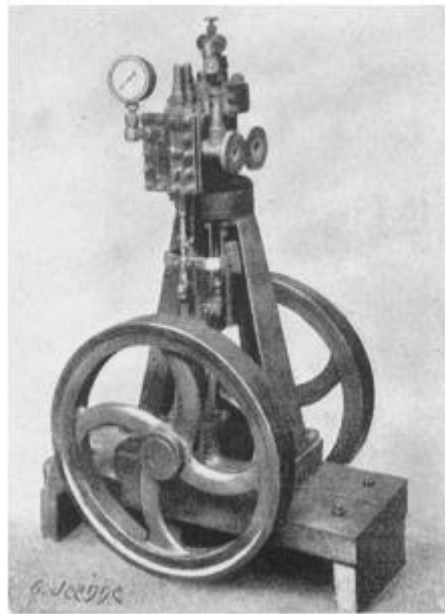


Figure 1: An image of George Claude's original expansion engine¹ (1913).

Although there are different approaches to air separation, such as adsorption and membranes, cryogenic distillation is the only process that combines high product purity (95-99.98%) and large production capacity (more than 5,000 tonnes of oxygen/day per ASU). The separation of air constituents in a distillation column during the intensive contact between the liquid and

vapour phases is promoted in the packing material's tortuous internal pathways. However, large production rates and purities come at the cost of high energy consumption. ASUs require a large amount of energy to function correctly and the investment cost to set up a plant is also high compared to other separation processes. The main challenge of this process is to achieve high separation performance and, at the same time, keep the column heights, investment and operation costs low. Significant progress of gain in performance was made in the mid-1980s when structured packings were used for the first time. Structured packings are widely used in the range of low liquid rate (typical in distillation column operating under 2500 Pa) applications where minimizing column pressure drop is important. Structured packings provide continuous contact between the liquid and vapour phases without full disengagement between top and the bottom bed of the packing whereas trays provide stepwise contact. Thus, structured packings offer a high void fraction (better use of column volume) and a high effective exchange area. In order for structured packing to function at its full capacity, it is crucial to guarantee good liquid distribution all along the packing surface. After having visualised the operating column internals through modern optical techniques, researchers have marked the importance of the geometry of surface features (corrugations, perforations, etc.) and the need for optimization to prevent maldistribution within the packing, particularly far from the distributor outlets or radially away from the center of the packing. Therefore, a comprehensive study is necessary to understand and quantify the flow structures on the surface features to optimize their shape and size, leading to both intensification of mass transfer between the two phases and homogeneous liquid distribution over the packing material.

Researchers dating back to the 80s have proposed innovative methods to understand the global liquid distribution within structured packing. This work has led to the development of original experimental techniques to visualise the interior of the packing in operation. However, these experiments face difficulties explaining the physical phenomena that occur at the liquid film scale during distillation. Very few attempts have been made to quantify the behaviour of the liquid phase on an individual metallic sheet with complex geometry. In this thesis, we aim to investigate the hydrodynamics of the liquid film on the simplified form of a corrugated and perforated metallic sheet. The objective of the thesis is to study different mechanisms of liquid distribution on the corrugated and perforated metallic sheets of structured packing.

This doctoral project is part of a CIFRE collaboration between Air Liquide and the Laboratoire de Genie des Procédés et Matériaux (LGPM). We isolate perforations from the corrugated perforated packing element to consider perforations on a flat plate. This simplification is done to adequately capture and quantify the physical mechanisms endured by the liquid film while

falling over perforations. We examined the liquid films on a vertical perforated metallic plate. To do this, we have designed and constructed an experimental test bench integrating non-intrusive optical techniques to measure liquid film thickness (Confocal Chromatic Imaging) and velocity. A state-of-the-art 3D 3C PTV with the concept of defocus, previously developed to measure the velocity around obstacles composed of a vertical set of cooling rods in nuclear power plants, is applied in the case of micro-scale liquid films on a flat and perforated plate to gain access to the 3C velocity components on the supported and suspended liquid film in 3D space. We propose physical models that account for the experimental results.

Structure of the thesis manuscript

The study is organized into five following chapters:

Chapter 1 provides a brief introduction of the cryogenic air distillation process with its historical evolution. Different types of column internals with their function, advantages and disadvantages are presented. The parameters associated with the performance of the structured packing column are discussed. Different physical phenomena such as: surface renewal, effective area of exchange, mass transfer between the two phases, pressure drop, and holdup of the column are explained. A literature review is conducted on the importance of liquid distribution within the structured packing, ranging from column scale (10 m) to liquid film scale (100 μm), considering both liquid-only and two-phase flow. The theoretical background of liquid film dynamics and its importance for the wetting phenomenon is discussed. A summary of existing works (both numerical and experimental) on liquid films on flat surfaces and topographical surfaces is presented. Finally, we complete this chapter by reviewing recent advancements in measurement techniques applied to liquid film characterization.

Chapter 2 describes the design of the experimental facility to test metallic sheets with complex surface features such as perforations on a flat plate, horizontal corrugations, wire mesh/grid type flat packing in a vertical configuration. This test bench allows two-face supply, which mimics industrial conditions. The geometrical and flow parameters used in chapters 3, 4 and 5 are detailed. Measurement methods are described, as well as their respective calibration and validation.

In chapter 3, we investigate the different regimes of a liquid film flowing around and over a single perforation for a wide range of perforation size (perforation diameter and plate thickness), fluid properties (Kapitza number), and flow parameters (Reynolds number). We focus on the liquid curtain mode. Transition to this regime is thoroughly characterized. A theoretical model is established to predict the curtain formation within a perforation. The

criterion of curtain formation is applied to liquid nitrogen flowing on an industrial packing (Mellapak 500Y).

In chapter 4, we study the volume flow rate transferred through the perforation in the case of a single perforation and then extended from one to several lines of perforations. The influence of the perforation diameter, spacing, and plate thickness on the transferred flow rate is studied. In the second part, we analyze the spreading of the rivulet that flows out of a perforation on the back of the plate. We examine the merging and the leveling of the rivulets flowing from a spanwise row of perforations. Finally, we study how fast the liquid flows balance on either side of a plate with a staggered array of perforations.

In chapter 5, we introduce a new measurement technique known as 3D 3C Particle Tracking Velocimetry by defocus. At first, the methodology is tested and validated on the liquid film over a flat plate. Then the flow structures in the vicinity of the perforation and the liquid curtain formed in the perforation are investigated for a plate with a single perforation. We post process the images using Dynamic Mode Decomposition (DMD) to identify the dominant modes associated with specific flow structures such as vortices.

A general conclusion closes this manuscript. We also propose some avenues in the continuation of this work, such as the quantification of liquid distribution on corrugated-perforated sheets and other industrial geometries (SiC packing, porous packing, gauze packings), the improvement of the newly developed 3D 3C PTV technique, its extensive use to study the different flow structures within a structured packing and their contribution to mass transfer.

1. Bibliographic review

1.1. Air distillation

1.1.1. Need of air distillation

Industrial gases are crucial for modern industries such as chemical industries, medical applications, aviation, steel making. In steel production, oxygen is used to lower iron's carbon content and convert it to steel. Oxygen is also needed in the gasification of hydrocarbon feedstocks to generate synthesis gas to produce fuels and chemicals. The global need² for pure O₂ between 2005 and 2010 is approximately 7.8% (per year), which resulted in a continuous increase in innovative production techniques. There are three leading air separation technologies for the production of nitrogen, oxygen, and argon production: cryogenic air separation, membrane separation processes, Pressure Swing Adsorption (PSA), and Vacuum Pressure Swing Adsorption (VPSA). The most efficient technology to obtain air gases (i.e., nitrogen, oxygen, and argon) in large quantity is cryogenic distillation³. Indeed, cryogenic air separation accounts for the production of air gases of high purity (99.8% of O₂) on a large scale (up to 5000 tons/day) with high reliability and in gaseous or liquid form. Moreover, the cryogenic distillation of air is the only viable source of rare gases (Neon, Krypton, and Xenon). **Table 1-1** presents a comparison of various air separation technologies with their economically feasible purity limits^{3,4}.

Separation Process	O ₂ Purity (vol.%)	Capacity* (tons/day)	By product capability	Energy demand (kWh/ton O ₂)
Cryogenic (Matured)	99+	Up to 5000	Excellent	> 200 (Electricity)
Adsorption (Matured)	95+	Up to 340	Poor	> 250 (Electricity, Heat (70-90 °C))
Chemical (Developing)	99+	-	Poor	Electricity
Membrane (Matured)	~40	Up to 20	Poor	Electricity
Ion transport membrane (R&D phase)	99+	Lab scale	Poor	Electricity, Heat (800 °C)

*Typical production range where the technology is currently economically feasible

Table 1-1 : Modern industrial air separation technologies listing its performance and energy demands

The cryogenic process is today's preferred route for the supply of industrial gases to large facilities.

Air Liquide is one of the world-leading organizations in gas, technologies, and services for industry and health. Present in 78 countries with approximately 65,000 employees, the group serves more than 3.8 million customers and patients. Founded in 1902, the group has excellent expertise in cryogenic separation. Air Liquide across the globe operates three hundred seventy-three large ASU plants. A typical ASU produces 330 to 5000 tons of oxygen per day at 99.6 to 99.8 % purity with a specific energy consumption of 200 to 350 kWh/ton of oxygen. Over the years, the separation process has evolved in design, capacity, efficiency, and energy consumption. However, cryogenic air separation accounts for 1% of the world's electricity, which is significant and demands further improvement in its design and operation.

1.1.2. Air separation challenges

The compressors of an ASU have a very high electricity requirement to compress the incoming air. A typical 3,000 tons of oxygen per day plant producing gaseous oxygen under pressure for industrial uses can consume about 31 MW. A network of oxygen plants for pipeline operation may require an electric power supply of several hundred megawatts. The low temperature operation required for cryogenic air separation is an energy-intensive process due to the compression-expansion cycles. The compressors are powered with electricity involving high costs. Electric power is the primary operating cost of an air separation plant since its feedstock is atmospheric air and is essentially free. Therefore, energy consumption is a challenge in ASU design and operation.

Over the years, researchers have focused on innovative methods to optimize the design of ASUs to lower the plant's energy use and thus the overall cost. Over the past four decades, the estimated power consumption⁵ of oxygen production shows a significant decrease (see **Figure 1-1**). The strategies to improve the power consumption of the separation process ranges from plant scale to packing material scale. Some plant scale strategies to reduce energy usage include using heat pumps to increase thermal efficiency⁶ and a dynamic model-based optimization⁷ for identifying design characteristics. Improvements in compressor and turbine manufacturing process using computational fluid dynamics (CFD) combined with three-dimensional machining to find the optimal form of the different parts have increased machine efficiency⁸. At the distillation column scale, the main challenge is to achieve high separation performance while keeping the column heights and the investment costs low. About 19 years ago, the use of structured packing as liquid vapour contactor had made low column height possible. Due to

high efficiency and reduced pressure drop⁹, structured packings have significantly influenced the energy performance of the overall process. The performance of structured packing is assessed by its capacity, its pressure drop, and its mass transfer characteristics at all operating conditions. The performance characteristics depend on the fundamental interactions between the liquid and vapour phases within the structured packing. Therefore, the efficiency of a structured packing translates into an economic advantage for both users and vendors through column height reduction, high capacity and low-pressure drop.

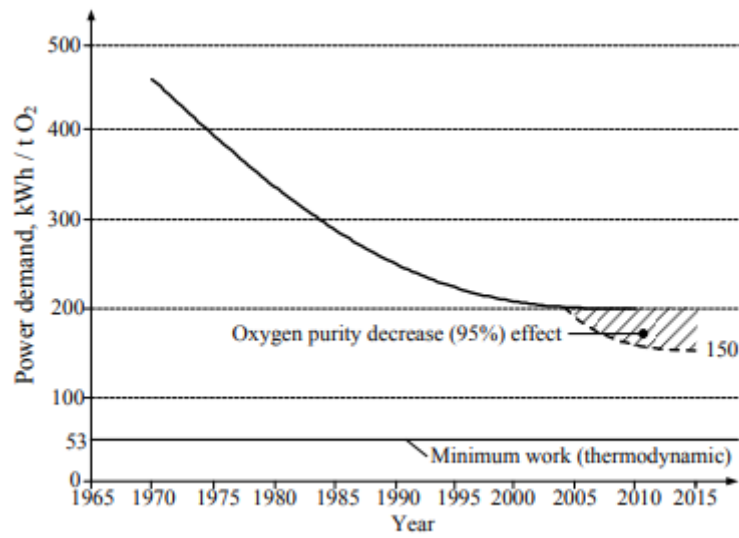


Figure 1-1 : Time evolution of energy demand for oxygen separation

1.1.3. Safety and reliability in design and operation

Industrial cryogenic air separation has some potential risks that must be recognized and addressed. The hazards include electricity, gases under pressure, very low temperatures, the ability of pure oxygen to accelerate combustion, and the asphyxiant properties of nitrogen, argon, and rare gases. Cryogenic air separation technology is rapidly growing due to the market demand for pure air products. Consequently, plant process cycles, equipment, and operating conditions can be of varying kinds.

Some health hazards associated with the compressed gas industry are exposed to extremely low temperatures, oxygen-deficient (asphyxiating) atmospheres, or oxygen-enriched (increased fire risk) atmospheres. Basic knowledge of the gas properties and taking precautions, such as wearing protective equipment, minimizes the risks of these hazards.

Materials used in a typical ASU are exposed to a wide range of temperatures, pressures, and purities during operation. Compatible materials must be selected to go along with the operating conditions of the column. For example: for a safe operating oxygen system, all parts must be

compatible with the oxygen exposure under all situations they encounter. The system must be designed to prevent oxygen combustion by selecting compatible material, operating within the designed pressure, temperature, and flow limits, and obtaining/maintaining cleanliness required for oxygen service.

Packing material is mainly made of aluminum, and they shall be kept clean and dry during storage, transport, and installation. A seal should be maintained to prevent water ingress into aluminum packing when stored outdoors or installed in the column. The packed column should be pressurized for transportation and checked for pressure at delivery.

1.2. Theory and working of ASU

1.2.1. Working principle and operation of ASU

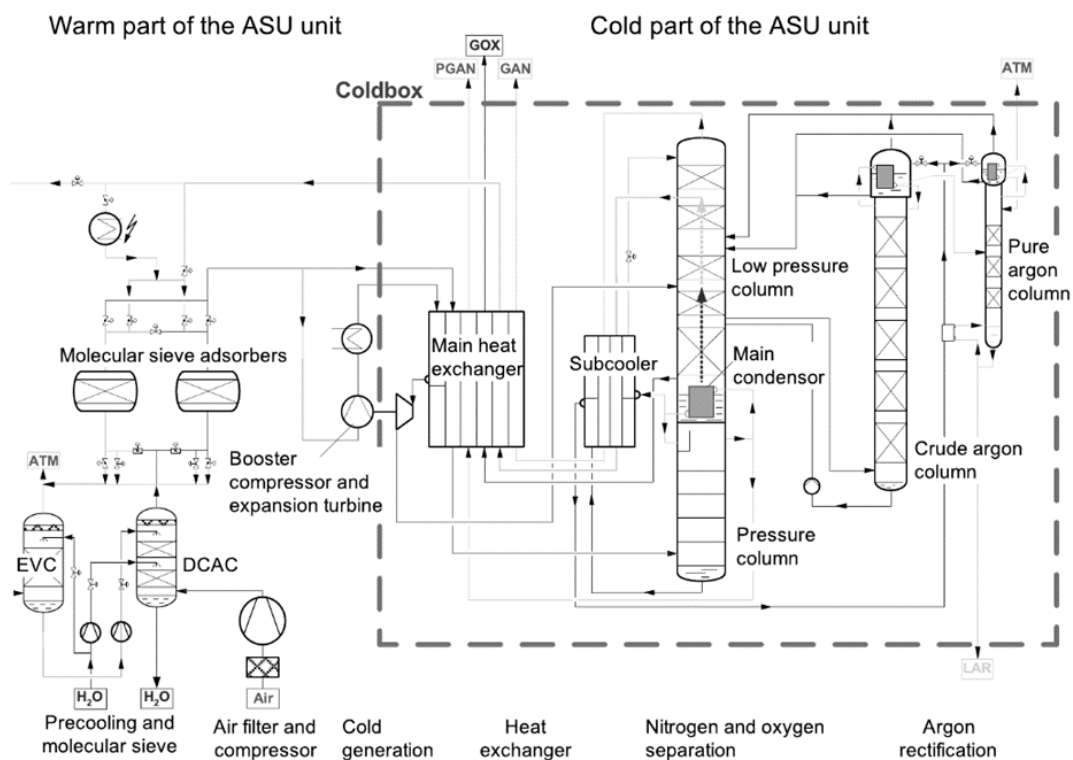


Figure 1-2: Flow diagram¹⁰ of a particular Air Separation Unit (ASU) process for the production of pure N₂, O₂ and Ar.

The general working principle of ASU is described in the flow diagram of **Figure 1-2**. The process takes place in 5 main steps explained in the following sections.

Air compression and purification

Air is first compressed to about 6 bar in a multi-stage compressor. As air separation occurs at cryogenic temperatures, impurities such as water vapour, carbon dioxide, and certain heavy hydrocarbons might solidify, thus plugging the cryogenic piping. Therefore, compressed air needs to be cleaned from impurities. Compressed air passes through a water-cooler which condenses any water vapour, and the condensed water is removed in a water separator. The air passes through an alumina bed and a molecular sieve adsorber, which traps CO₂, heavier hydrocarbons, and any remaining traces of water vapour.

Cooling

Part of the compressed air at the exit of adsorbers is 'boosted' to about 9 bar and sent to the main heat exchanger. The temperature of air mixture at the exit of the heat exchanger is -120 °C. The temperature is further lowered through the expansion in the turbine. Then the stream is injected directly into the low-pressure column to provide the required cold energy for operation. The other part of air exiting the adsorbers passes through the entire section of the main heat exchanger. The incoming air stream is cooled down to the dew point at -173 °C in counter-current flow to the cold products (oxygen and nitrogen streams coming from the columns) and fed to the bottom of the HP column.

Distillation

The heart of the air separation process is the distillation columns, where the liquid and vapour phases are brought into contact. Cryogenic distillation separates O₂, N₂, and Ar by fractional distillation. The process of separation takes place in large columns of a typical height of 15 to 60 m high and up to 6 m in diameter. The bottom column, known as the High Pressure (HP) column, typically operates at around 5.5 bar and is used to extract nitrogen. The top column, known as Low-Pressure (LP) column, operates at around 1.5 bar. The difference in working pressure between the two columns allows the liquid at the bottom of the LP column (nearly pure oxygen at ca. -180.5°C) to be boiled using the condensation of the vapour at the top of the HP column (nearly pure nitrogen at ca. -178°C).

At its dew point, air entering the HP column loses additional heat as it works its way up the column. The vapour that condenses is enriched with oxygen. The oxygen liquefaction

continues, forming an oxygen-rich mixture at the bottom of the high-pressure column, while most of the nitrogen flows to the top as a vapour. Some of the condensed nitrogen at the top of the HP column and the oxygen-rich liquid at the bottom are sent to the low-pressure column. The majority of the argon stays with oxygen in the enriched liquid sent to the LP column from the bottom of the HP column. To avoid partial vaporization due to expansion of the liquid streams sent to the LP column at their bubble point, the liquid streams are cooled down in a subcooler in the counter-current of the cold nitrogen product. The condenser/boiler between the two columns is interconnected to function as a condenser for the high-pressure column. Part of nitrogen from the top of the high-pressure column is liquefied, and it becomes the liquid reflux in the HP column, whereas the liquid bath of the low-pressure column is partially vaporized.

A gaseous mixture consisting mainly of oxygen, and argon is drawn from the low-pressure column and sent to the argon column to separate argon, leaving an oxygen-enriched stream with 10% of argon at the bottom of the argon column, which is sent back to the LP column. Almost pure argon (crude argon) in vapour form is recovered from the top of the argon column. High purity argon is obtained by removing the remaining nitrogen in a fourth column (**Figure 1-2**).

1.2.2. Vapour-liquid equilibrium and mass balance

The separation of pure components from the air is based on the principle of fractional distillation. This process involves an intimate contact between liquid and vapour phases. Air components' separation is based on the difference in their relative volatility. The driving force for the separation is the difference between composition in vapour phase and liquid phase due to the difference of properties such as boiling point and vapour pressure. The evolution of the vapour and liquid composition can be determined by a series of equilibrium stages within the column. In a steady state, liquid and vapour phases entering a stage are in complete contact with each other at all times, and the vapour leaving the stage is in equilibrium with the liquid leaving the stage. So, any distillation calculation, therefore, depends on the precision with which one estimates this liquid-vapour equilibrium. The graphical McCabe Thiele method is used to solve the equilibrium relation and the mass balance for binary distillation (see Appendix 1).

1.3. Column internals

1.3.1. Counter-current gas flow in the column

In the pressure columns, gas-liquid contact is achieved by counter-current flow in which gas flows upwards against the down-flow of liquid. The falling liquid phase comes in contact with the gas phase through the vapour-liquid contactors, which can be either tray or packing material (see **Figure 1-3**).

The liquid and gas are contacted in a tray column in a stage-wise manner on the trays, while gas-liquid contact is continuous in a packed column. These two types of packing material differ considerably in their performance characteristics. Various kinds of vapour-liquid contactors have their advantages and disadvantages depending on the mass transfer efficiency, capacity, and pressure drop, ability to handle high-pressure, high liquid loads, vacuum pressure, low liquid loads, foaming liquids, polymerization, fouling conditions, column subject to motion suitability for a given application, actual physical implementations (workshop on-site, new unit or revamping cylindrical or non-conventional configuration), in addition to an intrinsic cost. Other process-related constraints are operating pressure, product sensitivity, fouling; geometrical constraints include revamping, equipment size, column shape; performance constraints include efficiency, capacity, pressure drop, and final operating costs (energy, column, and contactor costs). Any liquid vapour contactor must:

1. Be chemically inert to fluids used and must be corrosion resistant
2. Be mechanically resistant without excessive weight or bad machinability.
3. Be optimized regarding its void volume: it contains adequate passages for vapour and liquid without excessive holdup or pressure drop.
4. Have a high surface area to provide good contact between vapour and liquid phase
5. Be low cost
6. Have fouling resistance: packing material should not trap suspended solid particles in the liquid.

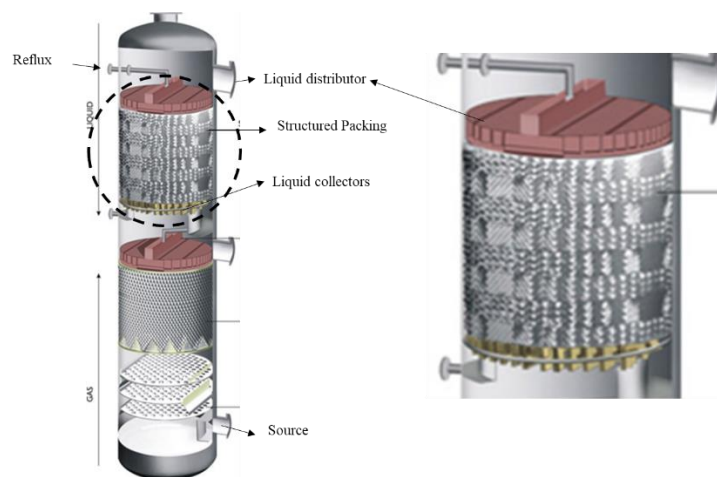


Figure 1-3: Different components in the distillation column.

1.3.1. Tray contactors

Tray towers are vertical cylindrical columns in which a vertical stack of trays or plates are installed across the column height, as shown in **Figure 1-4**. Tray columns are quite simple and more economical for high-pressure and high liquid flow rate applications than packed columns. There are three main types of plates: bubble cap type, valve type, and sieve trays. Each tray has one or more conduits called downcomers. Liquid falls through the downcomers by gravity from one tray to the one below it. A weir on the tray ensures that there is always a level of liquid retained on the tray. It is the pressure difference between inlets and outlets that drives the vapour. Vapour flows up the column and is forced to pass through the liquid via the openings on each tray. These trays in air separation were designed with very low tray spacing (100 to 200 mm instead of the usual 600 mm in other applications). The tray pressure drop depends on the detailed tray design. Generally, sieve trays provide the lowest pressure drop. The operation largely depends on the liquid or vapour feed rate. For example: if the feed rate is too high, the liquid will fill in downcomers and builds upon the trays. The increase in hydrostatic pressure restricts the vapour rising through the liquid. If overloading continues, flooding of the column occurs.

Consequently, if the vapour feed is low, the pressure exerted by the vapour is insufficient to holdup the liquid on the tray. Therefore, the liquid starts to leak through perforations (known as weeping). Dumping occurs at excessing weeping conditions, i.e., at a very low vapour flow rate when no liquid reaches the downcomer. The weeping increases with increasing fractional hole area and liquid flow rates.

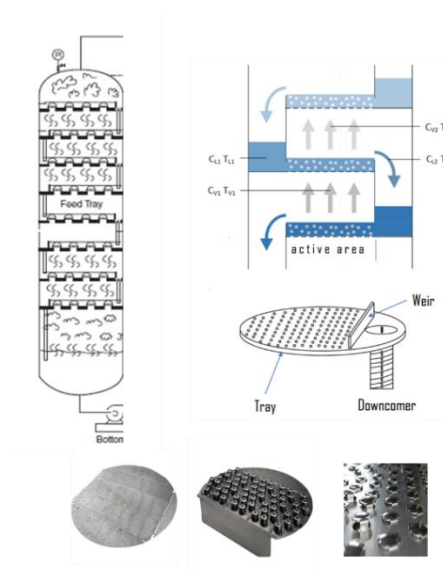


Figure 1-4: Inside of a tray column with an illustration of sieve, bubble cap and valve trays (respectively from left to right)

1.3.2. Random packings

Due to the limited operating range of tray columns, random packings were developed in the early 19th century with the use of broken glass or glass balls, pumice stone or pieces of coke. The individual elements of the random packing have well-defined shapes but are randomly arranged in the column. The idea of random packing is to impose randomness in gas-liquid interaction, favouring a longer path for the two phases. The efficiency of early random packings were unpredictable which was changed by the introduction of Raschig rings (see **Figure 1-5**) in early 20th century. They were developed by considering the importance of void fraction and the surface area in relation to mass transfer. New design feature was introduced with Pall rings. Pall rings consisted of openings on the wall (see **Figure 1-5**). This design reduced the limitations of prior packing types by improving packing area distribution, wetting, and liquid distribution. These packings had higher capacity, high efficiency and lower pressure drop. With the development in plastics, new plastic packing types were introduced. Many complex shapes became possible to construct, which would have been impossible to make from steel. Commonly used random packings are fabricated using stainless steel, ceramic or plastic material due to their corrosive resistant nature, high strength, fouling resistance, and easily interchangeable and cleanable.



Figure 1-5: Types of random packing¹¹

The liquid flows over the walls of these structures, leaving a certain amount of void to allow the circulation of vapour. Although these packings have a large interfacial area for exchange and low-pressure drop compared to trays, they suffer liquid holdup due to liquid retention in

the packing material. Random packings can perform well on both ends and in the middle of the range of operating pressures encountered in distillation. Still, cannot outperform structured packings' low-pressure drop and high interfacial area¹² (see **Figure 1-6**) in low liquid and vapour load application. However, random packing is an easy choice in high vapour and liquid load applications.

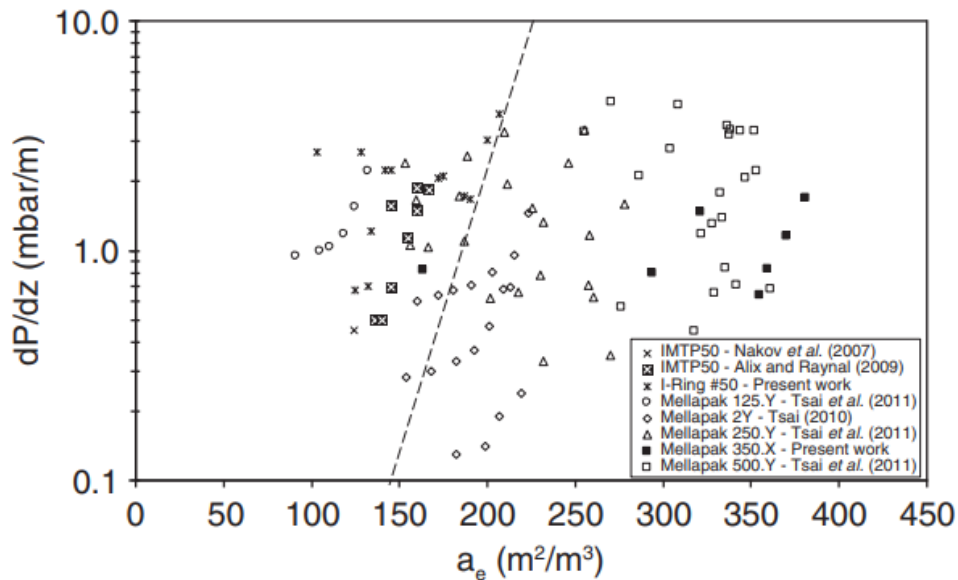


Figure 1-6: Comparison of the pressure drop of structured packings (Mellapak series) and random packings¹² (IMTP series, I-ring) for different effective interfacial area (a_e).

1.3.3. Structured packing

Structured packing was developed in the 1960s by Sulzer. However, a real breakthrough of structured packings occurred in the late 1970s, with the introduction of the Sulzer Mellapak series. The evolution of the structured packings over the years is shown in **Figure 1-7**. In 1982, B. Potier and J.-Y. Thonnellier from Air Liquide made a pioneering contribution by developing a range of structured packings for air distillation. And since then, structured packing has become predominant in cryogenic air separation columns. The packings are made of a stack of thin metallic sheets with complex structures which guide the liquid to spread across the metallic sheets flowing with long residence time, leading to a long vapour liquid contact time. Because of their tightly organized internal structure, these packings are capable of producing large capacity of pure substance for shorter packed bed height or a thinner column. At the same time, they offer low pressure drop¹³ resulting in a reduction of total volume. The advantage of structured packing over random packing is their low Height Equivalent Theoretical Plate (HETP) value (order of magnitude 0.1 m) and low-pressure drop (less than 100 Pa/m). HETP

will be defined in the later part of this chapter. At high operating pressures, it appeared that structured packings could not generally perform satisfactorily, whereas trays, particularly those handling large liquid loads with ease, remain the preferred choice. The cost of structured packing per cubic meter is significantly higher than the random packing, but its high efficiency compensates for this.

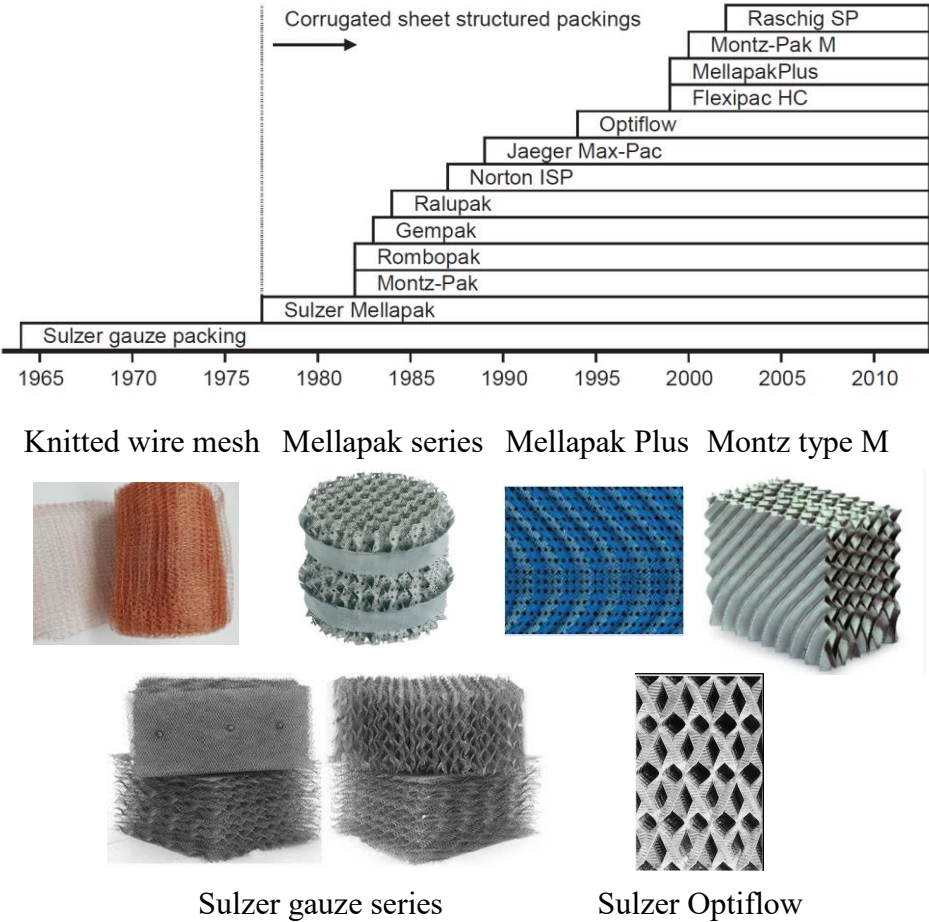


Figure 1-7: Historical timeline of structured packing¹⁴ (above). Photographs of some of the widely used structured packing (below).

1.3.4.1 Geometry of the structured packing

Structured packing comprises thin corrugated, textured, perforated, metallic or ceramic sheets stacked together to form a pile of packing material. The sheet thickness ranges from 0.1 to 0.5 mm. Certain structured packing elements are perforated ($d = 2 - 4$ mm). The fraction of the total perforation area is approximately 10 - 13% of the total surface area of the structured packing. The corrugations are usually inclined to the horizontal by an angle α , varying between 45° and 60° ¹⁵ (see **Figure 1-8ac**). The folding angle is the angle of crimp designated as β . The distance between two peaks of corrugations is b_c , the height of the corrugation is h_c and the

perforation of diameter d . A variety of structured packings can be created by varying these parameters. The direction of the corrugation crests of two consecutive sheets is alternated. The crests of one sheet make a 90° angle with the crests of adjacent sheets (see **Figure 1-8b**). This arrangement guides the flow in the transverse direction of the plate to facilitate liquid phase spreading. The height (h_s) of the structured packing bed depends on the desired purity of the product obtained from the column. Each packing element (or pack) is stacked vertically, one on top of the other and rotated by 90° . The packing is characterized by its specific area (a_p), which is the ratio of the total surface of the structured packing to its volume.

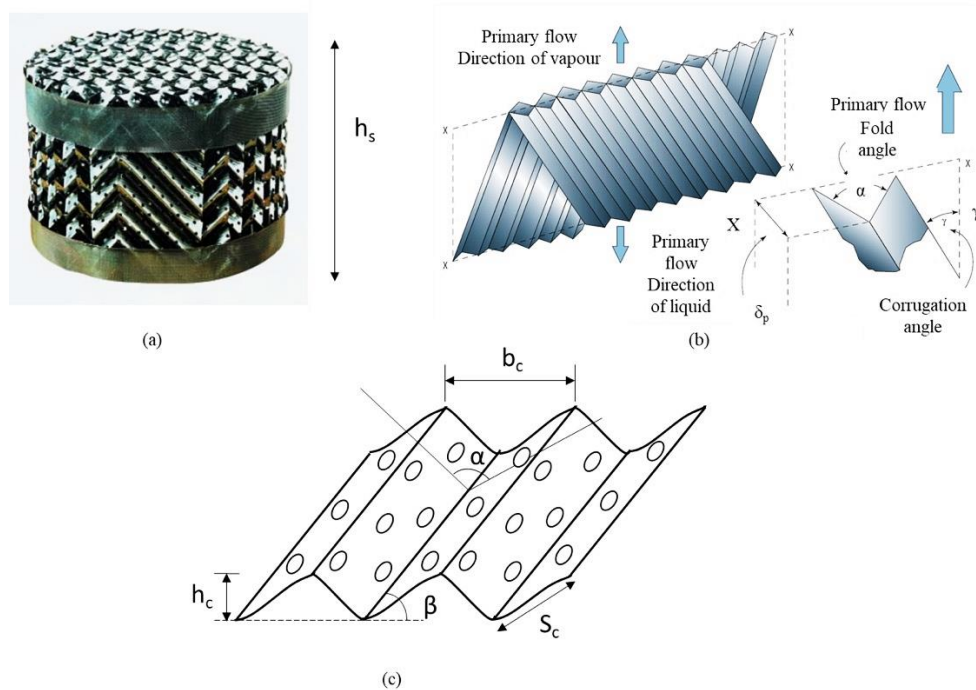


Figure 1-8: (a) Structured packing (b) Placing of the plates and flow paths through the channels (c) Sketch of a corrugated-perforated metallic sheet.

1.3.4.2 Surface features

The metallic sheets are sometimes chemically or mechanically treated to roughen the surface to improve wetting and promote the spreading of the liquid phase. Mechanical treatments can consist in folding the sheets into corrugations (at macro and micro-scale), at a given amplitude, woven metallic grids (like gauze type), surface indentations (small scale bumps of a characteristic size of the order of 1 mm). These features highly increase the intricacy of the flow in the column, augmenting surface instabilities and turbulence to enhance the mass transfer between two phases. In most structured packings (see **Figure 1-9a**), perforations, punching, and

grooving are made to facilitate the spreading and exchange of the liquid. Experiments performed on Mellapak 125X ($125 \text{ m}^2/\text{m}^3$) and WPA¹⁶ ($125 \text{ m}^2/\text{m}^3$) packing (see **Figure 1-9b**) show that the WPA packing yields a lower pressure drop, a higher capacity and a higher mass transfer efficiency compared with the traditional Mellapak 125.X packing for the same packing surface area. The difference in packing performance is explained by studying the effect of surface texture on the wetted area. A multi-scale hydrodynamic model based on VOF method¹⁶ is studied with and without counter-current gas. CFD simulation show that the average liquid thickness and the effective wetted area are higher on the rough surface than on the smooth surface (see **Figure 1-9c**). The free surface of the liquid film on the rough surface appears disturbed, which may have contributed to the increase of mass transfer.

The liquid passing through the holes creates a variety of gas–liquid contacts, like droplets^{17,18}, liquid sheet^{19,20}, liquid columns or bridges in addition to the contacts generated on the solid surface of the packing. According to Shi et al²¹, the effective interfacial area includes films on the packing surface and drops, jets, and sprays that flow through the voids of the packed bed. The wetted area can be divided into two parts: one occupied by the liquid film flowing over the surface of the packing and the other by the stagnant liquid.

In gas absorption, the fraction of the wetted surface occupied by the stagnant liquid quickly becomes saturated with gas. Since the renewal of this liquid is insignificant, it does not contribute to mass transfer. However, in distillation, these portions of stagnant liquid are also effective in the separation²².

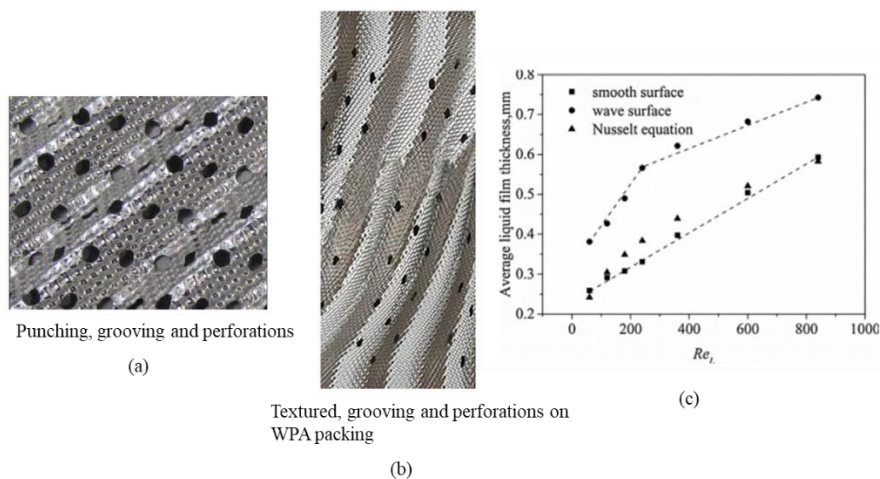


Figure 1-9 : (ab) Example of surface features on structured packing¹⁶, (c) Average liquid film thickness¹⁶ without counter-current gas flow

The liquid film on the sheet with surface features interacts with the gas through small amplitude waves¹⁸ or ripples at the gas/liquid interface. The recirculation motions of the liquid within the waves²³ favour mass and heat exchanges between the two phases. In another study²⁴, gas phase mass transfer is measured experimentally on flat and textured surfaces for pure components and then modelled by considering total wetting condition. Gas phase correlations were used to quantify liquid side resistance in binary mixtures. The dimensionless numbers characterising flow (Re_G, Re_L) and mass transfer (Sh_G) were used in the correlations to assess the influence of the different flow and physical properties on the mass transfer rate.

Sherwood number (Sh) is the ratio of the convective mass transfer to the rate of diffusive mass transport.

$$Sh = \frac{k_L L}{D_{AB}}$$

where k_c is the mass transfer coefficient, L is the Characteristic length and D_{AB} is the mass diffusivity, respectively.

Schmidt number (Sc) is the ratio of momentum diffusivity to mass diffusivity, used to and is used to characterize liquid film when momentum and mass diffusion convection occurs simultaneously.

$$Sc = \frac{\nu}{D}$$

The correlations also include the liquid flow term that incorporates the velocity of the film and the surface tension through the Weber number (We_L). Finally, the capillarity is incorporated through Bond number $Bo = g(\rho_L - \rho_G)\delta^2/\sigma$, a ratio of gravitational forces to capillary forces. The authors used the following correlations (highlighted in bold letters²⁵) (see **Table 1-2**) for gas and liquid phase mass transfer determined on flat and textured plate in the SRP and Delft distillation models²⁶. Performance of the textured surface was found better than the flat plate.

Flat plate	$Sh_G = 0.0044 Re_G Sc_G^{0.5}$
	$Sh_G = 0.0008 Re_{Gr}^{1.17} Sc_G^{0.5}$
	$Sh_G = 0.0030 Re_{Gr}^{0.96} Sc_G^{0.49} Re_L^{0.16}$
	$Sh_G = 0.0047 Re_{Gr}^{0.992} Sc_G^{0.537} We_L^{0.145}$
Textured plate	$Sh_G = 0.0463 Re_G^{0.76} Sc_G^{0.5}$
	$Sh_G = 0.0083 Re_{Gr}^{0.94} Sc_G^{0.5}$
	$Sh_G = 0.0375 Re_G^{0.78} Sc_G^{0.76} We_L^{0.21}$
	$Sh_G = 0.0067 Re_G^{0.77} Sc_G^{0.62} Re_L^{0.34}$
	$Sh_G = 0.0047 Re_G^{0.75} Sc_G^{0.55} Re_L^{0.39} Bo^{-0.09}$

Re_G : Gas Reynolds number; Re_{Gr} : Relative gas Reynolds number; Re_L : Liquid Reynolds number; We_L : Weber number;

Table 1-2 : Correlations proposed based on the experimental data²⁵

1.3.4.3 Performance criteria

Simple macroscopic models help to describe and quantify the packing performances including the mass transfer efficiency, the column capacity, and the pressure drop.

Mass transfer and packing efficiency

The Height Equivalent to a Theoretical Plate (HETP) is the first concept introduced to quantify the mass transfer efficiency within a packed column. The HETP is related to the packing height (Z) and the number of equilibrium theoretical plates (NETP) required for the separation through the relation:

$$Z = \text{NETP} \times \text{HETP} \quad (1.1)$$

where NETP is typically determined using the McCabe-Thiele method if the constant molar overflow assumption holds (see Appendix 1). NETP depends on the vapour-liquid equilibrium (VLE) data and the operating conditions such as the reflux ratio. The lower the HETP value, the greater the packing efficiency, meaning that a shorter packing bed would be required to reach a given product purity.

However, the concept of theoretical plate makes less sense for a packed bed where the compositions of the liquid and vapour phases vary continuously than for a tray column where changes in the composition occur stepwise. Furthermore, HETP values are specific to the

system being separated, the type of packing, and the hydraulics of the column. Another concept is often preferred for packed beds: the Height of a Transfer Unit (HTU).

HTU-NTU model

The concept of ‘transfer units’ was first proposed by Chilton T. and Colburn, A.²⁷ in 1935. It considers that the compositional changes throughout a packed column are continuous. The height of packings required for given separation specifications can be evaluated either from the gas-phase or the liquid-phase point of view. The packed height is then given by

$$Z = \text{NTU} \times \text{HTU} \quad (1.2)$$

where NTU is the Number of Transfer Units. NTU is a measure of the difficulty of the separation. HTU is a measure of the separation efficiency of the packing. Based on the liquid phase, the so-called overall NTU_{OL} reads:

$$\text{NTU}_{OL} = \int_{x_b}^{x_d} \frac{dx}{x - x^*} \quad (1.3)$$

where x_b is the bottom molar fraction of lighter (for example) component, x_d the molar fraction of the distillate, x the liquid current molar fraction, and x^* is the molar fraction of the liquid phase that would be in equilibrium with the current molar fraction of the vapour phase y .

The so-called overall height of a transfer unit based on the liquid phase is given by:

$$\text{HTU}_{OL} = \frac{u_L}{a_e k_L} \quad (1.4)$$

where u_L is the liquid superficial velocity (ratio of the liquid volume flow rate to the column section), k_L , is the overall mass transfer coefficient based on the liquid phase and a_e is the effective interfacial area. k_L incorporates the mass transfer coefficient in the liquid phase, the thermodynamic equilibrium at the interface between the liquid and the vapour phase, and the mass transfer coefficient in the vapour phase. The most commonly used models to estimate k_{OL} are the double-film model which assumes steady transfer through the boundary layers on the liquid and vapour sides, and the ‘‘Higbie’s model²⁸’’ which assumes that each liquid element at the vapour-liquid interface is exposed to the vapour for a short duration.

Capacity

The capacity of a column, i.e., its ability to handle a high vapour load, is limited by the onset of flooding. The capacity can be described in term of vapour load factor or F-factor:

$$F_G = u_G \sqrt{\rho_G} \quad (1.5)$$

where ρ_G is the density of the vapour and u_G is the vapour superficial velocity. The F-factor is proportional to the square root of the vapour kinetic energy.

An alternative descriptor is the capacity factor:

$$C_G = u_G \left(\frac{\rho_G}{\rho_L - \rho_G} \right)^{0.5} \quad (1.6)$$

where ρ_L corresponds to the density of liquid phase. This factor is defined from the force balance on a droplet entrained by the vapour at flooding velocity.

Spiegel *et al.*¹³ defined the capacity as the point of operation where the pressure drop attains a given threshold (Sulzer takes 12 mbar/m for a structured packing). Capacity mainly depends on the specific area of the packing, liquid load, vapour load, and physical properties of vapour and liquid. The Wallis diagram²⁹ is used to represent the capacity of a structured packing (see **Figure 1-10**). It gives a relation between the liquid and vapour load. Capacity and thus flooding are typically described by a linear relation between C_G and C_L . C_L is defined as

$$C_L = u_L \left(\frac{\rho_L}{\rho_L - \rho_G} \right)^{0.5} \quad (1.7)$$

where u_G, u_L are superficial gas and velocities, ρ_G, ρ_L are density of gas and liquid phases.

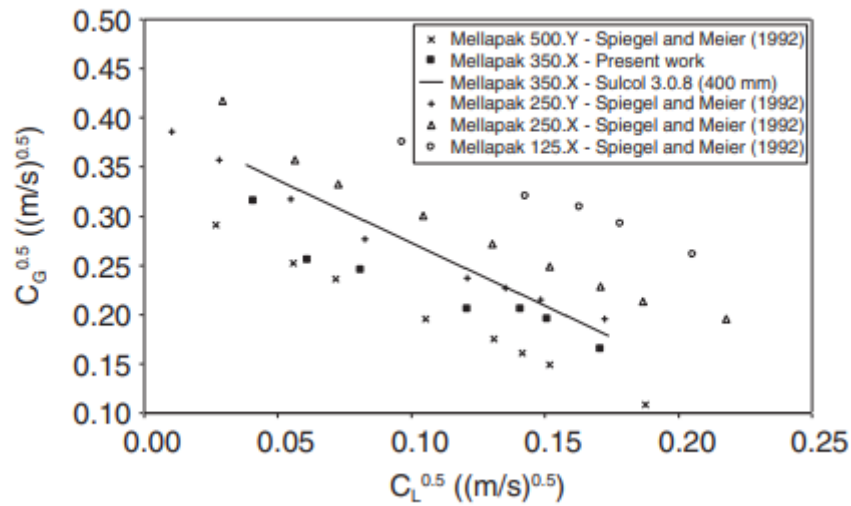


Figure 1-10: Wallis diagram of capacity for different structured packing material¹²

Effective surface area (a_e)

Mass transfer in air separation columns strongly depends on the effective interfacial area between the vapour and liquid phases. The design of the sheets is done to provide the maximum surface area possible to support the falling liquid film. In order to obtain a good liquid distribution and to achieve maximum effective surface area, liquid distributors are carefully

designed to introduce the liquid on several points on the structured packing. However, radial spreading of the liquid remains a challenge in packed columns. The surfaces far from the central zone of the packing often suffer from thin films or dry patches. Thus, the true wetted surface area, i.e., effective surface area a_e , is always less than the geometric surface area of the packing. a_e depends on the contact angle, liquid viscosity, and liquid surface tension. Wetting performance of Rompopak 4M³⁰ which is similar to Sulzer's Optiflow packing (undulatory metallic structures) is experimentally studied. The packing structure is different from classical Mellapak in their general shape, however, the textured surface is similar. In **Figure 1-11**, **A** corresponds to a liquid with high contact angle values, surface tension and viscosity. Liquid flows through the textures or undulatory surface in the form of rivulet. In **B**, rivulet spreads a little more with the increase in liquid flow rate. Some liquid leaks on the other side of the packing element. With the addition of surfactant as shown in **C**, contact angle, liquid surface tension are lower compared to (A). The liquid rivulet spreads significantly. Liquid leaks to the back through the formation of a bridge at the node. **D** corresponds to: for relatively low values of contact angle, surface tension and viscosity, uniform thin film is formed, wetting the packing surface on both sides.

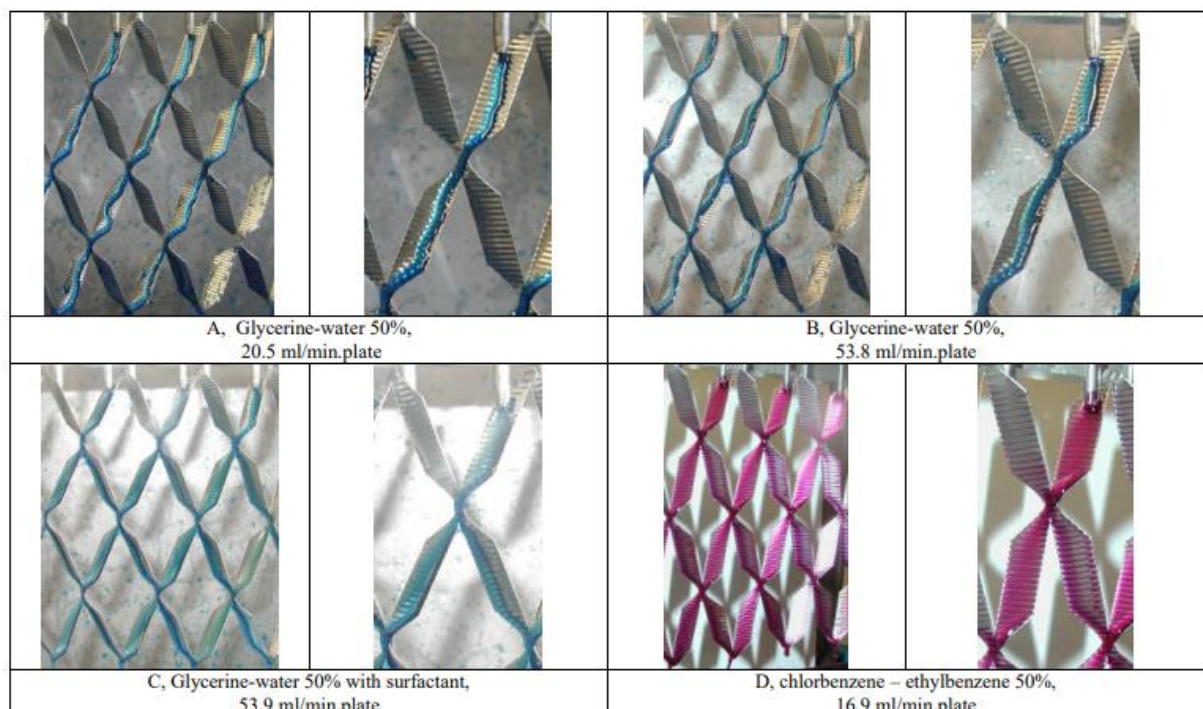


Figure 1-11 : Liquid flow patterns for different liquid systems³⁰ with a wide range of physical properties.

Another example shown in **Figure 1-12**, the injection point is slightly away from the surface of the packing element (10 mm away). This position of the irrigation point leads to drop formation in addition to the uniform liquid film on the packing surfaces.

Liquid viscosity has a stabilizing effect on the wetting of liquids but it is also a strong function of temperature. Due to which the viscosity varies widely in distillation columns. If the liquid viscosity is high, the rivulet is wide on both vertical and inclined plates. Increasing of the rivulet thickness produces higher interfacial area but also higher resistance to heat and mass transfer processes which is essential in packed columns. If the contact angle is small, rivulet profile is more flat (wetting degree³⁰ (a_e/a_p) increases from 0.499 to 0.59 if the liquid contact angles are reduced from 24.5° to 10° respectively) and the rivulet cross-sectional area increases with the decrease in velocity. Lower film thickness means lower resistance. Surface tension has small effect on the rivulet profile.



Figure 1-12: Liquid flow pattern for chlorobenzene – ethylbenzene 50% (16.9 ml/min.plate) with capillaries or irrigation points 10 mm distance apart from the plates surfaces³⁰

In some cases, effective interfacial area³¹ includes not only the surface area of the liquid film on the packing surface but also the surface area of the liquid jets and drops. Then, a_e may have a larger value than the specific surface area (a_p) of the structured packing. Regardless of their differences, both wetted surface area and interfacial area are adopted in the literature. Empirical models^{32,33} have been formulated for estimating the ratio $\frac{a_e}{a_p}$ for structured packings. Even if the use of corrugated sheet packings is well established for applications requiring a low-pressure drop and a high effective area, the liquid flow pattern within a structured packing needs to be studied in more detail.

Pressure drop & Liquid holdup

The ascending vapour in a structured packing suffers constant changes in direction due to the sheet structure. Furthermore, the liquid film makes the paths taken by the vapour narrower. If the vapour load is increased, the pressure drop increases up to the flooding point. An increase in pressure drop indicates that the counter-current gas flow through the column is restricted by liquid build up at some point in the column. Pressure drop is partly a consequence of the liquid hold up. The representation of pressure drop per meter as a function of vapour load factor is a common way of representing the pressure drop across a packing. The dry pressure drop is measured in a packed column in the absence of the liquid flow. It is always lower than the wet pressure drop measured with the liquid flow because the liquid flowing through the column changes the bed structure due to liquid holdup.

The liquid hold up is a crucial hydrodynamic parameter for the gas-liquid contact in packed columns. It is the amount of liquid held onto the surface and in the voids of the packing. The liquid holdup is normally expressed as a volume fraction (ratio of liquid volume to packed bed volume). Two kinds of holdup are distinguished:

- The static hold up is the accumulated liquid bound by capillary and adhesion forces that remains in the packing after irrigation is stopped. It is the liquid prevailing in the perforations, pores, gaps of the packing. The static liquid hold up is a function of the physical properties of the liquid phase (density, dynamic viscosity, and surface tension), the characteristics of the packing (packing void fraction and specific area), the liquid load, and the acceleration due to gravity
- The dynamic hold up is the amount of liquid that actively participates in the liquid flow. The dynamic hold up increases with the liquid velocity. An increase of the dynamic hold up results in a better mass transfer.

Olujić et al.³⁴ used a simple estimate of the liquid hold up. Under the assumption of well-distributed liquid without excessive entrainment, the liquid holdup (h_L) is simply the product of the packing surface area (a_p) and the liquid film mean thickness (δ).

$$h_L = \delta a_p \quad (1.8)$$

Based on experiments performed with liquid gas counter-current, Billet & Schultes³⁵ proposed the following correlation for the liquid hold up.

$$h_L = \left(\frac{12\mu_L u_L a_p^2}{g\rho_L} \right)^{0.33} \quad (1.9)$$

where μ_L is the liquid phase viscosity.

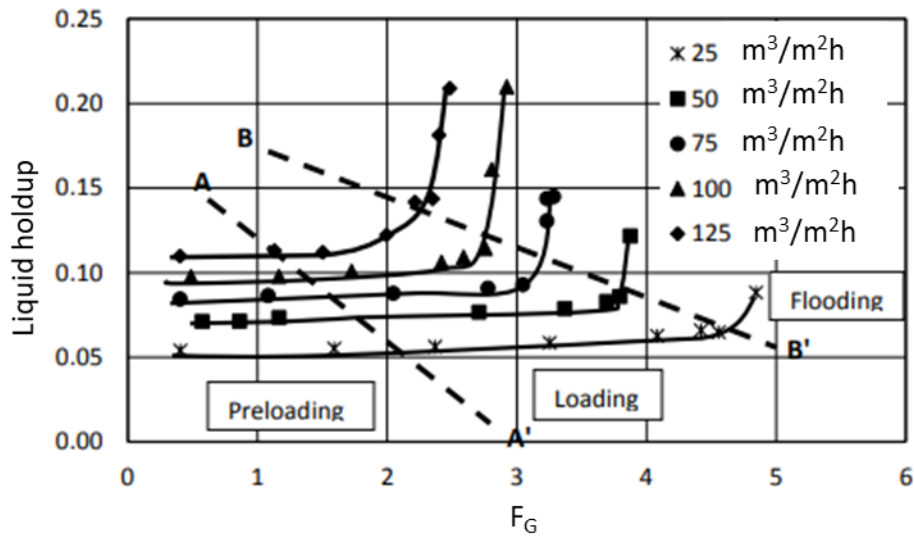


Figure 1-13: Experimental liquid holdup data³⁶ in different regions of operation for Sulzer Melapak 250X data, air/water, 1 bar.

Figure 1-13 show the typical variations of the liquid hold up as a function of the F-factor for varying liquid load. As the vapour load r increases, a change in the slope is observed at the so-called loading point. Above the loading point, the holdup increases significantly with the vapour load. As the F-factor is further increased, the holdup raises abruptly at the flooding point. Flooding poses a high risk in a packed column. At first liquid accumulates in local zones. With increase in gas flow rate liquid build-up eventually occurs. Liquid build-up has severe effects on the efficiency of mass transfer. At high gas flow rates, the liquid is pushed into the gas pipes leading to an adverse consequence like equipment damage.

1.4. Mechanism of liquid redistribution

1.4.1. Introduction

When the liquid is introduced at specific points on packing elements, it spreads longitudinally due to gravity and radially due to surface features such as corrugations, perforations, or micro-textures. Several mechanisms of redistribution are observed on the metallic sheets of structured packing:

1. The liquid phase is guided in the transverse direction of the sheets by the troughs of the corrugated sheets.
2. The liquid phase is transferred from one side of a sheet to another through the perforations, the slits, or the pores (of porous silicon carbide packings) of the sheets.
3. The liquid film flows from one sheet to another through the contact point between the corrugations of adjacent sheets.

- The microtexture of the sheets enhances the wettability and thus the spreading of the liquid on the sheets.

As liquid distribution in a packed column is a multiscale problem, it is often studied at different scales varying from the column scale (industrial column or pilot column) to the liquid film scale (see Figure 1-14).

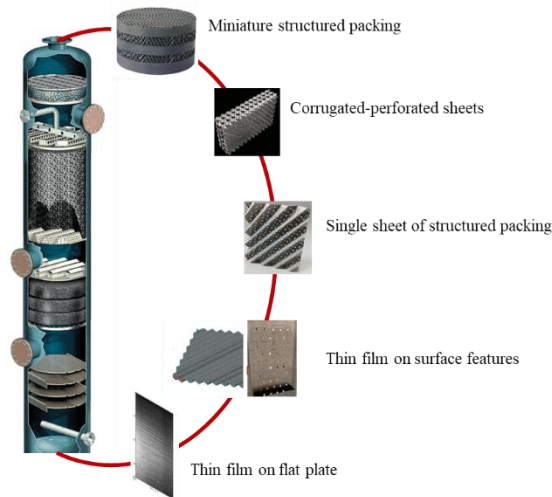


Figure 1-14: From structured packing scale to thin film scale.

1.4.2. Liquid redistribution at packing scale

Experimental study at column scale is necessary for validating theory and numerical models, quantifying global values of liquid holdup and effective mass transfer area, and the spatial distributions of these quantities. However, under cryogenic conditions, visualization of an operating column is challenging. The scaled-down column, operating at ambient temperature with a non-cryogenic liquid, is one of the most widely used approaches to perform experiments. Experiments are conducted using different designs of the packing elements^{37–39} (e.g., various corrugation angles, surface areas and surface treatments³⁷) to measure the pressure drop, the gas capacity, the liquid hold up, and the mass-transfer efficiency.

The most straightforward approach to studying the liquid distribution through a packing section is direct observation (transparent column) and collecting the liquid at different locations of the packing. Pavlenko et al.⁴⁰ studied the effect of liquid redistribution on separation efficiency in a column of 90 cm diameter and 6.8 m height with a counter-current gas flow. Using a mixture of Freon R21 and R114, they measured the distribution of the composition and the local liquid flowrates over the column cross-section in real industrial conditions. They found that the cross-

sectional liquid distribution is essentially non-uniform and is characterized by a noticeable decrease in the local liquid flowrate in a wall zone of a characteristic size approximately equal to the height of a single packing layer. Large-scale maldistribution within the packing is noted despite the uniform initial distribution at several points of the structured packing.

Since the early 2010s, promising non-intrusive methods have been developed to look inside a column: X-ray^{41-45,46} and gamma-ray^{41,47} Computed Tomography (CT) have been used to map the liquid distribution over a miniature-sized column.

X-ray CT has been applied to a non-cryogenic column equipped with Mellapak Plus 752.Y⁴². The study shows that the liquid introduced on the packing predominantly flows in liquid films on the packing surfaces. Due to surface tension forces, concave menisci form at the contact points between corrugations of adjacent packing sheets (see **Figure 1-15**). Flooded regions have also been observed. They result from a local increase in liquid load (see **Figure 1-15**).

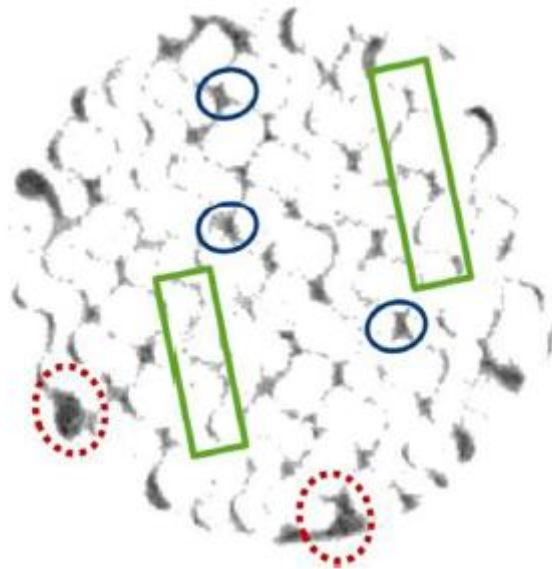


Figure 1-15: Flow patterns identified by X-ray CT. Green rectangles: film flow, blue circles: contact point liquid, red dotted circles: flooded regions⁴⁴

Using γ -ray tomography, Fourati et al.⁴⁷ obtained hold-up maps (see **Figure 1-16**) in different cross sections along with the height of a column packed with Mellapak 250X and fed with water. Their results show that the liquid distribution depends only on packing geometry and not on the liquid properties or liquid/gas flow rates.

CT analysis show that the packing elements are never evenly wetted with a constant liquid film thickness⁴².

Although computed tomography methods are used in small-scale columns to understand the effect of packing geometry, liquid load, and gas load, several pitfalls need to be overcome. One

limitation of computed tomography is that it can only be applied to non-cryogenic columns. The presence of thermal insulation layers around the packing may absorb most of the radiation. Moreover, it is difficult to capture the gas-liquid and liquid-solid interfaces because of the too-small film thickness and minor differences in ray absorptivity between liquid and solid.

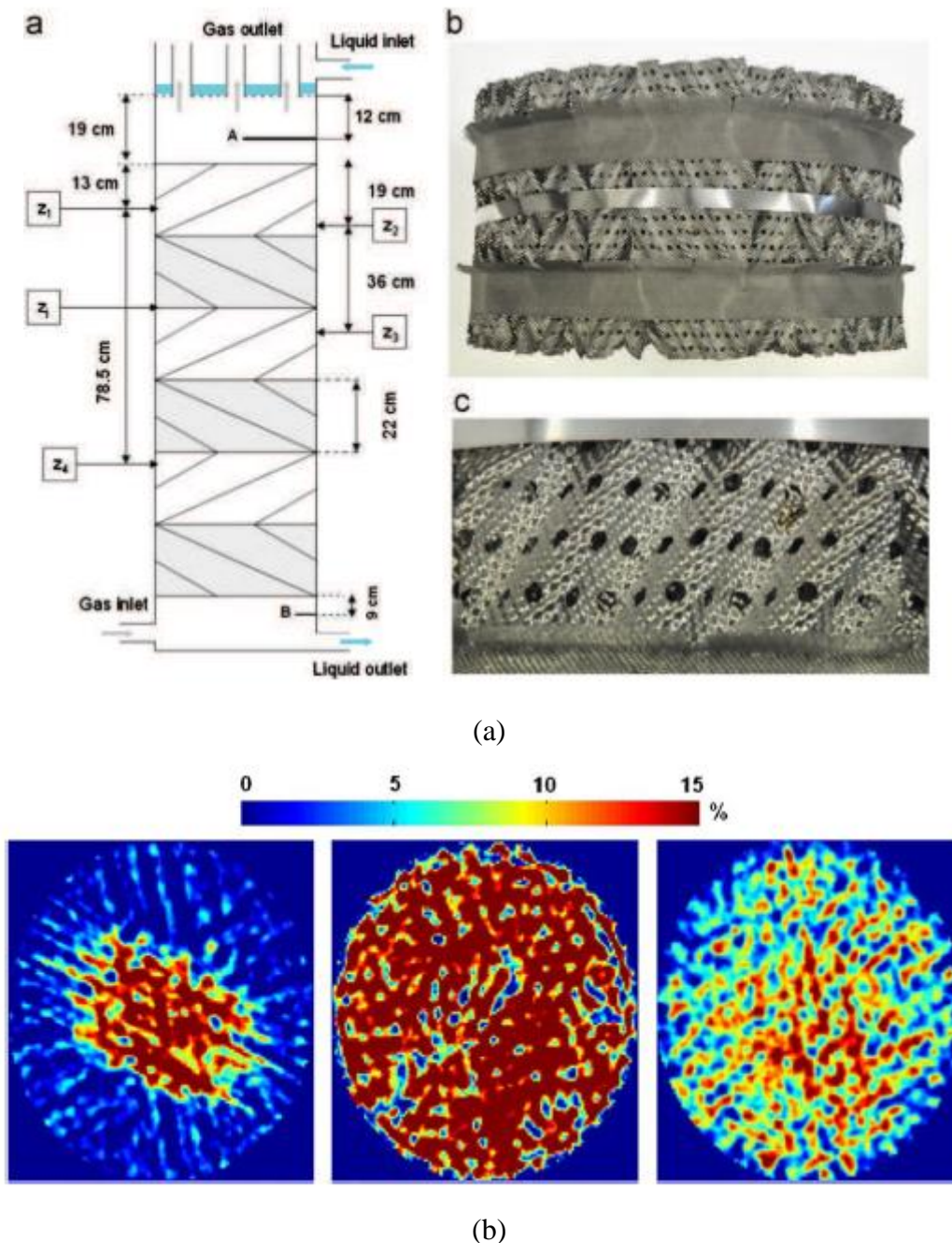


Figure 1-16: (a) Schematic representation of the experimental setup with a 400 mm diameter block of Mellapak 250.X, (b) Liquid holdup maps⁴⁷, at different positions (Z_2 , Z_j and Z_3) of the column; $Q_L = 16 \text{ m}^3/\text{m}^2\text{h}$, $F_C = 0.74 \text{ Pa}^{0.5}$, (20% F_G).

1.4.3. Redistribution at liquid film scale

A liquid flowing on an element of structured packing experiences free surface deformation and instabilities (waves) in response to surface features, i.e., corrugations and perforations. The morphology of the liquid film surface on a packing element is much more complex than the liquid films on a vertical/inclined flat plate.

Capillary, viscous and gravity forces shape the free surface of the film. The magnitude of these forces depends on (i) the geometry of the structured packing, (ii) the surface properties, and (iii) the physical properties of the liquid.

Before discussing the literature on the flow of liquid films on complex surfaces, we briefly present some basic theory and hypothesis used to study falling liquid film in general.

1.4.3.1. Wetting phenomena

Wettability is the ability of liquids to spread on a solid surface. It is measured by the equilibrium contact angle (see **Figure 1-17**). The contact angle, θ is defined as the angle formed by a liquid at the three-phase boundary where a liquid, gas and solid intersect (see **Figure 1-17**). When $\theta < 90^\circ$ (resp. $\theta > 90^\circ$), the surface is wettable (resp. non-wettable). Small contact angles ($\theta \ll 90^\circ$) correspond to high wettability. When the contact angle equals 0° , the wetting is complete.

$$\sigma_{sv} = \sigma_{sl} + \sigma_{lv} \cos \theta \quad (1.10)$$

where σ_{sv} , σ_{sl} and σ_{lv} are the solid/vapour, solid/liquid and liquid/vapour (or liquid/gas) interfacial tensions, respectively, while θ is the equilibrium contact angle.

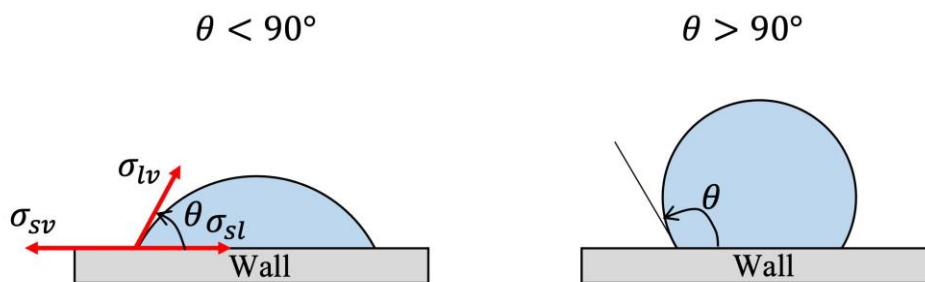


Figure 1-17: Sessile drop on a wettable (left) and non-wettable (right) solid.

Effect of surface tension⁴⁸ on the fractional area has been studied for two structured packing with different specific area, i.e., Sulzer Mellapak 250Y and 500Y (specific area of $250 \text{ m}^2/\text{m}^3$ and $500 \text{ m}^2/\text{m}^3$, respectively). The fractional area is defined as the effective area of the packing normalized by the specific packing area. The effect of surface tension is significant for the packing with the highest specific area. The authors report that a higher surface tension favours

"pooling" within corrugation troughs and "bridge formation" (i.e., the menisci⁴⁹ observed by X ray tomography⁴⁴) at contact points. This phenomenon results in the reduction of available areas for mass transfer on the packing surfaces (see **Figure 1-18**).

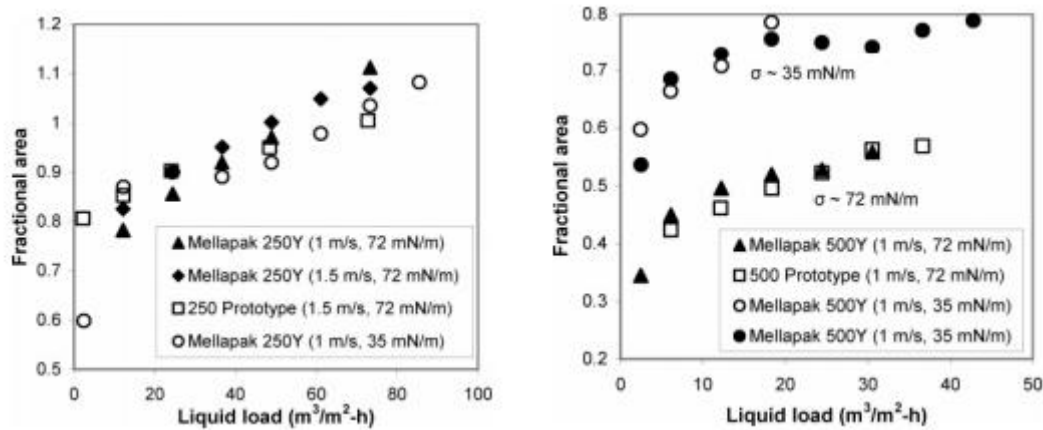


Figure 1-18 : Fractional area measurements⁴⁸ for Mellapak 250Y (left) and 500Y (right) series packings for two different surface tension values.

1.4.3.2. Liquid film on flat and complex surfaces

In this section, a brief literature review is conducted on the theory of liquid films flow on flat surfaces. Then we discuss the instabilities in the form of waves and their role in mass transfer intensification. Finally, the review is extended to the behaviour of liquid films on complex surfaces.

Inclined/vertical flat surface

The main forces acting on the liquid film are: a body force pushing the liquid to fall down, inertia, whose role is subtle along with that of viscosity and the last one is the cross stream component of gravity leading to a hydrostatic pressure that tends to maintain equipotential levels and hence prevent surface deformation⁵⁰. In 1916, Nusselt⁵¹ proposed the first theoretical model for a falling liquid film. He considered the balance between the gravitational force and the friction force acting on a fluid element. A steady, fully-developed, viscous liquid film is assumed with no shear or wave motion on the free surface. We shortly recapitulate the simple solution for the average velocity ($u(z)$) and the average liquid film thickness (δ) describing the flat-film primary flow on flat inclines (see **Figure 1-19**):

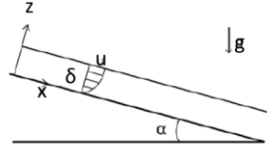


Figure 1-19: Sketch of 2D laminar liquid film on an inclined surface

$$u(z) = \frac{\rho_L g \sin\alpha}{\mu_L} \left(\delta - \frac{z}{2} \right) z \quad (1.11)$$

$$\delta = \left(\frac{3\mu_L Q_L}{\rho_L g \sin\alpha} \right)^{1/3} \quad (1.12)$$

where ρ_L is the density of liquid, g is acceleration due to gravity, μ_L is dynamic viscosity of the liquid, δ is mean film thickness, Q_L is liquid volume flowrate per unit width and α is the inclination angle of the solid surface (with respect to the horizontal).

Experimental observations of laminar falling liquid films show that the free surface of the liquid is often not a flat surface of uniform thickness, but exhibits a wavy structure (Kapitza⁵²). However, a smooth laminar regime near the inlet region is observed⁵³ before it transitions into the small-amplitude wavy-laminar flow.

The flow regimes of a liquid film on a inclined or vertical surface are classified into (Ishigai et al.⁵³):

- Laminar flow: a smooth homogeneous free surface with no wavy motion on the liquid film,
- Stable wavy flow: surface waves of partially laminar and partially turbulent nature,
- Fully turbulent regime: chaotic and random in nature. The flow becomes shear-flow type, and it can be assimilated to a turbulent boundary layer.

These regimes are defined by the film Reynolds number (Re_L). Depending on the authors, the film Reynolds number is given either by $Re_L = Q_L/\nu_L$ or $Re_L = 4Q_L/\nu_L$, where $\nu_L = \mu_L/\rho_L$ is the kinematic viscosity. In the following, unless otherwise stated, we use the former definition. Ishigai et al⁵³ gives the upper bound of the smooth laminar regime, as a function of the Kapitza number (Ka): $Re_L = 1.88 Ka^{0.1}$. The Kapitza number characterizes the liquid properties. It is given by:

$$Ka = \frac{\sigma_{lv}}{\rho_L \nu_L^{4/3} g^{1/3}} \quad (1.13)$$

For slightly higher Re , periodic waves are observed on the free surface of the film. Various theoretical attempts have been made to study the waves formed on free-falling liquid films

(Chang et al.⁵⁴, Trifonov et al.⁵⁵). At low Re , waves are smooth and 2D dimensional. The mean film thickness was given by Kapitza's⁵² theory which accounts for the effects of regular periodic waves as follows:

$$\delta = \left(\frac{2.4 \nu_L^2 Re_L}{g} \right)^{1/3} \quad (1.14)$$

where ν is the kinematic viscosity. The theory of Kapitza accounts for the wavy nature of free surface for a wavelength lower than 13.7 times the film thickness.

For higher Reynolds numbers, liquid film is in a transition zone where large waves tend to overtake the small capillary waves resulting in a complicated wave structure (Kharlamov et al.⁵⁶, Dietze et al.⁵⁷, and Charogiannis et al.⁵⁸).

The last category is turbulent liquid films, in which the thin liquid film presents complex spatial structures, and its evolution becomes chaotic. In literature, the Reynolds number of the onset of the turbulent regime in falling liquid films is still argued upon. However most commonly reported range of Re_L (Q_L/ν_L) is between 200 and 400. Turbulence creates many small ripples whose diffusivity can cause rapid mixing and increase heat and mass transfer rates.

Brauner⁵⁹ characterized wavy flow. He obtained an expression of the average film thickness, for laminar and turbulent flows:

$$\text{For laminar case: } \delta = \left(\frac{3 \nu_L^2 Re_L}{8 g} \right)^{1/3} \quad (1.15)$$

$$\text{For turbulent case: } \delta = 0.104 \left(\frac{\nu_L^2}{g} \right)^{1/3} Re_L^{7/12} \quad (1.16)$$

Nosoko et al.⁶⁰ performed many experiments on falling film with Re_L varying from 15 to 90. The authors measured the wave velocity (u_w), the wave peak height (h_p), and the wavelength (λ). They proposed the following empirical correlations for the wave celerity and the wave peak height:

$$N_{uw} = 1.13 Ka^{0.02} N_\lambda^{0.31} Re_L^{0.37} \quad (1.17)$$

$$N_{hp} = 0.49 Ka^{0.044} N_\lambda^{0.39} Re_L^{0.46} \quad (1.18)$$

where Nosoko et al.⁶⁰ define the Kapitza number as $Ka = (\rho_L^3 g \nu_L^4) / \sigma_{lv}^3$. $N_\lambda = \lambda \left(\frac{g}{\nu_L^2} \right)^{1/3}$ is the dimensionless wave separation, $N_{uw} = u_w / (\nu_L g)^{1/3}$ the dimensionless wave celerity, and N_{hp} the dimensionless wave peak height ($N_{hp} = h_p (g/\nu_L^2)^{1/3}$).

When a uniform film is formed on a vertical wall, at a certain distance from the entrance, 2D waves are observed to evolve. The 2D waves travel a certain distance maintaining their quasi-

stationary state. The separation between the consecutive wave humps may not be uniform. Further away from the inlet, the 2D waves evolve into 3D patterns due to secondary transverse instability. Park et al.⁶¹ identified wave structures consisting of a single large teardrop hump and several small capillary ripples (see **Figure 1-20**). These waves are also known as solitary waves⁶² and they preserve their shape while moving.

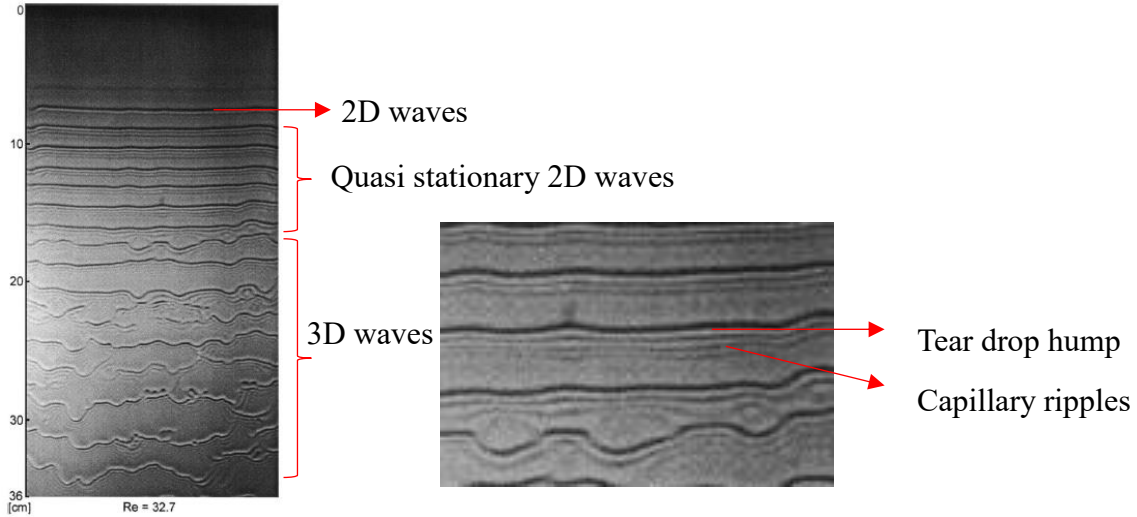


Figure 1-20: Naturally occurring waves on vertically falling film at $Re = 32.7$ without controlled perturbations imposed on film flow⁶¹.

In his doctoral thesis⁶³, Kofman studied the dynamics of waves on a liquid film flowing down a flat inclined surface, with and without counter-current gas flow, in cryogenic and non-cryogenic conditions. The instabilities of the liquid film evolve from 2D to 3D waves along the length of the plate. He studied the 2D wave dynamics for a liquid film flowing on a slightly inclined plate in non-cryogenic conditions. He obtained an empirical correlation for the phase velocity (u_w) as a function of the parameters of the system:

$$N_{uw} = N_f^{-0.32} Ka^{-0.15} \left(\frac{Re_L}{\frac{5}{6} \cot \alpha} \right)^{0.59} \quad (1.19)$$

where $N_{uw} = u_w / (\nu_L g)^{1/3}$ is the dimensionless wave velocity, $N_f = f / (\nu_L^{-1} g^2)^{1/3}$ the dimensionless frequency and f the forcing frequency.

He extended his study to liquid films falling vertically on a flat plate in cryogenic conditions with and without counter-current gas flow. The wave evolution and the liquid film pattern were assessed. Without gas flow, three different shapes of waves were observed: horseshoe shape, delta shape and oblique waves, were observed as a function of liquid Reynolds number (see **Figure 1-21**). The wave patterns are similar to the ones he observed on a slightly inclined plate

in non-cryogenic conditions. With gas flow, the shape of the waves changed due to the shear force exerted by the gas at the interface. The capillary waves observed along with the wave humps without gas flow (see **Figure 1-21**), appear faded with gas flow (see **Figure 1-22**). At high gas Reynolds number, i.e., $Re_G > 13000$ ($R_G = \frac{u_G d_H}{\nu_G}$ with d_H the hydraulic diameter), they observed flooding of the channel. 3D wave propagation stops and the waves appeared to touch the opposing wall of the channel. Another observed interesting phenomenon is the entrainment of droplets by the gas flow.

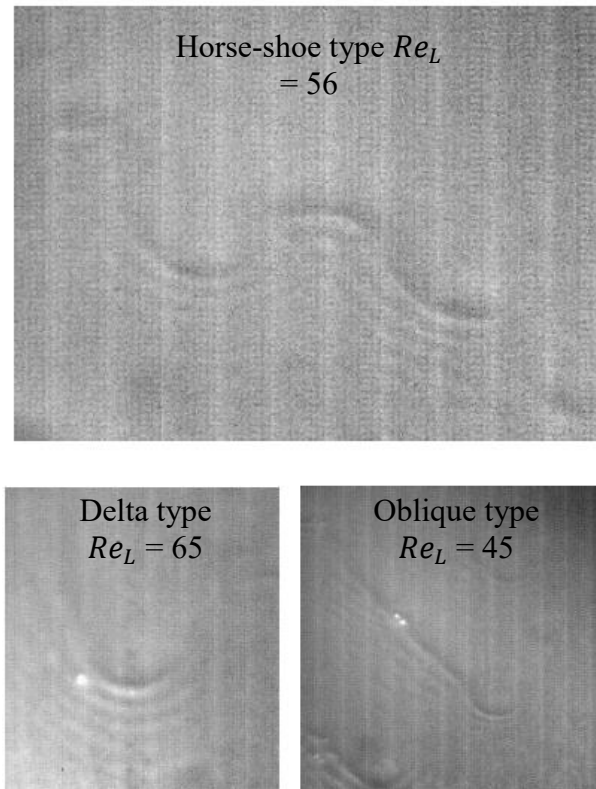


Figure 1-21: Waves on vertically falling liquid film without counter-current gas for different liquid Reynolds number



Figure 1-22: Visualizations of different wave forms for moderate gas backflow velocities ($Re_L = 56$; $Re_G = 11200$): U-shaped waves (left) and pocket waves (right).

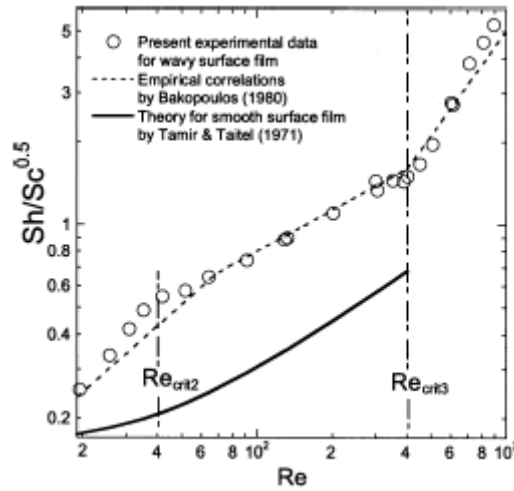


Figure 1-23: Mass-transfer enhancement by surface waves and two breaks of mass-transfer curve⁶⁴.

Yoshimura et al.⁶⁵ performed gas (oxygen) absorption into a falling liquid film in a vertical tube. The Schmidt number is equal to $Sc = \nu_L/\mathcal{D} = 479$ where \mathcal{D} is the gas diffusion coefficient in the liquid phase. They observed similar wave patterns as for a vertical plate. They measured the mass transfer coefficient of the liquid phase (k_L). **Figure 1-23** presents the variations of the Sherwood number $Sh_L = k_L \nu/\mathcal{D}$ as a function of the film Reynolds number Re_L . Sh_L increases with Re_L with different slopes depending on the wave regime. Mass transfer is enhanced in wavy films as compared to smooth films (solid line). The swirls and vortices in the teardrop humps (Nosoko et al.⁶⁰ and Yoshimura et al.⁶⁵) improves the mixing and thus the mass transfer from the free surfaces into the films.

Surfaces with complex features

Zhao et al.⁶⁶ investigated theoretically and experimentally the behavior of liquid films on corrugations. The film thickness measured in their experiments was always higher than the theoretical Nusselt film thickness except in the inflexion points where the film is thin and the interfacial velocity is higher. Depending on the surface type, the film Reynolds number and the capillary number ($Ca = \frac{\mu u_{th}}{\sigma}$), one observes recirculation zones or stagnation pockets in the trough regions of the corrugations. The instantaneous film thickness on the complex surface systematically differs from the mean film thickness calculated for films on flat surfaces. The interface of the film is observed to be wavy even at small Re_L .

Liquid films on an inclined wall with rectangular corrugations was investigated by Vlachogiannis et al.⁶⁷. They identified and characterized different flow regimes while increasing the supply flow rate. The flow pattern is steady in the first few corrugations, but further downstream, perturbations in the form of waves destabilize the flow and form solitary humps. The complex interplay between inertia, viscous stresses, and surface tension governs the hydrodynamics of solitary waves. If inertia is sufficiently high, a recirculation in the main wave hump can be observed. The solitary waves observed on the periodic surfaces is similar to the waves⁶⁸ on a flat plate. Recirculation regions are expected in the wave humps (or teardrop humps⁶¹) that may enhance the mass transfer between the two phases in packed columns. Pozrikidis et al.⁶⁹ numerically studied the effects of topography amplitude, inclination angle, flow rate, and surface tension for a sinusoidal periodic topography. Flow reversal occurs above a critical topography amplitude and then only for sufficiently high liquid flow rates. Correlatively, eddies may develop even at low flow rates, provided the topography amplitude is sufficiently large.

Similarly, Aksel et al.⁷⁰⁻⁷² studied the effect of topography (periodic corrugations, trenches) on the flow stabilization and destabilization. The shape of the linear stability charts for steep topographies (see **Figure 1-24**) differ significantly from the classical long-wave type instability valid for free surface flows over flat inclines. Typical streamline pattern with flow reversal are reported (see **Figure 1-25**).

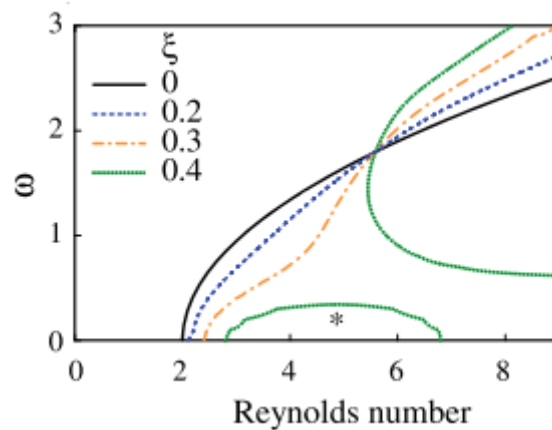


Figure 1-24: Linear stability chart of liquid films flowing over sinusoidal corrugations. ω (dimensionless frequency of the neutral disturbance) versus Re for different steepness $\xi = a/\delta$ of the topography. a is the amplitude of the topography and δ is the Nusselt film thickness.

Using the integral boundary method, a thorough parametric study of the sinusoidal topography is performed to study the effects of substrate amplitude, inclination angle, flow rate, and surface tension.

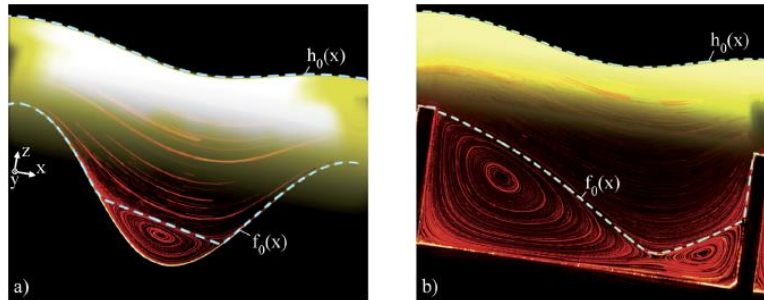


Figure 1-25: Free surface and streamlines of the steady film flow (a) the sinusoidal topography and (b) the rectangular topography⁷¹.

There is very little literature dealing with liquid film dynamics over real packing sheets. We can cite the work by Alekseenko et al.⁴⁹ and Pavlenko et al.¹⁸. Liquid accumulation and meniscus formation in the valleys of the corrugations and at the contact points between two elements of structured packing were measured for different operating conditions. Koch 1Y and Mellapak 250 series were used. Alekseenko et al.⁴⁹ performed experiments in a glass column with 3 to 4 stacks of structured packing (miniature-scale column). The film thickness was measured in the corrugation valley using reflective fiber optic sensors. They found that the liquid film mean thickness in the corrugations decreases radially towards the column wall. Pavlenko et al.¹⁸ performed experiments on a single packing sheet with or without corrugations, perforation, and microtexture (**Figure 1-26**), under cryogenic conditions. The sheet is supplied with liquid on one of its sides. Even though the study remains qualitative, their experiments showed some interesting results: the formation of dry patch downstream the perforations at low irrigation rate, the transfer of liquid through the perforations formation above a minimum film Reynolds number, the detachment of droplets from the top arc of the holes that irrigate the plate (see the large perforation in **Figure 1-27**).

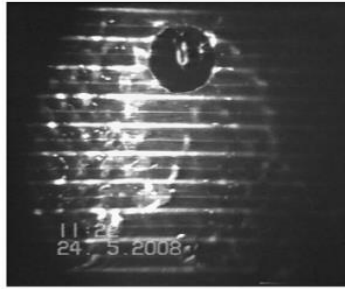


Figure 1-26: Flow of liquid nitrogen over a microtextured sheet at $Re_L = 860$ ($4Q_L/\nu_L$) and hole diameter of 4 mm¹⁸. Onset of droplet formation in the perforation.

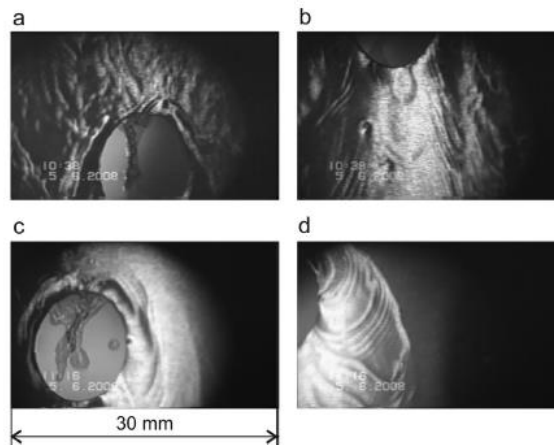


Figure 1-27: The flow of liquid nitrogen on the face (a and b) and back (c and d) sides of the sheets without microtexture at $Re = 860$ ($4Q_L/\nu_L$). Hole diameter - 10 mm¹⁸.

1.5. Evaluation of the measurement techniques: State of art

Various measurement techniques have been developed over the years to study the flow patterns on structured packing elements. These techniques allow visualization and quantification of liquid behaviour (both in space and time) via the measurement of film thickness, velocity components, wave celerity, etc.

In the past, Hot Wire Anemometry (HWA) and conductive probes⁵³ (similar to needle contact probe) were used to characterize the different flow regimes in vertically falling films. The contact probes were used to measure wave peak heights⁶⁰ at different points in the falling liquid film. A needle is positioned at a certain distance from the free surface of the film. It is brought closer by a micrometer until the tip is in contact with the wave peaks. These intermittent contacts are detected using a laser beam. The beam illuminates the needle tip and passes through the film and is then projected on a screen. The beam is deflected due to the refraction at the film surface and oscillates rapidly on the screen. When the needle tip makes contact with the wave peaks, the beam spreads because of the deformation of the wave peaks and illuminates a wider

area on the screen intermittently. The method lacks in accuracy due to the hysteresis between the liquid and the contact probes. Nevertheless, it is a simple method and is still used for quick validation of the theoretical film thickness.

In the past decade, optical techniques have gained popularity due their measurements accuracy and to their non-intrusiveness. Popovich and Hummel^{73,74} used a flow visualization method called Photochromic Dye Activation (PDA) technique. Kawaji^{75,76} and also used PDA to measure the local instantaneous velocity of falling liquid films in annular tubes with counter-current gas flow. A photochromic dye material, activated using light (mostly ultraviolet), is dissolved in a transparent liquid. The subsequent motion of the traces formed after the dye activation is tracked to obtain instantaneous velocity profiles. The velocity profile was measured simultaneously with the film thickness to have a comprehensive overview of the turbulence characteristics and the enhancement effect of interfacial waves on the mass transfer rate.

Mendez et al.⁷⁷ used a transparent plate and measured film thickness, wave celerity and wave profile using light absorption techniques (Level Detection and Recording (LDR)). The principle of the technique is to capture the illuminated light on the substrate by the camera (see **Figure 1-28**). Based on the light intensity captured, the Beer–Lambert law is used to determine the film thickness (see Eq. 1.27).

$$\delta(x, y, z, t) = \frac{1}{\gamma} \ln \left(\frac{I_0(x, z, t)}{I(x, z, t)} \right) = \frac{A(x, z, t)}{\gamma} \quad (1.20)$$

where γ is the light extinction coefficient of the liquid, I_0 is the light intensity of the reference image and I is the transmittance image (intensity of transmitted light through the liquid film), $A = \ln \left(\frac{I_0}{I} \right)$ referred to as the absorbance.

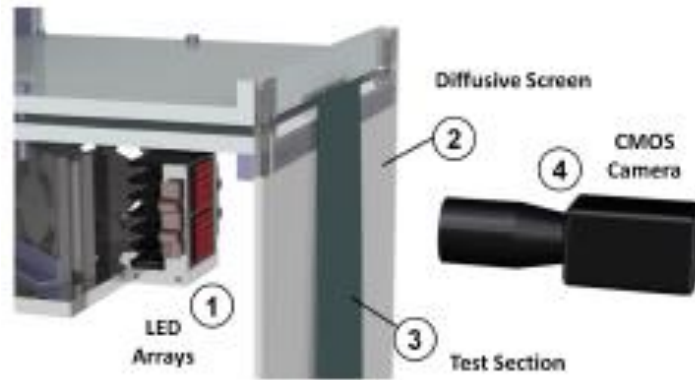


Figure 1-28: Simplified representation of Light Absorption (LABs) test section⁷⁷: LEDs (1), screen (2) to back-light the test section (3) with diffuse, monochromatic light. A CMOS camera (4), to measure the attenuation of light produced by the liquid film absorbance.

Vlachogiannis and Bontozoglou⁶⁷ measured the profile of a film flow over periodic corrugations using fluorescence imaging. The principle is similar to the PDA technique where liquid film is doped with a colored dye (200 to 300 ppm of sodium salt of fluorescein - $C_{20}H_{10}O_5Na_2$). The film fluoresces under ultraviolet illumination. A high-resolution Charge-Coupled Device (CCD) camera and a monochrome frame grabber board are used to capture digitized images. This technique is used to trace the variation of film thickness in space and time. The fluorescence intensity $I(x, y, t)$ is represented as a linear function of the local film thickness $h(x, y, z)$ (in the limit of $h < 1.5 \text{ mm}$).

$$I(x, y, t) = a(x, y) h(x, y, t) + b(x, y) \quad (1.21)$$

where $a(x, y)$ and $b(x, y)$ are the two linear coefficients, which depend on the concentration of dye, the solution, the surface roughness of the wall plate and the distance and the distribution of the ultraviolet source. This method is suitable for slightly inclined films over smaller disturbances.

Decré and Baret⁷⁸ characterised the free-surface shape of a thin liquid film flowing over an inclined plate with topography (step in, step out and trench) by applying the phase-stepped interferometry method. The method measures the phase of a wavefront by collecting an intensity interferogram for (usually) 4 different stepped positions of the reference mirror in a Twyman-Green interferometer⁷⁹ (see **Figure 1-29**).

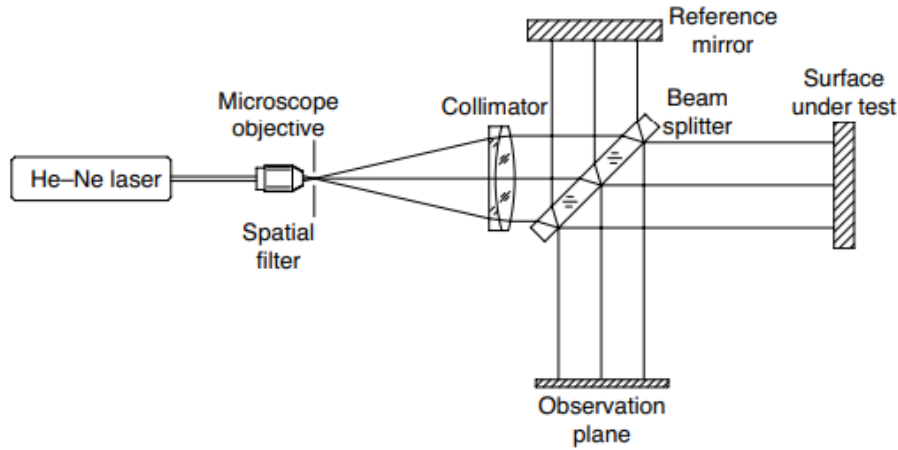


Figure 1-29: Schematic representation of basic Twyman–Green interferometer⁷⁹

The laser beam is expanded to cover the desired field of view and the fixed mirror (reference mirror) in the Michelson interferometer is rotatable. The interference phase between the two light waves reflected by the mirrors is measured. An interferogram is produced by superimposing two wavefronts, one of which is typically a flat reference wavefront and the other a distorted wavefront whose shape is to be measured. The images obtained by the method represents a set of intensity maps for different reference phases. The time-averaged spatial intensity distribution $I(x, y)$ of an interferogram, is written as follows:

$$I(x, y) = I_0(x, y)[1 + V(x, y) \cos\{\phi(x, y) - \phi_r(x, y)\}], \quad (1.22)$$

where $I_0(x, y)$ is the mean intensity, $V(x, y)$ is the local attenuation of the signal, and ϕ_r is the reference phase determined by the position of the reference mirror. The authors used the five-frame technique detailed in the monograph by Malacara⁷⁹ due to its advantages on measurement accuracy and error compensation. Any change in the free surface of the film is observed in the form of a change in the phase term. This phase information can be used to obtain the object surface information as below:

$$d(x, y) = \frac{\lambda}{4\pi} \phi(x, y) \quad (1.23)$$

where $d(x, y)$ is the distance between the beam splitter and the object surface and hence is the desired surface form information. The phase of the interferogram $\phi(x, y)$ is calculated by phase shifted measurements with the four positions (z_i) of the reference mirror, $\phi_{r,i} = \frac{2\pi z_i}{\lambda} = 0, \frac{\pi}{2}, \pi, \frac{3\pi}{2}$. A four-step phase $\phi_4(x, y)$ is given by:

$$\phi_4(x, y) = \arctan\left(\frac{I_4 - I_3}{I_2 - I_1}\right) \quad (1.24)$$

With I_1, I_2, I_3, I_4 are the intensity distribution of the interferogram with phase shifts of $0, \pi/2, \pi$ and $3\pi/2$ radians, respectively and \arctan is the inverse tangent function.

A continuation of the review of the optical techniques used to measure the velocity field of thin liquid film is described in Chapter 2 (*page 77*) of this manuscript while describing the experimental set up constructed to measure the velocity field of the falling liquid film on a perforated plate.

1.6. Conclusion and objectives

The “Cryogenic air separation” is a single process of producing pure components of air in large quantities to supply the needs of the growing industry. However, the cryogenic air separation process is energy-intensive, consuming 1% of global electrical energy.

The performance of ASUs is improved by optimizing their design from plant scale to individual component scale.

The working principle of ASU is briefly presented, followed by a review of performance characteristics of different types of vapour-liquid contactors (trays, random packing, and structured packing) are discussed. Structured packing type of vapour-liquid contactor has dominated trays and random packings due to relatively low-pressure drop per theoretical plate, making them the most effective among low-pressure applications. Their well-defined geometry and arrangement provide a high specific area to support the liquid phase for better exchange of heat and mass transfer. Several studies are performed to evaluate the performance and mass transfer criteria on a wide range of packing geometry, and column operating conditions.

The separation efficiency of the structure packing distillation column is closely linked to the homogeneity in the redistribution of the liquid and vapour phases. However, maldistribution due to liquid accumulation in certain zones and film detachment on packing elements are common problems even today regardless the optimised initial redistribution. The complexity of the tightly packed structured packing is a limiting factor to conduct experiments with the aim of packing geometry optimization. Recently a few novel experimental techniques such as X-ray and Gamma-ray computed tomography (CT) have been developed to gain visual access of the two-phase flow interactions through the narrow pathways of structured packing on the macroscopic scale. A local analysis of the liquid hold-up and liquid film thickness through the CT images at different segments along the packing height gives useful results on the geometry of the packing. The main observations do not confirm the total wetting of the packing. The liquid film thickness is not constant over the entire packing. Flow regimes in the form of

rivulets, drops and menisci are observed. These hydrodynamic phenomena are sensitive to the uneven geometry of the packing and liquid properties (viscosity and surface tension). A little experimental effort has been devoted to the understanding of the sources of liquid maldistribution.

An extensive study of the hydrodynamics of liquid films on flat (inclined or vertical) surfaces is performed. The simplicity of the flat surface is advantageous in performing reliable and reproducible measurements of wave characteristics and mass transfer coefficients for a broad range of parameters. Various studies are performed on the solitary waves as they augment heat and mass transfer in several multiphase industrial processes. Several hydrodynamic instabilities appearing in certain specific conditions are now well understood.

However, the liquid film behaves differently on a textured plate compared to flat plates. The mean liquid film thickness and mass transfer coefficients have been found higher on a textured plate. Few experimental observations of liquid film on topographical surfaces have qualitatively commented on mass transfer intensification.

In recent years, liquid film on microtextures, perforations, corrugations have been studied on a microscopic scale. The influence of liquid flowrate, rib inclination angle, and holes on liquid spreading has been studied. Various surface instabilities have been observed to manipulate the liquid film thickness and velocity. Eddies are formed in the valley zones of corrugations. Perforations, on the other hand, drain the liquid favouring liquid transfer to the other side. These insightful experimental results lack solid theoretical analysis and simple physical models.

Finally, we close the chapter by reviewing a few measurement techniques specifically used to study liquid film on topographies.

Summary and objectives

From the literature review, we note that existing knowledge on the subject of the hydrodynamics of liquid film on structure packing surfaces is limited, with much attention being given to the study of liquid films on flat surfaces (inclined or vertical). However, few macroscale studies have addressed the importance of surface features in liquid redistribution. Some studies have visually assessed the liquid film structure on corrugated and perforated elements of structured packing and conducted qualitative interpretations. Researchers focussed on corrugations without adding perforations to analyse the cross-section profile of the liquid

film. No quantitative studies in the interest of how perforation influences liquid phase distribution have thus been performed.

Suppose perforations were to favour liquid redistribution, then what are underlying mechanisms, and how do we quantify. Therefore, experimental research is needed to conduct a parametric study to establish correlations and physical models at a fundamental level.

The main aim of our work is to understand the mechanisms of liquid phase redistribution on corrugated and perforated structured packing elements. To study in detail the hydrodynamics associated with liquid film on the perforation, we choose a simplified configuration by considering perforations on a flat vertical plate. Corrugations add several parameters (crimp angle, inclination, etc.), the process of quantification becomes difficult to control. The results are usually noisy and non-reproducible. Therefore simplification of the packing element from the original geometry is essential.

We designed an experimental setup which is described in the next chapter (chapter 2 and Appendix 2). The experimental setup allows us to perform falling liquid film experiments on the perforated metallic sheets in a vertical configuration. The setup is integrated with a controlled liquid distribution with identical or different volume flow rates on either side of the plate. The setup can house a number of measuring instruments to visualize and measure the quantities, such as liquid film thickness and three-dimensional velocity components. Our interest is to observe and quantify liquid film patterns from a hydrodynamic point of view and propose analytical models to predict the transition mechanism.

Chapter 3 with the supplementary results (including Appendix 4) aims at understanding the different transition mechanisms of the liquid film falling on a thin vertical plate with a single perforation. Although perforations are known to favour liquid redistribution in corrugated and perforated packings, in-depth, comprehensive study of the hydrodynamics of liquid films on perforations is few. We will experimentally study the behavior of liquid film on a perforation machined on an aluminium plate to characterize the mechanisms of transition for a broad range of parameters. A physical model will be proposed to predict the onset of curtain transition (a mode of transition) and give a physical meaning.

The second part, detailed in chapter 4 with supplementary results (Appendix 5), concerns the liquid transfer and spreading through the perforation(s) when a vertical perforated plate is supplied on one of its faces with a uniform liquid film. The volume flowrate will be

characterized as a function of perforation diameter, supply flowrate, spacing. We will focus on the curtain mode of transfer to quantify the volume flow transferred to the back of the plate downstream any (k th) row of perforations. A recurrence model based on the flow balance between the front and back of the plate will be proposed. In the second part, we will measure the shape of the rivulet (leaked liquid from front to back) on the back of the plate. We will analyse the rivulet spreading downstream and merging into a continuous wavy film a perforation(s) with the theoretical models.

The last part of this thesis, detailed in chapter 5 with supplementary results (including Appendix 6) concerns an original and more complex setup dedicated to adapt an optical non-intrusive measurement methodology (3D 3C PTV by defocus) to investigate the fluid dynamics in twin films. The objective will be to measure three-component planar velocity vector fields in all three dimensions in the liquid film. We will first conduct experiments in the films on a non-perforated vertical plate to validate the method. Flow structures of twin films on a perforated plate will be observed using streamline patterns. 2D planar velocity, probability density distributions will be used to quantify recirculation zones in the liquid curtain. Other post-processing techniques, such as Dynamic Mode Decomposition (DMD) analysis, particle tracking statistics, will be used to investigate the liquid curtain. The study is ongoing, and the results need to be further analysed and interpreted.

2. Materials and Methods

This chapter presents the experimental setup originally constructed to study freely falling films in the liquid phase on a perforated plate in a vertical configuration. The test setup was carefully designed to have optical accessibility to quantify the mechanisms of transition by measuring film thickness and film velocity on a perforated plate. The measurement techniques like confocal chromatic imaging and 3D 3C particle tracking velocimetry are used in the scope of the present study. A detailed description of the setup, range of test parameters, calibration, and validation of the techniques are presented.

2.1 Mechanisms of transition, liquid transfer and distribution

We provide a general description of the test setup with all the materials used. The flow loop is common for all the experiments performed in the present study. New components are added to adapt to the study of different perspectives of the liquid film falling on a perforated plate.

2.1.1. Description of Experimental set-up

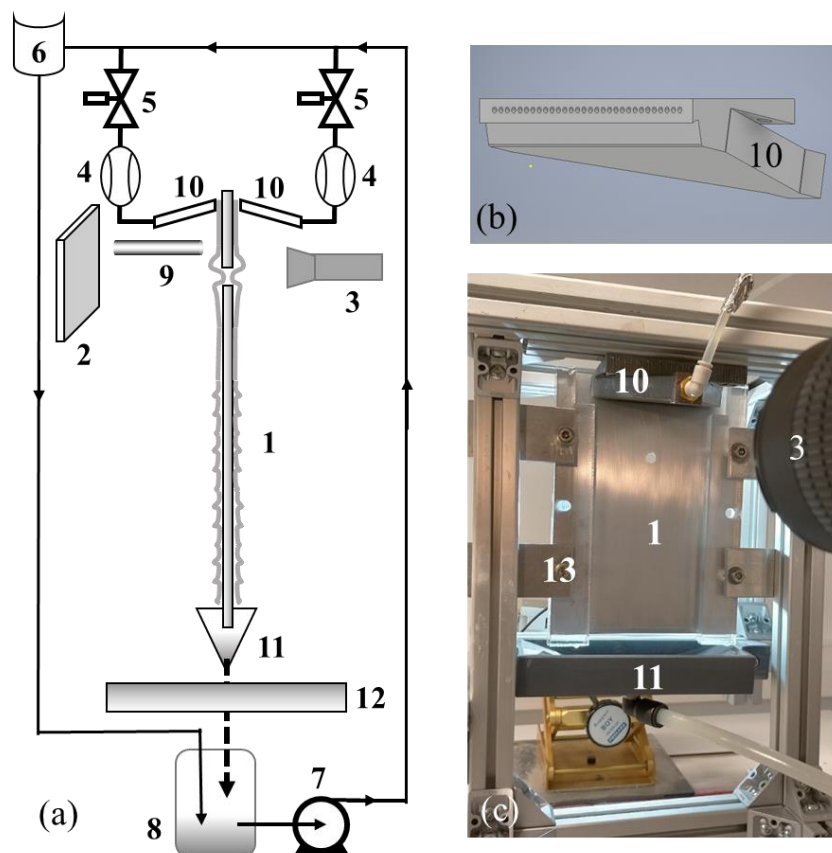


Figure 2-1: (a) Schematic representation of the experimental setup. (b) CAD (Computer Aided Design) model of the distributor. (c) Photograph of the setup. 1. Test plate 2. LED panel 3.

High-speed camera 4. Volumetric flow meters 5. Needle control valve 6. Spillway 7. Gear pump 8. Reservoir 9. CCI sensor 10. Distributor 11. Liquid Collector 12. Anti-vibration mount 13. Frame that holds the plate.

The experimental setup is divided into two parts (see **Figure 2-1** and CAD in Appendix 2):

- Hydraulic circuit and flow distribution
- Measuring instrumentation

The key feature of this setup is that it enables to study of liquid films on vertical surfaces while supplying both faces of the plate, which simulates the irrigation system in industrial packings. The test plate is inserted in a rigid frame to ensure its flatness. The liquid circuit and the instrumentation are mounted on a dedicated frame. The frame holding the test plate is decoupled from the other parts of the hydraulic circuit and instrumentation. The whole assembly is mounted an anti-vibration table to damp the parasitic vibrations that may affect the fluid film flowing on the plate (see **Figure 2-1**).

The hydraulic circuit comprises of a flow loop, which is from the reservoir to the sample plate and then back to the reservoir through the liquid collector. The liquid from the reservoir circulates through the magnet gear pump (MDG-M15T3B, Iwaki) to deliver the required flow rate to the distributors on each side of the plate. Two flowmeters independently control the flow rate delivered on each face of the test plate. Needle control valves with the spillway are installed to deliver a constant and calibrated flow rate at the output. However, in our experiments, we controlled the flow rate through a signal generator (by adjusting the voltage) which sends an analog signal to the variator that controls gear speed to adjust the flow.

Flow distribution: The centerpieces of the liquid circuit are the two distributors (see **Figure 2-2**). They have been carefully designed (over approximately ten iterations) to uniformly distribute the liquid in the spanwise direction of the plate. The main challenges faced in attaining uniform distributions were:

- Difficulty in obtaining and reproducing uniform thin films in spanwise and streamwise of the test plate.
- Dry zones or thinning of the liquid film in certain areas when the supply flow rate becomes low.
- Sensibility to frame's horizontality and verticality on which distributors are mounted.

With several designs trials of the prototype (see Appendix 3), the design of the distributor is optimized to overcome the above-mentioned difficulties. The distributors are in the shape of a diffuser and mounted with an inclination of 10° (see **Figure 2-2**) with respect to the horizontal. Because of the positive slope, the liquid ascends in the distributors. Entry of air is then avoided, and the distributors remain filled with liquid even at low liquid flow rates. The liquid inside the distributors is guided through a set of square blocks (see **Figure 2-2**) which spreads the flow in the spanwise direction and also breaks down the large eddies (pressure drop effect). Finally, the flow comes out laminar through 30 horizontally and equally spaced circular nozzles of 2 mm in diameter.

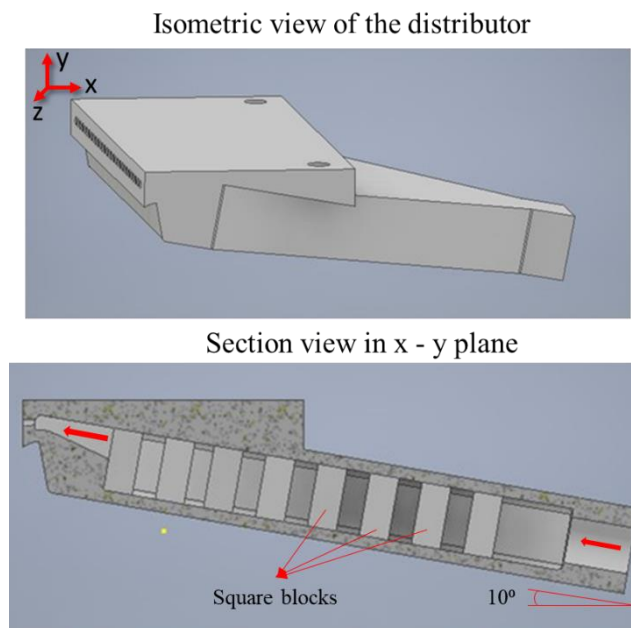


Figure 2-2: Image of a distributor with its section view

The distributors are produced using a 3D printer (Model: MK3s, PRUSA). The printer uses a three-dimensional object from a digital 3D model (Inventor 2020, Autodesk) to deposit material, in the form of wire, respecting the shape of the CAD model. The material used is PLA (extruder temperature of 215°C and plate temperature of 60°C). The material deposited solidifies and takes a required 3D shape. The design of the distributor is complex due to its intricate interior design. The parameters have been correctly adjusted in order to have a good precision between the CAD model and the prototype. It is very important to respect the flatness of the liquid exit surface of the distributor. The exit surface was slightly polished using a polishing device to ensure flatness.

The distance between the plate and the distributor is an important parameter. If the distance is too large, the flow regime transitions to rivulet due to the detached meniscus on a certain number of holes (the liquid bridge between the distributor and the plate). If the distance is too small, liquid overflows on the top surface of the distributor. A certain number of tests were conducted to fix the correct gap between the plate and the distributor. A distance of 0.9 – 1 mm was found suitable for all the range of volume flow rate per unit width used in our experimentation. A guide plate of 1 mm thickness was used in all the experimental test cases to set the test plate at a suitable distance from the distributor.

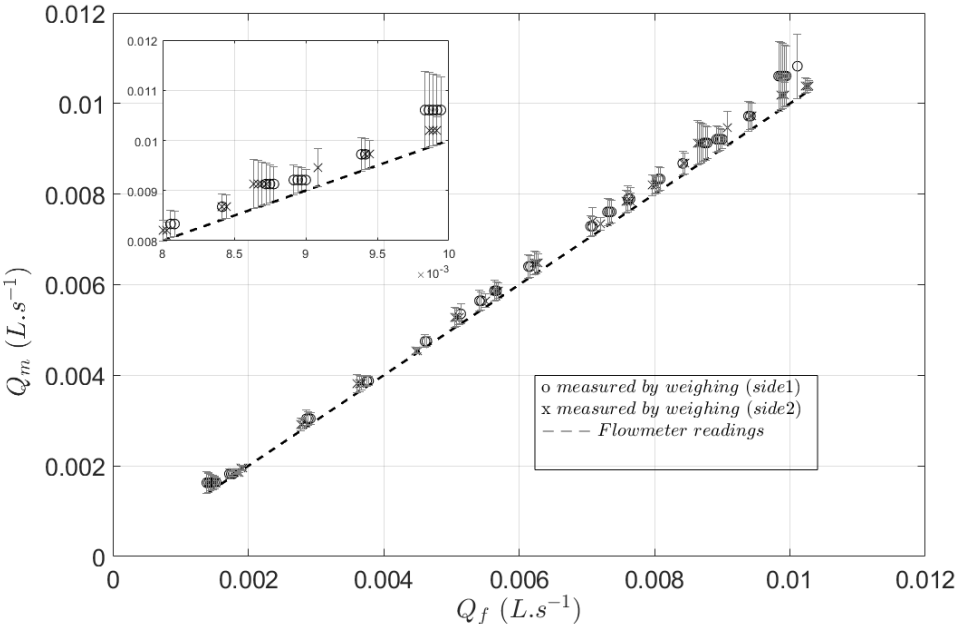


Figure 2-3: Flowmeter reading vs measured flow rate for flowmeter 1 and 2 when tested simultaneously with demineralized water.

Calibration and validation of flowmeters: The volumetric flow rate delivered by each flowmeter and via distributor is independently set by a needle control valve and monitored by an oval gear volumetric flow meter (MX06, MacNaught). We verified the values displayed by both flowmeter by comparing the value displayed on the flowmeter with the values obtained by measuring the liquid volume over time (volume was calculated by the product of mass obtained by weighing and the density of liquid). The flowmeters were calibrated individually and together (both operating in parallel). The results obtained show a very good agreement (see **Figure 2-3**) with flowmeter readings. However, uncertainty induced on the measurements due to the apparatus used (weight balance and chronometer) has been calculated. The sum of the percentage of error induced in the measures is 1% from the readings of the flowmeter. Tested flow rate values correspond to a range of Reynolds number used in the experimental test cases

(chapter 3, 4, and 5). The display resolution of the flowmeters is ± 0.03 L/min. A spillway is added to the hydraulic circuit to maintain the liquid pressure in the lines to deliver a constant flow rate from both the distributors regardless of gear oscillations and pressure drop. In all test cases, liquid flowing from the bottom of the plate comes into a collector and then returns to the feeding tank.

Local liquid collector: In the study of liquid transfer and distribution (Chapter 4), the set-up remains the same except for an addition of a local liquid collector to recover the transferred liquid on the back of the plate. The prototype is fabricated using a 3D printer (see item 13, **Figure 2-4**). The collector is first treated with a coat of epoxy resin to make the surface of the collector nonporous. Curing follows the application of resin for 24 hours. The collector is then glued to the back of the plate, 60 mm away from the center of perforation. Silicon glue is used to attach the collector to the aluminum plate. The bonding agent shows non-reactivity to the test fluid (propan-2-ol) if used for short periods (4 – 6 hours).

The liquid flowing from one side to the other side is channeled through the collector to recover in a beaker for a defined duration of time (monitored on a stopwatch). The weight of the liquid is measured and corresponding volume is calculated (mass x density). The error in flow rate calculated includes the error in measuring the mass of the liquid, error in the density of the liquid, and error in the time duration. Other errors are the error from apparatuses (analytical balance, stopwatch) and the error from the evaporation of test liquid. The order of magnitude of the other errors is not quite important and thus not considered.

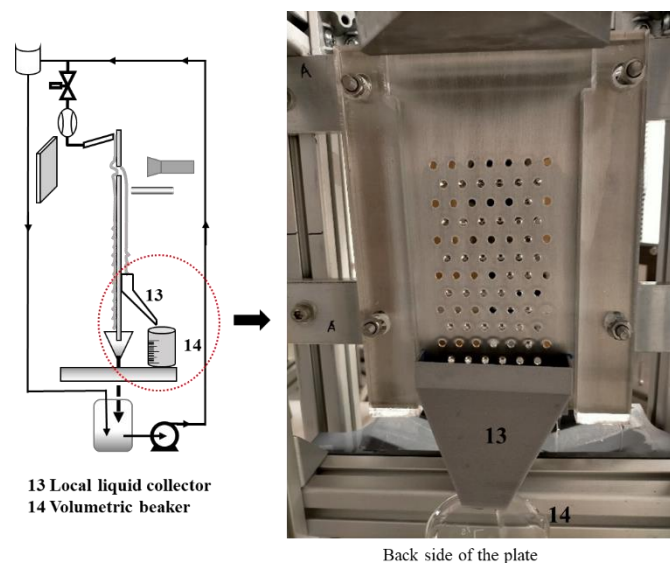


Figure 2-4: Demonstration of liquid retrieval system added to the initial set-up to study liquid transfer through perforations.

2.1.2. Preliminary tests

Industrial configurations of structured packing are usually quite complex¹⁸ with several surface features (corrugations, holes of different shapes, slits, etc.). The surface features are made to favor liquid spreading in the structured packing. Some initial simple visualization experiments were performed on the industrial corrugated and perforated packing to conduct qualitative observation of the flow structures. A typical industrial single corrugated and perforated sheet is supplied through a point source liquid injection (see **Figure 2-5**). A pipette of 50 mL volume is used. The sheet is held vertically by clamps. The fluid used is propan-2-ol due to its good wetting properties on the aluminum surface. A yellow dye (Tartrazine E102) is added to the liquid for the sake of visibility of the flow path of the fluid. We note that 25% of the plate surface is wet by the liquid. However, the fluid film is observed to take the easiest path, i.e., through the valleys of the corrugations. The fluid film is thicker in the valleys. This results in the non-uniform fluid distribution over the plate. With a proper understanding of the surface features, their role in the fluid distribution could be improved. If we consider industrial packing, it becomes quite challenging to control upstream flow conditions. It is difficult to thoroughly understand the underlying hydrodynamics associated with liquid distribution without controlling the supply conditions. Reproducibility of the results is another difficulty, usually observed in this configuration, which induces large errors in measurements.

A study with the simplified configuration could lead to a profound understanding of the mechanisms of liquid film distribution in the presence of surface features or topographies. To do this, we consider perforations on a flat vertical plate to study their role in transfer and redistribution of the liquid film.

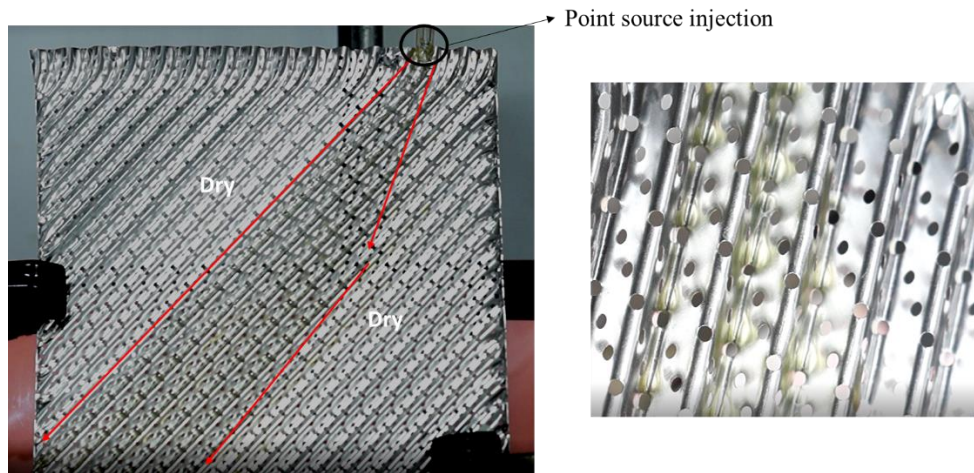


Figure 2-5: Visualization of the liquid film flow on a corrugated and perforated metallic sheet. An enlarged image showing the fluid film deformation around perforations.

2.1.3. Parameters of experiments

In this section, we describe different parameters investigated in the following chapters:

- Experimental study of a liquid film flowing over a perforation (Chapter 3).
- A comprehensive study of the liquid transfer from the front to the back of a vertical perforated sheet (Chapter 4)

We consider a Newtonian liquid with constant density (ρ), dynamic viscosity (μ) and surface tension (σ). ν is the kinematic viscosity of the liquid. The test plates are cut from aluminum sheets. x denotes the streamwise direction, y the spanwise direction and z the direction in the depth of the liquid film. The plate length in the streamwise direction is $L = 200$ mm and the plate width in the spanwise direction is $B = 150$ mm (see **Figure 2-6a**). The parameters investigated in our experiments in our studies are categorized as geometric/test plate and liquid system parameters. The perforation is characterized by its diameter (d) and the plate by its thickness (t). The perforation is made by drilling for $t = 1$ and 1.5 mm and by laser cutting for $t = 0.5$ mm. Special care is taken when machining to maintain the sheet's flatness and ensure that the edge of the perforation is sharp and perpendicular to the plate face. The center of the perforation is located on the midline of the plate, at 60 mm from the top edge.

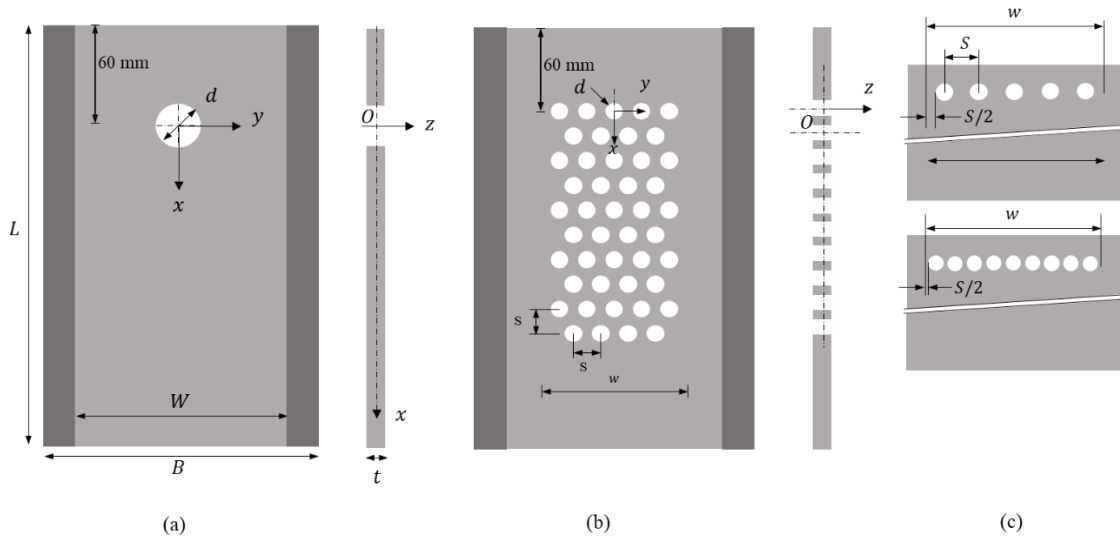


Figure 2-6: Front view of the plate and perforation dimensions along with x , y and z coordinate system in case of (a) single perforation (b) multiple perforations (c) two examples, widely spread and tightly packed perforations, to illustrate the notion of arrangement of perforations as a function of spacing.

Flow condition: Three flow conditions are considered in our experiments (see **Figure 2-7**). Each side (i) of the plate is supplied with liquid at a volume flow rate per unit width (Q_i) with $Q_2 \leq Q_1$.

1. One face flow: i.e. $Q_2 = 0$
2. Two face flow with equal volumetric flow rate on both faces: $Q_1 = Q_2$
3. Two face flow with unequal volumetric flow rate: $Q_1 \neq Q_2$

The third flow condition is an exceptional case explicitly considered in the study of liquid film transition mechanisms in the perforation (Chapter 3).

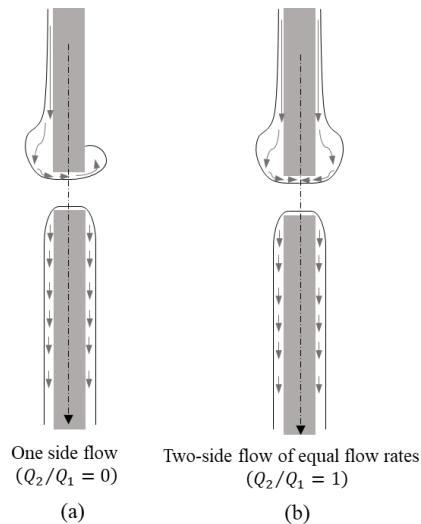


Figure 2-7: Side view of the perforated plate when plate is irrigated on (a) one face (b) both faces with equal volumetric flow rate.

Roughness measurements: The test plates are slightly polished with abrasive (grit size P1200) to get a matt rendering thus reducing the impact of parasitic reflections on optical based measurements. The resulting roughness parameter (R_a , arithmetical average of the roughness profile) of the plate is measured by confocal chromatic imaging (3D Measuring Station with CHR 150-N sensor, STIL). Measurements are performed in two orthogonal directions, streamwise (x) and spanwise (y), in the proximity of the perforation and far from the perforation. R_a ranges from 0.2 to 0.5 μm (see Appendix 3).

2.1.3.1. Experimental study of a liquid film flowing over a perforation (Chapter 3)

Test plates

A single perforation of eight different diameters ($d = 2, 4, 6, 8, 10, 12, 14$ and 16 mm) is machined on an aluminum plate (see **Figure 2-6a**). The thickness of the plate ($t = 0.5, 1, 1.5$ mm) is also varied for all eight perforation diameters. Totally, 24 test plates (see **Table 2-1**) were used to study the transition mechanism of the fluid film in the perforation.

Liquid system parameters

Four different Newtonian liquids with a range of parameters (ρ, μ, σ) are used in the experiments. Deionized water, propan-2-ol (VWR Chemicals (GPR Rectapur® >99.0%)), 25% aqueous glycerin mixture and 55% aqueous glycerin mixture are used. Preparation of aqueous glycerin mixtures are demonstrated in experimental protocol (see Appendix 3).

2.1.3.2. A comprehensive study of the liquid transfer from the front to the back of a vertical perforated sheet (Chapter 4)

Test plates

Single perforation configuration

At first, liquid transfer through a single perforation is studied. Seven different diameters ($d = 4, 6, 8, 10, 12, 14$ and 16 mm) of perforations are machined on an aluminum plate of $t = 1$ mm. The experiments are repeated used three different perforation diameters ($d = 4, 6, 8$ mm) for a plate of $t = 0.5$ mm.

Multiple perforations configuration

In test cases with multiple perforations, the diameter of the perforation is always kept constant to $d = 4$ mm. Perforations are machined on two variants of test plate of thickness $t = 0.5$ & 1 mm. The spacing between the perforations is varied within the values: $s = 14, 12, 10, 8$ and 6 mm. Spacing parameter is defined as a center-to-center distance between two adjacent perforations. Spacing parameter is scaled with the diameter of the perforation times a constant (c). The perforations are spread laterally within 70 mm distance for all five spacing parameters (see **Figure 2-6bc**). Number of perforations (N) within the lateral distance of 70 mm increases with the decrease in spacing between the perforations (see **Table 2-1** and demonstration in **Figure 2-6c**).

Liquid transfer through the perforation is studied in case of test plates with one, two and three lines of perforations (see **Table 2-1**) separately. Staggered or Zig-zag pattern of perforations is adopted in our study. Finally, two cases of test plates with ten lines of perforations are considered (see **Figure 2-6b**). We select two different values of hole spacing ($s = 14$ and 10 mm) to study the effect on liquid transfer due to a group of perforations (to replicate the industrial pattern of perforations). In this case $d = 4$ mm and $t = 1$ mm is kept constant.

Liquid system parameters

In the liquid transfer study, propan-2-ol ($Ka = 346$) is used as a test liquid throughout the study of liquid transfer and distribution. In all the experiments, the fluid supply is maintained on one face of the plate ($Q_2 = 0$). In the study of Pavlenko et al¹⁸, it can be seen that liquid nitrogen wets the aluminum packing surfaces with a low contact angle. Also in literature⁸⁰,

contact angle of liquid nitrogen on the aluminum surface at cryogenic condition measures between ($7^\circ - 9^\circ$). The dynamic contact angle of Propan-2-ol is also low ($11^\circ - 17^\circ$) compared to the other three liquids used in the study.

Perforation and plate parameter				
Flat plate with single perforation				
d (mm)	t (mm)	$s (= cd)$ (mm)	N	N_l
2*, 4, 6, 8, 10, 12,14, 16	0.5, 1, 1.5*	-	1	-
Multiple perforations				
4	0.5, 1	6, 8, 10, 12, 14	11, 9, 7, 5, 5	1
	1		21, 17, 13, 9, 9	2
	1		32, 26, 20, 14, 14	3

* Parameters not considered for the liquid transfer and spreading study (Chapter 4)

Table 2-1 : List of test plate parameters used in the experiments of transition of liquid film and liquid transfer and spreading through perforations

2.1.4. Physical properties of test liquids

2.1.4.1. Density

The density of the different liquids used in the experiments was measured at 25°C . The volumetric pipette of 10 mL of accuracy of 0.02 mL. 10 measures for each liquids are performed. The corresponding weight of the liquid from the pipette is measured using a digital balance of 0.01 g accuracy. The results obtained are tabulated in the table (see **Table 2-3**). After being used in the experiments, some of the test liquids are tested for the density values, especially hygroscopic liquids: aqueous glycerol mixtures. From **Figure 2-8**, we note that the change in density is not significant compared to the measured density values of the test liquid before using in the experimentation.

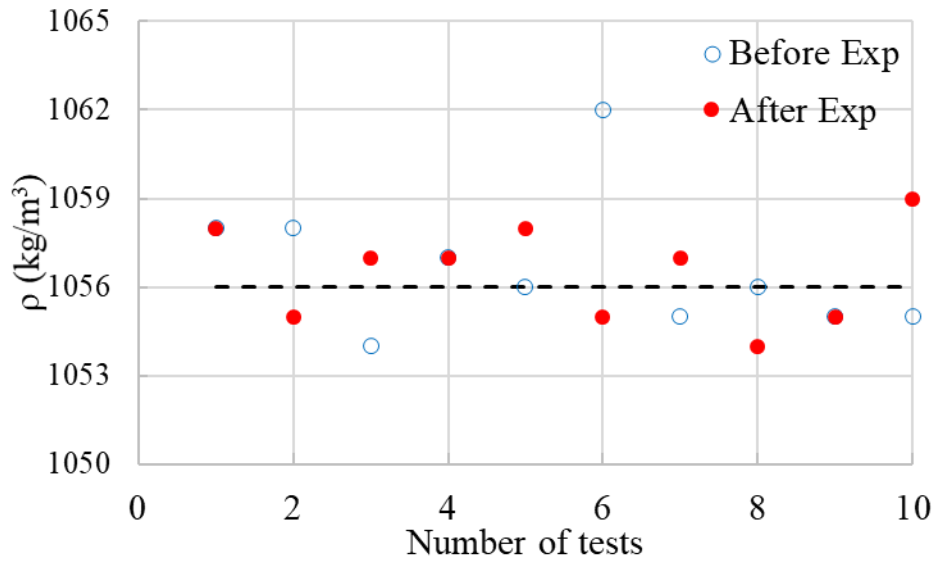


Figure 2-8: Comparison of the values of density measured before and after its use in the experiments for 25 wt% of aqueous glycerin mixture at 25 °C.

2.1.4.2. Viscosity

The dynamic viscosity of some of the test liquids (see **Table 2-3**) is measured with a Ubbelohde type viscosimeter (AVS310, Schott-Geräte). The apparatus uses the capillary based method for measuring viscosity: the time taken by the liquid to pass through a known capillary section of a given diameter is measured. By Poiseuille’s law, we can estimate dynamic viscosity as follows:

$$\mu = k_v(t_v - C_t)\rho$$

k_v is a viscosimeter constant and C_t is a correction for time or kinetic energy correction which is a function of time, specified by the manufacturer for a given capillary section dimensions (radius and length). The time is measured using a stop watch. Experiments are conducted at a temperature of 25 °C. The size of the capillary section, viscosity measurement limits and other specifications detailed by the manufacturer are shown in the **Table 2-2**.

Type	Capillary constant k_v (mm ² /s ²)	Capacity (mL)	Total length (mm)	Inner diameter (mm)	Limits (mPa.s)
0a	0.005	15 - 20	290	0.53	0.8 - 5

Table 2-2: Specifications of the Ubbelohde type viscosimeter to measure viscosities of propan-2-ol and 25% aqueous glycerin mixture

With the type 0a, the viscosity of two liquids (25% aqueous glycerin mixture and propan-2-ol), compatible with the range given in **Table 2-2** is measured. Five different measurements are

performed in both the cases. The value of dynamic viscosity measured is tabulated in **Table 2-3** with approximate uncertainty in the measures. Despite respecting all kinds of protocol, the error in the measured values was consistently present. The error in the measure is probably the resolution of the apparatus itself and also due to temperature sensitivity (precision of 0.1 °C).

2.1.4.3. Surface tension

With the known (measured and/or specified by the manufacturer) weight ratio, density, dynamic viscosity, and temperature, surface tension values are simply extrapolated from the existing literature^{81,82} for 55wt% glycerin, 25wt% glycerin, deionized water and propan-2-ol. Refer to the **Table 2-3**.

2.1.4.4. Dynamic contact angle

The dynamic contact angle was measured for all four liquids in triplicate with a tensiometer (Tracker, I.T. Concept, Teclis). The device consists of a cuvette surrounded by a thermostatic envelope. An automatic positioning platform to hold the sample in a horizontal position. A syringe was held on top of the test plate. It is equipped with a removable platform that allows the horizontality to be adjusted to measure the dynamic contact angle between a liquid and a solid. A camera and a light source to adjust and measure the contact angle at a given position. Temperature can be controlled for both the cuvette and the syringe by using a circulating bath. The contact angle is verified at locations near and far from the perforations. The surface of the plate is prepared following the protocol described in paragraph 2.3 (Experimental protocol). The dynamic contact angle measurement is accomplished by adding liquid to a static droplet on a surface and thus pushing the front of the liquid across the unwetted surface. The contact angle measured during droplet expansion is referred to as the advancing contact angle (θ_a). On the other hand, continuously removing liquid from a droplet will decrease its size and thus cause dewetting of the surface. The contact angle formed during the shrinking of the droplet is referred to as the receding contact angle (θ_r). Each measurement for each liquid is done for 60 s. Images are extracted during the time of measure. The images are analyzed using the plugin “dropsnake” in the Fiji software. The contact angle is obtained by a piecewise polynomial fit. The drop reflection is used to detect the interface and a small tilt in the image. The measured values are summarized in the table **Table 2-3**.

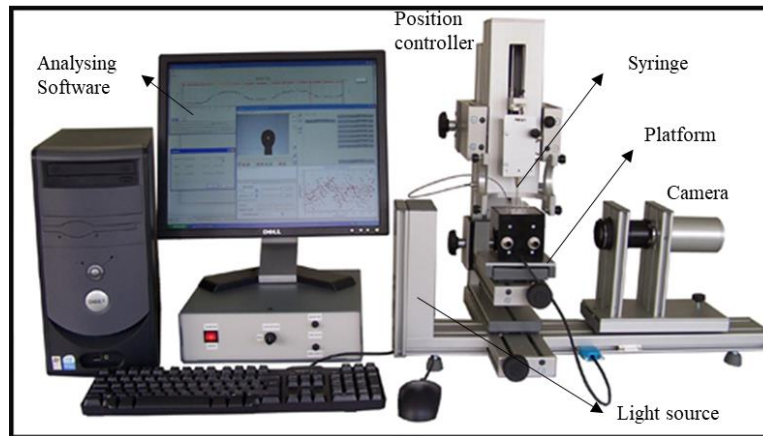


Figure 2-9: An image of the Tracker device (Teclis)

The measurement errors are mostly in the case of low contact angle liquid (propan-2-ol in the present case). The interfaces, far from the syringe, are blurred, which causes an error of approximately 1° .

Liquid	ρ ($\text{kg}\cdot\text{m}^{-3}$)	μ ($\text{mPa}\cdot\text{s}$)	σ ($\text{mN}\cdot\text{m}^{-1}$)	θ ($^\circ$)	Ka	Re range
Propan-2-ol	$786 \pm 3.3\%^a$	$2.05^c \pm 16\%^b$	21^c	$11-17^a$	348	6 - 80
55wt% glycerin	$1134 \pm 4.4\%^a$	7.05^d	68^d	$22-30^a$	245	2 - 35
25wt% glycerin	$1056 \pm 4.2\%^a$	$1.87^d \pm 30\%^b$	71^d	$23-35^a$	1470	9 - 115
Deionized water	997^a	0.891^e	72^c	$40-65^a$	3920	15 - 225

Table 2-3: Physical properties (at 25°C) of the liquids used in the experiments and range of Reynolds number investigated.

^ameasured, ^bfrom⁸³, ^cfrom⁸¹, ^dlinearly interpolated from⁸², ^efrom⁸⁴

2.1.5. Measurement techniques

In this section, methods of measurements used to quantify the transition mechanisms in the perforation is demonstrated.

2.1.5.1. Measurement by visualization and shadowgraphy

The optical method is popularly used to observe the temporal evolution of different transition mechanisms or instabilities in the liquid film over a perforation. The method reveals instabilities such as Rayleigh-Taylor and Rayleigh-plateau when the liquid film undergoes different transition mechanisms in the perforation. The measurement technique offers high temporal resolution (>2 kHz). We can create an adequate contrast between the fluid film suspended in the perforation and the surrounding for image analysis by correct light intensity adjustment. With the help of image processing techniques, key characteristics of the liquid films can be quantified.

Another type of visualization is to observe the free surface profile of the liquid film on the aluminum surface by illuminating the front side of the liquid film at a suitable angle. Due to the combination of reflection and refraction of light rays on the plate surface and the free surface of the liquid film, the camera perceives the crest regions as light areas and the trough regions as dark areas (see **Figure 2-10**). The wavelength of the 2D waves on the front side can be quantified. The resolution of the measurement is limited by the spatial resolution of the camera, thereby adding a constraint to capture images of a fully perforated plate. The sampling rate and exposure time are carefully adjusted to have less interference with the aluminum surface reflections.

Data acquisition parameters: The liquid flow pattern is observed and recorded using a Complementary Metal Oxide Semiconductor (CMOS (v310, Phantom)) high-speed camera mounted with a macro lens (AF Zoom-Micro Nikkor 70-180mm f/4.5-5.6D ED, Nikon). Images are captured with a resolution of 1200×800 px² and with an acquisition frequency of 1.8 kHz. The camera is adjusted to cover the area of the perforation, including the area around the perforation. For shadowgraph imaging of the suspended film, the backside of the plate is illuminated with a LED panel (SLLUB, PHLOX). The supported film on the front side is lit by a cold light illuminator (KL 2500 LCD, Schott).

Visualization of supported and suspended liquid film

The technique revealed the characteristics of a free surface of the film in the presence of perforations. Due to the difference in refractive index between the working fluid, test plate, and air, surface deformations are observed regardless of the opaque surface. Wavelength (λ) of the waves propagating is calculated after a calibration of image using Fiji (imagej) software. The homogeneous white background in the perforation area enabled us to characterize different

transition mechanisms of the fluid film in the perforation: rim, drop, column, partial and full curtain is observed (see **Figure 2-11**). The advantage of shadowgraph photography over other visualization techniques is it is non-invasive and allows the recording of images with a suitable acquisition in many cases. For example, the drop formation, its extension, and its detachment can be clearly visualized by adequately adjusting the acquisition time. Measurement of several characteristics such as wave celerity and sizes of instabilities like droplets and jets are also possible.

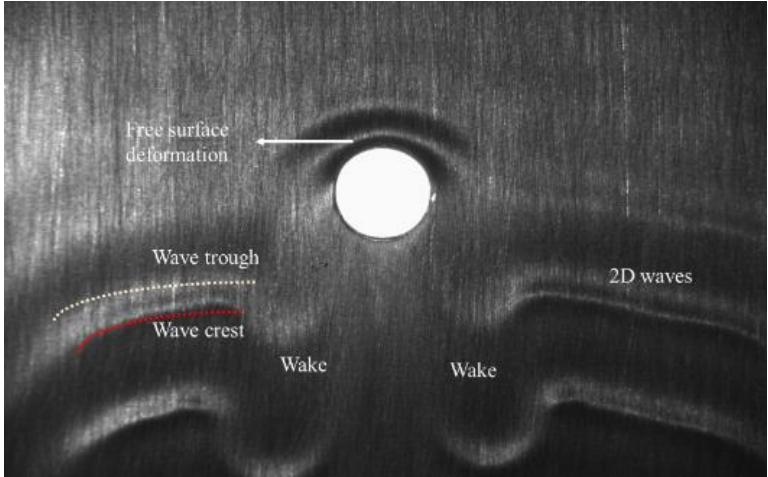


Figure 2-10 : Visualization of free surface deformation of the fluid film at low volume flow rate per width (W) of the film

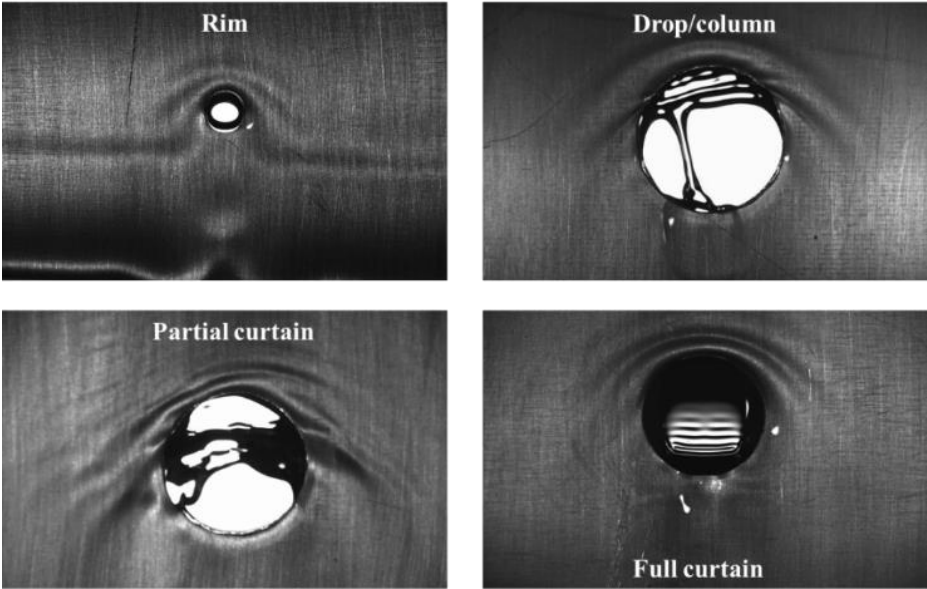


Figure 2-11: Visualization of rim, drop, column and full and partial curtain at moderate volume flow rate per width (W)

Frequency of rim oscillation by shadowgraph

Data acquisition parameters: The rim oscillation clinging in the inner surface of the perforation ($d = 2 - 8$ mm) is recorded for 3 - 5 s. using high-speed camera mounted with a macro lens. Images are captured with a resolution of 256×256 px² and with an acquisition frequency of 2 kHz. The camera is adjusted to cover the area of the perforation. The image resolution is reduced to focus on the uncovered part of the perforation. The back of the plate is illuminated with a LED panel, and the front is kept completely dark.

Volumetric flow rate: The frequency of oscillation is measured at a volumetric flow rate just before the transition to curtain mode. The list of parameters used in the measurement of oscillation frequencies is tabulated in the **Table 2-4**.

d (mm)	t = 0.5 mm		t = 1 mm		t = 1.5 mm	
	$Q_f = 0.9 Q_{cr} \text{ (m}^2\cdot\text{h}^{-1}\text{)}$					
	One face flow	Two face flow	One face flow	Two face flow	One face flow	Two face flow
4	0.29	0.18	0.29	0.19	0.35	0.21
6	0.36	0.30	0.34	0.26	0.36	0.27

Table 2-4: Flow and test plate parameters used in oscillation frequency measurements

The resulting image with the nomenclature of different zones is shown in the **Figure 2-12a**. During the oscillation of the rim, the region enclosed in red dotted lines enlarges and retracts due to the interplay between inertia and surface tension forces. The raw images are converted into black and white equivalents and then the highlighted region alone is selected in all images (see **Figure 2-12b**) using a short macro in ImageJ software (see **Figure 2-12b**). By doing this, we observed a large gain in computation time. Using in-house MATLAB code, the centroid of the shape retained is determined for all the images. The centroid point is calculated for each shape in each image. The movement of the centroid in y and x-direction is plotted (Y_g, X_g) (see **Figure 2-13ac**). To have more accurate calculations, the area of each shape (a_g) in each image is calculated (see **Figure 2-13e**). The continuous time variation signal of a_g is out of phase with X_g . This infers that when the position of X_g is small (with respect to the lower part of the image), the area a_g is higher (retracted rim corresponding to large area).

Finally, a spectral analysis of the periodic fluctuations of X_g, Y_g and a_g is performed using Fast Fourier Transform (FFT) (**Figure 2-13bdf**). From the single-sided amplitude spectrum of the FFT of these parameters as a function of frequency, the dominant frequencies can be accurately estimated (see **Table 2-5**).

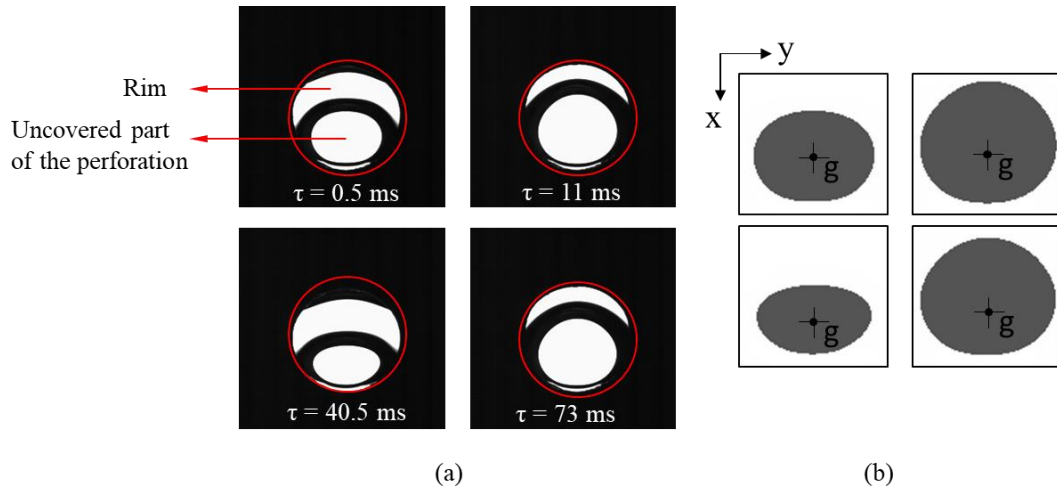


Figure 2-12: (a) Shadowgraph images of the suspended rim at different time intervals ($d = 6$ mm; $t = 1$ mm; $Q_2/Q_1 = 1$) (b) Zone of interest selected for image analysis

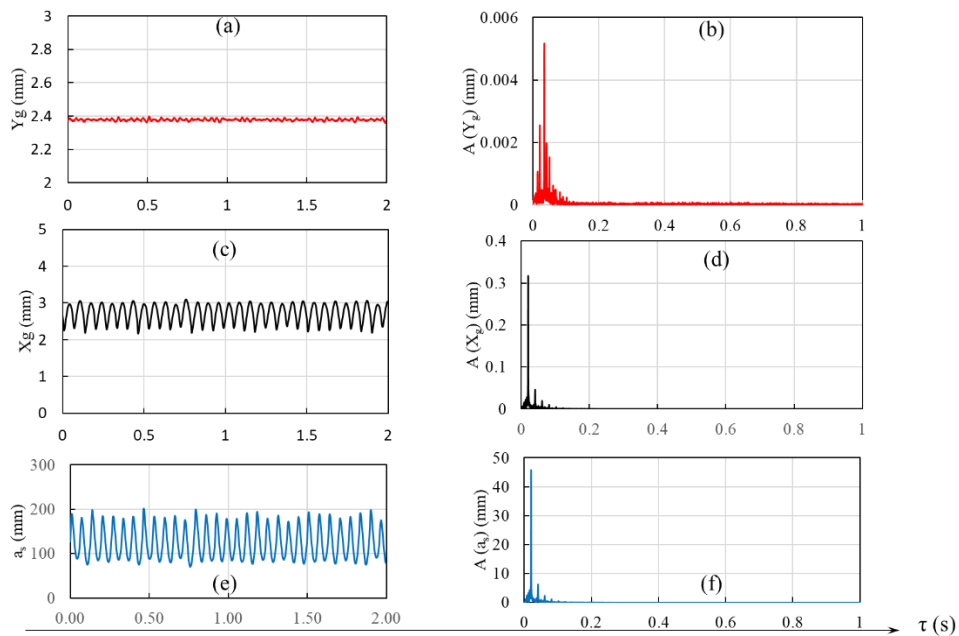


Figure 2-13: Periodic time variation of centroid and corresponding FFT of the signal in (a,b) horizontal (y) direction (c,d) vertical (x) direction (e,f) surface area of the shape.

Oscillation component	τ (s)	Frequency detected (Hz)
X_g	2.05E-02	15
	3.45E-02	26
Y_g	2.05E-02	15
a_s	2.05E-02	15

Table 2-5: List of frequencies detected corresponding to the highest amplitudes

2.1.5.2. Measurement of film thickness

This section presents methods used to measure the thickness film of a falling liquid film on a perforated plate. Due to the presence of the perforation, two types of film can exist: supported (on solid surface) and suspended (in the perforation) liquid film. Optical measurements have been extensively used in recent years for their precision and non-intrusiveness. A short review of different methods used to measure film thickness is presented before describing the methods used in the present study.

Confocal Chromatic imaging

Principle

Confocal Chromatic Imaging (CCI) is an optical measurement technique used generally to measure the surface topography. The method was initially used for the surface structure characterization of solids and in the applications of optical profilometry⁸⁵. In the recent years, it has been applied to measure the thickness of the film^{62,86} on the transparent surfaces. Polychromatic white light is focused onto the reflecting interface positioned in this continuum of a particular depth using a multi-lens optical system. The lenses are arranged in such a way that the white light is dispersed into a monochromatic light by controlled chromatic aberration. Light of selected wavelengths is reflected towards the front lens, which would image the interfacial reflection point onto the point source. Due to the presence of a semi-reflective mirror, reflected light is diverted into the signal detection unit. The spectral intensity distribution of the incoming light is measured with a spectrometer in discretized form. Subsequently, the wavelength of maximal intensity, which is linked to the distance, is determined from the distribution. The set-up consists of 2 components: a controller unit and an optical probe. The controller unit consists of the light source, semi-reflecting mirror, spectrometer, data processing hardware, and an optical probe, which holds the front lens. Both the parts are connected by

optical fiber. The advantages of CCI are the high sampling rates and spatial resolution, and the only drawback is that its sensitivity reduces in the presence of gradients.

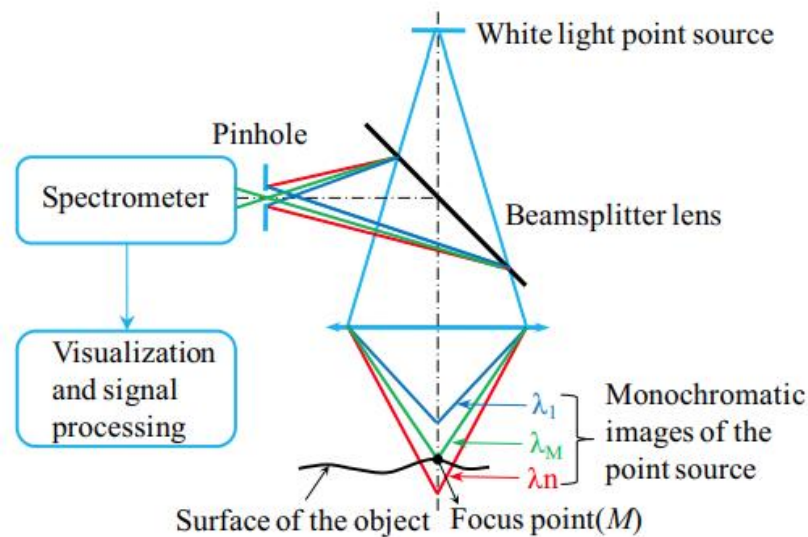


Figure 2-14: Demonstration of the principal of confocal chromatic imaging

In the present study, we have used 2 models of sensors from STIL group with CCS PRIMA optoelectronic controller CL3 and CL4 sensor. The sensor detects multiple interfaces (opaque solid surface/liquid, liquid/air). Thus it is adapted to measure liquid film on the solid surface as well as the suspended liquid sheet in the perforation. The sensors can directly measure the film thickness or the distance from the plate and free surface of the film. The specifications of the sensors:

CL3: measuring range is 1.4 mm, working distance 12.2 mm, max. inclination 25° , minimum measurable thickness $40 \mu\text{m}$.

CL4: measuring range is 4 mm, working distance 16.5 mm, max. inclination 21° , minimum measurable thickness $110 \mu\text{m}$.

The sensors used are adapted based on the volumetric flow rate per width of the film and the type of liquid used. The temporal resolution used in the present study is 5 kHz. However, it can be extended up to 10 kHz. The sensors are calibrated by the supplier specifically to function on highly reflective surfaces such as aluminum. The linearity error of the film thickness measurements is less than $0.5 \mu\text{m}$.

2.1.5.3. Validation with needle contact probe method

Methodology and set-up

The simplest of all the methods is by advancing the needle to make contact with the plate surface. The needle is retracted and advanced again in the presence of a liquid film to make contact with the free surface of the film. The displacement of the needle up to the free surface is measured. The thickness of the film is calculated as given in the expression below.

$$\delta_{NCP} = \delta_{plate} - \delta_{film} \quad (2.1)$$

A needle of thickness 0.1 mm, positioned on the micrometer displacement platform. The platform can translate in x, y, and z-axis with the precision of up to 0.001 mm in each axis. The needle holder and the aluminum were connected to the digital multimeter through the leads. Due to the property of electrical conductivity of the metal (aluminum), it was possible to detect the position where the needle touched the aluminum surface. Since propan-2-ol does not conduct electricity, the interface was detected using a combination of the light source and magnifying glass. Due to the good wetting property of propan-2-ol, contact point hysteresis is observed when the needle makes contact with the liquid. This is unavoidable in invasive tests.

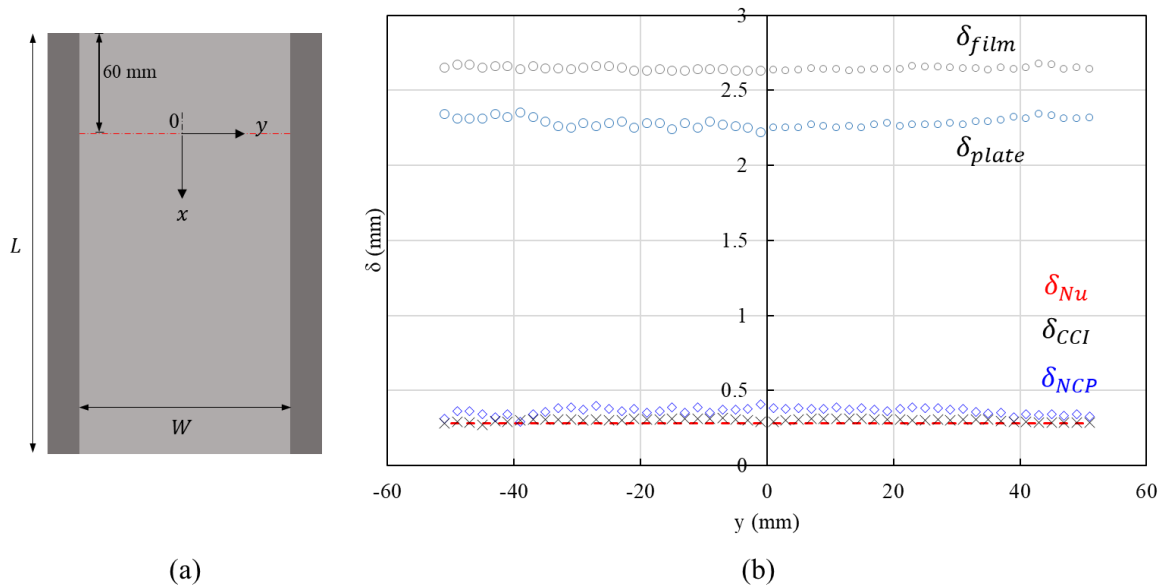


Figure 2-15: Comparison of the film thickness measured using needle contact probe for 3 different volumetric flow rate per unit width with the analytical Nusselt film thickness

An in-line (span-wise direction) measurement of film thickness is done in the zone where the perforations are made (60 mm from the top of the plate). The mean film thickness obtained by the needle contact method is compared with the theoretical value estimated by the Nusselt film

solution (see **Figure 2-15**). The experimental results are dispersive along the y-direction, yet the difference from the theoretical values is not high.

2.1.5.4. Comparison of δ between CCI and NCP

We compare the span-wise mean film thickness measurements obtained from two methods of NCP and CCI. It is not technically possible to perform the measurements simultaneously and exactly at the same point with the two systems. However, the measurements are performed in the fully developed film zone, identified at 60 mm from the top edge of the plate (see **Figure 2-16**). The low range of volumetric flow rate is selected because dry zones/thinning is highly susceptible at low flow rates. We aim to validate the uniform film condition in all conditions. We note an excellent agreement between the measurements obtained by the two techniques, as illustrated on the graphs of **Figure 2-16**. The results also signify the uniformity of the liquid film in y-direction.

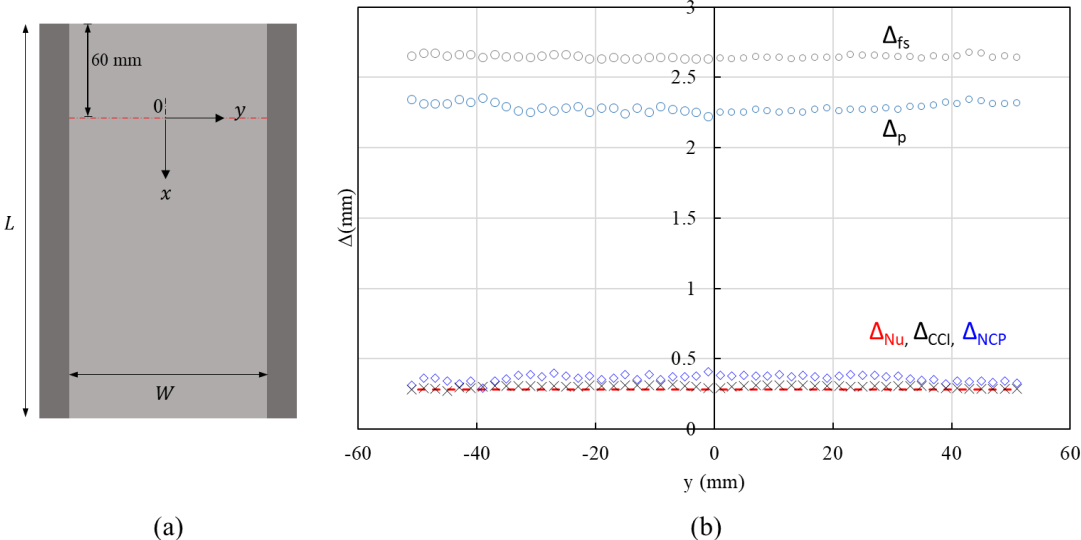


Figure 2-16: Comparison of film thickness measured in line in spanwise direction (y direction) by needle contact method and CCI with the theoretical estimation.

2.2 3D 3C Particle Tracking Velocimetry for the investigation of liquid films

In this section we describe the concept of optical setup and its layout along with the selected parameters used in the experiments of 3D 3C Particle Tracking Velocimetry (PTV). We use the main flow facility presented in *paragraph 2.1* and integrate the optical instruments necessary for velocimetry. The objective of the experimental set-up is: (i) to quantify the three-component velocity of the liquid film (ii) to explore and quantify and recirculation zones.

2.2.1. Description of the optical setup

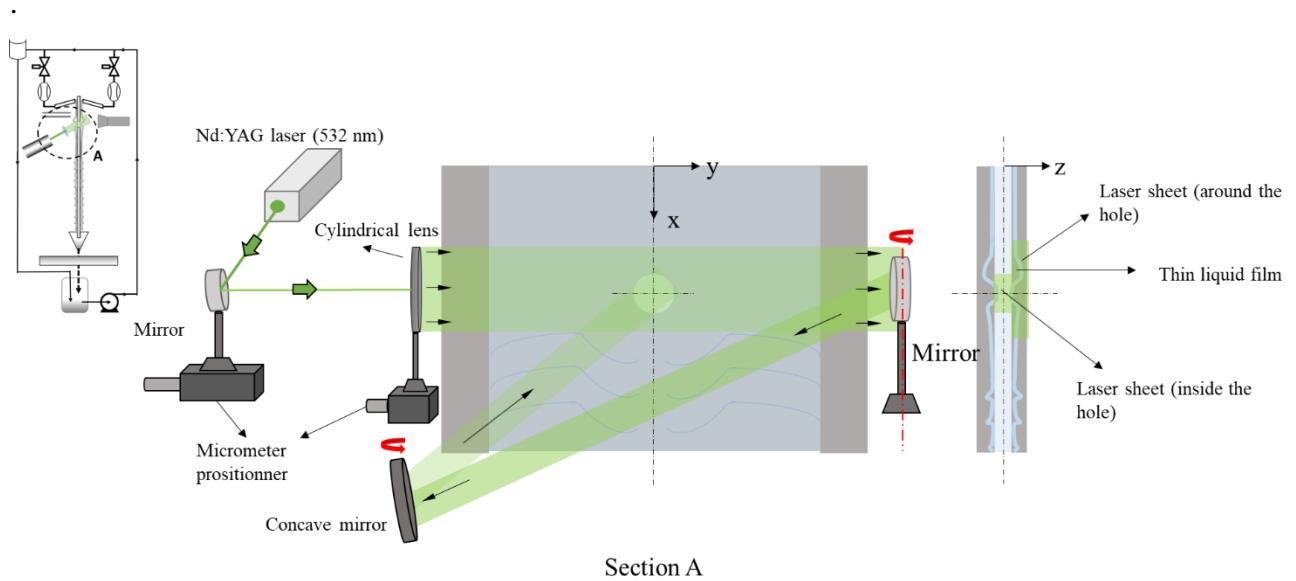


Figure 2-17: Demonstration of the light sheet optics: orientation of the laser sheet and collection optics from the front side.

The optical part of the setup consists of a CMOS high-speed camera (v310, Phantom) mounted with a macro lens (AF DC-Nikkor 105 mm f/2D, Nikon), fluorescence filter (centered around 570 nm), Nd: YAG laser (532 nm - 16W - finesse Quantum), optical lens and mirrors. The continuous laser beam excites the fluorescent tracer particles seeded in the flow. The maximum output power of the laser beam is maintained up to 16 W throughout all the measurements. The laser beam is directed in the direction parallel to the falling film flow using a mirror. Then, it passes through a cylindrical lens that converts it into a laser sheet. The laser sheet is then directed over the flow from the left side to the right side (seen by the camera) on the entire width of the plate (see **Figure 2-17**). The width of the sheet in the x-direction is approximately 12 mm. The intensity is homogeneous in the zone of measurement in the plate's streamwise (x) and span-wise (y). An additional optical setup is used to visualize the hole area (specific to

perforated plate). A combination of two mirrors and a convex lens with a pre-set tilt angle is used to refocus the laser beam in the hole.

Camera and acquisition parameters

All the images are captured with a resolution of $1200 \times 800 \text{ px}^2$ at a sample rate of 800 Hz and an exposure time of $1200 \mu\text{s}$. A fluorescence filter is used between the objective and the sensor to visualize the fluorescent tracer particles. The filter avoids capturing parasite reflections emitted by the aluminum plate, deformation on the free surface film and other reflective surfaces present around the setup. The frontal view of the plate is visualized by the camera (see **Figure 2-18**). The camera is installed on a precision positioning platform to adjust its orientation in all three dimensions precisely.

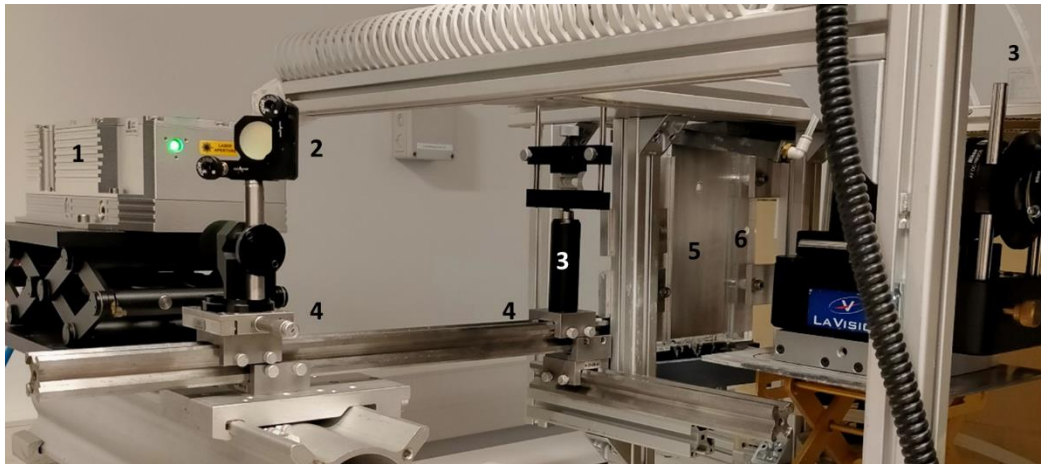


Figure 2-18: An image of the test setup: 1. Yag laser (532 nm) 2. Mirror 3. Cylindrical lens (75 mm) 4. Micrometer positioner 5. Test plate 6. Plexiglas support.

Tracer particles

The selection criterion for the properties of the tracer particles (diameter (d_p), density (ρ_p)) is based on the Stokes number (St). This number calculates the ratio between the response time of the particles (τ_p) to the Kolmogorov time scale (τ_κ) of the flow. We recall that τ_κ represents the smallest time scale of turbulence.

$$St = \frac{\tau_p}{\tau_\kappa} \text{ with } \tau_p = d_p^2 \cdot \frac{\rho_p}{18 \mu}$$

where ρ_p is the density of the particle, d_p is the diameter of the particle and μ is the dynamic viscosity of the liquid. $St \ll 1$ signifies that the particle perfectly follows the flow

streamlines. Furthermore, as the aim is to track individual particles, the amount of particles in the liquid remains limited. We therefore ensure that:

1. The particles do not significantly alter the physical properties of the fluid by using low concentration.
2. The particle interaction with each other do not alter the fluid mechanics.
3. And they emit sufficient signal to be perceived by the acquisition systems.

2.2.2. Parameters of experiments

Test plates

The validation of the capacity of the measurement is performed with the falling liquid films on a flat aluminum plate.

A single perforation of two different diameters ($d = 4, 8$ mm) is machined on an aluminum plate (see **Figure 2-6a**). The thickness of the plate ($t = 0.5, 1$ mm) is also varied for both perforation diameters. Totally, 5 perforated test plates (see **Table 2-1**) were used to perform the particle tracking velocimetry.

For qualitative trajectory measurements, a flat perforated plate with a row of perforations are also used.

Liquid system parameters

Two different Newtonian liquids with a range of parameters (ρ, μ, σ) are used in the experiments. Deionized water and propan-2-ol are used as test liquids. Six different volumetric flow rates per unit width ranging from 16 – 35 L.h⁻¹ are investigated. The list of parameters (camera, particles, acquisition, d, t, Q and liquid type) used in the present study is tabulated in **Table 2-6** For perforated plates, experiments are conducted with both one face and two face supply conditions.

Test plate parameters	Test liquid	Particles	fstop	Exposure time (μs)	Frames per second fps (Hz)	Laser power (W)	Distance b/w lens and plate (cm)	Defocus control	Lens	Number of images	Flowrate (L.h ⁻¹)	Annual aperture	field of view (l × b) (mm)
Flat plate	Propan-2-ol (Ka = 348), Deionized water (Ka = 3920)	5 to 8 x 60 μL in 2 L of propan-2-ol*; 3x60 μL dans 1.8 L of water	2	800	1200	16	<14	F2	AF-DC	4000	16.6	Mask No. 1	42 x 26
Single perforation d = 4, 8 mm t = 0.5, 1 mm											20.2		
Multiple perforation d = 4 mm, t = 1 mm, S = 14 mm											23		
											26		
											28.2		
	35												

* Liquid was filtered to remove old particles and seeded with new particles if the experiments were performed on different days.

Table 2-6: List of test plate, liquid, camera and optical parameters used in the study

2.2.3. Measurement techniques

The method was developed, validated, and implemented in an experimental study by Baudoin *et al.*⁸⁷ in cooling rods within a reactor core application. A brief review of optical measurement

techniques, particularly applied in falling liquid films on flat or complex surfaces.

Optical techniques for velocity measurements

Vertical falling liquid films are unconditionally unstable, and the measurements are easily affected by the interface shapes. The liquid film is susceptible to the disturbances induced by measurement and calibration devices. Therefore, it is essential to use non-intrusive methods. Considerable efforts have been devoted to the experimental study of falling liquid films on flat plate. Particle Image Velocimetry (PIV), Particle Tracking Velocimetry (PTV), Planar Laser Induced Fluorescent (PLIF) on widely applied on the liquid films on flat surfaces^{58,88}, annular channels^{86,89}. Planar laser-induced fluorescence (PLIF) is based on fluorescent imaging. It allows spatiotemporally resolved velocity information to be recovered simultaneously with the film thickness data. For example Rhodamine-B is one of the suitable velocity tracers used in PLIF to seed the flow. On the contrary to PLIF technique, particle image velocimetry (PIV) and particle tracking velocimetry (PTV) allow the measurement of 2D and 3D flow-field with one or more cameras. The measurement area is illuminated using a high-power laser sheet. The scattered non-fluorescence or fluorescence signals generated by particles in the flow are tracked as control volume (PIV) or individual particles (PTV). The imaging is done with a short acquisition time. A typical multipass FFT-based cross-correlation approach is used for image post processing. PIV measurements enable to detect eddies or recirculating flow regions and PTV determines selected particle trajectory and residence times. **Figure 2-19b** shows an example of the 2D planar velocity vectors obtained by PIV and PTV technique in a falling liquid film on flat surface.

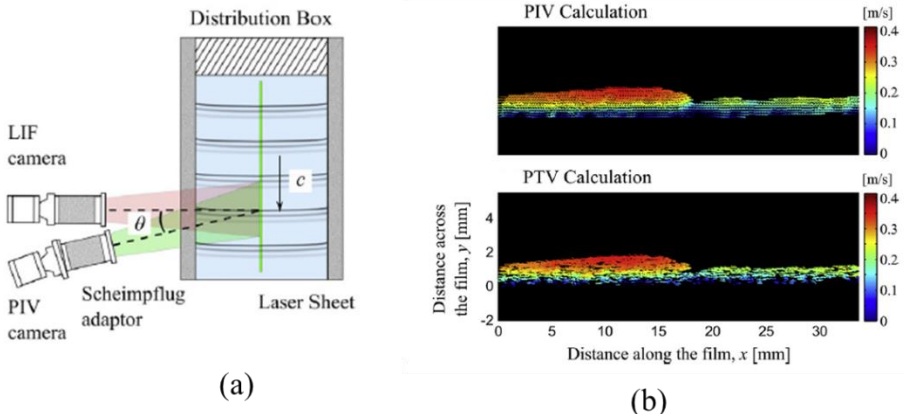


Figure 2-19 : (a) Schematic of the test section showing the orientation of the laser sheet and collection optics (top view). (b) Velocity vector maps of the film cross-section from PIV and PTV⁵⁸.

Gerke *et al.*⁹⁰ developed a μ -Stereoscopic Particle Image Velocimetry (μ -SPIV) to investigate the hydrodynamics of the liquid film on inclined corrugated packings. The velocity distribution measurements are performed on a transparent corrugated and textured surface. The method captures the three-component velocity fields in a 2D planar cross-section of the corrugated surface (see **Figure 2-20**). 2D velocity vector map reveals static recirculation zones on the free surface of the liquid film (corrugation valleys). **Figure 2-21bc** shows the liquid accumulation and rivulets forming downstream the holes in the valleys of corrugations. The corresponding 2D velocity vectors were measured by μ -SPIV around the contact region in a real packing surface (although not a metallic packing surface). The flow is being blocked in the valleys at the hole entrance, displaying the capillary ridge. However, the liquid flows around the hole in the form of rivulets. **Figure 2-21a** shows the condition of the structures when there is no liquid film. However, the measurements are limited by the spatial resolution of the corrugated surface. The exhaustive study of Hampel *et al.*⁹¹ presents the recent development of laser-based optical techniques applied on complex surfaces at multiple scales. The review emphasizes the different experimental measurements developed to study the underlying mechanisms of the liquid film on structured packings surface at numerous scales.

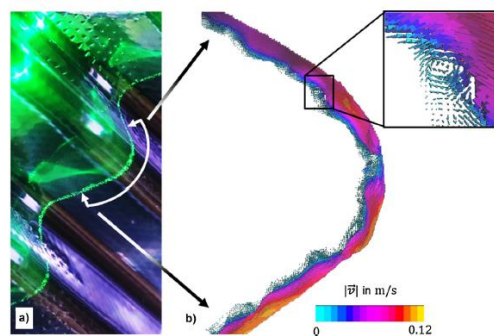


Figure 2-20: Microtextured corrugated surface inclined at 45° . A static recirculating eddy in the zoomed image.

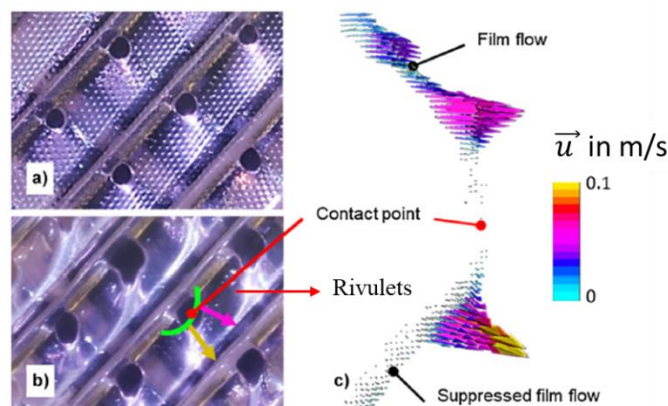


Figure 2-21: Images of the closed transparent packing channel: (a) with minimal static liquid hold-up (no liquid load) and (b) static holdup for $Q_L = 40 \text{ m}^3\text{m}^2\text{h}^{-1}$ (green arc) (c) measured velocity vectors.

Originality of the work

Experiments are conducted on the liquid films on aluminum plates to well represent the industrial packing surface. To gain in spatial resolution, the camera is placed in front of the test plate rather than in the film cross-section view (see **Figure 2-18**). We measure velocity distribution on both wall-bounded and suspended films (liquid curtain) on perforated plates. Finally, to access the depth component, we use a defocus technique while creating a laser sheet in the entire depth of the film. By setting defocus on the camera, the apparent size of the tracer particles increases. Their apparent size is linked to the distance from the focal plane through thin lens approximation. By measuring the distance from lens to plate and lens to free surface of the liquid film, it is thus possible to determine the position of the tracer particles in the depth of the film. The static particles on the plate surface are used for calibration purposes (reference size of the particles on the wall). A detailed description of the methodology and measurements made is presented in chapter 5.

2.3 Experimental protocol

Before each experiment, the test plate is cleaned with a surfactant solution (3 vol%, Mucosol, Merz), thoroughly rinsed with distilled water, and dried with compressed air. Then, it is inserted and fixed in the vertical frame.

The outlet of the distributors is positioned on the plate faces, about two millimeters below the top edge of the plate. Since the outlet is located 58 mm upstream of the perforation, the film flow is fully developed at the location of the perforation.

The distance between plate and the distributor (in z direction) is adjusted to 1 mm using a guide plate. The parallelism of the test plate is carefully adjusted in order to obtain a liquid film of uniform thickness in the spanwise (y) direction.

Both faces of the plate are supplied with the highest flow rate, i.e. $65 \text{ L}\cdot\text{h}^{-1}$, such that the liquid is forced to wet the whole usable width of the plate, i.e. $W = 90 \text{ mm}$. Then, the liquid flow rate can be reduced down to $5 \text{ L}\cdot\text{h}^{-1}$ and the region upstream of the perforation remains totally covered by the liquid film.

For two face supply condition $Q_1/Q_2 \neq 1$ ($Q_2 < Q_1$) (3rd flow condition), the flow rate that supplies the backside of the plate (Q_2) is first fixed at its target value. Then, the flow rate of the plate front side (Q_1) is progressively increased, in increments of 1 L.h^{-1} , in order to explore the different regimes of the film flow around and over the perforation. We determine the flow rate per unit width at the curtain transition (Q_{cr}) as follows: Q_{cr} is associated with the smallest flow value for which there is a stable curtain that entirely closes the perforation.

For the supply condition $Q_1/Q_2 = 1$, the flow rates are identically initialized and increased simultaneously with the same increments.

For each set of parameter values, experiments were performed at least in triplicate to ensure the reproducibility of results.

Protocol specific to 3D PTV measurements

At first, we consider to add a volume of $60 \mu\text{L}$ per $1.8 - 2 \text{ L}$ of test liquid in order to avoid high particle density in the flow. The particles (PMMA-RhB-10) of $1-20 \mu\text{m}$, suspended in water (50 g of particles suspended in 200 ml of water). The particle concentration is verified by visualization. If the density is too low, we gradually increased the seeding volume up to $3 - 8 \times 60 \mu\text{L}$. The liquid in the reservoir is constantly agitated with a magnetic agitator to prevent particle agglomeration and settling of the particle at the bottom of the reservoir.

Before each experiment, the condition of the test liquid is verified. Test liquid is filtered frequently and new particles are added (refer to **Table 2-6**). The other flow loop components (mass flowmeters, distributors, tubing, valves, etc.) are purged with demineralized water after certain number of tests to avoid particle agglomeration.

For cleaning, preparation and adjustment of the test plates, refer to the *paragraph 1.5*.

Each test is conducted by supplying six different flow rate ($16, 20, 23, 26, 28$ and 35 L.h^{-1}). At all six flow rate, curtain formed in the perforation is maintained in both one face and two face supply conditions.

2.4 Conclusions and Perspectives

To summarize, we presented the two configurations of experimental setup designed and constructed to study liquid films on a perforated vertical plate. The specificity of the setup is that it allows to test the two face flow condition i.e., supplying liquid on both faces of the plate. The volumetric flow rate can be independently controlled on each side to supply equal and/or unequal flow rate on both faces. Metallic sheets in the industrial structured packings are supplied on both faces and our experimental setup allows to achieve similar supply condition. The test plate parameters, liquid system parameters, and various measurement devices parameters are listed.

The first configuration of experimental setup contributes to studying different transition mechanisms of the liquid film in the perforation for a wide range of geometrical (hole diameter d and plate thickness t) and liquid system parameters (Re & Ka). The setup is slightly modified to integrate the measurement of liquid transfer through the perforation(s). The design enables to install optical devices used for shadowgraph technique and film thickness measurements (using CCI and needle contact methods).

In the second configuration, the main flow loop is not modified. We discussed a specific optical setup used to conduct 3D 3C particle tracking velocimetry (defocus) on wall-bounded and suspended liquid films on flat and perforated plates. A range of test plate parameters and flow conditions, including camera and acquisition parameters, are tabulated. We present a non-exhaustive bibliography review of specific laser-based optical measurements with their applications within the falling liquid films on flat/complex surfaces.

The experimental facility constructed can be used to study test samples like: 1. horizontally corrugated plates, 2. porous plates with/without corrugations (horizontal), 3. micro-textured plates. The facility is equipped with various measurement devices (optical techniques: PIV, PTV, CCI) that can be further exploited. For instance, 3D 3C PTV can be performed in locally selected regions within the valleys of corrugated and perforated plates, wave can be characterized by well calibrated imaging techniques.

3. Experimental study of a liquid film flowing over a perforation

Manasa IYER^{1,2}, Joel CASALINHO¹, Jacopo SEIWERT², Mikael WATTIAU², Hervé DUVAL¹

1 Université Paris-Saclay, CentraleSupélec, Laboratoire de Génie des Procédés et Matériaux, 91190, Gif-sur-Yvette, France.

2 Campus Innovation Paris, Air Liquide Research & Development, 1, chemin de la Porte des Loges, 78350 Les Loges-en-Josas, France.

Corresponding author: Hervé Duval (herve.duval@centralesupelec.fr)

Abstract: Perforations are one of the recognized geometrical features that contribute to liquid redistribution in corrugated sheet packings. Our experimental study focuses on a simplified but relevant configuration: a thin liquid film flowing on either side of a vertical plate with a circular perforation.

We focus on the curtain mode when the liquid fills the perforation. Confocal chromatic imaging reveals a capillary ridge upstream of the perforation, an inertial ridge downstream and a varicose capillary wave standing on the liquid curtain. We show that the wavelength is selected such that the velocity of the wave both satisfies Taylor's dispersion relation and matches the curtain local speed.

We examine the effect of perforation size, supply conditions and liquid properties on the curtain transition. Lastly, we propose a simple model based on a momentum balance that describes the effect of these parameters on the Reynolds number at which curtain forms.

Topical Heading: Transport Phenomena and Fluid Mechanics

Key Words: Structured packing, perforated sheet, liquid curtain, film thickness, varicose waves

1. Introduction

Corrugated sheet packings have been introduced in the 1970s and widely applied since then in distillation and absorption columns¹⁴. Such packings are composed of thin vertical crimped sheets stacked parallel to each other. In cryogenic air separation, the sheets are typically made of aluminum. These structured packings combine high packing void fraction and high interfacial area. This results in lower pressure drop, higher efficiency and higher capacity as compared to trays. The way the liquid distributes, spreads over the packing sheets and

eventually forms a film impacts the liquid-vapor interfacial area, the mass-transfer and the subsequent separation efficiency of the column⁹². In a corrugated sheet packing, three kinds of geometrical features contribute to liquid distribution: the corrugations⁴⁹, the perforations¹⁸ and optionally the microtexture whose characteristic length scale is typically one to several orders of magnitude lower than the corrugations. Perforations let the liquid flow from one side of corrugated sheet to the other side. As a consequence, they promote liquid exchange between the two sides of a same sheet and reduce the accumulation of liquid in the corrugation trough to avoid channel flow¹⁸. A common value of hole diameter is 4 mm and the standard opening rate of the sheets is 12.6%. Most of the corrugated sheet packing have perforations.

Whereas the effect of the corrugations on liquid distribution⁴⁹, liquid film thickness^{66 93}, liquid film stability^{67,70,71,94}, waves formation⁹⁵ and mass-transfer^{96,97} has been extensively investigated, there is very little published work on perforations and their impact on liquid film flow.

Pavlenko *et al.*¹⁸ studied experimentally the effect of perforations on liquid distribution for a single vertical aluminum perforated-corrugated sheet (although the main subject of this paper is the effect of microtexture). Only one side (front) of the sheet was supplied with liquid (the rear side is irrigated by the holes). Two perforation diameters were investigated: 4 mm and 10 mm. The liquid was liquid nitrogen. Pavlenko *et al.*¹⁸ distinguished different regimes depending on the film Reynolds number (Re defined in the next section). For $100 \leq Re \leq 225$, the entire surface of the sheet front side is wetted by liquid nitrogen, with no dry patch. 3D waves of high amplitude travel on the liquid free surface except in regions beneath the holes. These calm waveless zones become narrower and shorter as the flow rate increases. Droplets and jets detach periodically from the top edge of the 10 mm holes. For $50 \leq Re \leq 100$, longer and wider waveless zones extend below the 4 mm holes. Non-wetted areas appear beneath the 10 mm holes. For $10 \leq Re \leq 50$, dry zones extend beneath the 4 mm and 10 mm holes. These patches become wider and longer as the liquid flow rate decreases. Detachment of droplets and jets from hole top edge ceases. Travelling waves become 2D. For the whole range ($10 \leq Re \leq 225$), a significant flow of liquid through the holes (from the front side to the rear side) is observed.

Xie *et al.*⁹⁸ experimentally studied the film flow over a vertical aluminum plane plate with a single large perforation. Only one face of the plate was supplied with liquid. Six liquids were used with Kapitza number (Ka defined in the next section) from 52 up to 2930. The film Reynolds number was varied in the range 0-200. Xie *et al.*⁹⁸ investigated different perforation geometries but most of the results concern centimetric rectangular perforations. These so-called

“open windows” are actually novel elements for gas-liquid contact that show interesting mass transfer performances^{99,100}. Xie *et al.*⁹⁸ found a diversity of flow patterns. For $Re < 14$ (interval given for water), the liquid “passes around” the window forming a rim upstream, no liquid in the window and a dry patch downstream. For $14 \leq Re < 125$, droplets form periodically from the top edge of the window and spill on the bottom edge. As Re is increased, the liquid drops more and more frequently and turn to steady columns, which bridge the top edge to the bottom edge of the window. For $Re > 125$, the columns coalesce to form a pendant sheet. For even greater values of Re , a liquid curtain completely fills the window. This curtain exhibits a pattern of capillary waves. When liquid “passes through” the window (in the form of droplets, columns, pendant sheet or curtain), a part of the liquid flows from the front side to the back side of the plate. Xie *et al.*⁹⁸ also propose an empirical correlation for the film Reynolds number at liquid curtain transition. They note a hysteresis: the film Reynolds number for liquid curtain rupture is several times lower. In a second paper, Xie *et al.*¹⁰¹ further investigated the curtain regime using computational fluid dynamics (CFD). This regime is referred to as twin-liquid films by these authors because of the coexistence of a supported film on the solid plate and a suspended liquid film in the open window. Simulations were performed with two side liquid inlets. The suspended liquid film exhibits stationary varicose capillary waves. The characteristics of the wave pattern agree well with the experimental observations (carried out with two face supply). Furthermore, the numerical simulations evidence strong vorticity generation both inside the wavy suspended film and on its free surface. These phenomena contribute to the mass transfer intensification observed for the plate with open window (as compared to the unperforated plate)¹⁰⁰.

The sequence of flow patterns observed for a large rectangular perforation is close to the sequence typically seen in horizontal-tube falling-film heat exchangers. Bundles of horizontal tubes are widely used in refrigeration, desalination and food industries for example. Hu & Jacobi¹⁰² distinguished three idealized modes, i.e. droplet, jet and sheet modes (classified by increasing Reynolds number) and, in between, mixed modes, i.e. combination of two idealized modes. For each mode transition, Hu & Jacobi¹⁰² propose an empirical correlation for the transitional Reynolds number as a function of the Galileo number ($Ga = Ka^3$), for increasing and decreasing flow rate (since the transitions exhibit hysteresis). The correlation of Xie *et al.*⁹⁸ for rectangular perforation involves the same dimensionless numbers.

The film flow over a perforation (through hole) has also some similarities with the flow over topographies such as step-in, step-out, trench or blind (non through) holes. There is an abundant literature on this subject¹⁰³. It appears that a topography step is preceded by a standing capillary

wave: a capillary ridge before a step-in, a free surface depression before a step-out^{104,105}. As the film Reynolds number increases, a so-called inertial ridge appears after a step-out¹⁰⁶. The same features were observed by Xie *et al.*^{98,101} at the entrance and at the exit of a rectangular open window.

To better understand the effect of perforations on liquid redistribution and potential mass transfer enhancement in corrugated sheet packings, we presently consider a thin liquid film flowing on a vertical plane plate with a circular perforation. We address the different flow patterns and focus on the curtain mode: we will carefully characterize the curtain transition and the curtain mode for a broad range of perforation diameters (including standard values encountered in industrial packings), several plate thickness, different flow conditions (one side and two side supply with independent and controlled liquid flow rates) and various liquids. In particular, the local deformation of the film around and within the perforation will be assessed using confocal chromatic imaging (CCI).

In the first part of the paper, we briefly address the physics of the problem and identify the main dimensionless numbers that control the curtain transition. In the second part, we describe our original experimental setup and the measurement methods used to characterize the thin liquid film. In the third part, the different patterns of a liquid film flowing over a perforation are presented as a function of hole diameter and flow rate conditions. In the fourth part, we study in-depth the effect of hole parameters, plate supply conditions and liquid physical properties on the curtain transition threshold. In the fifth part, dedicated to the discussion, we propose a simple momentum balance to account for the curtain transition and give a physical picture of the curtain behavior.

2. Problem description

Liquid flows within industrial corrugated-perforated packing are very difficult to observe directly since the stacked sheets are opaque and the geometry is very intricate. In order to experimentally investigate the hydrodynamics of the thin liquid film flowing in and around the perforations of a sheet, we simplify the structure of a packing and consider a single perforation on a vertical flat plate (see **Figure 3-1** and **Figure 3-2**). x denotes the streamwise direction, y the spanwise direction and z the direction in the depth of the liquid film. In this simple geometry, upstream conditions can be carefully monitored and the effect of perforation on the film hydrodynamics is isolated from other topography effects such as corrugations. The

perforation is characterized by its diameter (d) and the plate by its thickness (t). The front side and the back side of the plate are indexed by $i = 1$ and 2 , respectively.

We consider a Newtonian liquid with constant density (ρ), dynamic viscosity (μ) and surface tension (σ). We suppose that the equilibrium contact angle (θ_E) of the liquid on the plate is significantly lower than $\pi/2$. Then, wetting is favorable. Each side (i) of the plate is supplied with liquid at a volume flow rate per unit width (Q_i) with $Q_2 \leq Q_1$. Two limiting cases are considered, i.e. $Q_2 = 0$ corresponding to one face supply and $Q_1 = Q_2$ corresponding to two face supply with equal flow rates. When a face is supplied with a non-zero volume flow rate, we suppose that this volume flow rate is high enough to completely wet the solid face. We assume that the film flows are steady and laminar and that the perforation is placed in the fully developed region. We are aware that a liquid film falling on a vertical flat plate is unconditionally unstable. However, we suppose that the amplitude of the waves travelling on the free surface remains much lower than the film thickness. Under these assumptions, in the established regime and in absence of perforation, the liquid film has a uniform thickness and the velocity profile is semi-parabolic as found by Nusselt⁵¹. The film thickness on the i side is then given by $\delta_{Nu}(Q_i) = (3\nu Q_i/g)^{1/3}$ for a vertical plate, where ν denotes the liquid kinematic viscosity. This thickness is called the Nusselt thickness of the falling film. Two other characteristic lengths can be defined, i.e. the capillary length $l_c = (\sigma/\rho g)^{1/2}$ by balancing the surface tension forces with gravity and the visco-gravitational length $l_v = \nu^{2/3}/g^{1/3}$ by balancing the viscous forces with gravity²³.

Let us assume that the perforation diameter is large, i.e. greater than the plate thickness and the capillary length of the liquid.

When the volume flow rate is low, the film flows around the perforation without filling it. On the contrary, when the volume flow rate is high, a liquid curtain closes the perforation (see the photographs displayed later in the paper). The transition between these two modes is expected to occur when the inertia of the film balances the surface tension forces, i.e. when the Weber number of the film is of the order of 1 ¹⁰⁷. For two face supply with equal flow rates, this reads $\rho (Q_{cr})^2/(\delta_{Nu}(Q_{cr})\sigma) \approx 1$ where Q_{cr} is the flow rate per unit width on one side of the plate at the curtain transition. In other words, curtain transition occurs when the liquid mean velocity $Q_{cr}/\delta_{Nu}(Q_{cr})$ is of the order of the Culick¹⁰⁸ retraction velocity of the curtain $(\sigma/(\rho \delta_{Nu}(Q_{cr})))^{1/2}$. This relation can be recast in the following scaling law

$$\text{Re}_{cr} \approx \text{Ka}^{3/5} \quad (3.1)$$

Re_{cr} is the Reynolds number of the film flow at the curtain transition. For the sake of brevity, we will later refer to it as the curtain Reynolds number. Re compares the inertial forces with the viscous forces acting on the film flowing on the front side ($i = 1$) of the plate. It is given by $Re = Q_1/\nu = \frac{1}{3}(\delta_{Nu}(Q_1)/l_\nu)^3$. Ka is the Kapitza number. It compares the effects of surface tension to the viscous and gravitational effects, i.e. $Ka = (l_c/l_\nu)^2 = \sigma/(\rho g^{1/3} \nu^{4/3})$. Ka only depends on the physical properties of the liquid.

In the general case, the problem is governed by 8 parameters, i.e. ρ , ν , σ , g , Q_1 , Q_2 , d and t , that can be expressed in terms of 3 independent dimensions. According to the Vaschy-Buckingham theorem, the problem can be fully described by 5 dimensionless parameters. From the above analysis, we choose the next set of independent dimensionless parameters: Re, Q_2/Q_1 , Ka, d/l_c and t/d . Then, the Reynolds number of the film flow at the curtain transition reads $Re_{cr} = f(Ka, Q_2/Q_1, d/l_c, t/d)$.

In the following, the dimensionless parameters are varied in order to investigate the flow modes of the film falling on the front side of the perforated plate and determine the Reynolds number at the curtain transition.

3. Experimental setup

3.1. Materials

The test plates are cut from aluminum sheets. The plate length in the streamwise direction is $L = 200$ mm and the plate width in the spanwise direction is $B = 150$ mm (see **Figure 3-1**). Three different plate thickness are studied: $t = 0.5, 1$ and 1.5 mm. The perforation is made by drilling for $t = 1$ and 1.5 mm and by laser cutting for $t = 0.5$ mm. Special care is taken when machining in order to maintain the flatness of the sheet and ensure that the edge of the perforation is sharp and perpendicular to the plate face. The center of the perforation is located on the midline of the plate, at 60 mm from the top edge. Eight perforation diameters are studied: $d = 2, 4, 6, 8, 10, 12, 14$ and 16 mm. The test plates are slightly polished with abrasive (grit size P1200) to get a matt rendering thus reducing the impact of parasitic reflections on optical based measurements. The resulting roughness parameter (Ra, arithmetical average of the roughness profile) of the plate is measured by confocal chromatic imaging (3D Measuring Station with CHR 150-N sensor, STIL). Measurements are performed in two orthogonal directions, streamwise (x) and spanwise (y), in the proximity of the perforation and far from the perforation. Ra ranges from 0.2 to 0.5 μm .

Four liquids are used in the experiments: pure propan-2-ol, 55 wt% glycerin aqueous solution, 25 wt% glycerin aqueous solution and pure water. Pure propan-2-ol has been purchased from VWR Chemicals (GPR Rectapur® >99.0%). Pure water is delivered by a Millipore Milli-Q purification system. Glycerin solutions are prepared from pure glycerin (Rotipuran® >99.5%, p.a., anhydrous, Carl Roth) and pure water: after weighing the components, the mixture is stirred until a homogeneous and perfectly clear solution is obtained. The final density of the solution is adjusted to the tabulated value²⁸ by a small addition of glycerin. Since liquid properties may alter over time (due to contamination, development of microorganisms and/or biochemical degradation), glycerin solutions are used within 36h after making. Milli-Q water is used the day of the delivery. Propan-2-ol is used in the week. The physical properties of the working liquids are reported in Table 1. We choose these liquids to cover a wide range of Kapitza numbers, i.e. more than one order of magnitude. Furthermore, the wetting of the aluminum sheets is favorable for the four liquids (equilibrium contact angle $\theta_E < 90^\circ$).

Liquid	ρ (kg.m ⁻³)	μ (mPa.s)	σ (mN.m ⁻¹)	θ (°)	Ka	Re range
Propan-2-ol	786 ^a	2.05 ^b	21 ^c	11-17 ^a	348	6 - 80
55wt% glycerin	1134 ^a	7.05 ^d	68 ^d	22-30 ^a	245	2 - 35
25wt% glycerin	1056 ^a	1.87 ^d	71 ^d	23-35 ^a	1470	9 - 115
Pure water	997 ^a	0.891 ^e	72 ^c	40-65 ^a	3920	15 - 225

^ameasured, ^bfrom⁸³, ^cfrom⁸¹, ^dlinearly interpolated from⁸², ^efrom⁸⁴

Table 3-1. Physical properties (at 25°C) of the liquids used in the experiments and range of Reynolds number investigated. The bounds of the contact angle (θ) interval correspond to the receding contact angle and to the advancing contact angle, respectively. The equilibrium contact angle (θ_E) lies in-between.

3.2. Experimental setup

The setup itself (**Figure 3-1**) comprises three parts: the frame that holds the perforated plate, the liquid circuit and the instrumentation dedicated to liquid film observation and measurement. The perforated plate is inserted in a rigid frame to ensure its flatness. The frame is held vertically. It is decoupled from the other parts of the device and mounted on an anti-vibration table to damp the parasitic vibrations that may affect the fluid film flowing on the plate. Each

face of the plate is supplied with liquid by a distributor. The liquid circulates thanks to a magnet gear pump (MDG-M15T3B, Iwaki). The volumetric flow rate delivered by each distributor is independently set by a needle control valve and monitored by an oval gear volumetric flow meter (MX06, MacNaught). The liquid flowing from the bottom of the plate comes into a collector and then returns to the feeding tank.

The centerpieces of the liquid circuit are the two distributors. They have been carefully designed (over approximately ten iterations) in order to uniformly distribute the liquid in the spanwise direction of the plate. They are made in the shape of a diffuser and mounted with an inclination of 10° with respect to the horizontal. Because of this slope, the liquid ascends in the distributors. Entry of air is then avoided and the distributors remain filled with liquid even at low liquid flow rates. Liquid inside the distributors is guided through a set of square blocks which spreads the flow in the spanwise direction and also breaks down the large eddies. Finally, the flow comes out laminar through 30 horizontally and equally spaced circular nozzles of 2 mm in diameter. The liquid flow pattern is observed and recorded using a CMOS high-speed camera (v310, Phantom) mounted with a macro lens (AF Zoom-Micro Nikkor 70-180mm f/4.5-5.6D ED, Nikon). Images are captured with a resolution of 1200×800 px² and with an acquisition frequency of 1.8 kHz. For shadowgraph imaging of the suspended film, the back side of the plate is illuminated with a LED panel. When looking at the supported film free surface, the front side is lit by a cold light illuminator (KL 2500 LCD, Schott).

The instantaneous local thickness of the liquid film is measured using confocal chromatic imaging (sensor CL4, STIL). This technique has already been implemented to measure the thickness of films flowing on a flat surface^{68 86}. Since the sensor is capable of detecting multiple interfaces such as solid-liquid, liquid-liquid and liquid-gas, the plate-supported film and the suspended film that bridges the perforation can be both characterized. Film thickness is measured with a precision better than $0.5 \mu\text{m}$ at acquisition frequency of 5 kHz.

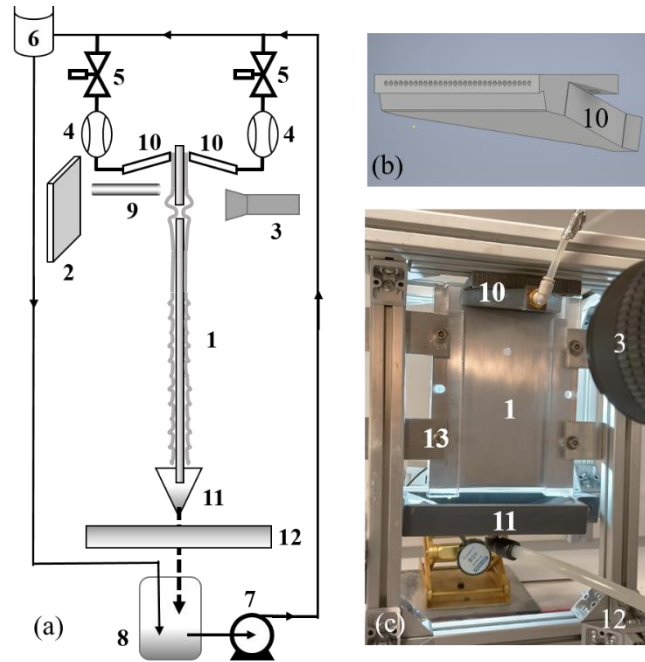


Figure 3-1 : (a) Schematic representation of the experimental setup. (b) CAD (Computer Aided Design) model of the distributor. (c) Photograph of the setup. 1. Test plate 2. LED panel 3. High speed camera 4. Volumetric flow meters 5. Needle control valve 6. Spillway 7. Gear pump 8. Reservoir 9. CCI sensor 10. Distributor 11. Liquid Collector 12. Anti-vibration mount 13. Frame that holds the plate.

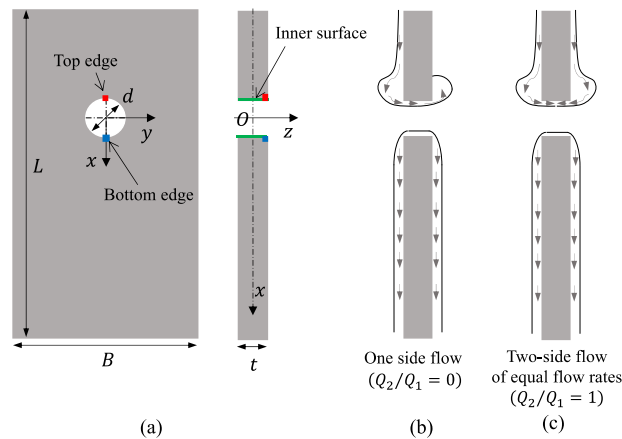


Figure 3-2: Perforated plate front view and cross-section along x - z plane: (a) dimensions, coordinate system and definitions of perforation top edge, bottom edge and inner surface, (b) One face supply ($Q_2/Q_1 = 0$), (c) two face supply with equal flow rates ($Q_2/Q_1 = 1$). Arrows indicate the flow path followed by the fluid film before the curtain transition.

3.3. Experimental protocol

First, the test plate is cleaned with a surfactant solution (3 vol%, Mucosol, Merz), thoroughly rinsed with distilled water and dried with compressed air. Then, it is inserted and fixed in the vertical frame. The outlet of the distributors is positioned on the front side and on the back side of the plate, about two millimeters below the top edge of the plate. The distance (in z direction) and parallelism between the nozzles and the plate is carefully adjusted in order to obtain later on a liquid film with a uniform thickness in the spanwise (y) direction. Since the outlet is located 58 mm upstream of the perforation, the film flow is fully developed at the location of the perforation. We also rigorously checked that the amplitude of the waves travelling on the liquid film upstream of the perforation remains small compared to the film thickness (see A1 in Supplementary Material).

Both faces of the plate are fed with the highest flow rate, i.e. 65 L.h^{-1} , such that the liquid is forced to wet the whole usable width of the plate, i.e. $w = 90 \text{ mm}$. Then, the liquid flow rate can be reduced down to 5 L.h^{-1} and the region upstream of the perforation remains totally covered by the liquid film.

For the supply condition $Q_1/Q_2 \neq 1$ ($Q_2 < Q_1$), the flow rate that supplies the back side of the plate (Q_2) is first fixed at its target value. Then, the flow rate of the plate front side (Q_1) is progressively increased, in increments of 1 L.h^{-1} , in order to explore the different regimes of the film flow around and over the perforation. We determine the flow rate per unit width at the curtain transition (Q_{cr}) as follows: Q_{cr} is associated with the smallest flow value for which there is a stable curtain that entirely closes the perforation. For the supply condition $Q_1/Q_2 = 1$, the flow rates are identically initialized and increased simultaneously with the same increments. The transitions of the film flow are observed by shadowgraph imaging. Optionally, the topography of the liquid film near the perforation is investigated point-by-point by CCI. For each set of parameter values, experiments were performed at least in triplicate. Details about calibration and reliability tests are given in A1 (see Supplementary Material).

4. Flow modes over a perforation

4.1. Far below the curtain transition

We presently report experiments carried out with propan-2-ol at low values of the Reynolds number. We find that the liquid film flow is deflected by the perforation and does not fill it (see the photograph of **Figure 3-3**). We observe an arch-shaped stationary capillary ridge: its apex is located upstream of the perforation close to the stagnation point and the legs of the arch extend downstream. The ridge flattens and widens far from the perforation. It divides the

downstream region of the flow in an outer region and an inner region, the film thickness in the outer (resp. inner) region being generally larger (resp. lower) than the Nusselt thickness of the film far upstream. In the outer region, the liquid film thickness decays in an oscillatory manner and tends towards the Nusselt thickness far from the ridge (see **Figure 3-3**).

In the inner region, (just downstream of the perforation), the liquid film is very thin or even missing when $Q_2/Q_1 = 0$. When $Q_2/Q_1 = 1$ (we remind that $Q_1 \geq 5 \text{ L}\cdot\text{h}^{-1}$), the liquid also flows along the inner surface of the perforation from both sides of the plate and a thin liquid film forms downstream of the perforation. When $Q_2/Q_1 = 0$, the contact line is pinned at the inner surface of the perforation, there is a dry patch downstream of the perforation and there is no fluid transfer from the front side to the back side of the plate. This dry region expands downstream as the perforation diameter increases. The presence of a dry zone beneath the holes at low flow rates was also observed by Pavlenko *et al.*¹⁸ on corrugated-perforated sheets and by Xie *et al.*⁹⁸ behind centimetric rectangular perforations.

The graph of **Figure 3-3** focuses on the free surface profile in the $y = 0$ plane near the perforation. CCI film thickness measurements are reported for $Q_2/Q_1 = 1$ and $Q_2/Q_1 = 0$. Data are missing close to the top and bottom edges of the perforation: CCI fails to capture the film thickness because the local slope of the free surface is too steep with respect to the vertical plate. **Figure 3-3** shows that the height of the capillary ridge for one face supply is significantly greater than for two face supply with equal volumetric flow rate. Indeed, in case of a liquid film flowing over a step-in or trench, it is well known that the ridge height increases with the depth of that topography^{105,50}. In two (resp. one) face supply, the depth of the topography seen by the liquid film is the plate half-thickness (resp. entire thickness). Thus, the capillary over-pressure and the ridge height required to push the liquid inside the perforation are greater for one face supply.

Lastly, we also observe 2D horizontal waves traveling in the streamwise direction downstream of the perforation (see **Figure 3-3**). The wavelength is estimated at about 10 mm, i.e. one order of magnitude greater than the film thickness. These are Kapitza waves⁵².

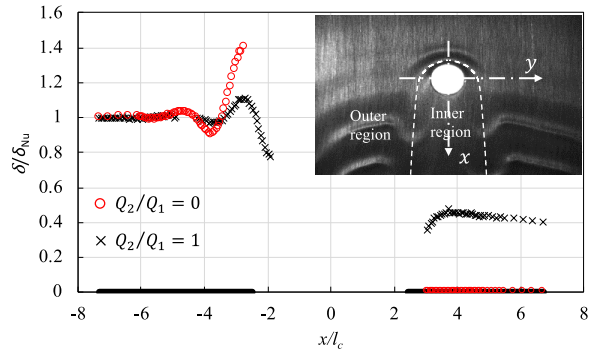


Figure 3-3: Film thickness profile in the $y=0$ plane far below the curtain transition: CCI measurements for perforation diameter $d = 8$ mm, plate thickness $t = 1$ mm, propan-2-ol, $Ka = 348$, $Re = 23$, supply conditions $Q_2/Q_1 = 0$ and $Q_2/Q_1 = 1$. The thick black segments on the x -axis correspond to the plate surface and the gap between them to the perforation. The origin of the coordinate frame coincides with the center of the perforation. The streamwise direction (x) is rescaled by the capillary length (l_c), and the current film thickness (δ) by the Nusselt flat film thickness (δ_{Nu}) measured far upstream of the perforation. Insert: Image of the flow pattern far below the curtain transition, same experimental conditions, $Q_2/Q_1 = 1$.

4.2. Prior to the curtain transition

As the liquid flow rate increases, the train of upstream capillary ridges shifts toward the perforation. Ultimately, the leading ridge may go down into the perforation and form a rim within the perforation. This phenomenon occurs at $Re = 23$ for propan-2-ol and one face supply. It coincides with the onset of liquid transfer from the front side to the back side of the plate. On the backside, the liquid climbs over the top edge of the perforation and makes an arch-shaped capillary ridge whose legs extend in the form of two parallel rivulets. The rivulets widen and flatten downstream.

Depending on perforation diameter and Q_2/Q_1 , different rim dynamics and transitions to the curtain mode are observed. We report thereafter a diversity of flow patterns (see **Figure 3-4**). We emphasize that this diversity cannot be seen sequentially for a same perforation when increasing the film Reynolds number (as for a large rectangular perforation for example⁹⁸). The transition from the “pass around” mode to the curtain mode occurs generally through one intermediate mode that depends on the perforation diameter

Hereafter are reported the transitions observed for propan-2-ol. Unless otherwise specified, the same modes are observed for water and glycerin mixtures.

Oscillating rim

For small perforation diameters ($d = 2 - 8$ mm), irrespective of plate thickness and liquid properties, an oscillating liquid rim is observed in the perforation as shown in **Figure 3-4a-b**. The hole (in the liquid film) that the rim surrounds is circular for $d = 2$ mm or $d = 4$ mm and deforms to become bean-shaped for $d = 8$ mm. A sequence of images showing the rim dynamics for $d = 8$ mm is reported in Figure S3.2 (see Supplementary Material). We measured the oscillation frequencies of the rim for the different diameters by image processing using Fast Fourier Transform. At the same time, for the same volume flow rate, the frequency of the waves travelling in the downstream direction was determined by measuring the variations of the film thickness using CCI at a point far upstream of the perforation. For $Q_2/Q_1 = 0$, the dominant oscillation frequency of the rim (mode of highest energy) coincides with the frequency of the Kapitza waves travelling in the upstream region. The rim oscillation frequency is equal to 29 Hz for $d = 4$ mm, $t = 1$ mm, $Ka = 348$ and $Re = 31$. For $Q_2/Q_1 = 1$, the frequencies are of the same order but do not coincide.

It should be noted that the general wave pattern may be complicated by waves travelling in the upstream direction: as the rim bounces back in the upstream direction and impinges the perforation edge, it creates a train of circular waves (similarly to the waves generated by a drop impacting on a liquid surface) that propagate in the opposite direction of the flow and decay due to viscous effects.

We also studied the effect of plate thickness at fixed perforation diameter (see Figure S3.3 of the Supplementary Material): as the plate thickness is increased, the amount of liquid flowing along the inner surface of the perforation increases, the quantity of liquid discharged at the bottom edge of the perforation increases and the film thickness in the wake of the perforation is greater.

Drops and liquid columns

For large perforation diameters ($d = 10 - 16$ mm) with one face supply, the suspended liquid rim destabilizes and forms drops or liquid columns (or jets). This mode is not observed with 55wt% glycerin solution. Similar flow patterns have been reported for film flow on corrugated sheet with 10 mm perforations¹⁸, for film flow on a plane plate with a large rectangular window⁹⁸ and for flow between horizontal circular tube¹⁰². The rim destabilization is attributed to Rayleigh-Taylor instability^{109,110}. The so-called critical Taylor wavelength is given by $\lambda = 2\pi(\sigma/\rho g)^{1/2}$. λ is equal to 10 mm for propan-2-ol and drops/columns are actually observed for perforation diameter $d \geq 10$ mm. For the present perforation diameter range ($d = 10 - 16$ mm), there is only one drop departure-site. Dripping proceeds as follows: a drop grows from

the rim, elongates due to the gravity and contacts the bottom edge of the perforation (**Figure 3-4c**). At the same time, a liquid neck forms between the drop and the suspended rim. The drop drains on the bottom edge of the perforation. The neck shrinks until pinch-off and the detached drop leaves behind a liquid thread that recedes to the rim.

Dripping is not periodic. The intermittency is explained by the curvature of the perforation (as compared to a rectangular window⁹⁸): the liquid tends to drain around the perforation instead of flowing straight down, the volume flow rate entering the pendant drop, is therefore irregular and the departure-site moves on the rim. For the same reason, for the largest diameters, the rim forms intermittently drops and liquid columns. When the volume flow entering the drop/column is lower, gravity and capillary effects dominate, and dripping is promoted. When the volume flow and the associated momentum flux are higher, inertia competes with gravity and capillary effects, and liquid jetting is promoted¹⁰⁹.

Pendant sheet

For large perforation diameters ($d = 10 - 16$ mm) with two face supply and equal flow rates, the curtain mode is preceded by the formation of a stable liquid sheet that partially close the perforation. This mode is also observed for one-face supply with 55wt% glycerin mixture. (instead of the drop/column mode). The bottom of the sheet is bounded by a cylindrical-shaped rim (see **Figure 3-4d**), which oscillates slightly in the vertical direction. The oscillation frequency is equal to 14 Hz for the conditions of **Figure 3-4d**. For the greatest perforation diameters, the rim undergoes the Plateau-Rayleigh instability and appears wavy (see the bead-on-a-string structure in **Figure 3-4d**). We also detect stationary capillary waves on the pendant sheet. Similar waves are observed just beyond the curtain transition. In the latter case, the waves are more visible: they are characterized in the discussion section for the curtain mode.

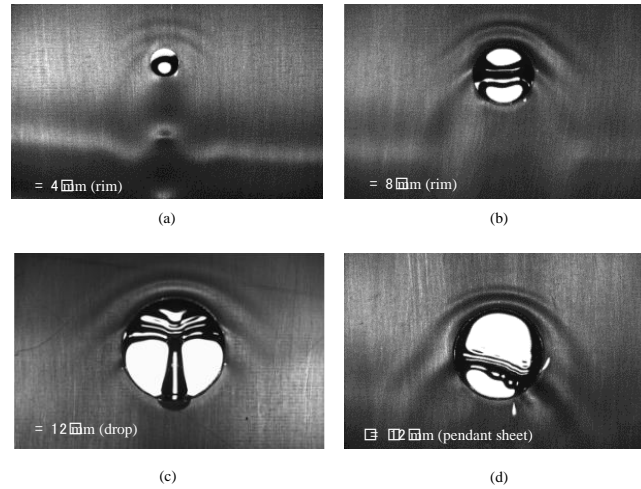


Figure 3-4: Rim dynamics and transition to the curtain mode as a function of perforation diameter and Q_2/Q_1 : observations for plate thickness $t = 1$ mm, propan-2-ol, $Ka = 348$. Re values are different since Re_{cr} depends on d . (a) Oscillating rim with circular hole ($d = 4$ mm, $Q_2/Q_1 = 1$, $Re = 28$) ; (b) Oscillating rim with bean-shaped hole ($d = 8$ mm, $Q_2/Q_1 = 1$, $Re = 34$) ; (c) Drops or liquid columns ($d = 12$ mm, $Q_2/Q_1 = 0$, $Re = 29$) ; (d) Pendant sheet ($d = 12$ mm, $Q_2/Q_1 = 1$, $Re = 32$).

4.3. Curtain transition and just beyond

With further increase in flow rate, the fluid film fills entirely the perforation forming a thin liquid curtain, as shown in **Figure 3-5**. For one face supply, we clearly observe the transfer of liquid from the frontside to the backside of the plate. However, the flow pattern on the rear side differs from that before the curtain transition: the liquid now leaks from the bottom edge of the perforation in the form of a single rivulet.

The liquid curtain exhibits a stationary field of 2D capillary waves (see **Figure 3-5bcd**). The waves appear in the form of dark and bright horizontal stripes by shadowgraphy. The stripes are straight for $d = 2 - 8$ mm. Transverse (y -direction) distortions of the 2D waves arise for $d = 10 - 16$ mm.

Figure 3-6 presents the free surface profile of the liquid film along $y = 0$ for $Q_2/Q_1 = 1$ and $d = 8$ mm, as deduced from film thickness measurements. Measurements were performed upstream of the perforation (supported film), within the perforation (suspended) and downstream of the perforation (supported). The free surface profile upstream and downstream of the perforation are measured only on one face and duplicated for clarity on the other side of the plate assuming symmetry. As already observed below the curtain transition, the perforation is topped with a stationary capillary ridge. The curtain free surface profile (within the

perforation) exhibits standing waves. According to the literature^{111,112}, two kinds of waves can propagate on a curtain: varicose waves (symmetric mode) corresponding to thickness modulation and sinuous waves (antisymmetric mode) corresponding to modulation in z-direction of the curtain median position¹¹³. **Figure 3-6** shows that the standing waves on the curtain are varicose. A curtain of viscous liquid is actually expected to be stable with respect to temporally as well as spatially changing varicose disturbances¹¹².

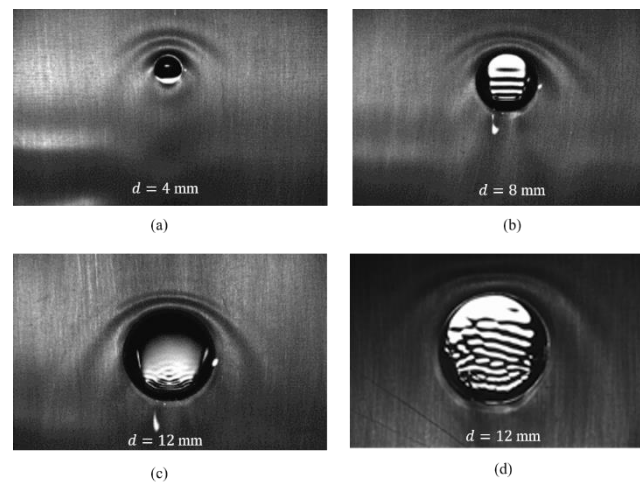


Figure 3-5: Curtain images just beyond the transition: $t = 1$ mm, $Q_2/Q_1 = 1$; (a) $d = 4$ mm, propan-2-ol ($Ka = 348$), $Re_{cr} = 31$; (b) $d = 8$ mm, propan-2-ol, $Re_{cr} = 37$; (c) $d = 12$ mm, propan-2-ol, $Re_{cr} = 35$; (d) $d = 12$ mm, pure water ($Ka = 3920$), $Re_{cr} = 125$. The curtain exhibits parallel stationary waves in (b) and a rugged wave pattern in (c) and (d).

Since the pattern appears immobile in the laboratory's reference frame, it means that the wave speed is opposite to the local curtain speed. On the curtain, the wave amplitude decreases rapidly with distance from the bottom edge of the perforation (in the upstream direction). This trend is consistent with the exponential decrease due to viscous damping established by Lin¹¹². Then, the transition from the suspended film to the supported film results in an abrupt increase in the film thickness downstream of the perforation bottom edge. Superimposed to this phenomenon, there is a ridge right downstream of the perforation. This feature, called inertial ridge, is also observed right downstream of a step-out or trench¹⁰⁶. The present experimental results exhibit the same features (ridges upstream and downstream of the perforation, standing varicose waves on the curtain) as the simulation results reported by Xie *et al.*¹⁰¹ for liquid films flowing over a rectangular open window with two face supply ($Q_2/Q_1 = 1$).

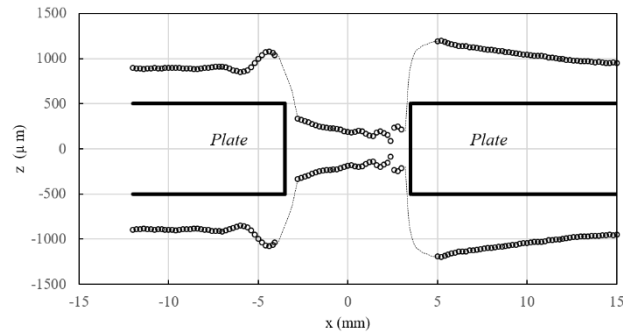


Figure 3-6: Free surface profile in the $y=0$ plane (streamwise direction) just beyond the curtain transition: CCI measurements (circles) for perforation diameter $d = 8$ mm, plate thickness $t = 1$ mm, propan-2-ol, $Ka = 348$, $Re = 36$, $Q_2/Q_1 = 1$. The thick black segments correspond to the plate surface. The origin of the coordinate frame coincides with the perforation center. The thin grey dotted lines are drawn to indicate the probable shape taken by the free surface of the film (data are missing because the local slope of the free surface is too steep for the CCI to capture the film thickness).

4.4. Hysteresis

When the volume flow rate is decreased from Q_1^{cr} , the film flow remains in the curtain mode for values of Q_1 much lower than Q_1^{cr} : the curtain transition is thus hysteretic as already noted by Hu & Jacobi¹⁰² and by Xie *et al.*⁹⁸.

We further investigate this phenomenon with propan-2-ol for $Q_2/Q_1 = 1$ and $Q_2/Q_1 = 0$. In order to determine the width of the hysteresis, the volume flow rate is first increased up to Q_1^{cr} to reach the curtain mode and then gradually reduced until the break up of the curtain is observed. It should be noted that right before the rupture, the curtain is affected by vibrations in z -direction: they are probably associated with the antisymmetrical mode of the curtain (sinuous waves).

It appears that for perforation diameter $d = 6 - 16$ mm and plate thickness $t = 1 - 1.5$ mm, the Reynolds number of the film flow at the curtain rupture is equal to about 6 for $Q_2/Q_1 = 1$ and lies between 5 and 11 for $Q_2/Q_1 = 0$. This is significantly lower than the Reynolds number at the curtain transition which ranges typically between 20 and 50 for propan-2-ol. Moreover, for $d = 2 - 4$ mm and $t = 1 - 1.5$ mm, the curtain maintains even when the volume flow rate vanishes.

Last, we observed that for a given flow rate (lower than Q_1^{cr}), the height of the capillary ridge upstream of the perforation is lower in the curtain mode than when the film flows around the

perforation without filling it. As an example, for $t = 1$ mm, $d = 4$ mm, one face supply and $Re = 18$, we found that the ridge height in the curtain mode is 24% lower.

5. Parametric study

Since the curtain transition is associated with profound modifications of the flow pattern on the front side and backside of the plate, we expect that the same phenomenon, when occurring in an actual distillation column, should significantly affect the liquid redistribution, the pressure drop and the mass transfer. To trigger the curtain mode or, on the contrary, to avoid it, it is helpful to know the Reynolds number at the curtain transition (Re_{cr}). We set up a parametric study to examine the effect of perforation dimensions, flow rate ratio, and liquid type on Re_{cr} .

5.1. Influence of perforation dimensions

We examine the effect of perforation diameter (d) and plate thickness (t) on Re_{cr} for one face supply ($Q_2/Q_1 = 0$) and for two face supply with equal volume flow rates ($Q_1/Q_2 = 1$). Experiments are carried out with propan-2-ol. It should be noted that for $d = 2$ mm and $t = 1.5$ mm, the curtain transition is very sensitive to parasitic vibrations and the determination of Re_{cr} requires a lot of care.

Figure 3-7 presents the variations of Re_{cr} as a function of the perforation diameter rescaled by the capillary length (d/l_c). For both supply conditions, Re_{cr} increases with d as long as $d \leq 6$ mm. For $t = 1$ mm and $t = 1.5$ mm, Re_{cr} is more or less on a plateau for $d \geq 6$ mm. For $t = 0.5$ mm, Re_{cr} significantly decreases from its maximum value reached at $d \cong 6$ mm, before arriving at a plateau. This decrease is attributed to the formation of liquid columns or pendant sheets (observed prior to the curtain transition for large perforation diameters) that helps to transit to curtain.

The increasing trend found at small perforation diameters is in line with the data reported by Xie *et al.*⁹⁸ for rectangular open windows with streamwise length ranging from 5 mm to 7 mm and fixed spanwise width of 28 mm. Unfortunately, Xie *et al.*⁹⁸ do not report Re_{cr} data for windows of greater streamwise length. The presence of a plateau at large perforation diameters is consistent with Eq. (3.1) established in the problem description.

At fixed perforation diameter, Re_{cr} is significantly greater for $Q_2/Q_1 = 0$ than for $Q_1/Q_2 = 1$. In both cases, the film inertia required to overcome the surface tension forces and generate the curtain is roughly the same. However, in the former case, the momentum is solely brought by Q_1 . In the latter, momentum is provided equally by Q_1 and Q_2 .

For $Q_2/Q_1 = 0$, at given value of d , Re_{cr} increases significantly with the plate thickness. This phenomenon can be explained with one of the mechanisms responsible for the so-called teapot effect¹¹⁴. At the top edge of the perforation (corresponding to the lip of the plate in Kistler & Scriven’s analysis¹¹⁴), the liquid flow is deflected from vertical direction toward the horizontal direction (parallel to the inner surface of the perforation). Since the liquid wets the inner surface of the perforation, this deflection increases with the plate thickness and “delay” the curtain transition: higher inertia forces are required for the fluid film to form a curtain. The effect of t on the plateau value is less pronounced for $Q_1/Q_2 = 1$. Indeed, on each face, the film flow experienced only half of the plate thickness. Furthermore, the symmetry of the system prevents the liquid to flow from one face to the other.

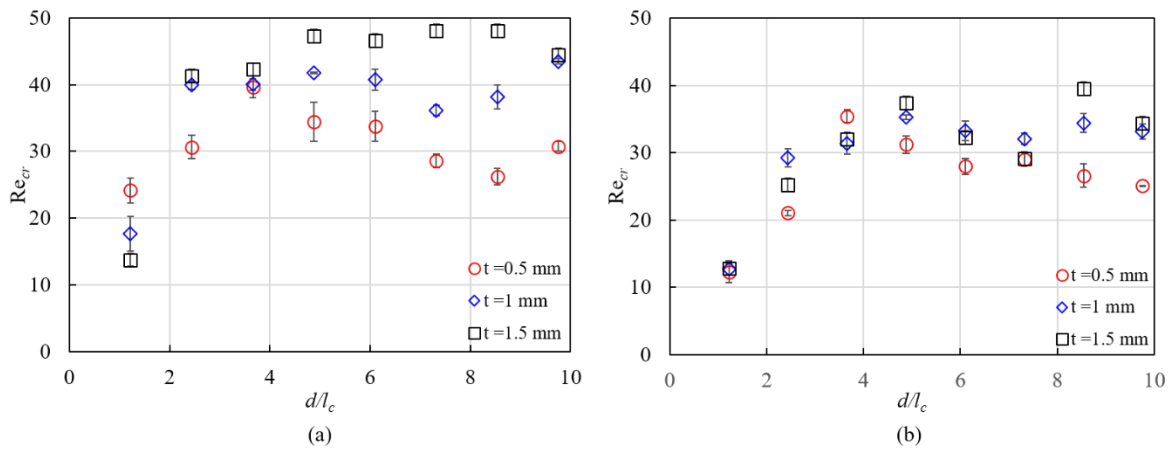


Figure 3-7: Variations of the curtain Reynolds number as a function of the perforation diameter rescaled by the capillary length (d/l_c) for three plate thickness values ($t = 0.5, 1, 1.5$ mm). The tested liquid is propan-2-ol ($Ka = 348$). (a) One face supply. (b) Two face supply with equal volume flow rates.

5.2. Influence of the flow rate ratio Q_2/Q_1

The flow rate ratio in a real corrugated sheet packing lies typically between the two limiting cases $Q_2/Q_1 = 0$ and $Q_2/Q_1 = 1$ (with $Q_2 \leq Q_1$). We thus examine the effect of the fluid flow ratio on the curtain Reynolds number. Two different values of the perforation diameter are investigated, i.e. $d = 4$ mm and $d = 8$ mm. The plate thickness is equal to $t = 1$ mm in both cases. The tested liquid is propan-2-ol.

The variations of Re_{cr} are represented as a function of Q_1/Q_2 instead of Q_2/Q_1 for a better rendering (see **Figure 3-8**). It appears that the curves associated with $d = 4$ mm and $d = 8$ mm look the same except that the latter is shifted away from the former toward higher Reynolds

number values. Irrespective of the perforation diameter, we observe that Re_{cr} grows significantly in the range $1 \leq Q_1/Q_2 \leq 3$, and stabilizes to a plateau when $Q_1/Q_2 \geq 3$.

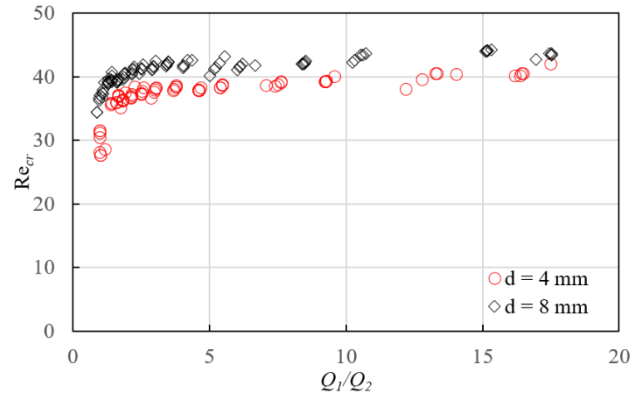


Figure 3-8: Variations of the curtain Reynolds number as a function of Q_1/Q_2 for two different values of the perforation diameter ($d = 4$ mm and $d = 8$ mm). The plate thickness is equal to $t = 1$ mm. The tested liquid is propan-2-ol. Re_{cr} is calculated from Q_1^{cr} , the volume flow rate on the front side that induces curtain transition at given Q_2 .

5.3. Influence of liquid type

We examine the effect of the liquid type on the curtain Reynolds number. Experiments are carried out with four different liquids covering a large range of Kapitza numbers, i.e. propan-2-ol ($Ka = 348$), 55 wt% glycerin aqueous solution ($Ka = 245$), 25 wt% glycerin aqueous solution ($Ka = 1470$) and pure water ($Ka = 3920$).

Figure 3-9 presents the variations of Re_{cr} as a function of the perforation diameter rescaled by the capillary length, for one face supply and for two face supply with equal volume flow rates. Regardless of the Kapitza number value, the shape of the curve Re_{cr} versus d/l_c is essentially the same: Re_{cr} first increases with d , reaches a maximum, then eventually decreases (for $Ka = 1470$ and $Ka = 3920$) and finally stabilizes to a plateau. The greater the Kapitza number, the greater the width of the increasing phase and the steepest the slope of the curve in this phase. Furthermore, the plateau value (reached at large values of d/l_c) increases with the Kapitza number. This trend is consistent with the scaling law of Eq. (3.1) established in the problem description.

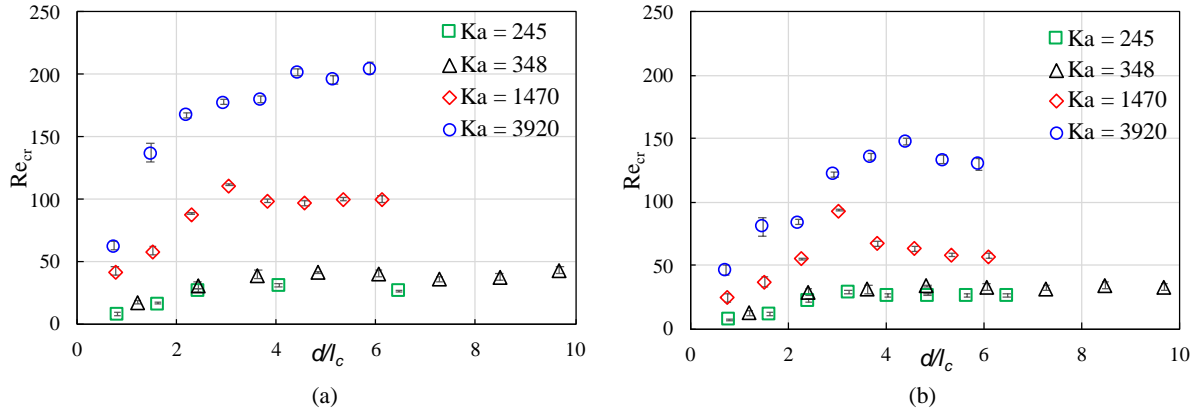


Figure 3-9: Variations of the curtain Reynolds number as a function of the perforation diameter rescaled by the capillary length for four different liquids, i.e. propan-2-ol ($Ka = 348$), 55 wt% glycerin aqueous solution ($Ka = 245$), 25 wt% glycerin aqueous solution ($Ka = 1470$) and pure water ($Ka = 3920$). The plate thickness is equal to $t = 1$ mm. (a) One face supply. (b) Two face supply with equal volume flow rates.

6. Discussion

6.1. Model for curtain transition

We compared our experimental results with the empirical correlations of Hu & Jacobi¹⁰² and Xie *et al.*⁹⁸ mentioned in the introduction. It appears that these correlations only provide a rough estimate of the curtain transition (see A4 in Supplementary Material). Indeed, they are specific to the system with which they have been established (large rectangular window with one face supply⁹⁸ or spaced horizontal tubes¹⁰²), and they do not explain the physics of the phenomena. We propose to establish a criterion for the curtain formation from a macroscopic momentum balance on the upstream portion of the rim, near the stagnation point. The details of the derivation are given in Appendix 4.

This approach revisits a model first proposed by Hartley and Murgatroyd¹¹⁵ for the break-up of thin liquid films flowing over solid surfaces (criterion for the formation of dry patches). At the onset of curtain formation in a perforation of large diameter, we expect that the rim is essentially subjected to two forces: the surface tension force that resists curtain formation and the fluid inertia that drives this transition. In order to express the surface tension force, we idealize the film profile as follows: we consider that the film profile is flat on both sides of the plate and axisymmetric with respect to the perforation axis (see **Figure 3-10**).

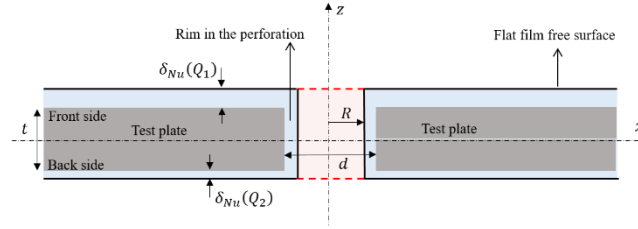


Figure 3-10: Section along the plane $y=0$: idealized flat film profile on the perforated plate before the curtain transition. The red dotted lines represent the idealized curtain free surface.

We denote R the radius of the hole surrounded by the rim. The surface tension force per unit circumference of the rim acting in the radial direction (f_σ) is given by:

$$f_\sigma = \sigma \left(1 - \frac{t}{R} - \frac{\delta_{Nu}(Q_1)}{R} - \frac{\delta_{Nu}(Q_2)}{R} \right) \quad (3.2)$$

f_σ is an increasing function of R and is maximal when $R = d/2$. As a first approximation, let us consider that $f_\sigma = f_\sigma(R/2)$ at the curtain transition. We keep in mind that this assumption tends to overestimate the capillary force. Therefore, the inertial force required to drive the curtain transition should be overrated as well.

f_σ cancels for $d = t + \delta_{Nu}(Q_1) + \delta_{Nu}(Q_2)$ and spontaneous curtain formation (due to capillary action only) is expected for perforation diameter $d \leq t + \delta_{Nu}(Q_1) + \delta_{Nu}(Q_2)$. f_σ opposes the formation of the liquid curtain for $d \geq t + \delta_{Nu}(Q_1) + \delta_{Nu}(Q_2)$.

The x-component of the momentum net flux entering the rim close to the stagnation point reads (per unit length of rim):

$$f_u = \int_0^{\delta_{Nu}(Q_1)} \rho u_x^2(y) dy + \int_0^{\delta_{Nu}(Q_2)} \rho u_x^2(y) dy$$

where $u_x(y)$ is the Nusselt velocity profile. After substitution and integration, we find:

$$f_u = \frac{2}{15} \times \frac{\rho g^2}{\nu^2} \left((\delta_{Nu}(Q_1))^5 + (\delta_{Nu}(Q_2))^5 \right) \quad (3.3)$$

The curtain forms when the momentum flux balances the maximal surface tension force. When expressed with the dimensionless parameters determined in the problem description, the criterion for the curtain formation reads

$$\text{Re}_{cr} = \frac{1}{3} \left(\frac{15 \text{Ka}}{1 + \left(\frac{Q_2}{Q_1}\right)^{5/3}} \left(1 - \frac{t}{d} - 3^{1/3} \text{Ka}^{-1/2} \left(\frac{d}{l_c}\right)^{-1} \text{Re}_{cr}^{1/3} \left(1 + \left(\frac{Q_2}{Q_1}\right)^{1/3} \right) \right) \right)^{3/5} \quad (3.4)$$

Figure 3-11 shows that Eq. (3.4) is in good agreement with the experimental data obtained for two face supply of equal flow rates. We emphasize that the present model does not involve any ad hoc adjustable parameter. It can be seen that the model overestimates the curtain Reynolds number for one face supply. Eq. (3.4) predicts that the plateau value for the supply condition $Q_2/Q_1 = 0$ is $(2^{3/5} - 1) \cong 50\%$ higher than that for $Q_2/Q_1 = 1$. This difference is significantly greater than the 25% found experimentally. We expect that gravity effects (not accounted for by our simple model) promote the curtain transition and thus reduce the momentum flux otherwise required. For two face supply, the liquid rim on the inner surface of the perforation is drained by the film flow on both side of the plate. On the contrary, for one face supply, the rim is only drained on the front side. Subsequently, liquid tends to accumulate on the inner surface, close to the back side of the plate. Since the rim is thicker, gravity effects are enhanced. If we assume that the liquid rim has a size $(d/2 - R)$ of the order of the plate thickness, we find that the Bond number (which compares gravity to interfacial tension forces) is slightly lower than 1.

The present model also predicts that for sufficiently small values of the perforation diameter (compared to the plate thickness, i.e. $d \leq t$), the hole within the liquid film is not thermodynamically stable. Consequently, the liquid should spontaneously fill the perforation by capillarity and the curtain Reynolds number should vanish. However, since the equilibrium contact angle is not zero, a minimum volume flow rate per unit width is practically required otherwise the contact line remains pinned on the edge of the perforation. We experimentally investigated the case $d = t = 1$ mm with propan-2-ol for one face and two face supply. We found that the curtain Reynolds number is equal to $Re_{cr} = 14$ and $Re_{cr} = 8$, respectively. But, when the curtain is formed, it maintains even when the volume flow rate vanishes.

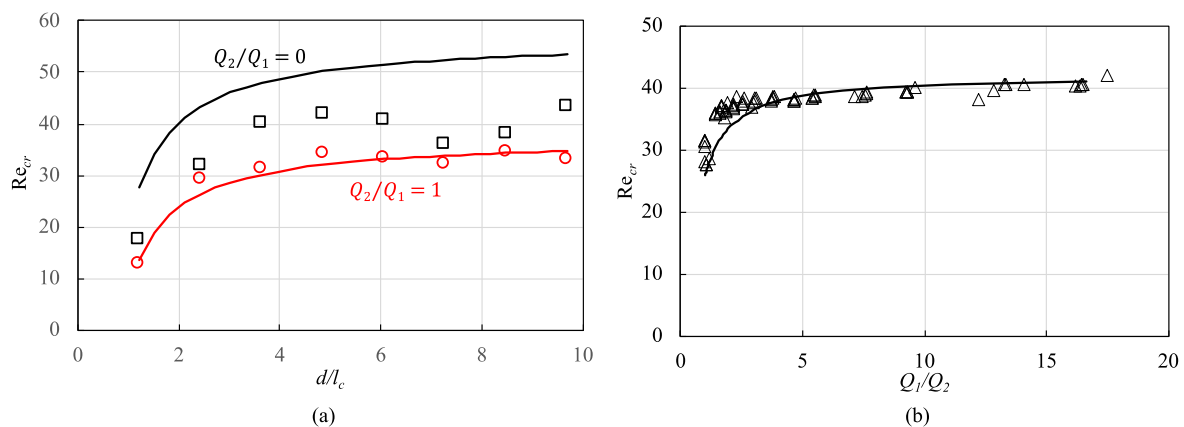


Figure 3-11: Comparison between prediction of Eq. (3.4) (solid lines) and the experimental results (points) obtained with propan-2-ol ($Ka = 348$) and perforated plates of thickness $t = 1$

mm. (a) variations of Re_{cr} as a function of the perforation diameter rescaled by the capillary length for $Q_2/Q_1 = 0$ and $Q_2/Q_1 = 1$. (b) variation of Re_{cr} as a function of the ratio Q_1/Q_2 for perforation diameter $d = 4$ mm.

We also compared our model to the experimental data obtained with various liquids for the supply condition $Q_2/Q_1 = 1$ (see A6 in Supplementary Material). It can be seen that the variations of Re_{cr} as a function of d/l_c are well represented for the liquids characterized by a low Kapitza number. The agreement is less satisfactory for liquids with high Ka. However, it gives a good estimate of the plateau value reached at high perforation diameters.

Last, we used Eq. (3.4) to predict the curtain transition for a flat plate with 54° inclination to horizontal fed with liquid nitrogen ($Ka = 4690$ for 54° inclination), details are given in A7 (see Supplementary Material). We found that $Re_{cr} = 170$ for two face supply. This result gives a first estimate of the curtain threshold in a 500Y (gravity angle of 54°) type structured packing operating with liquid nitrogen. In these conditions, the liquid load would be of the order of $60 \text{ m}^3 \cdot \text{m}^{-2} \cdot \text{h}^{-1}$ and the holdup of 6%. These results have to be validated on a real perforated corrugated sheet packing. We emphasize that the present work has been carried out on flat plates with a single perforation. Further comprehensive studies are needed to examine the effects of corrugations, location of the perforations (with respect to the crest of the corrugations) and optionally sheet microtexture on the curtain transition.

6.2. Liquid behavior within and around the perforation in curtain mode

Let us recall the main features of the liquid film free surface observed in the curtain mode (see **Figure 3-6**). Right upstream of the perforation, the supported liquid film exhibits a stationary capillary ridge. This ridge produces the capillary over-pressure required to push the liquid inside the perforation since the gravity that drives the film flow on the plate acts perpendicularly to the perforation inner surface^{50,105}. Right downstream of the perforation, there is an inertial ridge, caused by an overshoot of the liquid film as it is deflected in the vertical direction by the step²⁵. Within the perforation, the curtain free surface profile results from two superimposed phenomena, i.e. the stretching of the curtain due to the acceleration of the gravity and the excitation of varicose capillary waves that propagate upstream (in the liquid's reference frame). The capillary waves are excited by the impact of the liquid curtain on the bottom edge of the perforation. The pattern appears immobile in the laboratory's reference frame, indicating that the wave speed is opposite to the local curtain speed. Similar phenomena have already been reported by Ruschak⁴¹ for liquid films or jets entering a relatively large pool and more recently

by Hancock and Bush for a laminar liquid jet impinging on a deep liquid reservoir⁴². According to Xie *et al.*¹⁰¹, the varicose waves induce strong generation of vorticity which is expected to enhance mass transfer.

Let us further analyze the curtain behavior for $Q_2/Q_1 = 1$. We first omit the standing varicose waves and describe the variations of the curtain half-thickness (h) by a simple free fall model. Expressing the mass conservation of the free-falling liquid between x_e and x , we get

$$h(x) \cong \frac{Q_1^e}{\left((Q_1^e/h(x_0))^2 + 2g(x - x_0) \right)^{1/2}} \quad (3.5)$$

for $x \geq x_e$. Q_1^e is the volume flow rate per unit width at location x_e .

Eq. (3.5) is fitted to the experimental curtain profile of **Figure 3-6**, by adjusting the volume flow rate per unit width to an effective value $Q_1^e = 0.65 \times Q_1$. x_e is presently the highest measuring point within the perforation. Results are displayed in **Figure 3-12a**. We also fitted the experimental data obtained for a greater perforation diameter $d = 12$ mm (see Figure S3.6 in Supplementary Material) and found $Q_1^e = 0.75 \times Q_1$. The difference between Q_1^e and Q_1 is attributed to the significant deviation of the flow around the perforation that persists at the curtain transition. We expect that downstream of x_e , viscous effects negligibly affect the stretching of the curtain and cannot be responsible for the difference above mentioned. Indeed, in **Figure 3-6**, x_e is located 1.1 mm away from the perforation top edge (2.3 mm for $d = 12$ mm in Figure S3.6), this distance is slightly greater than the “entrance” length¹⁰⁷ of the order of $10 \times l_v \cong 0.9$ mm.

The velocity (c_{var}) of the varicose waves propagating on a curtain of uniform thickness ($2h$) has been established by Taylor¹¹¹ in the limit of small disturbance of the free surface and inviscid ambient gas:

$$c_{var}^2 = \left(\frac{\sigma}{\rho h} \right) (kh \tanh(kh)) \quad (3.6)$$

where k is the wave number. Since the waves appear presently immobile in the laboratory’s reference frame, the wave velocity should match the curtain local speed, i.e.

$$c_{var} = \frac{Q_1^e}{h} \quad (3.7)$$

Then, the wavelength (λ) of the wave that stands on the curtain with given local thickness ($2h$) can be deduced from Eq. (3.6-3.7). By solving Eq. (3.5-3.7), we obtain the theoretical wavelength (λ) of the standing wave at a given position (x) on the curtain. The wavelength varies along the curtain since the curtain thickness ($2h$) decreases as x increases.

To validate these findings, let us return to the data of **Figure 3-6**. The standing varicose wave can be isolated by subtracting the pure stretching curve to the experimental curtain profile (see Figure S3.7 in Supplementary Material). The local wavelength of the varicose wave is measured between successive peaks along the curtain. These values are reported in **Figure 3-12b** where x corresponds to the midpoint between successive peaks used to estimate the local wavelength. It can be seen that there is a very good agreement between the theoretical and the experimental values. This validates the matching assumption Eq. (3.7) and the picture to explain the curtain behavior.

Incidentally, we can estimate the damping length of the varicose wave for the conditions of **Figure 3-6**, i.e. $c_{var}/(8\pi^2\nu/\lambda^2) \cong 2$ mm where the denominator is the damping rate established by Lin¹¹². This estimate is consistent with the observations.

We also deduce from **Figure 3-12ab** that the adjustment of Q_1^e is relevant and should provide a good estimate of the real volume flow rate over the perforation. From this estimate and from the measured thickness profile (**Figure 3-6**), we can determine the variations of the local Weber number $We = \rho(Q_1^e)^2/(h\sigma)$ along the curtain. We find that We ranges between 0.4 at x_e and 0.8 close to the bottom edge of the perforation. According to Brown¹⁰⁷ and Lin¹¹², a curtain that includes a domain with $We < 1$ is unstable with respect to spatially growing sinuous disturbances propagating upstream. It appears that the curtain seems not affected by sinuous waves beyond the curtain transition. However, in the hysteresis loop, when the curtain still stands although the volume flow rate is significantly lower than the curtain flow rate (Q_{cr}), the curtain is thinner and its rupture (when observed) seems to be triggered by growing sinuous waves. Indeed, at given wavelength, as the curtain thickness decreases, the velocity of the varicose waves becomes much smaller than the velocity of the sinuous waves. Subsequently, sinuous waves are expected to dominate.

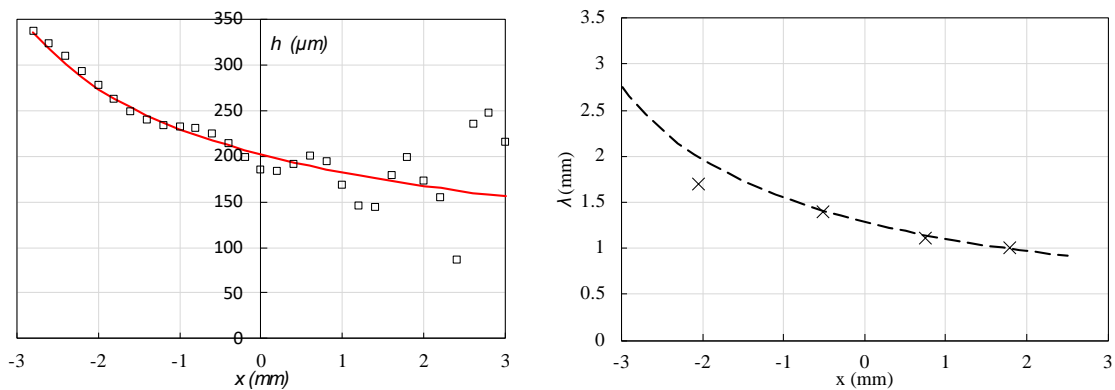


Figure 3-12: (a) Measured half thickness profile of the curtain (squares) and calculated profile assuming free fall and omitting varicose waves (red solid line). (b) Predicted wavelength values

along the liquid curtain (dashed line) and wavelength values measured on the waves that stand on the real curtain (crosses), same experimental conditions as **Figure 3-6**.

7. Conclusion

We experimentally studied the local hydrodynamics of a liquid film flowing over a round hole perforation. Such topographies are typically found in the corrugated sheet packings used in distillation columns. Perforations are known to contribute to liquid phase redistribution and mass-transfer enhancement.

We first characterized the different flow patterns occurring on a singly perforated plate as a function of the Reynolds number of the film, for one face supply and two face supply with equal volume flow rates. At low values of the Reynolds number, the liquid film flow is deflected by the perforation and the liquid does not fill the perforation. An arch-shaped stationary capillary ridge forms at the (upstream) stagnation point and extends downstream of the perforation. As the Reynolds number increases, the apex of the capillary ridge shifts toward the perforation and a liquid rim grows within the perforation. Beyond a critical value of the Reynolds number, referred to as the curtain Reynolds number (Re_{cr}), the liquid entirely fills the perforation and forms a liquid curtain. The curtain exhibits stationary varicose capillary waves. The curtain transition is preceded by specific patterns that depend on the perforation diameter, i.e. oscillating rim, dripping drops and liquid columns, or pendant sheet (for increasing perforation diameter, respectively). The curtain transition is highly hysteretic: when Re is decreased from Re_{cr} , the liquid curtain may persist within the perforation for Reynolds numbers well below Re_{cr} .

We emphasize that the curtain transition occurs well above the onset of liquid transfer from the front side to the back side of the plate. The transfer starts with the formation of the liquid rim within the perforation. For one face supply, liquid transfer is clearly observed until and above the curtain transition.

We carefully examined the influence of perforation diameter, plate thickness, liquid type and volume flow rate ratio on the curtain Reynolds number. We found that (i) Re_{cr} increases with the perforation diameter, possibly goes through a maximum, and reaches a plateau for higher diameter values; (ii) Re_{cr} increases with the plate thickness as a consequence of the so-called teapot effect, this increase is more pronounced for one face supply; (iii) Re_{cr} increases with the Kapitza number (Ka) of the liquid and the plateau value of the curtain Reynolds number scales

as $Ka^{3/5}$; (iv) Re_{cr} (defined with the volume flow rate on the front side of the plate) decreases as the volume flow rate on the back side increases.

We propose a new criterion for the curtain formation. This criterion was derived from a macroscopic momentum balance on the rim near the stagnation point. We considered that the rim is essentially subjected to two forces: the surface tension force that resists the curtain formation and the fluid inertia that drive the transition. This model adequately describes the effect of perforation diameter, Kapitza number and flow rate ratio on the curtain Reynolds number.

Finally, we showed that the dynamics of a curtain within a perforation results from two superimposed phenomena: the stretching of the curtain due to the acceleration of the gravity and the excitation of varicose waves consequently to the impact of the curtain on the bottom edge of the perforation. The stretching is well described by a simple free fall model. We found that the wavelength of the varicose wave is selected such that the velocity of the waves both satisfies Taylor's dispersion relation and matches the curtain local speed. As a consequence, the varicose wave appears immobile in the plate reference frame. The varicose waves are expected to enhance mass-transfer through the liquid curtain.

In the future, we plan to further investigate the curtain mode, i.e. by quantifying the fluid flow rate transferred through a perforation from one side of the plate to the other, by performing velocimetry to determine the velocity and vorticity fields within the supported and the suspended liquid film.

8. Supplementary Material

A1. Calibration and reliability tests

The flowmeters have been preliminary calibrated for each working liquid by weighing the fluid collected at the exit.

CCI thickness measurement was validated on a test case using the needle contact method⁶⁶. The results obtained from both methods confirm the uniformity of the film thickness in the spanwise direction and agree with Nusselt thickness⁵¹. By measuring the local variations of the film thickness as a function of time (see Figure S3.1), we rigorously checked that the amplitude of the waves travelling on the liquid film upstream of the perforation remains small compared to the film thickness. This is no more true downstream the perforation since the edge of the perforation excites (or amplifies) Kapitza waves on the liquid film free surface.

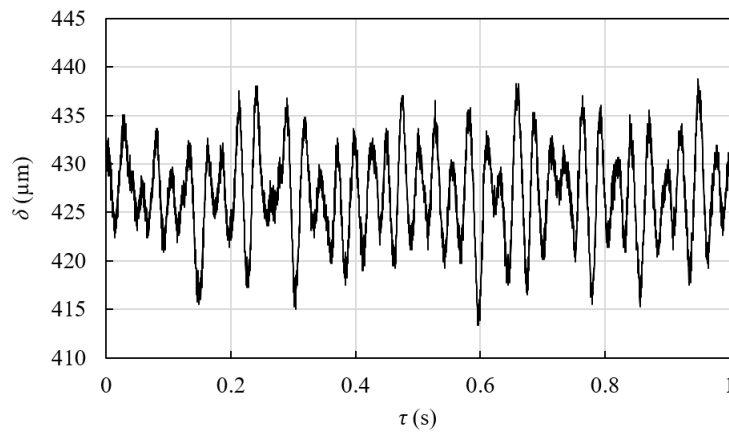


Figure S3.1. Example of temporal evolution of the film thickness (δ) at a point located upstream of the perforation for $Re = 40$, propan-2-ol ($Ka = 348$), plate thickness $t = 1$ mm, perforation diameter $d = 4$ mm: CCI measurement with acquisition frequency of 5kHz.

For each experiment, the uniformity of the film thickness upstream of the perforation is checked by CCI measurements in the spanwise direction. We also ensure that the level of parasitic vibrations is low enough. In that case, the free surface of the supported film far upstream of the perforation appears smooth to the eye.

Finally, the overall reliability and reproducibility of the setup was controlled throughout the study by repeating a specific experiment, i.e. the determination of Q_{cr} for propan-2-ol, $d = 4$ mm, $t = 1$ mm, $Q_2/Q_1 = 1$.

A2. Oscillation of the rim before the transition to liquid curtain

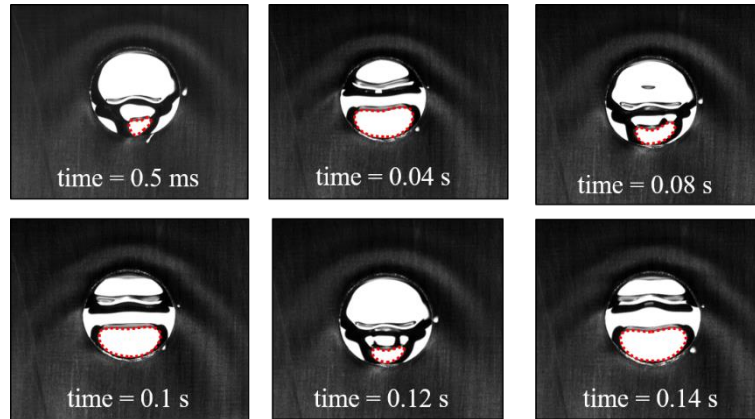


Figure S3.2. Rim's oscillations within the perforation just below the curtain transition: perforation diameter $d = 8$ mm, plate thickness $t = 1$ mm, propan-2-ol, $Ka = 348$, $Re = 34$, $Q_2/Q_1 = 1$. The film hole below the rim is indicated by a red dotted circle. The hole enlarges and reduces periodically with time. Sampling frequency of images: 2000 Hz.

The frequency at which the rim oscillates is determined by image processing. The surface area of the film hole (bounded by a red dotted circle in Figure S3.2) is first isolated in each image. Then, the location of the center of gravity of the film hole surface is calculated for each image as well. Finally, Fast Fourier Transform (FFT) is performed (i) on the variations of the hole area as a function of time and (ii) on the variations of the x-position of the hole center of gravity. It appears that the modes of highest energy of (i) and (ii) are associated with the same frequency. We expect that this frequency coincides with the rim oscillation frequency.

A3. Effect of the plate thickness on the rim dynamics

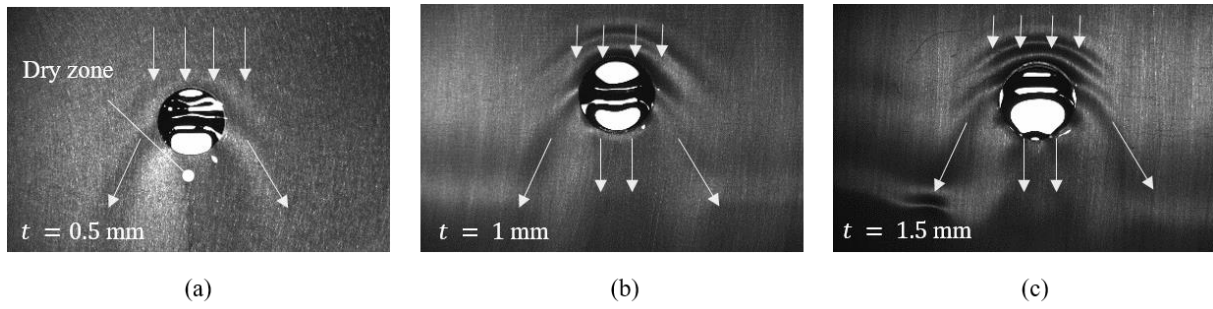


Figure S3.3. Flow pattern and rim shape as a function of the plate thickness (t): observations for perforation diameter $d = 8 \text{ mm}$, propan-2-ol, $Ka = 348$, $Q_2/Q_1 = 1$. Re values are different since Re_{cr} depends on t . (a) dry patch in the wake of the perforation ($t = 0.5 \text{ mm}$, $Re = 29$), (b) axial liquid discharge ($t = 1 \text{ mm}$, $Re = 34$), (c) liquid bulge at the bottom edge of the perforation ($t = 1.5 \text{ mm}$, $Re = 35$). Arrows indicate the liquid flow path around the perforation.

Figure S3.3 illustrates the flow patterns for increasing values of the plate thickness (t) at fixed perforation diameter $d = 8 \text{ mm}$. It appears that lower t offers less support to the liquid rim formed in the inner surface of the perforation. For $t = 0.5 \text{ mm}$ (Figure S3.3a), the rim stays attached only in the upper half of the perforation and liquid discharges from the rim in an oblique direction with respect to the x -axis (arrows shown in the Figure S3.3a). As a consequence, there is dry patch in the wake of the perforation. As the plate thickness is increased, a greater quantity of liquid flows in the inner surface of the perforation, forms a bulge at the bottom edge of the perforation and discharges in the x -direction (Figure S3.3bc).

A4. Comparison with existing empirical correlations

Since the Reynolds number (Re) and the Kapitza number (Ka) are the main dimensionless numbers that arise from the dimensional analysis of the curtain transition, it is not surprising that the empirical correlations established in the literature are based on these numbers.

Hu & Jacobi¹⁰² propose correlations for the different flow transitions between horizontal tubes. Assuming a power law between Re and Ka and using a least-squared error criterion to fit about 50 flow observations (per flow transition), they find for the jet-sheet/sheet transition,

$$\text{Re} = 2.088 \times \text{Ga}^{0.220} \quad (\text{S1})$$

where Ga is the Galileo number equal to Ka^3 . We can use this correlation to predict the curtain transition for the supply condition $Q_1/Q_2 = 1$ when the perforation diameter is large. We find $\text{Re}_{cr} = 50$ for propan-2-ol and $\text{Re}_{cr} = 246$ for water. It should be noted that the volume flow rate per unit width entering the Reynolds number of Eq. (S1) corresponds to the sum $Q_1 + Q_2$ (whereas Re_{cr} is defined with Q_1). The values of Re_{cr} determined from Hu & Jacobi's¹⁰² correlation are about two times greater than the plateau values of **Figure 3-9b**.

Xie *et al.*⁹⁸ proposed an empirical correlation to predict the curtain transition for the liquid film flowing over a vertical plate with an open window. This correlation has been established for one face supply ($Q_1/Q_2 = 0$):

$$\text{Re} = 10^{-0.89} \text{Ka}^{0.8} \text{Nx}^{0.4} \quad (\text{S2})$$

Nx is an additional dimensionless number that accounts for the window geometry

$$\text{Nx} = a^{0.6} b^{0.4} / l_c \quad (\text{S3})$$

where a and b are the streamwise and spanwise length of the window, respectively. For a perforation of diameter d , Eq. (S3) reduces to $\text{Nx} = d/l_c$. We use Eq. (S2) to predict the variations of the curtain Reynolds number (Re_{cr}) as a function of the perforation diameter for propan-2-ol, plate thickness $t = 0.5$ mm (close to the plate thickness used by Xie *et al.*⁹⁸, i.e. $t = 0.4$ mm) and supply condition $Q_1/Q_2 = 0$. The experimental results and the prediction of Eq. (S2) are compared in Figure S3.4. It appears that Eq. (S2) underestimates the curtain Reynolds number for d/l_c ranging between 1 and 5. Furthermore, Eq. (S2) does not account for the plateau observed at high values of d/l_c .

We conclude that such empirical correlations can only provide a rough estimate of the curtain transition. They are specific to the system with which they have been established. They do not explain the physics of the phenomena.

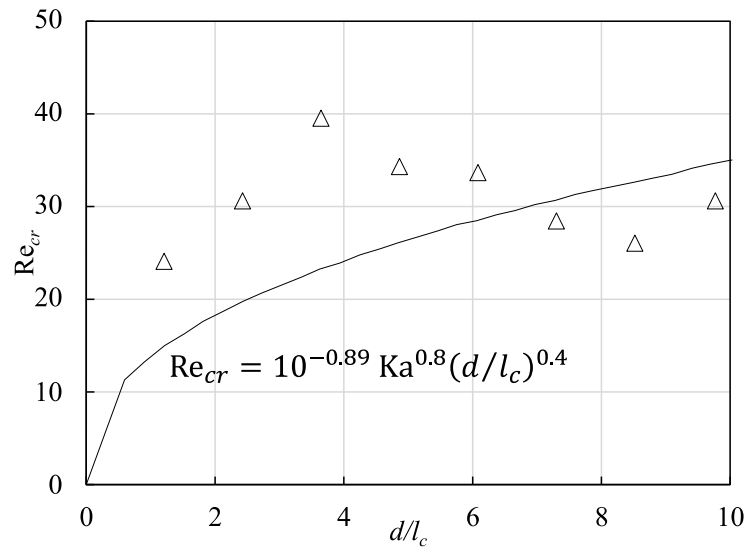


Figure S3.4. Comparison between the curtain Reynolds number (Re_{cr}) predicted by the Xie *et al.* correlation⁹⁸ (solid line) and our experimental data (triangles): plate thickness $t = 0.5$ mm, propan-2-ol ($Ka = 348$), one face supply.

A5. Comparison between the model and the experimental data for various liquids

Figure S3.5 compares our model (Eq. (3.4)) to the experimental data obtained with various liquids for the supply condition $Q_2/Q_1 = 1$. It can be seen that the variations of Re_{cr} as a function of d/l_c are well represented for the liquids characterized by a low Kapitza number. The agreement is less satisfactory for liquids with high Ka. Indeed, the present model fails to account for the non monotonous behaviour observed experimentally (peak of Re_{cr} before reaching a plateau). The model overestimates the curtain Reynolds number at low values of d/l_c but gives a good estimate of the plateau value reached at high perforation diameters.

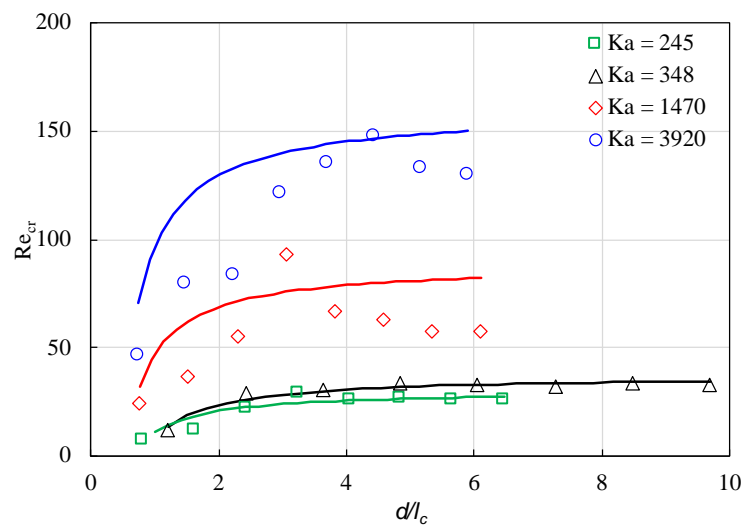


Figure S3.5. Comparison between the model for curtain transition (solid lines) and the experimental results (points) obtained with 55wt% glycerin (Ka = 245), propan-2-ol (Ka = 348), 25wt% glycerin (Ka = 1470), pure water (Ka = 3920). Two face supply of equal flow rates. Perforated plates of thickness $t = 1$ mm.

A6. Prediction of the curtain transition for a real packing with liquid nitrogen

We may use equation Eq. (3.4) to estimate the curtain Reynolds number in the case of liquid nitrogen flowing on a corrugated-perforated sheet with the same characteristics as Pavlenko *et al.*¹⁸, i.e. sheet thickness of 0.2 mm, perforation diameter of 4 mm, rib inclination angle (φ) of 47° (with respect to horizontal) and crimp angle (β) of 60°. This is a sheet of a 500Y type structured packing. The so-called gravity flow angle (α) is calculated from Shilkin *et al.*¹¹⁶:

$$\alpha = \arctan \left(\frac{\tan \varphi}{\sin \left[\arctan \left(\sin \varphi \cot \left(\frac{\beta}{2} \right) \right) \right]} \right)$$

α is equal to 54°. The gravity component that drives the flow is equal to $g \sin \alpha$, the dimensionless perforation diameter (d/l_c) to 3.4 and the Kapitza number to 4690. For one face supply, Eq. (3.4) gives $Re_{cr} = 258$. This value lies above the Re range, i.e. 10-225, investigated by Pavlenko *et al.*¹⁸. This probably explains why the curtain mode is not mentioned by these authors. It should be noted that for two face supply, which is the standard operating condition of corrugated sheet packing, the curtain Reynolds is significantly lower, i.e. $Re_{cr} = 170$.

A7. Curtain profile for $d = 12$ mm

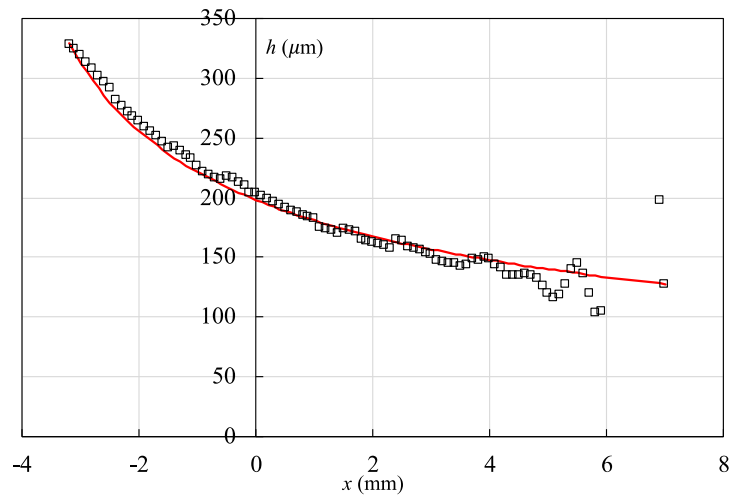


Figure S3.6. Curtain half thickness profile ($h = \delta/2$) in the $y = 0$ plane: CCI measurements (squares) for perforation diameter $d = 12$ mm, plate thickness $t = 1$ mm, propan-2-ol, $Ka = 348$, $Re = 33$, $Q_2/Q_1 = 1$. The origin of the coordinate frame coincides with the perforation center. The red curve corresponds to the calculated profile of the stretched curtain assuming free fall and omitting varicose wave.

Figure S3.6 presents the curtain half thickness profile ($h = \delta/2$) in the $y = 0$ plane for $Q_2/Q_1 = 1$ and $d = 12$ mm, as deduced from film thickness measurements. Eq. (3.5) is fitted to this profile by adjusting the volume flow rate per unit width to the effective value $Q_1^e = 0.75 \times Q_1$. x_e in Eq. (3.5) corresponds to the data point with the lowest abscissa on Figure S3.6. The red curve of Figure S3.6 is the result of this fitting.

A8. Oscillations of the curtain half-thickness with respect to its free fall profile (perforation diameter $d = 8$ mm)

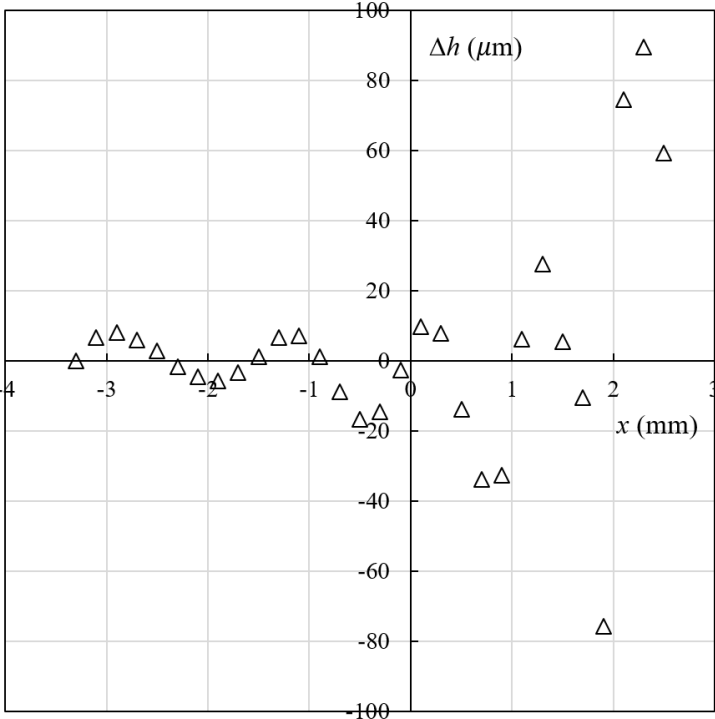


Figure S3.7. Oscillations of the curtain half thickness with respect to its free fall profile: perforation diameter $d = 8$ mm, plate thickness $t = 1$ mm, propan-2-ol, $Ka = 348$, $Re = 36$, $Q_2/Q_1 = 1$. The origin of the coordinate frame coincides with the perforation center.

The standing varicose wave are isolated by subtracting the pure stretching curve (red curve of **Figure 3-6** associated with Eq. (3.5)) to the experimental curtain profile (data points of **Figure 3-6**). The resulting data are reported in Figure S3.7 as a function of streamwise coordinate (x). The local wavelength of the varicose wave is measured between successive peaks along the curtain.

4 A comprehensive study of the liquid transfer from the front to the back of a vertical perforated sheet

Manasa IYER^{1,3}, Joel CASALINHO¹, John PACHÓN-MORALES³, Jacopo SEIWERT³,
Mikael WATTIAU³, Laurent ZIMMER², Hervé DUVAL^{1*},

*1 Université Paris-Saclay, CentraleSupélec, Laboratoire de Génie des Procédés et Matériaux,
F-91190 Gif-sur-Yvette, France*

*2 Université Paris Saclay, CentraleSupélec, CNRS, Laboratoire EM2C, F-91190 Gif-sur-
Yvette, France*

*3 Campus Innovation Paris, Air Liquide Research & Development, 1, chemin de la Porte des
Loges, 78350 Les Loges-en-Josas, France*

***Corresponding author**

Abstract:

Perforations contribute to liquid redistribution in corrugated sheet packings. We focus on a simplified but relevant experimental configuration where a vertical perforated flat sheet is supplied with liquid on its front side. We examine how the perforations irrigate the back of the plate. We successively consider a single perforation, a spanwise row of perforations, and a staggered array of perforations.

We quantify the liquid transfer through a single row of perforations and find that the transferred flow rate per unit perforation diameter varies linearly with the supply flow rate per unit width. We also analyze the spreading of the rivulets leaking from the perforations, their merging into a continuous wavy film, and the leveling of this film as it falls down the plate. The spreading and the merging exhibit a power-law behavior in agreement with theoretical models. The leveling exhibits exponential decay behavior.

Topical Heading: Transport Phenomena and Fluid Mechanics

Key Words: Structured packing, liquid film, liquid curtain, rivulet, spreading, film leveling

1. Introduction

Corrugated sheet distillation packings were first used in applications where low-pressure drop was essential. As they became cheaper in the early 80s, they spread out in a much wider

application range, especially for their great ability to handle high vapour load. . These packings are typically used in the petrochemical, oil and gas industries, as well as in exhaust air cleaning or in the stripping of volatile constituents from wastewater. In the present paper, the target application is the cryogenic air separation. The corrugated sheet packings consist of metallic crimped sheets placed vertically, side by side, with the corrugations of adjacent sheets crisscrossing one another. Such packings combine a high void fraction and a high interfacial area, resulting in a lower pressure drop and a higher capacity than trays or random packings at the same efficiency. However, the separation performance of corrugated sheet packings is very sensitive to the uniformity of liquid distribution over the column cross-section compared to random packings. Indeed, in corrugated sheet packings, the liquid redistribution over the column cross-section is favored mostly by the inclination of the corrugated channels, but the vapor flow cannot redistribute the liquid as in columns with random packings. The addition of perforations that transfer liquid from one side of a sheet to another decreases the sensitivity of corrugated sheet packings to irrigation irregularity¹¹⁷.

Two scales of liquid distribution / maldistribution can be distinguished: small-scale (packing element) and large-scale (column). Small-scale distribution is inherent to the packing itself (such as channeling along the corrugations) whereas large-scale distribution is determined by the initial distribution, the radial spreading and the build-up of wall-flow^{111,118}. The present paper focuses on small-scale distribution.

Liquid spreading or distribution throughout the packing essentially depends on the packing geometry⁴⁷, the liquid flow rate⁴⁴, the liquid viscosity⁴⁴, and the contact angle of the liquid on the sheets^{119,120}. Liquid distribution further affects the liquid hold up, the liquid-vapor interfacial area, and, ultimately, the mass transfer within the packing.

At the packing sheet scale, three geometrical features contribute to liquid distribution: the corrugations, the perforations, and, optionally, the microtexture of the sheets. Whereas the liquid tends to flow vertically from the pour points, the troughs of the corrugated sheets guide the liquid in the transverse direction of the sheets. The contact points between the corrugations of adjacent sheets divide the liquid flow between the sheets. The perforations transfer the liquid from one side of a sheet to the other side. Last, the microtexture enhances the wettability of the sheets.

Liquid distribution and spreading over corrugated sheet structured packings have been investigated at different scales: (pilot) column scale, sheet scale, and geometrical feature scale. Tomographic techniques are efficient, non-intrusive tools to view inside a packed column and analyze the liquid flow distribution at the column scale. Fourati et al.⁴⁷ used gamma-ray

tomography to investigate liquid distribution in a counter-current gas-liquid column equipped with Mellapak 250.X packing and fed with a central liquid jet at the top. The working liquids were water and MEA 30wt%. They obtained hold-up maps (expressed in liquid volume fraction) at different axial positions in the column. They found that the overall liquid hold-up increases with the liquid flow rate and the liquid viscosity. The liquid phase disperses radially with a characteristic length called spreading factor¹²¹ of the order of a few millimeters. Since the spreading factor does not significantly vary with the liquid load, the gas load, and the liquid viscosity, Fourati et al.⁴⁷ concluded that liquid distribution is mainly controlled by the packing geometry.

Most of the 3-D images of the packed column inside have been obtained using X-ray computed tomography (XCT)^{42,44,122}. For instance, Janzen et al.⁴⁴ investigated the liquid flow morphology in a small column (inner diameter of 105 mm) equipped with MellapakPlus 752.Y packing and fed either with pure water or water-glycerin mixtures. Similarly to Fourati et al.⁴⁷, they found that the overall liquid hold-up and the gas-liquid interfacial area increase with the liquid load and the liquid viscosity. They distinguished three flow patterns: film flow, liquid menisci/bridges at the contact points between corrugations of adjacent sheets, and flooded regions. The relative contribution of the film-flow pattern to hold-up decreases with both the liquid load and the liquid viscosity, while the relative contribution of the flooded regions increases correspondingly. The contribution of the liquid menisci appears independent of the varied parameters. Schug & Arlt⁴² imaged the liquid flow morphology in different Mellapak 500.Y packings, i.e., with smooth, fluted, and gridded microtexture, with or without perforations. Packings were irrigated with water. The liquid hold-up in the packing with the gridded texture and holes shows the highest values, and the results indicate that the more complex the surface modification is, the higher is the liquid hold-up. The evaluation of the liquid film thickness shows that the packings are not totally wetted. Dry areas (or covered by a film below the resolution limit) subsist even at high liquid loads. Most of the liquid is located in the troughs of the packings in the form of rivulets, and at the contact points between sheets in the form of liquid bridges. Wehrli et al.¹²² examined liquid flow in Mellapak 250.Y and Mellapak 500.Y packings fed either with water or propan-2-ol. They found that the packings are better wetted by propan-2-ol than by water. They also distinguished three flow patterns, i.e., liquid films, rivulets, and bridges. Water tends to form rivulets in the troughs and bridges at the contact points, while a significant fraction of the packing surface remains not covered. Propan-2-ol tends to form liquid films that cover the packing surface uniformly.

Liquid distribution mechanisms have also been investigated with experiments carried out on a single corrugated sheet. Many studies at this scale have been carried out by Pavlenko's group at the Low-Temperature Thermophysics Laboratory (Kutateladze Institut of Thermophysics)^{18,20,92}. The sheet is placed vertically and supplied with liquid on one side only. Either one or several channels (i.e., troughs) on the upper edge of the corrugated sheet are irrigated. For X and Y packings, it is found that the liquid flow pattern and the subsequent wetted area depend on the corrugation angle, the surface microtexture, the perforations, and the flow parameters. In addition, the wetted surface area increases with the liquid flow rate. Below a minimum film Reynolds number ($Re \cong 100$ for liquid nitrogen⁹), the liquid cannot cross the channel crests: it flows along the valley of the irrigated channel and does not fall into the underlying (non-irrigated) channels. The transferred flow through the perforations (from the supplied side to the non-supplied one) also depends on the local liquid flow rate and their position on the channel surface (flank, crest, or valley). The liquid is only transferred above a minimum film Reynolds number ($Re \cong 100 - 160^{18}$). Then, the transferred flow rate increases with the local liquid flow rate (on the front of the plate, just upstream of the hole). Perforations may also facilitate the liquid flow from a channel to the underlying ones by multiple transfers, i.e., from the supplied side of the plate to the opposite one and back.

Gorodilov et al.¹¹⁷ quantified the transferred flow rate from the supplied side (front) to the non-supplied side (back) of a corrugated plate perforated with slits (instead of the standard round perforations). Corrugations and slits were parallel to the horizontal plane. The working liquid was water. They found that the liquid transfer starts above a minimum film Reynolds number and exhibits a hysteresis loop when varying the supply flow rate at the upper edge of the corrugated sheet. The threshold and the hysteresis loop are attributed to the liquid meniscus blockage at the slit entrance.

Studies focusing on a single geometrical feature (perforation or channel, for example) provide helpful insight into the elementary mechanisms involved in packed column. Xie et al.^{98,101} and Iyer et al.¹²³ considered the liquid flow down a vertical plate with a single perforation, round¹²³ or rectangular^{98,101}. The plate was supplied with liquid either on one or two sides. At low values of the film Reynolds number, the liquid film flow is deflected by the perforation, and the liquid does not fill the perforation. Above a critical value of the Reynolds number, referred to as the curtain Reynolds number, the liquid fills the perforation entirely and forms a liquid curtain. Xie et al.^{98,101} and Iyer et al.¹²³ further investigated the curtain regime when the plate is supplied with equal volume flow rate on its front and on its back. The varicose capillary waves standing on the liquid curtain and the strong vorticity generation both inside the curtain and on its free

surface could explain the mass transfer intensification observed for the plate with perforation (as compared to the unperforated plate)¹⁰⁰. However, the authors did not examine the effects of perforation on liquid redistribution.

Shetty & Cerro¹²⁴ investigated the spreading of a rivulet over an inclined flat solid surface. Such a simplified configuration typically mimics the rivulet flowing in a channel of a corrugated sheet. Experiments were performed with silicone oils of two different viscosities and a brass plate at a varying inclination angle. The plate was fed at a single drip point by a small liquid jet. They observed that the rivulet spanwise profile evolves self-similarly and is well represented by a Gaussian. They used a viscous long-wave approximation to derive a film evolution equation and obtain the scaling laws followed by the rivulet. They distinguished two spreading regimes, i.e., capillary-dominant and gravity-dominant. When the capillarity (resp. gravity) controls the spreading, the spanwise spreading follows the $3/13^{\text{th}}$ (resp. $3/7^{\text{th}}$) power of the distance traveled along with the flow (with appropriate rescaling) while the rivulet peak thickness thins out as the $-1/13$ (resp. $-1/7$) power of the traveled distance. They found a good agreement between the theory and the experiments. For an angle of inclination to the vertical greater than 10° , the spreading is controlled by gravity. It should be noted that the scaling laws for the gravity-dominant regime were first obtained by Smith¹²⁵, who derived a similarity solution for a viscous source flow down an inclined plane. Duffy & Moffatt^{126,127} later obtained a similarity solution for a viscous source flow down a vertical plane and recovered the exponents of the capillary-dominant regime first found by Shetty & Cerro¹²⁴.

Hoffmann et al.^{128,129} and Xu et al.¹³⁰ investigated experimentally and numerically the liquid flow behavior on inclined flat plates with film flow inlet and gas counter-current. Most of the experiments concern water on a stainless steel plate with a counter-current of air. The inclination angle to the horizontal was 60° . The static contact angle of water-air on steel was estimated at $70\text{-}80^\circ$. Film flow velocities were measured using a particle tracking velocimetry method, the wetted wall area and the liquid film thickness were determined by optical means. They found that the liquid flow pattern is mainly conditioned by the liquid flow rate. For (inlet) film Reynolds number $Re > 168$, the liquid film flow is stable: no dry patches form. For $84 < Re < 168$, the liquid film destabilizes to form rivulets. For $Re < 56$, the rivulets destabilize into droplets.

To better understand how the perforations contribute to liquid distribution in corrugated sheet packings, in this work, we consider a simplified configuration where a vertical perforated flat sheet is solely supplied with liquid on its front. Experimentally, we examine how the perforations irrigate the back of the plate. Plates have either a single perforation, a spanwise

row of perforations, or a staggered array of perforations. We quantify the liquid transfer through the perforations as a function of the supply flow rate. After examining the impact of the flow regime on the transfer, we further focus on the curtain regime. We explore the effects of the perforation diameter, the perforation spacing, and the plate thickness. We carefully analyze the spreading of the rivulets leaking on the back of the plate from the perforations, the merging of the rivulets into a continuous film, and the leveling of this film as it falls down the plate. Liquid film thickness profiles are assessed using confocal chromatic imaging (CCI).

In the first part of the paper, we briefly address the physics of the problem. In the second part, we describe our experimental setup and the associated measurement methods. The third part presents our experimental data. The fourth part discusses the results and compares them to models either found in the literature or newly developed.

2. Problem description

We consider a vertical flat plate or sheet of thickness t with single or multiple circular perforations of diameter d (**Figure 4-1**). The plate is supplied with liquid on its front, above the perforations. We study the liquid transfer from the front to the back of the plate. x denotes the streamwise direction, y the spanwise direction, and z is the direction in the thickness of the liquid film. Three perforation patterns are examined: (i) single perforation, (ii) spanwise row of equally-spaced perforations, and (iii) staggered array of perforations. s is the (centre-to-centre) spacing between the perforations in y -direction as well as the pitch (in x -direction) between the rows of perforations (see **Figure 4-1**).

We consider a Newtonian liquid with constant physical properties such as density (ρ), kinematic viscosity (ν) and surface tension (σ). $\mu = \rho\nu$ is its dynamic viscosity. We suppose that the wetting is highly favorable (equilibrium contact angle of the liquid on the plate $\theta_E \ll 90^\circ$)

The front of the plate is supplied with liquid at a volume flow rate q . We define Q the supply flowrate per unit width, i.e., $Q = q/w$, where w is the width of the channel bounded by the frame that holds the plate (see **Figure 4-1**). The flow upstream of the perforations is characterized by the film Reynolds number $Re = Q/\nu$ which we call thereafter the supply Reynolds number.

We assume that the film flow upstream of the perforations is steady, laminar and fully developed. If we suppose that the amplitude of the waves that may travel on the free surface remains much lower than the film thickness, the upstream film thickness is well described by the Nusselt⁵¹ thickness, $\delta_{Nu}(Q) = (3\nu Q/g)^{1/3}$.

For a single perforation or a single spanwise row of perforations, we note q_t the total volume flow rate transferred through the perforations. In the absence of supply on the back of the plate, q_t coincides with the volume flow rate q_b flowing on the back of the plate beneath the perforations. We define the transferred volume flow rate per unit diameter of perforation $Q_t = q_t/(Nd)$ with N the number of perforations. Following Gorodilov et al.¹¹⁷, we also introduce the so-called overflow number $X = Q_t/Q$ which quantifies the liquid transfer efficiency of a perforation.

For a staggered array of perforations, we index the rows from top ($k = 1$) to bottom ($k = n$). N is the number of perforations of the odd numbered rows, $(N - 1)$ the number of perforations of the even. The width of the array is defined as $w_a = Ns$. We note $q_b(k)$ the volume flow rate on the back of the plate just beneath the k^{th} row of perforations. The volume flow rate per unit width on the back of the plate just beneath the k^{th} row of perforations is defined as $Q_b(k) = q_b(k)/w_a$.

Last, we define $\delta(x, y)$ the local thickness of the liquid film on the back of the plate.

When a liquid film flows over a single perforation of small diameter ($d \leq 8$ mm), different regimes may be distinguished depending on (1) the value of the film Reynolds number and (2) the history of the film flow. We recall below the main results of a previous study by the authors¹²³. When Re is low, the film flow is deflected by the perforation and does not fill it. The contact line is pinned at the top edge of the perforation (front of the plate) and there is no fluid transfer from the front to the back of the plate. When Re is moderate, a liquid rim forms within the perforation and liquid is transferred from the front to the back of the plate. On the back, the liquid climbs over the top edge of the perforation and makes an arch-shaped capillary ridge that extends in the form of two parallel rivulets (see Figure S4.1 in Supplementary Material). Thereafter, this regime will be referred to as the rim mode. When Re is high, a liquid curtain closes the perforation. Liquid is still transferred from the front to the back of the plate but the flow pattern on the rear side differs from that encountered in the rim mode: the liquid leaks from the bottom edge of the perforation in the form of a single rivulet (see Figure S4.1 in Supplementary Material). The curtain transition occurs when the inertia of the film balances the surface tension forces. We note Q_{cr} the supply flow rate per unit width at the curtain transition. The curtain Reynolds number Re_{cr} is the Reynolds number associated with Q_{cr} . This regime will be referred to as the inertial curtain mode.

When the supply flow rate is decreased from the inertial curtain mode, the film flow remains in the curtain mode for Re values much lower than Re_{cr} ¹²³. Liquid is transferred from the front to

the back of the plate with the same flow pattern as for $Re > Re_{cr}$. This regime will be referred to as the hysteretic curtain mode. This mode is metastable: if a hole is made in the curtain, the film flow switches to the rim mode.

In the rest of the paper, we investigate the effect of perforation diameter (d), perforation spacing (s), plate thickness (t), supply flow rate per unit width (Q) and flow mode (rim, inertial curtain, hysteretic curtain) on (i) the transferred flow rate per unit diameter of perforation (Q_t) and (ii) the subsequent wetting of the back of the plate (by measuring the liquid film profile).

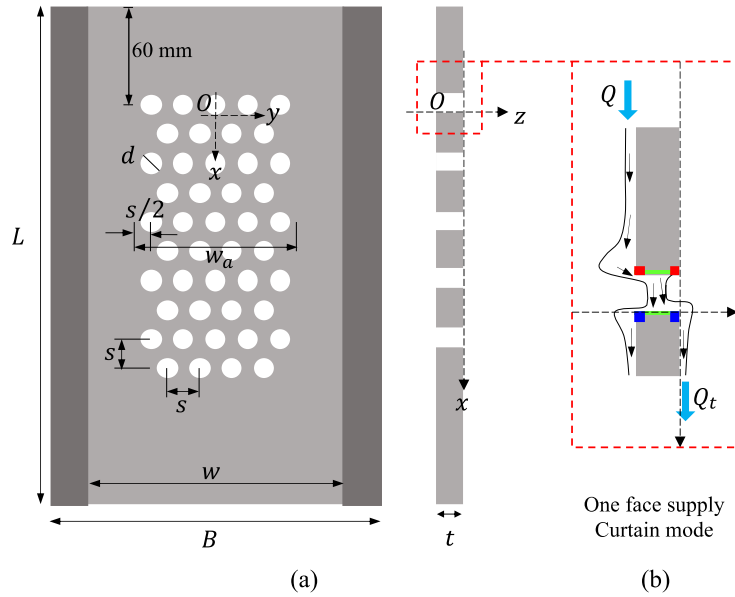


Figure 4-1: Perforated plate front view and cross-section along x - z plane: (a) geometric parameters and coordinate system (b) Scheme of the film flow on the front and on the back of the plate (the plate is supplied solely on its front, the film flows in the curtain mode). The arrows indicate the flow path followed by the fluid. We define the top edges of the perforation on the front and on the back of the plate (red squares), the bottom edges (blue squares) and the perforation inner surface (in green).

3. Experimental set-up

Materials

The test plates are cut from aluminum sheets. Aluminum is the packing material most often used for cryogenic air distillation. The plate length in the streamwise direction is $L = 200$ mm and the plate width in the spanwise direction is $B = 150$ mm (see **Figure 4-1**).

For the single perforation pattern, two different plate thicknesses, i.e., $t = 0.5$ and 1 mm, and six perforation diameters, i.e., $d = 4, 6, 8, 10, 14$ and 16 mm, are tested. We define $d = 4$ mm

and $t = 1$ mm as the reference case. The centre of the perforation is located on the midline of the plate, at 60 mm from the top edge.

For the single spanwise row of perforations, the plate thickness is $t = 1$ mm, the perforation diameter $d = 4$ mm. Five centre-to-centre spacing, i.e., $s = 6, 8, 10, 12$ and 14 mm are examined. For each spacing, the number N of perforations is the maximal value satisfying $N \times s \leq 70$ mm, which equates to 11, 9, 7, 5 and 5, respectively. Perforations are spread within 70 mm and not within the entire channel width $w = 90$ mm to reduce side wall effects (the film flow is laterally bounded by the frame that holds the plate).

For the staggered array of perforations (with 2, 3 or 10 rows of perforations), we selected $t = 1$ mm, $d = 4$ mm, and $s = 14$ mm. The pitch between the rows is fixed to $s = 14$ mm.

For the plates of 0.5 mm thickness, the perforations were made by laser cutting. For the plates of 1 mm thickness, single perforation and single row of perforations were made by drilling, staggered array of perforations by laser cutting. Special care was taken when machining in order to maintain the flatness of the sheets and ensure that the edge of the perforations is sharp and perpendicular to the plate face.

The test plates are slightly polished with abrasive paper (grit size P1200) to get a matt rendering and thus reduce the impact of parasitic light reflections on optical measurements. The resulting roughness parameter (R_a , arithmetical average of the roughness profile) of the plate ranges from 0.2 to 0.5 μm with a standard deviation of the order of 0.01 μm as measured by confocal chromatic imaging (3D Measuring Station with CHR 150-N sensor, STIL).

Pure propan-2-ol (VWR Chemicals, GPR Rectapur®, purity >99.0%), is used as a test liquid. Its physical properties are reported in Table 1 (see Supplementary Material). We emphasize that, similarly to cryogenic liquids, the wetting of the aluminum sheets by propan-2-ol is highly favorable ($\theta_E \ll 90^\circ$).

Experimental set-up

The details of the setup have already been presented in a previous work by the authors¹²³. We recall hereafter some of its main features. It comprises three parts (see **Figure 4-2**): the frame that holds the perforated plate, the liquid circuit, and the instrumentation dedicated to the observation and measurement of the liquid film. The perforated plate is inserted in a rigid frame to ensure its flatness. The frame is held vertically. It is decoupled from the other parts of the device and mounted on an anti-vibration table to damp the parasitic vibrations that may affect the fluid film flowing on the plate. The front of the plate is supplied with liquid by a distributor

carefully designed to uniformly distribute the liquid in the spanwise direction of the plate: the flow comes out laminar through 30 horizontally and equally spaced circular nozzles of 2 mm in diameter¹²³. The liquid circulates thanks to a magnet gear pump (MDG-M15T3B, Iwaki). The volumetric flow rate delivered by the distributor is set by a needle control valve and monitored by an oval gear volumetric flow meter (MX06, MacNaught). The liquid flowing from the bottom of the plate comes into a collector and then returns to the feeding tank.

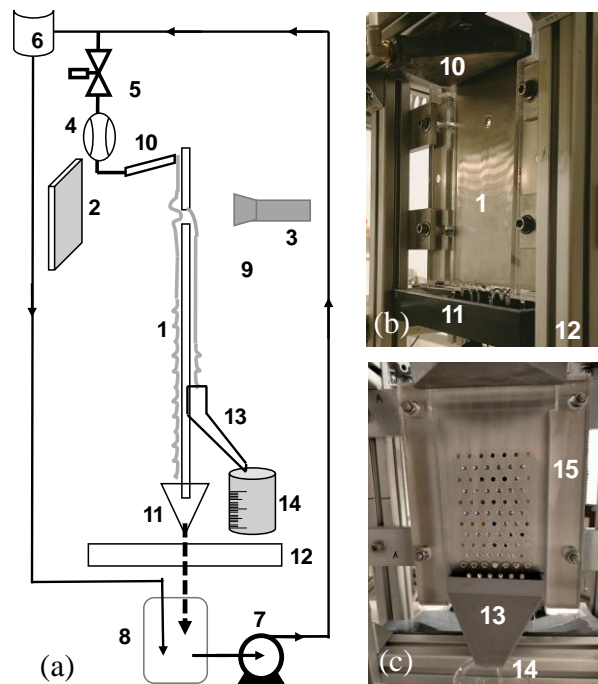


Figure 4-2: (a) Schematic representation of the experimental set-up. (b) Photograph of the front of the plate (with a single perforation). (c) Photograph of the rear side (with a staggered array of perforations). 1. Test plate 2. LED panel 3. High-speed camera 4. Volumetric flow meter 5. Needle control valve 6. Spillway 7. Gear pump 8. Reservoir 9. CCI sensor 10. Distributor 11. Liquid Collector 12. Anti-vibration mount, 13. Removable collector, 14. Measuring beaker. 15. Frame that holds the plate to ensure plate flatness.

The liquid flow pattern is observed and recorded using a CMOS high-speed camera (v310, Phantom) mounted with a macro lens (AF Zoom-Micro Nikkor 70-180mm f/4.5-5.6D ED, Nikon). Images are captured with a resolution of 1200×800 px² and at an acquisition frequency of 1.8 kHz. For shadowgraph imaging of the suspended film, the plate is illuminated with a LED light panel (SLLUB, PHLOX). When looking at the free surface of the supported film, the plate is lit by a cold light illuminator (KL 2500 LCD, Schott).

The instantaneous local thickness of the liquid film is measured at different locations using confocal chromatic imaging (CCS OPTIMA+, CL4 chromatic lens, STIL) with a resolution better than 0.5 μm at an acquisition frequency of 5 kHz.

The volume flow rate of liquid transferred by the perforations is measured by diverting the liquid flow through a removable collector attached to the back of the plate 10 to 15 mm distance from the last row of perforations and weighing (**Figure 4-2**).

Experimental protocol

First, the test plate is cleaned with a surfactant solution (3 vol%, Mucosol, Merz), thoroughly rinsed with distilled water and dried with compressed air. Then, the plate is inserted and fixed in the vertical frame. The outlet of the distributor is positioned on the front of the plate about two millimeters below its top edge. Since the outlet is located 60 mm upstream of the first row of perforations, we expect that the film flow is fully developed on the front side at the location of the perforations (we estimated the entrance length at a few millimeters). In the studied flow range, the liquid film flow is laminar. The film remains essentially flat upstream of the first perforations: we are aware that a liquid film falling on a vertical flat plate is unconditionally unstable. However, we checked that the amplitude of the waves travelling on the liquid film upstream of the first perforations remains small compared to the liquid film thickness (within 5% of the film thickness¹²³). The distance (in z direction) between the distributor nozzles and the plate is carefully adjusted in order to obtain a uniform film thickness in the spanwise (y) direction. The front of the plate is first fed with the highest flow rate, i.e., 38 L h^{-1} , such that the liquid is forced to wet the whole usable width of the front side, i.e., $w = 90$ mm. Then, the liquid flowrate can be reduced down to 5 L h^{-1} (or at any intermediate value in between) and the region upstream of the perforations remains totally covered by the liquid film.

The supply flow rate (q) is incrementally swept from 5 L h^{-1} to 38 L h^{-1} and then down to 5 L h^{-1} to explore the rim mode, the inertial curtain mode, and the hysteretic curtain mode until curtain rupture. We determine if liquid is transferred through the perforations for each flow rate value (in the forward and backward sweep) and measure the average volume flow rate on the back of the plate beneath the perforations (q_b). We remind that in the absence of supply on the back of the plate, q_t (transferred by a single perforation or a single row of perforations) coincides with q_b just beneath the perforations. Optionally, the topography of the liquid film on the backside of the plate is investigated point-by-point by CCI. For each set of parameter values, experiments were performed at least in triplicate.

4. Results

Thereafter, we successively report the experimental data obtained with a single perforation, a spanwise row of perforations, and a staggered array of perforations.

4.1. Single perforation

Fluid transfer in rim and curtain modes

For the reference case, i.e., $d = 4$ mm and $t = 1$ mm, **Figure 4-3** presents the variations of the transferred volume flow rate per unit diameter of perforation (Q_t) as a function of the supply flow rate per unit width (Q). The same data are presented in a different way in Figure S4.2 (see Supplementary Material): we plot the variations of the overflow number (X) as a function of the supply Reynolds number (Re). We observe that the variations of Q_t in the rim mode are non-monotonous: Q_t first increases steeply with Q and then decreases as Q approaches Q_{cr} . Q_t reaches its peak value ($Q_t = 0.16 \text{ m}^3 \text{ m}^{-1} \text{ h}^{-1}$) for $Q = 0.23 \text{ m}^3 \text{ m}^{-1} \text{ h}^{-1}$. In that case, the transferred flow rate per unit diameter is even greater than half of the supply flowrate per unit width: as the flow rate entering the perforation divides between the front and the back of the plate, a greater proportion flows to the back. We advance the following explanation: since the wetting is highly favorable, the contact line climbs over the top edge of the perforation on the back of the plate (see Figure S4.1 in Supplementary Material). The vorticity inherent to the shear flow along the front of the plate (vorticity vector parallel to y -axis) help the liquid to rotate around the perforation top edge and irrigate the back of the plate (see Figure S4.1 in Supplementary Material). At $Q_{cr} = 0.30 \text{ m}^3 \text{ m}^{-1} \text{ h}^{-1}$ ($Re_{cr} = 33$), the transition from the rim to the (inertial) curtain mode occurs. As Q is further increased beyond Q_{cr} , Q_t grows. Ultimately, Q_t seems to tend asymptotically to the line $Q_t = 0.5Q$ corresponding to an equal partition of Q between the front and the back of the perforation (overflow number $X = 0.5$). As Q is swept down from Q_{cr} , the film flow remains in the curtain mode, and Q_t linearly reduces with the decrease in Q . We note that a minimal supply flow rate is required for the liquid to be transferred through a perforation. In the rim mode, the threshold for liquid transfer is equal to $Q = 0.18 \text{ m}^3 \text{ m}^{-1} \text{ h}^{-1}$ ($Re = 19$). In the hysteretic curtain mode, the liquid transfer stops when the curtain breaks, i.e., $Q = 0.10 \text{ m}^3 \text{ m}^{-1} \text{ h}^{-1}$ ($Re = 11$).

When active, the rim mode is more efficient to transfer liquid than the hysteretic curtain mode. However, the curtain mode (inertial or hysteretic) permits transfer over a broader range of supply flow rate. Furthermore, the variations of the transferred flow rate as a function of the supply flow rate are monotonous and more predictable when operating in curtain mode.

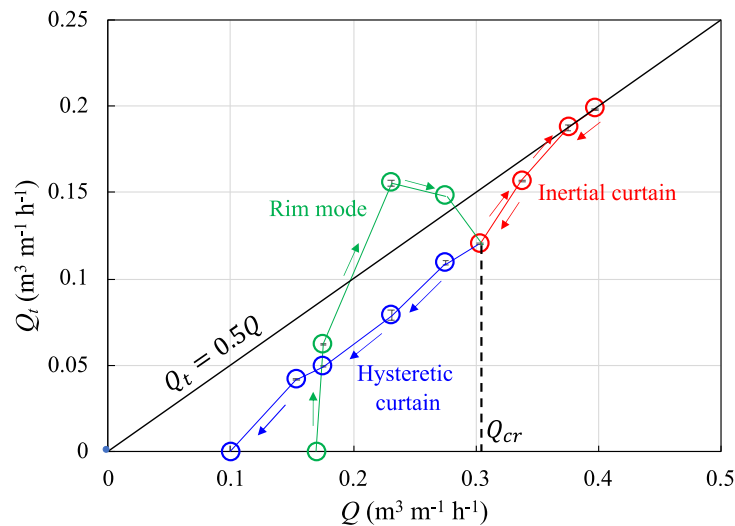


Figure 4-3: Single isolated perforation: transferred volume flow rate per unit diameter of perforation (Q_t) as a function of the supply flow rate (on the front of plate) per unit width (Q). The diameter is $d = 4$ mm, the plate thickness $t = 1$ mm. The straight lines linking the dots are intended to guide the eye along the data points. Arrows indicate how Q_t evolves as Q is swept up and down. Rim mode (green), inertial curtain (red), hysteretic curtain (blue).

Effect of perforation diameter on liquid transfer in curtain mode

We focus on the curtain mode (either inertial or hysteretic) and measure the transferred volume flow rate as a function of the supply flow rate on the front of the plate, for six values of perforation diameter, i.e. $d = 4, 6, 8, 10, 14, 16$ mm. The plate thickness is $t = 1$ mm. Regardless of the value of d , the variations of Q_t with Q follow the same increasing trend (see Figure S4.3 in Supplementary Material and **Figure 4-4**). The liquid curtain ruptures and the liquid transfer ceases in the range $Q = 0.04$ to $0.1 \text{ m}^3 \text{ m}^{-1} \text{ h}^{-1}$ ($Re = 5$ to 11). At lower Q values (larger than $0.1 \text{ m}^3 \text{ m}^{-1} \text{ h}^{-1}$), the transferred flow rate Q_t is significantly lower (up to 30%) for $d = 4$ mm than for the other (larger) perforation diameters. The effect of d on Q_t decreases as Q increases. For the higher values of Q , Q_t is close to $0.5Q$ (overflow number $X = 0.5$) regardless of d .

Effect of plate thickness on fluid transfer in curtain mode

We measure the transferred volume flow rate in the curtain mode as a function of the supply flow rate for two plate thicknesses $t = 0.5, 1$ mm, and three perforation diameters $d = 4, 6, 8$ mm. There is a clear and significant effect of plate thickness on Q_t for $Q \gtrsim 0.3 \text{ m}^3 \text{ m}^{-1} \text{ h}^{-1}$ ($Re \gtrsim$

30): all else being equal, the transfer is lower for smaller plate thickness $t = 0.5$ mm (see **Figure 4-4**). The overflow number at large Q values is close to $X = 0.4$ for $t = 0.5$ mm.

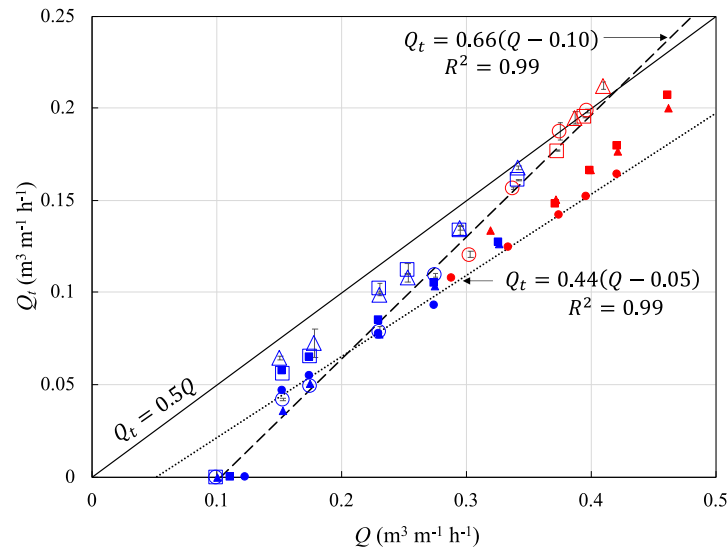


Figure 4-4: Transferred volume flow rate per unit diameter of perforation (Q_t) as a function of the supply flow rate (on the front of plate) per unit width (Q): effect of plate thickness. Single perforation with $d = 4$ mm (circle), 6 mm (square), 8 mm (triangle), plate thickness $t = 0.5$ mm (filled), 1 mm (empty). Curtain mode (hysteretic in blue, inertial in red). Linear fit for $d = 4$ mm and $t = 0.5$ mm (dotted line), for $d = 4$ mm and $t = 1$ mm (dashed line).

Profile of the rivulet on the rear side of the plate

We focus on the curtain mode and examine how the transferred liquid spreads over the back of the plate for the reference case ($t = 1$ mm, $d = 4$ mm) and different values of the supply Reynolds number, i.e., $Re = 24, 29, 33, 38, 42$. We observed that the liquid leaks from the bottom edge of the perforation and forms a single rivulet. We measured its spanwise profile at $x = 2, 20, 40, 60, 80, 100$ mm from the bottom edge of the perforation (see **Figure 4-5** and Figure S4.4 in Supplementary Material). We also measured its streamwise profile along $y = 0$ (see Figure S4.5 in Supplementary Material). Since the minimum measurable thickness of the CCI sensor is about $100 \mu\text{m}$, it was not possible to measure the thickness profile near the thinner parts of the rivulet close to the contact line. **Figure 4-5** and Figure S4.4 (Supplementary Material) show that the rivulet widens and flattens as it flows in the x -direction. The spanwise profile is approximately symmetric along the y axis and the thickness reaches its peak value

close to $y = 0$. We observe slight deviations from symmetry: they are attributed to flow disturbances within the perforation and to wetting heterogeneities on the back of the plate. We exclude meandering instability since the volume flow rate out of the perforation is at least one order of magnitude lower than the meandering threshold¹³¹. Figure S4.5 shows that the rivulet is thicker as the supply Reynolds number increases. Streamwise profiles are slightly rough because the rivulet is not perfectly straight, the flow out of the perforation is not rigorously constant, and waves may travel on the rivulet surface.

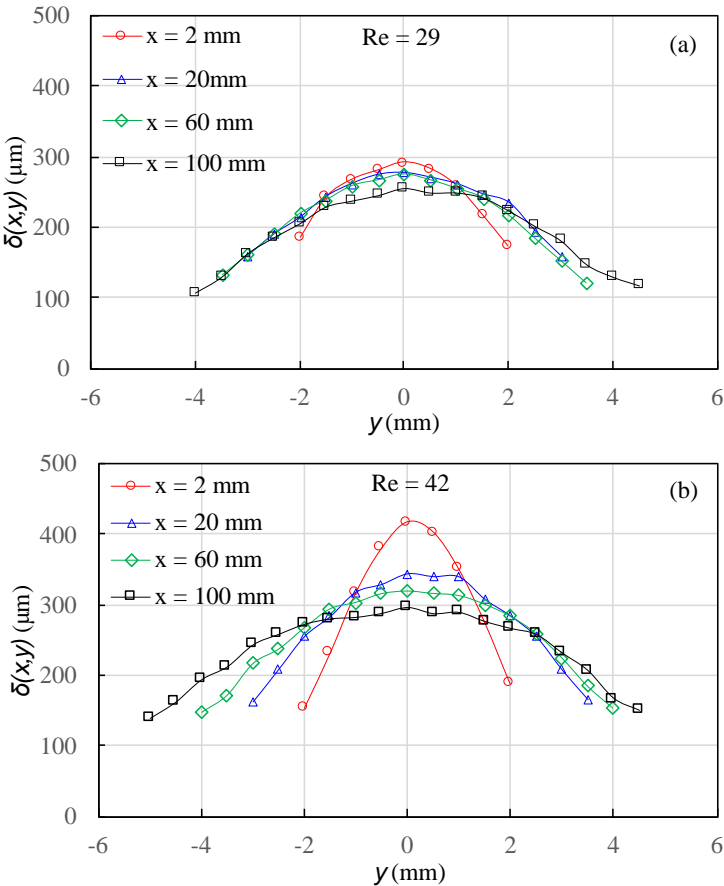


Figure 4-5: . Spanwise rivulet profile on the rear side of the plate at $x = 2, 20, 60, 100$ mm from the bottom edge of the perforation. Plate thickness $t = 1$ mm, perforation diameter $d = 4$ mm. Curtain mode. (a) $\text{Re} = 29$; (b) $\text{Re} = 42$. The lines linking the dots are intended to guide the eye along the data points.

4.2. Spanwise row of perforations

Effect of spacing on fluid transfer

We investigate the effect of one row of perforations on the liquid transfer from the front to the back of the plate. The perforation diameter is $d = 4$ mm and the plate thickness $t = 1$ mm. We study five perforation spacings $s = 6, 8, 10, 12$ and 14 mm. The curtain Reynolds number, i.e., the Reynolds number at which curtain forms, ranges between $Re_{cr} = 33$ and $Re_{cr} = 36$ (see Figure S4.6 of the Supplementary Material). These slight variations seem not correlated with the perforation spacing. The variations in Re_{cr} could instead be due to the variability of the plate curvature. A slight curvature of the sheet affects the liquid distribution upstream of the perforations and thus the curtain transition. The residual curvature of the plate depends on its clamping within the frame.

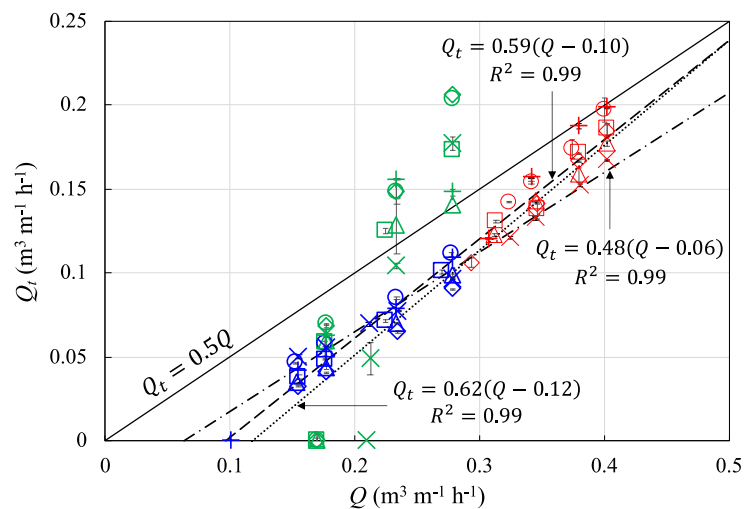


Figure 4-6: Average volume flow rate transferred per unit diameter of perforation (Q_t) as a function of the supply flow rate (on the front of plate) per unit width (Q): effect of perforation spacing (s). Perforation diameter $d = 4$ mm, perforation spacing $s = 6$ mm (\times), 8 mm (\diamond), 10 mm (\triangle), 12 mm (\circ), 14 mm (\square), single isolated perforation or $s = \infty$ ($+$). Plate thickness $t = 1$ mm. Rim mode (green), inertial curtain mode (red), hysteretic curtain mode (blue). Linear fit on the curtain mode data for $s = 6$ mm (dashdotted line), $s = 8$ mm (dotted line), and $s = 14$ mm (dashed line).

In the rim mode, the onset of fluid transfer through the perforations occurs at $Q = 0.17$ $\text{m}^3 \text{m}^{-1} \text{h}^{-1}$ ($Re = 19$) for all s except for $s = 6$ mm. In the latter case, the threshold is slightly higher: $Q = 0.21$ $\text{m}^3 \text{m}^{-1} \text{h}^{-1}$ ($Re = 23$). As already observed for a single perforation, at a given supply flow rate, the rim mode, when active, is more efficient than the curtain mode to transfer fluid from the front to the back of the plate. Whatever the spacing, the variations of Q_t with Q in the rim mode follow the same increasing trend. However, at fixed Q , no rule emerges from

the variations of Q_t with s . The highest transfer per perforation is obtained for $s = 8$ mm and $s = 12$ mm.

In the curtain mode (inertial and hysteretic), the dependence of Q_t on s is weaker. On average Q_t tends to be higher at greater perforation spacing.

Merging of the rivulets on the back of the plate

We focus on the curtain mode and examine how the rivulets, flowing from the perforations, merge downstream and tend to form a liquid film of even thickness. Two Reynolds numbers are considered: $Re = 26$ (hysteretic curtain mode) and $Re = 38$ (inertial curtain mode).

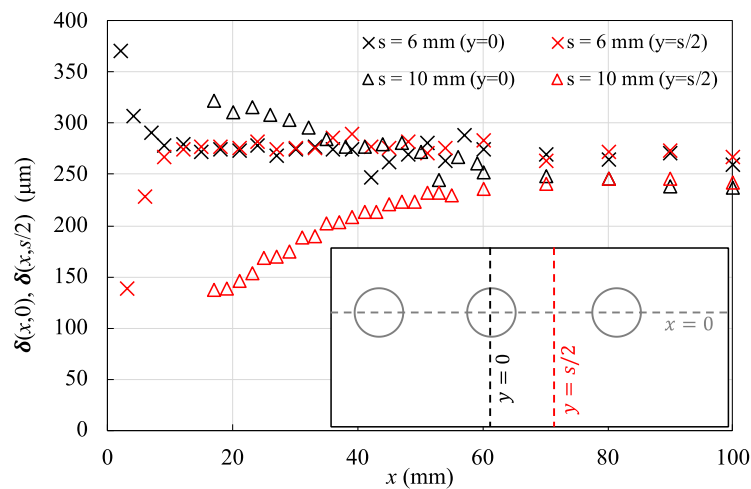


Figure 4-7: Streamwise film profile along $y = 0$ and $y = s/2$ (see the inset in the graph) for spacing $s = 6, 10$ mm. Single spanwise row of perforations, perforation diameter $d = 4$ mm, plate thickness $t = 1$ mm, and Reynolds number $Re = 38$ (curtain mode).

We measure the streamwise film profile along the lines of equation $y = 0$ and $y = s/2$ (see **Figure 4-7** and Figures S4.7 and S4.8 in Supplementary material). The line $y = 0$ (resp. $y = s/2$) coincides with a crest (resp. a trough) of the free surface (see **Figure 4-8**). Since the minimum measurable thickness of the CCI sensor is about $100 \mu\text{m}$, it is not possible to capture the beginning of the merging between two adjacent rivulets. Thus, at given spacing, merging starts at a distance slightly lower than the abscissa of the first measuring point along the line $y = s/2$ (**Figure 4-7**, Figure S4.7, and Figure S4.8). We observe that the film thickness along $y = 0$ (resp. $y = s/2$) decreases (resp. increases) with x and reaches a plateau. The smaller the spacing, the faster the plateau is reached and the higher is the plateau value. For the smaller spacing values, the film thickness tends to decline after the plateau: this is due to the further spreading of the liquid film. It is worth noting that the width of a perforation row (about 70 mm) is narrower than the channel width available for the liquid ($w = 90$ mm).

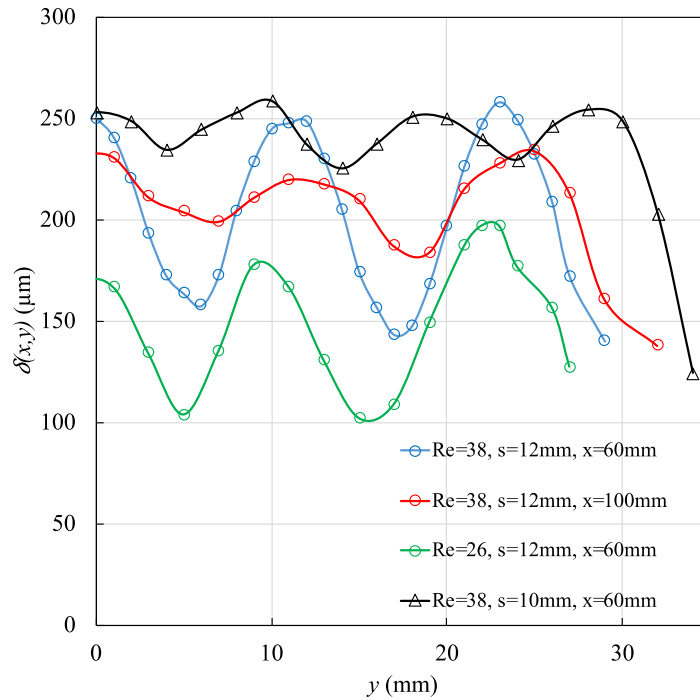


Figure 4-8: Film spanwise profiles for different streamwise locations (x), supply Reynolds numbers (Re) and perforation spacings (s). Single spanwise row of perforations, diameter $d = 4$ mm, plate thickness $t = 1$ mm, curtain mode. The lines linking the dots are intended to guide the eye along the data points.

Figure 4-8 shows spanwise film profiles at distances $x = 60$ mm and 100 mm (for $Re = 38$). Rivulets have already merged. We observe that the profiles are still wavy with a wavelength close to the perforation spacing. The amplitude of these ripples decreases along with the x -axis (compare the blue and the red curves in **Figure 4-8**): the film surface progressively levels as it flows downstream. At fixed values of x and Re , the spanwise profile is flatter and the average film thickness is larger when the perforation spacing is smaller (compare the blue and the black curves in **Figure 4-8**). These findings are coherent with the observations of **Figure 4-8**, Figure S4.7 and Figure S4.8. Last, all other things being equal, the average film thickness increases with the supply flow rate per unit width (compare the blue and the green curves in **Figure 4-8**).

4.3. Staggered array of perforations

We perform experiments on a plate with a staggered array of perforations (up to 10 rows). The plate thickness is $t = 1$ mm, the perforation diameter $d = 4$ mm, and the spacing $s = 14$ mm. Perforations are spread laterally within 70 mm: odd (resp. even) rows comprise five perforations

(resp. four). The opening rate of the perforation arrangement is equal to 6.4% (about half of the standard opening ratio in industrial packing, which ranges between 10% and 14%).

Observations

The supply flow rate on the front of the plate is swept from $Re = 10$ to Re_{cr} and beyond.

Three flow patterns depending on the supply Reynolds number are distinguished.

At low Re ($Re < 23$), the liquid film passes around the perforations of the odd numbered rows and flows in the curtain mode over the perforations of the even numbered rows. On the front of the plate, the perforations of the odd (resp. even) rows are topped by a U-shaped (resp. W-shaped) capillary ridge. There is no fluid transfer through the perforations of the odd rows: the contact line is pinned either at the top edge of the perforation or in its inner surface.

On the contrary, the fluid transfer is active in the perforations of the even rows. As the perforations of the odd rows deflect the liquid film, the spanwise distribution of flow rate per unit width becomes strongly heterogeneous. The flow rate is depleted along $y = 0$ (modulo s) and enhanced along $y = s/2$ (modulo s), causing the film to flow in the curtain mode over the next (even numbered) row of perforations.

At $Re = 23$, a liquid rim forms within the perforations of the odd rows. Then, at a moderate flow rate ($23 < Re < Re_{cr}$), the perforations of the odd rows operate in the rim mode, and those of the even rows are in the curtain mode (see **Figure 4-9**). On the back of the plate, all the perforations are topped by a U-shaped capillary ridge. A dry patch remains just below the perforations of the odd rows. Its area decreases as Re increases, and the patch finally disappears at even higher Re .

For the perforations operating in the rim mode, the liquid climbs over the top edge of the perforation (back of the plate), makes an arch-shaped capillary ridge and drains in the form of two parallel rivulets. Furthermore, the Kapitza waves traveling on the front of the plate make the rims oscillate. For the perforations in the curtain mode, the liquid leaks from the bottom edge of the perforation as a single rivulet. These observations are consistent with those for a single isolated perforation¹²³ (see also Problem description).

The alternation of row of perforations operating either in rim mode or in curtain mode is a consequence of the array symmetry and orientation with respect to the vertical. In industrial corrugated sheet packings, perforations operating in curtain mode would coexist with perforations in rim mode, but their spatial distribution within the packing will not be as regular. At $Re = Re_{cr}$, curtain transition is observed simultaneously for all odd rows. At Re_{cr} and above, all the perforations (odd and even numbered rows) operate in the curtain mode (see

Figures S4.9 and S4.10 in Supplementary Material). The liquid leaks from the bottom edge of the perforations. The corresponding rivulets widen as they flow in the x -direction. The liquid free surface is disturbed by waves traveling downstream. This phenomenon is clearly seen beneath the third row of perforations (see Figure S4.10).

As the supply flow rate is swept down below $Re = Re_{cr}$, curtain mode and associated liquid transfer maintain in both odd and even rows. Curtain rupture is observed at low flow rates (about $Re = 10$).

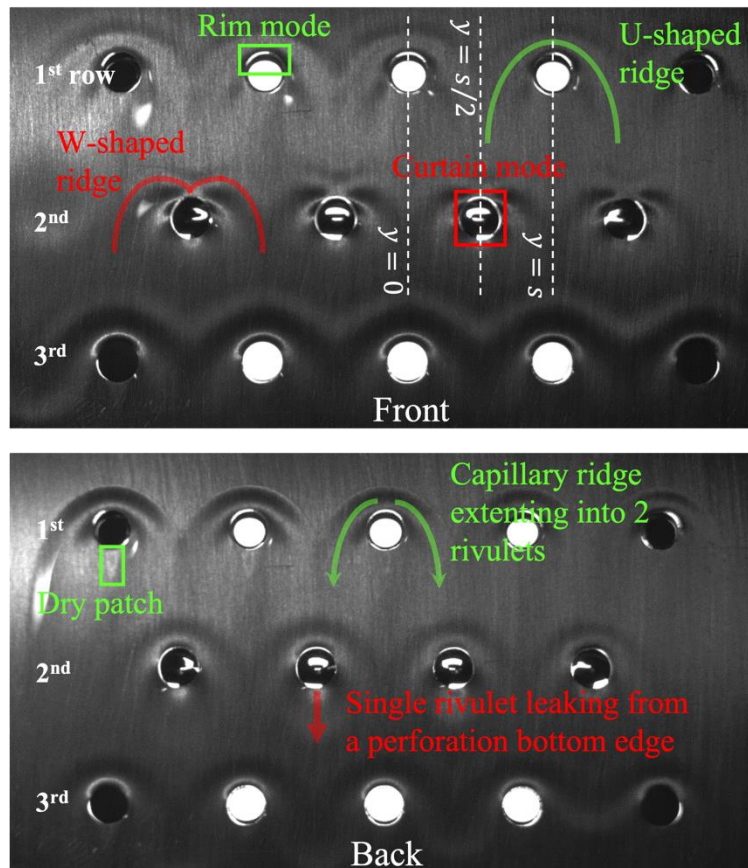


Figure 4-9: Liquid film pattern on a staggered array of perforations at $Re = 23$ when rim mode (in odd rows) and curtain mode (in even rows) coexist. Plate thickness $t = 1$ mm, perforation diameter $d = 4$ mm and spacing $s = 14$ mm. (Top) front of the plate, (bottom) back of the plate. Some holes without curtain appear completely black because they are not adequately lit.

Fluid transfer

We measure the total volume flow rate on the back of the plate beneath the 1st, 2nd, 3rd and 10th row of perforations. Using plates with either 1, 2, 3, or 10 rows of perforations, the fluid is collected on the back of the sheet with the dedicated collector (see Experimental set-up). A

focus is made on the curtain mode, either hysteretic or inertial. **Figure 4-10** presents the variations of Q_b as a function of the supply flow rate per unit width Q . We remind that the volume flow rate per unit width ($Q_b(k)$) flowing on the back of the plate downstream of the k^{th} row of perforations is the ratio of the volume flow rate ($\text{m}^3 \text{h}^{-1}$) beneath the k^{th} row to the array width ($w_a = 70 \text{ mm}$). It can be seen that after ten rows of perforations, Q_b is already close to $Q/2$, the expected asymptotic limit (when the flows on the front and on the back of the plate equalize, and the liquid transfer vanishes). Beneath the third row of perforations, $Q_b(3)$ already reaches 65% to 90% of the final Q_b measured beneath the 10th row.

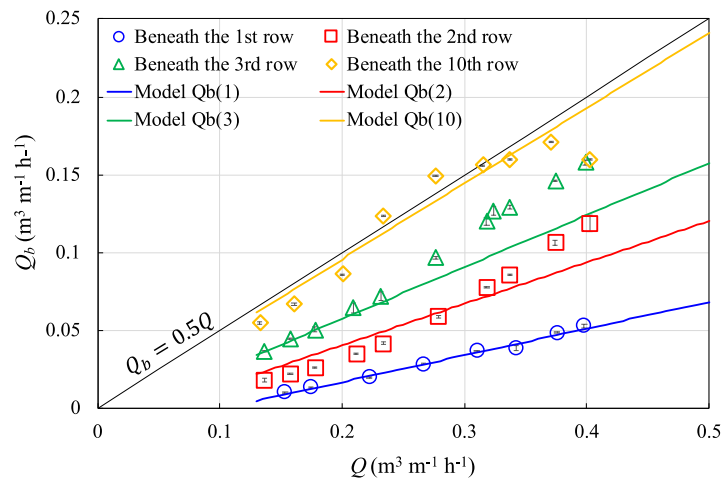


Figure 4-10: Volume flow rate per unit width (Q_b) on the back of the plate beneath the 1st, 2nd, 3rd and 10th row as a function of the supply flow rate per unit width on the front (Q). Plate thickness $t = 1 \text{ mm}$, perforation diameter $d = 4 \text{ mm}$, and spacing $s = 14 \text{ mm}$. Curtain mode. The solid black line represents the asymptotic value of Q_b , i.e., after a large number of perforation rows. The beam of colored straight lines corresponds to the model predictions of Q_b flowing on the back of the plate after $k = 1$ to $k = 10$ rows of perforations.

5. Discussion

Hysteresis loop and liquid transfer thresholds

The variations of the transferred flow rate as a function of the supply flow rate (on the front of the plate) exhibit a hysteresis loop with two liquid transfer thresholds. The first one appears when the supply flow rate is increased from low values, the second when the flow rate is decreased from values above the curtain transition (see **Figure 4-3** and **Figure 4-6**). In the former case, there is initially no fluid transfer from the front to the back of the plate: the contact line is pinned at the top edge of the perforation (front of the plate) or within its inner surface. As the contact line is released, the liquid transfer starts in the rim mode. This threshold is equal

to $Re = 19$ for $d = 4$ mm, $s \geq 8$ mm and $t = 1$ mm. In the latter case (flow rate descent), the liquid is transferred in hysteretic curtain mode, and the liquid transfer stops when the curtain breaks. This threshold is equal to about $Re \cong 10$.

A similar hysteresis loop is reported by Gorodilov et al.¹¹⁷: they performed experiments on a structured packing perforated with slits and found that the liquid (water) transfer through the slits starts at $Re \cong 1300$. They attributed this threshold to the liquid meniscus blockage at the slit entrance. Pavlenko et al.¹⁸ found that for liquid nitrogen flowing on an aluminum sheet of 500.Y type packing, the liquid transfer through the perforations starts when $Re \geq 100 - 160$. To reconcile the results of this work with the literature data, the Weber number ($We = \rho Q^2 / (\delta_{Nu}(Q)\sigma)$) is calculated. The Weber number is more relevant since it compares the inertia force (which triggers depinning) to the capillary force. We find $We \cong 5$ from Gorodilov et al. data, and $We = 0.3 - 0.7$ from Pavlenko et al.¹⁸ In this work, $We = 0.27$. The agreement with Pavlenko et al.¹⁸ results is satisfactory. The Weber value calculated from the data of Gorodilov et al.¹¹⁷ is unexpectedly high, and the discrepancies with our results may stem from the sheet structure and type of perforations studied (slits versus circles).

5.1 Transferred volume flow rate per perforation (in the curtain mode)

The transferred volume flow rate through a single isolated perforation (in $m^3 h^{-1}$) reads $q_t = Q_t d$. Beneath a single row of perforations, the volume flow rate per unit width flowing on the back of the plate is given by $Q_b = Q_t d / s$ (in $m^3 m^{-1} h^{-1}$). In the curtain mode, for $0.15 \leq Q \leq 0.5 m^3 m^{-1} h^{-1}$, Q_t is adequately described by a linear model $Q_t = p(Q - Q_{th})$ (see Figure S4.3, **Figure 4-4**, and **Figure 4-6**). The slope (p) and the threshold flow rate (Q_{th}) were obtained by least squares regression. Q_{th} lies in the Q range where curtain ruptures. Q_{th} and p depend a priori on the plate thickness, on the perforation diameter, and the perforation spacing. However, Figure S4.3 and **Figure 4-6** show that, in the limited range $4 \text{ mm} \leq d \leq 8 \text{ mm}$ and $8 \text{ mm} \leq s \leq 14 \text{ mm}$, p and Q_{th} depend slightly on d and s . On the contrary, the dependence of p and Q_{th} on the plate thickness seems significant (see **Figure 4-4**). The effect of plate thickness can be explained by one of the mechanisms responsible for the so-called teapot effect¹¹⁴. At the top edge of a perforation on the front of the sheet (corresponding to the lip of the plate in Kistler & Scriven's analysis³⁸), the liquid flow is deflected from the vertical direction toward the horizontal direction (parallel to the inner surface of the perforation). Since the liquid wets the inner surface of the perforation, this deflection increases with the plate thickness. Liquid transfer from the front to the back of the plate is expected to grow as well. The teapot effect is

maximal at intermediate Reynolds numbers¹¹⁴. Kistler & Scriven found that for $Ka = 7.3$ (resp. 63.5) the hydrodynamic deflection is maximal for $Re = 7$ (resp. 20). The deflection peak shifts to higher values of Re for increasing values of Ka . This may explain why the effect of plate thickness is more significant at $Re = 30 - 45$ (see **Figure 4-4**). We remind that $Ka = 348$ for propan-2-ol used in our experiments. The teapot effect¹¹⁴ is driven by inertia, which may explain why the effect of plate thickness is more significant at higher values of the Reynolds number (see **Figure 4-4**). The teapot effect¹¹⁴ also explains why the overflow number increases with Q (or with the supply Reynolds number Re) at fixed t .

For the standard perforation diameter $d = 4$ mm (used in industrial packing) and the plate thickness $t = 1$ mm, we retain that $Q_t [\text{m}^3 \text{m}^{-1} \text{h}^{-1}] = 0.66(Q - 0.10)$ for a single isolated perforation, $Q_t = 0.48(Q - 0.06)$ for $s = 6$ mm, and $Q_t = 0.60(Q - 0.10)$ for $8 \text{ mm} \leq s \leq 14$ mm (linear fit on the curtain mode data for $s = 8, 10, 12$ and 14 mm, $R^2 = 0.98$, not displayed in **Figure 4-10**).

5.2 Rivulet spreading

A focus is made on a single isolated perforation with $d = 4$ mm and $t = 1$ mm. In the curtain mode, some liquid is systematically transferred through the perforation from the front to the back of the plate. The fluid leaks from the bottom edge of the perforation and forms a single rivulet on the back of the plate. The rivulet flattens and widens as it flows in the x-direction.

The appearance of the rivulet is very similar to Shetty & Cerro¹²⁴ findings but strongly differs from Hoffmann et al.^{128,129} and Xu et al.¹³⁰. In the former case, the wetting is highly favorable ($\theta_E \ll 90^\circ$), the rivulet flow is steady, and the regime is viscous or at the most slightly inertial: the Reynolds number of the rivulet is of the order of $Re \sim 1$ in Shetty & Cerro¹²⁴, $Re \sim 10$ in our experiments (we remind that the transferred volume flow rate per unit diameter of perforation is about half of the supply flow rate per unit width). In the latter case¹²⁸⁻¹³⁰, the static contact angle is significantly higher ($\theta_E \cong 70^\circ - 80^\circ$), the rivulet flow is highly inertial: the Reynolds number is estimated at $Re \sim 1000$. Indeed, as the film flow destabilizes to form a rivulet, its width reduces by an order of magnitude whereas its thickness increases by the same amount. Then, the Reynolds number of the rivulet is an order of magnitude higher than the film Reynolds number at the inlet. These large Re -values explain why meandering is observed in Hoffmann et al.¹²⁸ experiments and not in ours.

Thereafter, we thoroughly analyze the rivulet spatial evolution and compare it to the model of Shetty & Cerro¹²⁴. The derivation of the model and the checking of the assumptions in our experimental conditions are detailed in A8 of the Supplementary Material.

Following Shetty & Cerro¹²⁴, the rivulet spanwise profiles are described by a Gaussian distribution:

$$\delta(x, y) = \delta_c(x) \exp\left(-\left(\frac{(y - y_c(x))^2}{2 m^2(x)}\right)\right) \quad (4.1)$$

where $\delta_c(x)$ is the maximum film thickness, $y_c(x)$ the spanwise location of the peak, and $m(x)$ the standard deviation of the Gaussian, which measures the lateral spreading of the rivulet. These parameters are calculated for each spanwise profile (at given supply Re and given x) using the least-squares method (Table S4-2 in A8 of the Supplementary Material). The relative error is of the order of 1 to 2% for most of the fits, and it never exceeds 5%. We used $y_c(x)$ as a fitting parameter to improve the estimation of $\delta_c(x)$. However, since $y_c(x) \ll d$, the deviation of the peak from $y = 0$ is neglected in the next analytical calculations and the rivulet is assumed symmetric with respect to $y = 0$.

Figure 4-11 shows that the spanwise profiles collapse into a single curve when $\delta(x, y)$ and y are appropriately rescaled. Therefore, the rivulet spanwise profiles are self-similar and well described by a Gaussian distribution. These results concord with the findings of Shetty and Cerro¹²⁴. We checked that the Gaussian law is a better approximation of the present rivulet profiles than the quartic similarity solution obtained by Duffy and Moffatt¹²⁶.

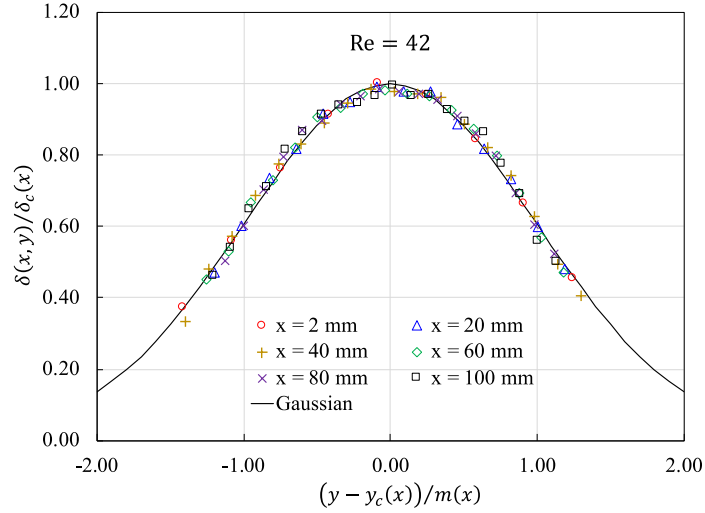


Figure 4-11: Collapse of the rivulet spanwise profiles with appropriate rescaling. Supply Reynolds number $Re = 42$ (inertial curtain mode). Data are well described by the Gaussian law (solid line).

Assuming a Nusselt velocity profile within the rivulet thickness, the volume flow rate of the rivulet is given by

$$q_t = \frac{g}{3\nu} \sqrt{\frac{2\pi}{3}} \delta_c^3(x) m(x) \quad (4.2)$$

If this model is appropriate, the right-hand side of Eq. 4.2 calculated from the fitted Gaussian profile at the current abscissa x should be independent on x . We find that this quantity remains constant within a few percent along x for $x \geq x_0$ (see Figure S4.11 in Supplementary Material). $x_0 = 20$ mm for $Re = 24, 29, 33$ and $x_0 = 2$ mm for $Re = 38, 42$.

The rivulet thickness can be described by the thin-film equation¹²⁶

$$\delta \frac{\partial^4 \delta}{\partial y^4} + 3 \frac{\partial \delta}{\partial y} \frac{\partial^3 \delta}{\partial y^3} + 3 \frac{\rho g}{\sigma} \frac{\partial \delta}{\partial x} = 0 \quad (4.3)$$

given for a steady rivulet flowing down a vertical plate.

Restricting the analysis to $y = 0$, where the rivulet peaks, and assuming a Gaussian spanwise profile centered at $y = 0$ (Eq. 4.1 with $y_c(x) = 0$), Eq. 4.3 becomes:

$$\frac{d\delta_c}{dx} + \frac{\sigma}{\rho g} \frac{\delta_c^2}{m^4} = 0 \quad (4.4)$$

Introducing the rescaled quantities:

$$x^\# = \frac{x - x_0}{2m(x_0)} \quad ; \quad \delta_c^\#(x) = \frac{\delta_c(x)}{\delta_c(x_0)} \quad ; \quad m^\#(x) = \frac{m(x)}{m(x_0)}$$

Using Eq. 4.1, 4.2 and 4.4, the scaling laws first established by Shetty & Cerro¹²⁴ are obtained:

$$\delta_c^\#(x^\#) = \left(1 + \frac{208 \alpha^3}{3 \text{Ca}} x^\#\right)^{-1/13} \quad (4.5)$$

$$m^\#(x) = \left(1 + \frac{208 \alpha^3}{3 \text{Ca}} x^\#\right)^{3/13} \quad (4.6)$$

where α and Ca are the aspect ratio and capillary number of the rivulet at $x = x_0$, respectively:

$$\alpha = \frac{\delta_c(x_0)}{2m(x_0)} \quad ; \quad \text{Ca} = \frac{\mu}{\sigma} \left(\frac{g \delta_c^2(x_0)}{3\nu} \right)$$

The derivation of Eq. 4.5 and 4.6 involves the quantity $c_1 = 2(\delta_c^3(x)m(x))^2$ (see A8 in the Supplementary Material). Since this quantity is not strictly conserved experimentally (even for $x > x_0$) and slightly fluctuates along x , it is relevant to distinguish between the “best” estimate of $2(\delta_c^3(x)m(x))^2$ over the region $x > x_0$ (taken as its mean value) and denoted \bar{c}_1 , and the value of $2(\delta_c^3(x)m(x))^2$ at $x = x_0$, i.e., $c_0 = 2(\delta_c^3(x_0)m(x_0))^2$. The former appears when removing m from Eq. 4.4 using Eq. 4.2. The latter appears when rescaling. Then, the argument of the power-laws (Eq. 4.5-4.6) should be transformed as follows:

$$\left(1 + \frac{208 \alpha^3}{3 \text{Ca}} x^\#\right) \rightarrow \left(1 + \frac{208 \alpha^3}{3 \text{Ca}} \beta x^\#\right) \quad (4.7)$$

with $\beta = \left(\frac{c_0}{\bar{c}_1}\right)^2$. We recast the data of Table 2 (Supplementary Material) for $x > x_0$ into $\left(1 + \frac{208 \alpha^3}{3 \text{Ca}} \beta x^\#\right)$, $\delta_c^\#$, and $m^\#$. We plot them on log-log scale in **Figure 4-12**. It can be seen that the thickness (resp. width) data collapse into a single line with a slope equal to -0.075 (resp. 0.25), very close to the theoretical slope $-1/13 \cong -0.077$ (resp. $3/13 \cong 0.23$) originally established by Shetty & Cerro¹²⁴ and Duffy & Moffatt¹²⁶. We retain that, far downstream of the perforation, the rivulet peak-thickness (resp. width) decreases as $x^{-0.075}$ (resp. $x^{0.25}$), very close to $x^{-1/13}$ (resp. $x^{3/13}$).

The theoretical exponents 1/13 and 3/13 characterize the rivulet spreading when driven by the capillary pressure (as opposed to hydrostatic pressure). This is indeed the case for the rivulet falling down a vertical plate.

These small exponents (in absolute value) explain why the rivulet pattern may persist over the whole height of a corrugated sheet packing⁴².

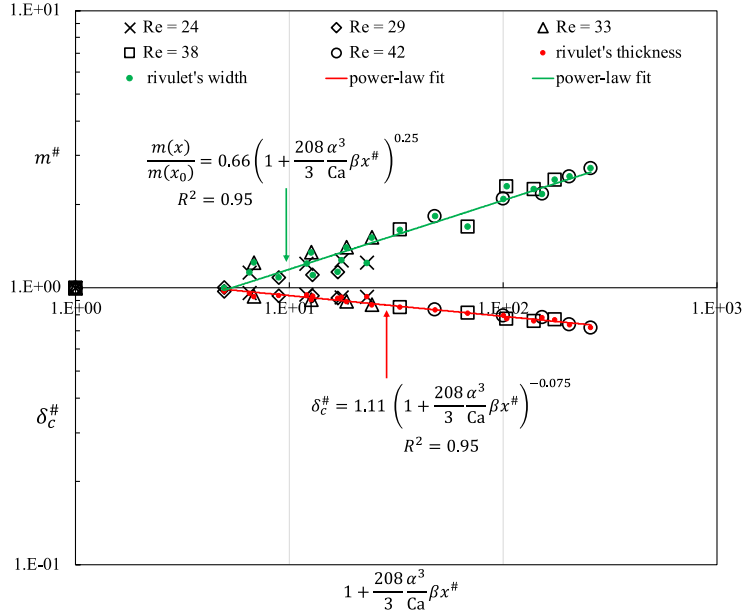


Figure 4-12: Rescaled peak film thickness and width as a function of the rescaled streamwise coordinate. Data (except the point (1;1)) are fitted with a power-law using the least-squares method.

5.3 Rivulet merging and film leveling

Figure 4-7, S4.7, and S4.8 show the merging dynamics of adjacent rivulets for $d = 4$ mm, $t = 1$ mm, $Re = 38$ and $s = 6, 8, 10, 12, 14$ mm. The merging is considered to start close to the first measuring point (point with the smallest x -value at fixed s) on the centerline between two perforations ($y = s/2$). Thus, as the perforation spacing increases, the merging of the rivulets occurs further downstream. When the spacing increases from 10 mm to 12 mm, i.e., by 20%, the distance between the onset of merging and the row of perforations doubles.

The results established for a single rivulet help explain the strong effect of s on the rivulet merging. If the rivulet half-width at a distance x from the perforation is approximately equal to $2m(x)$, two adjacent rivulets start to merge when $4m(x) \approx s$. Therefore, the rescaled distance $x_{mer}^{\#}$ between the onset of merging and the row of perforations satisfies:

$$1 + \frac{208 \alpha^3}{3 \text{Ca}} x_{mer}^{\#} \cong \left(\frac{s}{4m(x_0)} \right)^{13/3} \quad (4.8)$$

The prominent exponent (13/3) explains the strong effect of s on the onset of merging. As seen earlier, it is relevant to introduce the correction factor β :

$$1 + \frac{208 \alpha^3}{3 \text{Ca}} \beta x_{mer}^{\#} \cong \left(\frac{s}{4m(x_0)} \right)^{13/3} \quad (4.9)$$

The left-hand side of Eq. 4.9 is estimated for $Re = 38$ and $s = 6, 8, 10, 12, 14$ mm from the data of **Figure 4-7**, S4.7, and S4.8. Figure S4.12 (Supplementary material) presents the variations of $1 + \frac{208}{3} \frac{\alpha^3}{Ca} \beta x_{mer}^\#$ as a function of $s/(4m(x_0))$. The data points are fitted by a power law using the least-squares method. The exponent (4.58) is close to the theoretical value ($13/3 = 4.33$). The prefactor (4.73) is significantly greater than the expected value (1). We presently overestimate $x_{mer}^\#$ because the first measuring point (corresponding to a film thickness close to 100 μm) used to estimate the onset of merging is systematically located downstream of the actual position where the rivulets start to merge (corresponding to a vanishing film thickness).

It is of interest now to examine how the surface of the film formed from the recently merged rivulets relaxes downstream to a flat free surface. As seen earlier, the local film thickness $\delta(x, y)$ satisfies the thin-film equation, i.e., Eq. 4.3. **Figure 4-8** suggests describing the film surface as a sine wave. We thus seek a solution of the form:

$$\delta(x, y) = \delta_\infty \left(1 + \varepsilon(x) \cos\left(\frac{2\pi y}{s}\right) \right) \quad (4.10)$$

where δ_∞ is the flat-film thickness (reached far downstream of the perforation row) and ε the dimensionless perturbation amplitude of the film thickness. We consider $\varepsilon(x) \ll 1$.

Replacing Eq. 4.10 into Eq. 4.3, a first-order approximation leads to:

$$\varepsilon(x) = \frac{\delta(x_{mer}, 0) - \delta_\infty}{\delta_\infty} \exp\left(-\left(\frac{x - x_{mer}}{\mathcal{L}}\right)\right) \quad (4.11)$$

where x_{mer} corresponds to the streamwise location where the rivulets start to merge. The film surface relaxes exponentially with streamwise coordinate. The characteristic length of the relaxation to a flat surface is given by:

$$\mathcal{L} = \frac{3s^4}{(2\pi)^4 l_c^2 \delta_\infty} \quad (4.12)$$

where $l_c = \sqrt{\sigma/\rho g}$ is the capillary length. Recasting the data of **Figure 4-7**, S4.7, and S4.8 into $(x - x_{mer})/\mathcal{L}$ and $(\delta(x, 0) - \delta(x, s/2))/(\delta(x_{mer}, 0) - \delta(x_{mer}, s/2))$, the plot in **Figure 4-13** can be drawn. The flat-film thickness (δ_∞) is presently estimated as the mean value of $(\delta(x, 0) + \delta(x, s/2))/2$ over x . \mathcal{L} ranges from 3.3 mm for $s = 6$ mm to 121 mm for $s = 14$ mm. Interestingly, all the data collapse into a single exponential curve. The characteristic length of the exponential decay is equal to $\mathcal{L}/1.36$, in good agreement with the theoretical prediction.

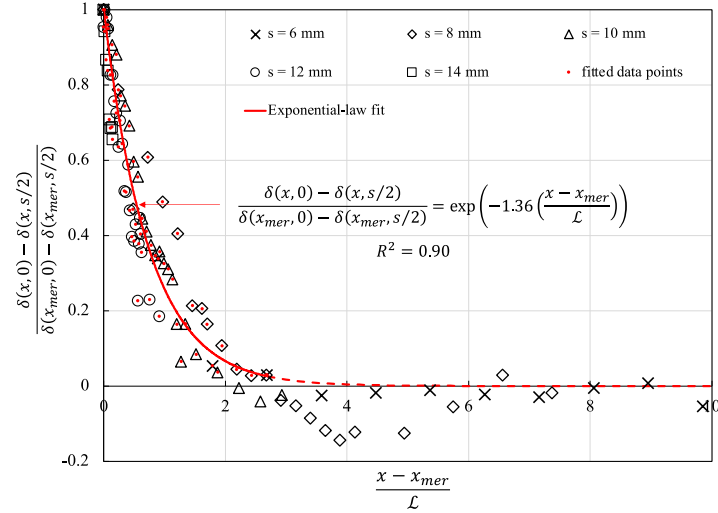


Figure 4-13: Rescaled perturbation amplitude of the liquid film flowing on the back of the plate as a function of the rescaled streamwise coordinate. Single row of perforations, perforation diameter $d = 4$ mm, plate thickness $t = 1$ mm, and Reynolds number $Re = 38$ (curtain mode). The data points with red dots are fitted with an exponential law using the least-squares method (red solid line extended with dashes).

The flat-film thickness (δ_∞) depends on the volume flow rate per unit width flowing on the back of the plate (Q_b) via $\delta_{Nu}(Q_b) = (3\nu Q_b/g)^{1/3}$. Since $Q_b = Q_t d/s$, it follows from Eq. 4.12 that at a given supply flow rate on the front of the plate, the characteristic length of the film relaxation (on the back of the plate) scales as $s^{13/3}$.

5.4 Flow balancing between the front and the back of the plate

The variations of the volume flow rate per unit width on the back of the plate in a staggered array of perforations can be described by a recurrence model. This model relates the volume flow rate on the back of the plate just downstream the k^{th} row of perforations ($Q_b(k)$) to the flow rates just downstream of the $(k - 1)^{th}$ row on the front of the plate ($Q(k - 1)$) and on the back ($Q_b(k - 1)$). The variations of $Q(k - 1)$ and $Q_b(k - 1)$ over the width are not taken into account since these quantities are volume flow rates per unit width averaged over the width. All the perforations of the plate are supposed to operate in the curtain mode.

For $d = 4$ mm, $t = 1$ mm, and $s = 14$ mm, the transferred volume flow rate per unit diameter of perforation through the first row of perforations is well described by:

$$Q_t(k = 1)[\text{m}^3 \text{ m}^{-1} \text{ h}^{-1}] = 0.6(Q(0) - 0.1)$$

where $Q(0) = Q$ is the supply flow rate per unit width on the front of the plate.

To establish an analogous relationship for the next rows ($k > 1$), we first estimate the curtain flow over a perforation as $d_p(Q(k-1) + Q_b(k-1))$ and consider that this flow divides equally between the front and the back of the plate. Then, the transferred volume flow rate per unit diameter of perforation through the k^{th} row of perforations expresses as:

$$Q_t(k) = (Q(k-1) - Q_b(k-1))/2$$

$Q_t(k)$ is counted positively from the front to the back. This transferred flow is assumed to be distributed evenly over the width w_a , so that the volume flow rate per unit width on the back of the plate beneath the k^{th} row of perforations is given by:

$$Q_b(k) = Q_b(k-1) + \frac{d}{s} Q_t(k)$$

And the volume flow rate per unit width on the front of the plate beneath the k^{th} row of perforations:

$$Q(k) = Q(k-1) - \frac{d}{s} Q_t(k)$$

In this formulation, it is supposed that the number of perforations per row is large ($N - 1 \cong N$) and the border effects are neglected.

The model is computed for $k = 1$ to $k = 10$, and the results are reported in **Figure 4-10** and Figure S4.13 (Supplementary Material). $Q_b(k)$ flowing on the back of the plate beneath the k^{th} row of perforations varies linearly with the supply flow rate $Q(0)$ (see the colored straight lines of **Figure 4-10**). Remarkably, the model adequately describes the variations of the volume flow rate per unit width on the back of the plate when the supply volume flow rate $Q(0)$ is low. For high values of $Q(0)$, the model underestimates the liquid transfer. An explanation for this could reside in the fact that flow inertia pushes the liquid curtain to the back of the plate (teapot effect¹¹⁴), which affects the partition of the curtain flow between the front and the back: the liquid transfer from the front to the back is then enhanced.

Figure S4.13 shows that the volume flow rates on the front and the back of the plate tend to equalize as the row number (k) increases: the asymptotic limit of $Q_b(k)$ when k tends to infinity is $Q(0)/2$. The transferred volume flow rate decreases with k since the driving force ($Q(k-1) - Q_b(k-1)$) decreases. Q_b reaches 90% of its asymptotic value ($Q(0)/2$) beneath the 7th row of perforations.

6. Conclusion

To better understand the effect of the perforations on the liquid redistribution in corrugated sheet packings, a simplified but relevant configuration was studied in this work. The liquid transfer from the front to the back of a vertical flat perforated sheet was experimentally assessed: the front of the plate was supplied with liquid (above the first perforation row), and we examined how the perforations irrigate the back of the plate. Above a certain Reynolds number of the order of 30, all perforations operate in curtain mode (where a liquid curtain closes each perforation), and our analysis focuses on this regime. On the bottom edge of the perforations, the curtain flow divides between the plate's front and back. The transferred liquid leaks in the form of rivulets (one per perforation). The transferred volume flow rate through the perforations was measured and the spreading and merging of the rivulets on the back of the plate were characterized. We successively investigated plates with a single perforation, a spanwise row of perforations, and a staggered array of perforations.

Regarding the single perforation and spanwise row of perforations: the transferred volume flow rate per unit diameter of perforation (Q_t) was found to vary linearly with the supply flow rate per unit width (Q). For the standard perforation diameter $d = 4$ mm, the plate thickness $t = 1$ mm, the perforation spacing (centre-to-centre) lying in the range $8 \text{ mm} \leq s \leq 14 \text{ mm}$, and the supply flow rate per unit width in the interval $0.15 \text{ m}^3 \text{ m}^{-1} \text{ h}^{-1} < Q < 0.4 \text{ m}^3 \text{ m}^{-1} \text{ h}^{-1}$, Q_t is well described by $Q_t [\text{m}^3 \text{ m}^{-1} \text{ h}^{-1}] = 0.60(Q - 0.10)$.

The rivulet leaking from a perforation widens (resp. flattens) as the 0.25 (resp. -0.075) power of the traveled distance from the perforation (after appropriate rescaling). Adjacent rivulets merge into a continuous wavy film at a traveled distance which scales as the 4.58 power of the perforation spacing. The scaling exponents are very close to the theoretical exponents established by Shetty & Cerro¹²⁴ and Duffy & Moffatt¹²⁶ for a rivulet spreading in the capillary-dominant regime.

The wavy surface of the newly formed film relaxes downstream to a flat surface. The amplitude of crests and troughs at the film surface decay exponentially with the streamwise coordinate. The characteristic length of this relaxation theoretically scales as the 13/3 power of the perforation spacing.

Regarding the staggered array of perforations, from one row of perforations to another, the volume flow rate per unit width (and averaged over the width) flowing on the back (resp. front) of the plate increases (decreases) and relaxes toward its asymptotic value. This value is equal to half the supply flow rate. Beneath the third row of perforations, the flow rate on the back of the plate already reaches 65% to 90% of its asymptotic value. The relaxation is more rapid as

the supply flow rate increases: the teapot effect¹¹⁴ (driven by the flow inertia) could explain this enhancement of the liquid transfer from the front to the back of the plate.

Finally, we propose a simple recurrence model that gives the volume flow rate per unit width on the back of the plate beneath each row of perforations. This model adequately represents the data obtained at low supply flow rate. It predicts that the flow rate on the back of the plate reaches 90% of its asymptotic value beneath the 7th row of perforations.

The present work provides helpful insight into the elementary mechanisms involved in the liquid redistribution through perforations in a flat plate. Future work includes extending this study to vertical perforated sheets with horizontal corrugations as a next step to understand the interplay between perforations and corrugations in corrugated distillation packings.

Acknowledgments

This research was supported by Air Liquide Research & Development and by Association Nationale de la Recherche et de la Technologie ANRT (CONVENTION CIFRE N° 2017/1472). The authors express their gratitude to Sebastien Gauthier and Frederic Lesage for their technical contribution to the project.

7. Supplementary Material

A1. Rim mode and curtain mode: typical flow patterns

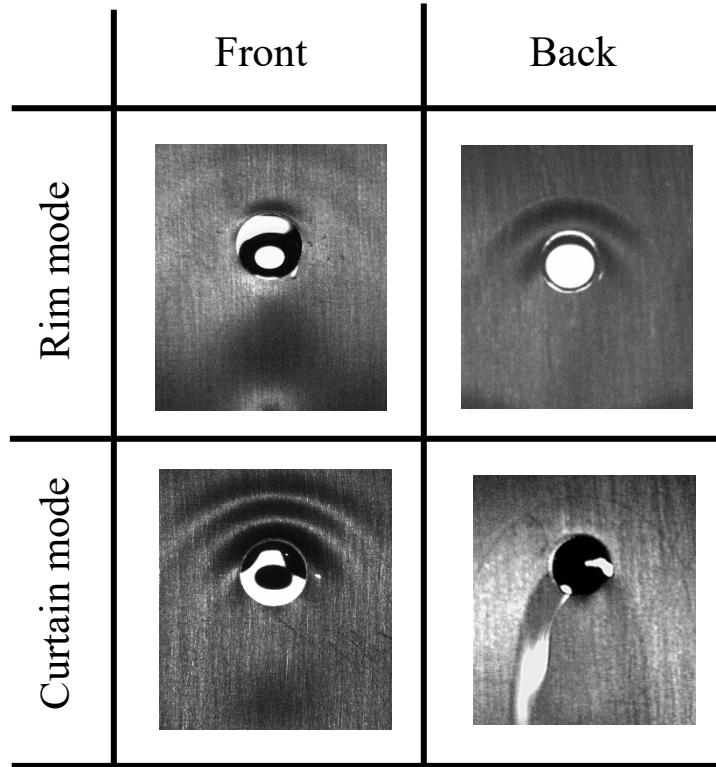


Figure S4.1. Flow patterns on the front and back of the plate in the rim mode and curtain mode.

The top of Figure S4.1 presents the typical flow pattern encountered in the rim mode: a liquid rim forms within the perforation and covers its inner surface. On the front of the plate, the perforation is topped by a capillary ridge. On the back, the liquid climbs over the top edge of the perforation and makes a capillary ridge that extends in the form of two parallel rivulets.

In the curtain regime (bottom of Figure S4.1), the liquid fills the perforation. On the front of the plate, the perforation is topped by a train of capillary ridges. On the back of the plate, the liquid leaks from the bottom edge of the perforation in the form of a single rivulet.

A2. Liquid properties

Liquid	ρ (kg m ⁻³)	μ (mPa s)	σ (mN m ⁻¹)	θ (°)	Ka	Re range
Propan-2-ol	786 ^a	2.05 ^b	21 ^c	11 ^o -17 ^{oa}	348	10 - 45

^ameasured, ^bfrom[†], ^cfrom[‡].

Table S4-1. Physical properties of propan-2-ol at 25°C and range of Reynolds number investigated. The bounds of the contact angle (θ) interval correspond to the receding contact angle and to the advancing contact angle, respectively. The equilibrium contact angle (θ_E) lies in-between.

Table 1 reports the physical properties of the working fluid, i.e. propan-2-ol. We stress that the wetting of the aluminum sheets with propan-2-ol is highly favorable: the contact angle lies between 11° and 17°. We introduce the Kapitza number of the liquid, it compares surface tension to the viscous and gravitational effects, i.e., $Ka = \sigma / (\rho g^{1/3} \nu^{4/3})$. Re is the film Reynolds number, defined in the Problem description (see the main document).

[†]Paez S, Contreras M. Densities and Viscosities of Binary Mixtures of 1-Propanol and 2 Propanol with Acetonitrile. J Chem Eng Data. 1989;34(4):455-459.

[‡]Vazquez G, Alvarez E, Navaza JM. Surface Tension of Alcohol + Water from 20 to 50 °C. J Chem Eng Data. 1995;40(3):611-614.

A3. Liquid transfer from a single perforation

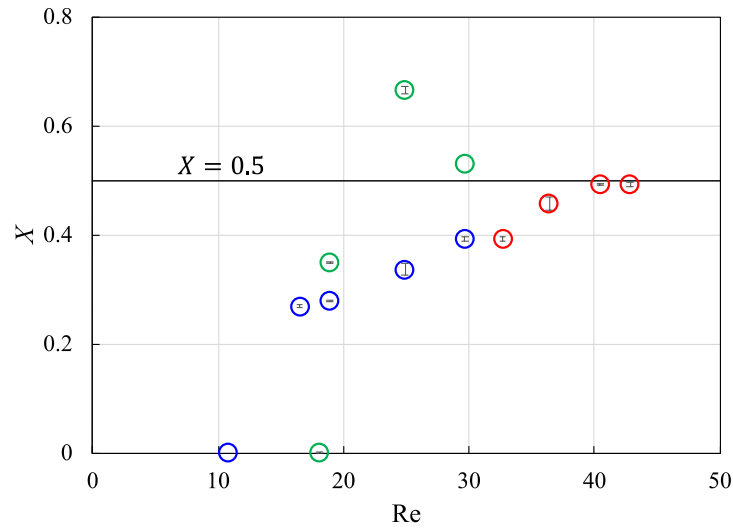


Figure S4.2. Overflow number (X) as a function of the supply Reynolds number (Re). Single isolated perforation. The diameter is $d = 4$ mm, the plate thickness $t = 1$ mm. Rim mode (green), inertial curtain (red), hysteretic curtain (blue).

Following Gorodilov et al.¹¹⁷, we plot (Figure S4.2) the variations of the overflow number (X) as a function of the supply Reynolds number (Re). We observe that the variations of X in the rim mode are non-monotonous: X first increases steeply with Re and then decreases as Re tends to Re_{cr} . X reaches its peak value ($X = 0.67$) for $Re = 25$. At Re_{cr} , the transition from the rim to the (inertial) curtain mode occurs. As Re is further increased beyond Re_{cr} , X grows. Ultimately, X seems to reach a plateau $X = 0.5$ corresponding to an equal partition of Q between the front and the back of the perforation. As Re is swept down from Re_{cr} , the film flow remains in the curtain mode, and X regularly reduces with the decrease in Re .

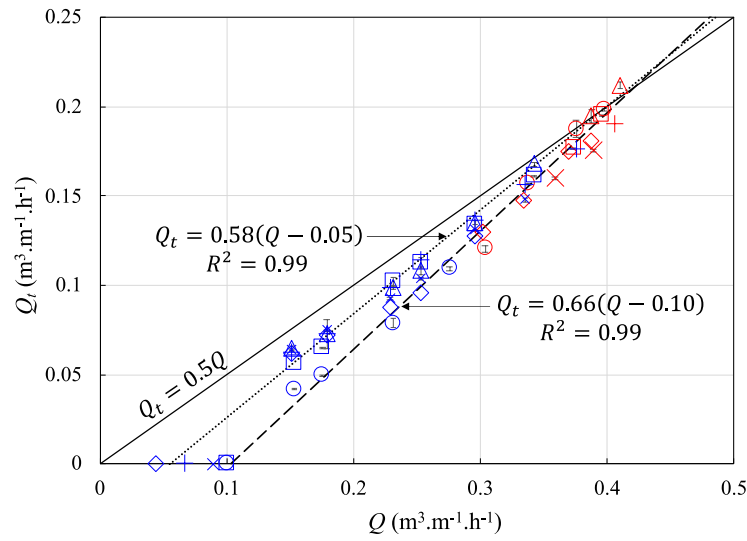


Figure S4.3. Transferred volume flow rate per unit diameter of perforation (Q_t) as a function of the supply flow rate (on the front of plate) per unit width (Q): effect of the perforation diameter. Single perforation with $d = 4$ mm (\circ), 6 mm (\square), 8 mm (\triangle), 10 mm (\diamond), 14 mm (\times), 16 mm ($+$), plate thickness $t = 1$ mm. Curtain mode (hysteric in blue, inertial in red). Linear fit for $d = 4$ mm (broken line), for $d = 8$ mm (dotted line).

We focus on the curtain mode (either inertial or hysteric) and measure the transferred volume flow rate as a function of the supply flow rate on the front of the plate, for six values of perforation diameter, i.e., $d = 4, 6, 8, 10, 14, 16$ mm. The plate thickness is $t = 1$ mm. Regardless of the value of d , the variations of Q_t with Q follow the same increasing trend (Figure S4.3). The liquid curtain ruptures and the liquid transfer ceases in the range $Q = 0.04$ to $0.1 \text{ m}^3 \text{ m}^{-1} \text{ h}^{-1}$ ($Re = 5$ to 11). At lower Q values (larger than $0.1 \text{ m}^3 \text{ m}^{-1} \text{ h}^{-1}$), the transferred flow rate Q_t is significantly lower (up to 30%) for $d = 4$ mm than for the other (larger) perforation diameters. The effect of d on Q_t decreases as Q increases. For the higher values of Q , the overflow number is close to $X = 0.5$ regardless of d .

A4. Rivulet from a single perforation: spanwise and streamwise profiles

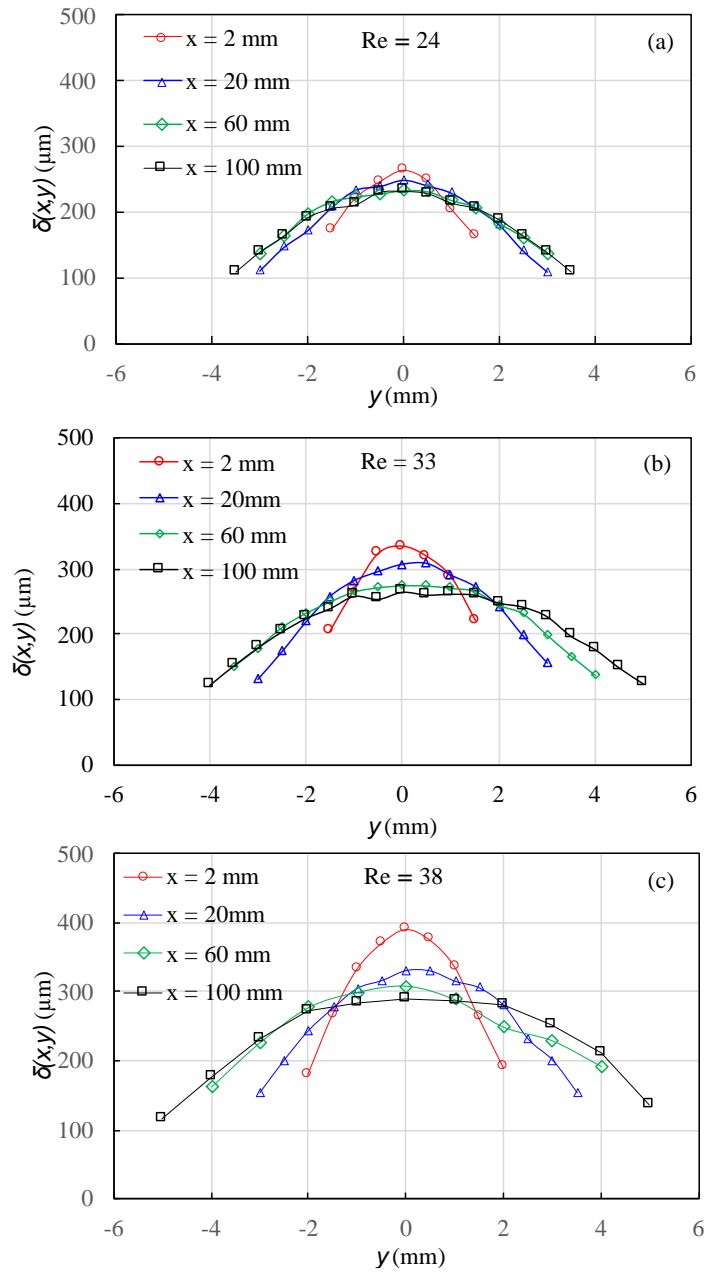


Figure S4.4. Spanwise rivulet profile at $x = 2, 20, 60, 100$ mm from the bottom edge of the perforation. Plate thickness $t = 1$ mm, perforation diameter $d = 4$ mm. Curtain mode. (a) $Re = 24$; (b) $Re = 33 = Re_{cr}$; (c) $Re = 38$. The lines linking the dots are intended to guide the eye along the data points.

Figure S4.4 completes the **Figure 4-5** displayed in the main document and presents the rivulet spanwise profiles for supply Reynolds number $Re = 24, 33, 38$. We observe that the rivulet widens and flattens as it flows in the x -direction. The spanwise profile is approximately

symmetric about the axis $y = 0$ and the thickness reaches its peak value close to the line $y = 0$.

Figure S4.5 presents the streamwise rivulet profile along the line $y = 0$ for different values of the supply Reynolds number. The rivulet flattens as it flows down the plate. At given streamwise position, the rivulet thickness increases with the supply Reynolds number. Streamwise profiles are slightly rough because the rivulet is not perfectly straight, the flow out of the perforation is not rigorously constant, and waves may travel on the rivulet surface.

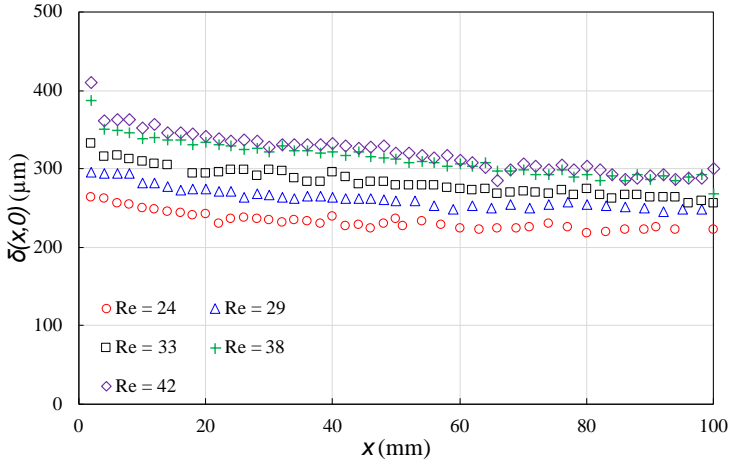


Figure S4.5. Streamwise rivulet profile along $y = 0$ for different values of the supply Reynolds number, $Re = 24, 29, 34, 38, 42$. Plate thickness $t = 1$ mm, perforation diameter $d = 4$ mm. Curtain mode.

A5. Effect of the perforation spacing on the curtain Reynolds number

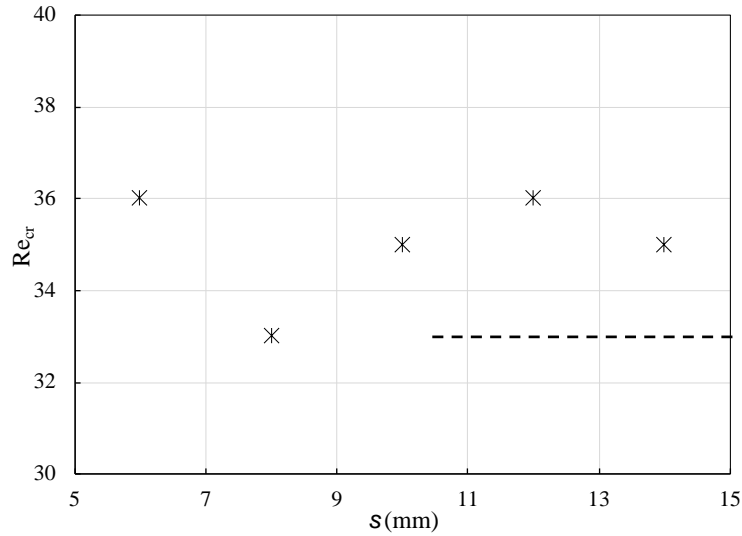


Figure S4.6. Curtain Reynolds number determined for different values of the perforation spacing, $s = 6, 8, 10, 12, 14$ mm. Perforation diameter $d = 4$ mm and plate thickness $t = 1$ mm. The broken line corresponds to the curtain Reynolds number for a single isolated perforation ($s = \infty$).

Figure S4.6 summarizes the curtain Reynolds number (Re_{cr}) values determined for different perforation spacings. It appears that Re_{cr} ranges between 33 and 36. These slight variations seem not correlated with the perforation spacing. Otherwise, Re_{cr} would increase with s : the broader the spacing, the more the flow can be deflected by a perforation, delaying the curtain transition. We instead believe that the variations in Re_{cr} are due to the variability of the plate curvature. A slight curvature of the sheet affects the liquid distribution upstream of the perforations and then the curtain transition. The residual curvature of the plate depends on its clamping within the frame.

A6. Merging of the rivulets flowing from a row of perforations: streamwise profiles

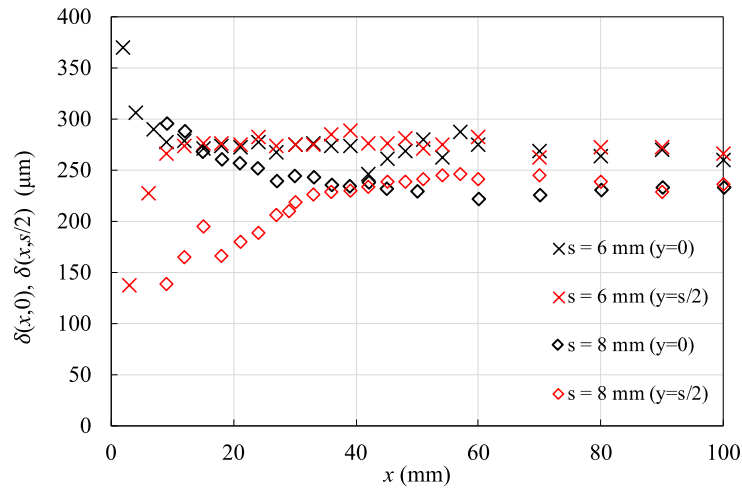


Figure S4.7. Streamwise film profile along $y = 0$ and $y = s/2$ for spacing $s = 6$ mm and 8 mm. Single row of perforations, Perforation diameter $d = 4$ mm, plate thickness $t = 1$ mm, and Reynolds number $Re = 38$ (curtain mode).

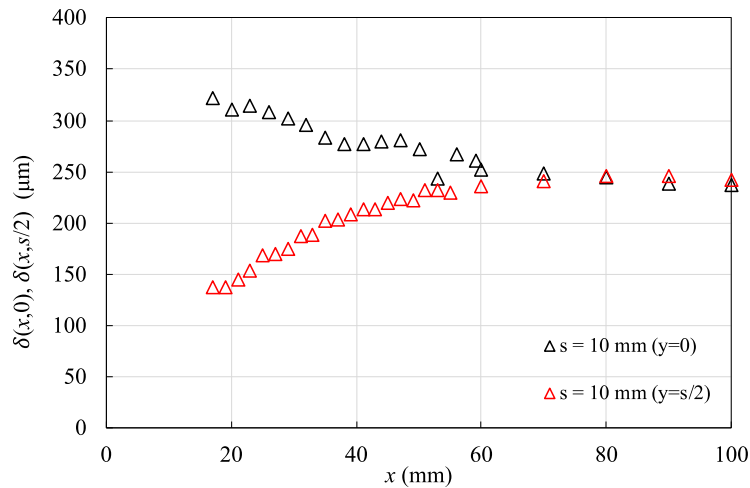


Figure S4.8. Streamwise film profile along $y = 0$ and $y = s/2$ for spacing $s = 10$ mm. Single row of perforations, Perforation diameter $d = 4$ mm, plate thickness $t = 1$ mm, and Reynolds number $Re = 38$ (curtain mode).

Figures S4.7 and S4.8 complete **Figure 4-8** displayed in the main document and present the streamwise film profile along $y = 0$ and $y = s/2$ for $s = 6, 8, 10$ mm. $y = 0$ (resp. $y = s/2$) coincides with a crest (resp. a trough) of the free surface. Since the minimum measurable thickness of the CCI sensor is about $100 \mu\text{m}$, we cannot capture the beginning of the merging between two adjacent rivulets. Thus, at given spacing, merging starts at a distance slightly lower than the abscissa of the first measuring point along $y = s/2$. We observe that the film thickness

along $y = 0$ (resp. $y = s/2$) decreases (resp. increases) with x and reaches a plateau. The smaller the spacing, the faster the plateau is reached and the higher is the plateau value.

A7. Liquid film pattern on a staggered array of perforations

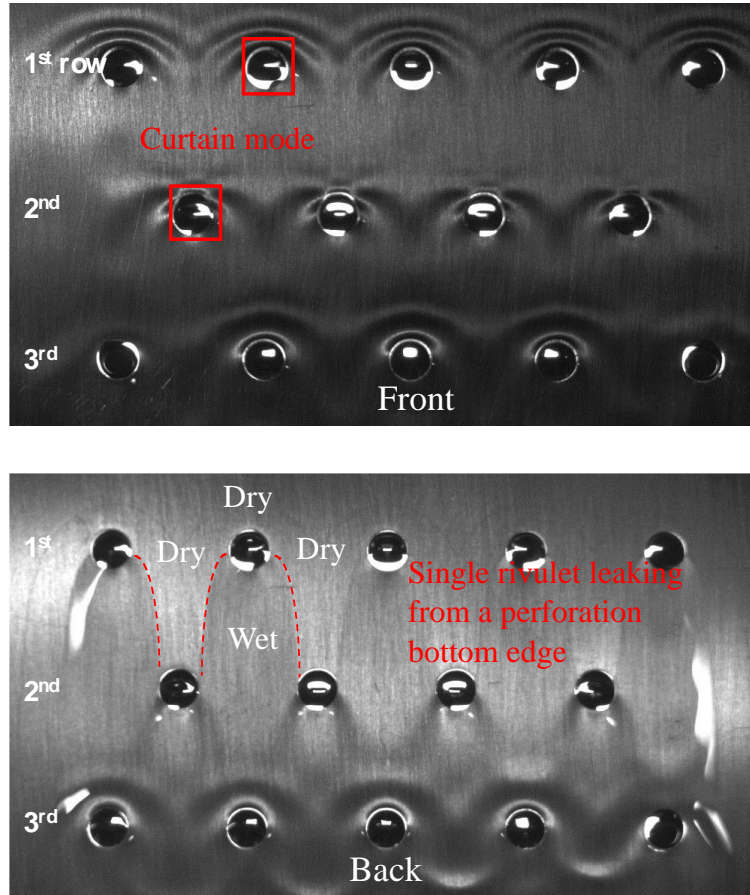


Figure S4.9. Liquid film pattern on a staggered array of perforations at $Re = 35 \cong Re_{cr}$ when all perforations are in curtain mode. Plate thickness $t = 1$ mm, perforation diameter $d = 4$ mm and spacing $s = 14$ mm. (Top) Front of the plate (bottom) back of the plate.

Figure S4.9 and S4.10 show the flow pattern on a staggered array of perforation at Re_{cr} and above. In that case, all the perforations (odd and even rows) operate in the curtain mode. The liquid leaks from the bottom edge of the perforations on the back of the plate. The corresponding rivulets widen as they flow in the x -direction. The liquid free surface is disturbed by waves traveling downstream. This phenomenon is clearly seen beneath the third row of perforations (Figure S4.10).



Figure S4.10. Liquid film pattern on a staggered array of perforations at $Re = 35 \cong Re_{cr}$ when all perforations are in curtain mode. Plate thickness $t = 1$ mm, perforation diameter $d = 4$ mm and spacing $s = 14$ mm. Full view of the back of the plate.

A8. Derivation of the rivulet model and assessment of the assumptions

Following Shetty & Cerro¹²⁴, we fit the rivulet spanwise profiles with a Gaussian law:

$$\delta(x, y) = \delta_c(x) \exp\left(-\left(\frac{(y - y_c(x))^2}{2 m^2(x)}\right)\right) \quad (A1)$$

$\delta_c(x)$ is the maximum film thickness, $y_c(x)$ the spanwise location of the peak, and $m(x)$ the standard deviation of the Gaussian, which measures the lateral spreading of the rivulet. We determine these parameters for each spanwise profile (at given supply Reynolds number Re and given x) using the least-squares method. The parameter values of the best fits are reported in Table S2. The relative error is of the order of 1 to 2% for most of the fits, and it never exceeds 5%. We use $y_c(x)$ as a fitting parameter to improve the estimation of $\delta_c(x)$. However, since $y_c(x) \ll d$, we neglect the deviation of the peak from $y = 0$ in the further analysis.

Figure 4-11 shows that the spanwise profiles collapse into a single curve when $\delta(x, y)$ and y are appropriately rescaled. We deduce that the rivulet spanwise profiles are self-similar and well described by a Gaussian law. These results concord with the findings of Shetty and Cerro¹²⁴, who studied a rivulet draining down a vertical prewetted plate. We checked that the Gaussian law is a better approximation of the present rivulet profiles than the quartic similarity solution obtained by Duffy and Moffatt²⁷.

However, we remind that we could not measure the rivulet thickness close to the lateral contact line. Thus, the Gaussian law has only been validated against the core of the rivulet profile. We suppose hereafter that the Gaussian law holds over the whole rivulet spanwise profile. We will come back to this hypothesis later.

Q (L h ⁻¹)	Re	$x =$	2 mm	20 mm	40 mm	60 mm	80 mm	100 mm
20	24	δ_c (μm)	261	251	240	237	232	233
		y_c (mm)	-0.062	-0.004	0.119	-0.072	0.273	-0.005
		m (mm)	1.60	2.38	2.71	2.91	2.99	2.94
		Err (%)	1.5	1.7	1.4	2.0	2.1	2.1
24	29	δ_c (μm)	293	279	271	262	261	256
		y_c (mm)	-0.093	0.062	-0.057	0.249	0.121	0.219
		m (mm)	2.06	2.89	2.89	3.15	3.21	3.29
		Err (%)	2.0	1.9	2.1	1.4	3.9	2.2
28	33	δ_c (μm)	336	310	289	280	277	269
		y_c (mm)	0.061	0.152	0.405	0.160	0.245	0.479
		m (mm)	1.58	2.49	3.06	3.34	3.47	3.78
		Err (%)	1.4	1.9	2.6	2.3	3.1	2.9
32	38	δ_c (μm)	395	336	320	305	299	303
		y_c (mm)	0.014	0.233	-0.225	0.020	0.354	0.257
		m (mm)	1.66	2.68	2.75	3.84	3.76	4.06
		Err (%)	1.7	2.1	1.4	4.1	4.2	4.9
35	42	δ_c (μm)	416	347	330	325	306	299
		y_c (mm)	0.122	0.248	-0.101	0.114	0.264	-0.106
		m (mm)	1.50	2.73	3.15	3.29	3.79	4.07
		Err (%)	0.5	1.8	2.8	2.2	2.1	3.0

Table S4-2. Parameters of the Gaussian function that best fits the rivulet spanwise profile: δ_c , y_c and m as a function of the supply Reynolds number (Re) and streamwise location x , relative error (Err, L2-norm) between the experimental profile and the fitting curve.

To go further, we also assume that the velocity component in the x-direction is semi-parabolic (Nusselt profile):

$$u(x, y) = \frac{g}{2\nu} (2 \delta(x, y) z - z^2) \quad (A2)$$

This assumption is reasonable if the rivulet is thin, its flow laminar, steady, and locally fully developed: data of Table S2 show that the rivulet thickness is at least one order of magnitude lower than its width, i.e., $\delta_c(x)/2m(x) \lesssim 0.1$. The upper bound of the rivulet Reynolds number Re_{rv} at the abscissa x equals $Re_{rv} = \frac{1}{3}(\delta_c(x)/l_v)^3$ where $l_v = \nu^{2/3}/g^{1/3}$ is the visco-gravitational length. In the present dataset, the rivulet Reynolds number is systematically lower than $Re_{rv} = 35$, the value reached at $x = 2$ mm for the supply Reynolds number $Re = 42$. We expect that the flow is locally fully developed a few millimeters downstream of the perforation (see A9).

Then, the volume flow rate is given approximately by

$$q_t = \frac{g}{3\nu} \int_{-\infty}^{+\infty} \delta^3 dy \quad (A3)$$

or

$$q_t = \frac{g}{3\nu} \sqrt{\frac{2\pi}{3}} \delta_c^3(x) m(x) \quad (A4)$$

If this model is appropriate, the right-hand side of Eq. A4 calculated from the rivulet profile at the current abscissa x should be constant, i.e., independent on x . This quantity remains constant within a few percent along x , except close to the perforation (see Figure S4.11): the right-hand side of Eq. A4 estimated at $x = 2$ mm is up to 25% lower than the value calculated further downstream.

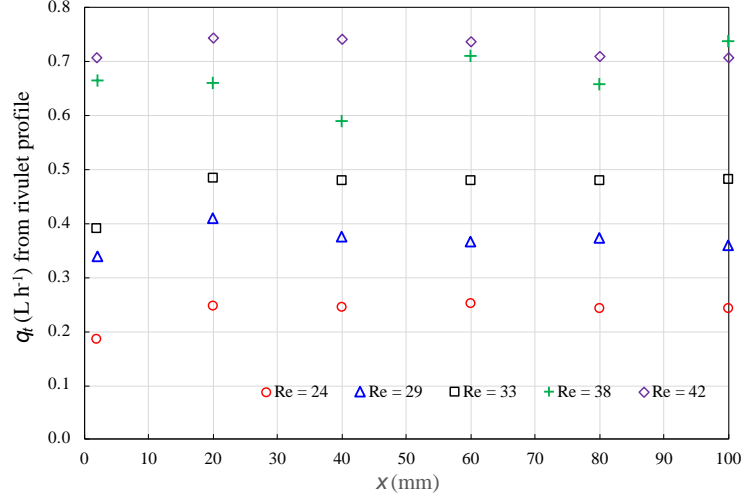


Figure S4.11. Transferred volume flow rate (q_t) as a function of the distance (x) from the perforation. q_t is estimated from Eq. A4 with the parameters of the rivulet spanwise profile.

We also compared the right-hand side of Eq. A4 to the transferred volume flow rate q_t measured experimentally. It appears that the former is significantly lower than the latter, i.e., from about 10% up to 35%. The discrepancy decreases as the supply Reynolds number increases. Two main reasons can be advanced. (i) As the supply Reynolds number decreases, the part of the rivulet cross-section satisfying $z > 100 \mu\text{m}$ decreases. Then, the identification of the Gaussian parameters and the estimate of q_t from Eq. 4.4 become less reliable. (ii) The Gaussian law fails to describe the region of the rivulet close to the lateral contact line because the liquid contact angle on the plate is low but not equal to zero as in Shetty & Cerro's experiments, where the plate was prewetted. We retain that the product $\delta_c^3(x) m(x)$ is approximately constant for $x \geq x_0$.

If the flow is viscous and $1 \gg |\partial\delta/\partial y| \gg |\partial\delta/\partial x|$, the rivulet thickness satisfies the thin-film equation given by Duffy & Moffatt²⁷. This equation reads for a steady rivulet flowing down a vertical plate:

$$\delta \frac{\partial^4 \delta}{\partial y^4} + 3 \frac{\partial \delta}{\partial y} \frac{\partial^3 \delta}{\partial y^3} + 3 \frac{\rho g}{\sigma} \frac{\partial \delta}{\partial x} = 0 \quad (\text{A5})$$

We must be careful: the Reynolds number of the rivulet is small but the flow is not strictly viscous in our experiments. The conditions on the thickness derivatives are fulfilled. $\partial\delta/\partial y$ is of the order of $\delta_c(x)/m(x)$ which is much smaller than 1 for $x \gtrsim 20 - 40$ mm. The ratio of $\partial\delta/\partial x$ to $\partial\delta/\partial y$ is of the order of $m(x)/x$ which is much lower than 1 for $x \gtrsim 20 - 40$ mm (see Table S2).

We now restrict our analysis to $y = 0$, where the rivulet peaks, and assume a Gaussian spanwise profile centered at $y = 0$ (Eq. 4.1 with $y_c(x) = 0$). Then, Eq. A5 becomes:

$$\frac{d\delta_c}{dx} + \frac{\sigma}{\rho g} \frac{\delta_c^2}{m^4} = 0 \quad (A6)$$

We further proceed as Shetty & Cerro¹²⁴ to get the scaling law followed by δ_c and m . We have just seen that the quantity $\delta_c^3(x)m(x)$ remains constant along x if x is large enough. We note x_0 the first measuring point where $\delta_c^3(x)m(x)$ reaches this plateau value (see Figure S4.11). $x_0 = 20$ mm for $Re = 24, 29, 33$ and $x_0 = 2$ mm for $Re = 38, 42$. For $x > x_0$, let

$$c_1 = 2(\delta_c^3(x)m(x))^2 \quad (A7)$$

and replace in Eq. A6:

$$\frac{d\delta_c}{dx} + \frac{4\sigma}{c_1^2 \rho g} \delta_c^{14} = 0 \quad (A8)$$

The streamwise coordinate (x), the maximum thickness (δ_c), and the standard deviation of the Gaussian (m) are rescaled as follows:

$$x^\# = \frac{x - x_0}{2m(x_0)} \quad ; \quad \delta_c^\#(x) = \frac{\delta_c(x)}{\delta_c(x_0)} \quad ; \quad m^\#(x) = \frac{m(x)}{m(x_0)}$$

Then, Eq. A8 is recast as:

$$\frac{d\delta_c^\#}{dx^\#} + \frac{16\alpha^3}{3Ca} (\delta_c^\#)^{14} = 0 \quad (A9)$$

α and Ca are the aspect ratio and capillary number of the rivulet at $x = x_0$:

$$\alpha = \frac{\delta_c(x_0)}{2m(x_0)} \quad ; \quad Ca = \frac{\mu}{\sigma} \left(\frac{g\delta_c^2(x_0)}{3\nu} \right)$$

The integration of Eq. A9 from $x^\# = 0$ to an arbitrary value of $x^\#$ gives¹²⁴:

$$\delta_c^\#(x^\#) = \left(1 + \frac{208}{3} \frac{\alpha^3}{Ca} x^\# \right)^{-1/13} \quad (A10)$$

By combining Eq. A7 and A10, we get the evolution of the rescaled rivulet width:

$$m^\#(x) = \left(1 + \frac{208}{3} \frac{\alpha^3}{Ca} x^\# \right)^{3/13} \quad (A11)$$

Since the quantity $2(\delta_c^3(x)m(x))^2$ is not strictly conserved experimentally (even for $x > x_0$) and slightly fluctuates along x , it is relevant to distinguish between the “best” estimate of c_1 taken as the mean value of $2(\delta_c^3(x)m(x))^2$ over the region $x > x_0$ and denoted \bar{c}_1 , and the value of $2(\delta_c^3(x)m(x))^2$ at $x = x_0$, i.e., $c_0 = 2(\delta_c^3(x_0)m(x_0))^2$. The former appears when

deriving Eq. A8 from Eq. A6 and Eq. A7. The latter appears when rescaling Eq. A9. Then, the argument of the power-laws (Eq. A10-A11) should be transformed as follows:

$$\left(1 + \frac{208}{3} \frac{\alpha^3}{\text{Ca}} x^\# \right) \rightarrow \left(1 + \frac{208}{3} \frac{\alpha^3}{\text{Ca}} \beta x^\# \right) \quad (\text{A12})$$

with $\beta = \left(\frac{c_0}{\bar{c}_1}\right)^2$.

A9. Length required for a rivulet flow to be locally fully developed

Let us estimate the length required for the rivulet flow to be locally fully developed. We consider the rivulet peak thickness at the first measuring point downstream of the perforation: $\delta_c(x = 2\text{mm})$ ranges between $261\mu\text{m}$ to $416\mu\text{m}$ (see Table S2). An estimate of the fluid mean velocity (U) on the rivulet centerline is given by:

$$U \cong \frac{g \delta_c^2}{3\nu}$$

The length to establish a Poiseuille flow between two parallel plates reads[†]:

$$\frac{L_m}{D_h} = 0.3125 + 0.011 \times \text{Re}_{D_h}$$

where D_h is the hydraulic diameter. $D_h = 2H$ for two parallel plates spaced a distance H apart.

We then deduce the length required for the rivulet flow to be locally fully developed:

$$\frac{L_m}{\delta_c} \cong 1.25 + 0.044 \frac{U \delta_c}{\nu}$$

We find that L_m ranges from 0.7 mm to 3 mm when the supply flow rate on the front of the plate varies between $Q = 20 \text{ L h}^{-1}$ and $Q = 35 \text{ L h}^{-1}$, respectively.

[†] Atkinson B, Brocklebank MP, Card CCH, Smith JM. Low Reynolds number developing flows. *AICHE Journal*. 1969;15:548-553.

A10. Scaling law of the rivulet merging

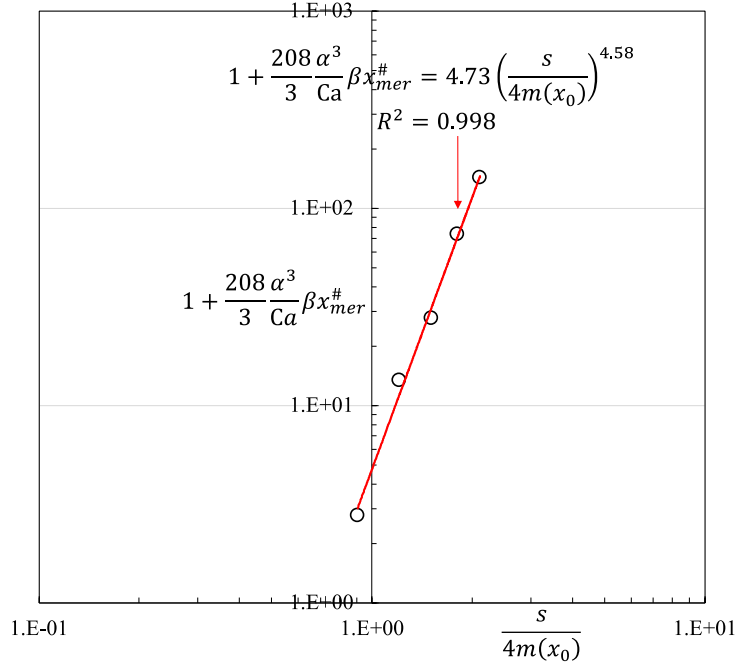


Figure S4.12. Rescaled distance between the onset of rivulet merging and the row of perforations as a function of the rescaled perforation spacing. $d = 4$ mm, $t = 1$ mm, $Re = 38$ and $s = 6, 8, 10, 12, 14$ mm. Data points are fitted by a power law (red solid line) using the least-squares method.

Figure S4.12 presents the variations of rescaled distance required for rivulet merging ($1 + \frac{208 \alpha^3}{3 Ca} \beta x_{mer}^{\#}$) as a function of the rescaled perforation spacing ($s / (4m(x_0))$). The data points are fitted by a power law using the least-squares method. The exponent (4.58) is close to the theoretical value ($13/3 = 4.33$). The prefactor (4.73) is significantly greater than the expected value (1). We presently overestimate $x_{mer}^{\#}$ because the first measuring point (corresponding to a film thickness close to 100 μm) used to estimate the onset of merging is systematically located downstream of the actual position where the rivulets start to merge (corresponding to a vanishing film thickness).

A11. Model of liquid transfer through a staggered array of perforations

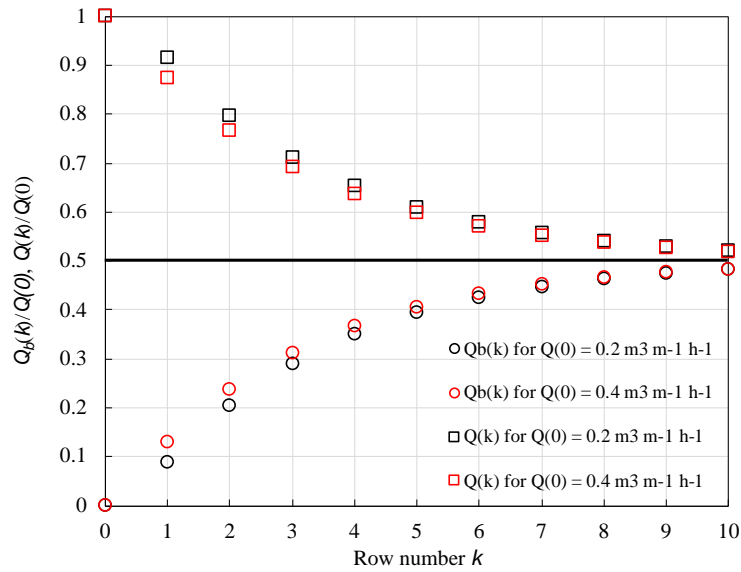


Figure S4.13. Rescaled volume flow rate per unit width on the back ($Q_b(k)$) and on the front ($Q(k)$) of the plate as a function of the row number (k): results provided by the model for $d = 4$ mm, $t = 1$ mm, $s = 14$ mm, $Q = 0.2$ m³ m⁻¹ h⁻¹ and $Q = 0.4$ m³ m⁻¹ h⁻¹.

Figure S4.13 shows the variations of the volume flow rate per unit width along the front and the back of the perforated plate computed from our simple recurrence model. It appears that the volume flow rates on the front and the back of the plate tend to equalize as the row number (k) increases. The asymptotic value is equal to half the supply flow rate. The transferred volume flow rate decreases with k since the driving force ($Q(k-1) - Q_b(k-1)$) decreases. Q_b reaches 90% of its asymptotic value ($Q(0)/2$) beneath the 7th row of perforations.

The solutions computed for $Q = 0.2$ m³ m⁻¹ h⁻¹ and $Q = 0.4$ m³ m⁻¹ h⁻¹ are not proportional since Eq. 4.18 describing the liquid transfer through the first row of perforations contains a constant term, i.e., the threshold flow rate $Q_{th} = 0.1$ m³ m⁻¹ h⁻¹. Then, the points associated with $Q = 0.2$ m³ m⁻¹ h⁻¹ and $Q = 0.4$ m³ m⁻¹ h⁻¹ do not superimpose. However, if $Q_{th} = 0$, the pointset would be unique.

For $Q(0) = 0.4$ m³ m⁻¹ h⁻¹, we expect that $Q_b(k)$ and $Q(k)$ relax even more rapidly to their asymptotic value ($Q(0)/2$) than the predictions of Figure S4.13. Indeed, experiments show that the liquid transfer through the perforations is enhanced when the supply flow rate ($Q(0)$) increases (see **Figure 4-10**).

5 3D 3C PTV and optical flow applied to wall bounded and suspended liquid films

Summary: The dynamics of liquid film over the perforated metallic sheets of structured packing highly influences mass transfer and pressure drop characteristics. Regarding the perforations, their role in mass transfer enhancement and liquid redistribution is yet not well understood. On perforated packing, liquid films can be either supported or suspended ("curtain" regime), also known as "twin film". Twin films account for intensive capillary waves and strong recirculation zones on the free surfaces. Therefore, experiments are required to assess the curtain formation in the perforations and relate it to the dynamics that intensify interfacial mass transfer.

A 3D 3C Particle Tracking Velocimetry (PTV) is first presented through the concept of particle defocus. This technique makes it possible to obtain three-component velocity vectors in all three dimensions by using just one camera. This quality is advantageous in velocity measurements of thin films on complex surfaces (structured packing elements) in which gain in optical accessibility is often challenging demanding a complex optical setup.

We also implement a new post-processing technique by using "optical flow algorithms" to gain spatial resolution and high sensitivity to even low signal strength instead of classical FFT based cross-correlation algorithms.

Validation of method: The measurement technique is developed in liquid films falling on the flat aluminum plate in vertical configuration. As a validation, the measured mean axial velocity of the flow is examined and compared with the theoretical Nusselt solution under steady flow conditions. The deviation in mean axial velocity up to 20% from the theoretical solution is observed.

Liquid films on a perforated plate: Under steady conditions, a qualitative analysis by examining streamline patterns in the liquid film on a perforated plate is performed to recognize the recirculation zones or vortex structures.

The mean axial velocity is measured in the case of liquid film on the perforated plate, particularly in curtain mode. Single point and 2D probability density function of the velocity values reinforces the presence of recirculation zones in the liquid curtain.

The spatial modes from the Dynamic mode decomposition analysis of the liquid curtain demonstrates a low-frequency oscillation type of instability, starting at the entrance of the perforation.

Key words: PTV, defocus, Dean Vortex, Horse-shoe Vortex, liquid curtain, perforation

1. Introduction

In the corrugated and perforated metallic sheets of structured packing, liquid films coexist as supported and suspended fluid film^{18,98,101,123}, known as twin films. The liquid film flowing into the perforation undergoes different transition mechanisms such as the rim, drop/column before forming a thin liquid curtain/sheet. In counter-current gas flow systems within corrugated and perforated packings, hydrodynamics of twin films are different from film on solid surfaces. The liquid film presents the rapid change in velocity, strong variation of thickness profiles and allows phase interaction on both faces through suspended liquid film. The profile of the liquid film around the perforation is somewhat similar to the falling liquid film on step-in/step out^{105,106}, trench, occlusions^{132,133} type of surface feature. The profile of the suspended liquid film in the perforation varies with the size of perforation and liquid properties.

In response to the perforation, the free surface of the liquid film deforms, resulting in a capillary ridge preceded by high amplitude waves. At “Curtain Reynolds number¹²³” (Re_{cr}), inertia forces take over surface tension forces and liquid curtain forms. In our study, this Reynolds number criterion is identified as a threshold at which liquid curtain forms. In curtain mode, based on the variation of film thickness profile, we have identified three characteristics regions starting from the entrance to the exit of the perforation (Refer to Chapter 3) (see **Figure 5-1**):

1. At the entrance: A stagnation point in the inner surface of the perforation and a resulting capillary ridge,
2. In the liquid curtain: A part of liquid flows along the curved rim attached to the upper curvature of perforation ($\frac{1}{3}d$). The other part of liquid film accelerates with free-fall acceleration in large diameter perforation¹²³ ($d > 6$ mm) (window region¹⁰¹). The thin liquid curtain presents capillary varicose standing waves (parallel/checkerboard¹¹³).
3. Just before the exit: liquid film encounters the edge of the perforation, causing local flow reversal.

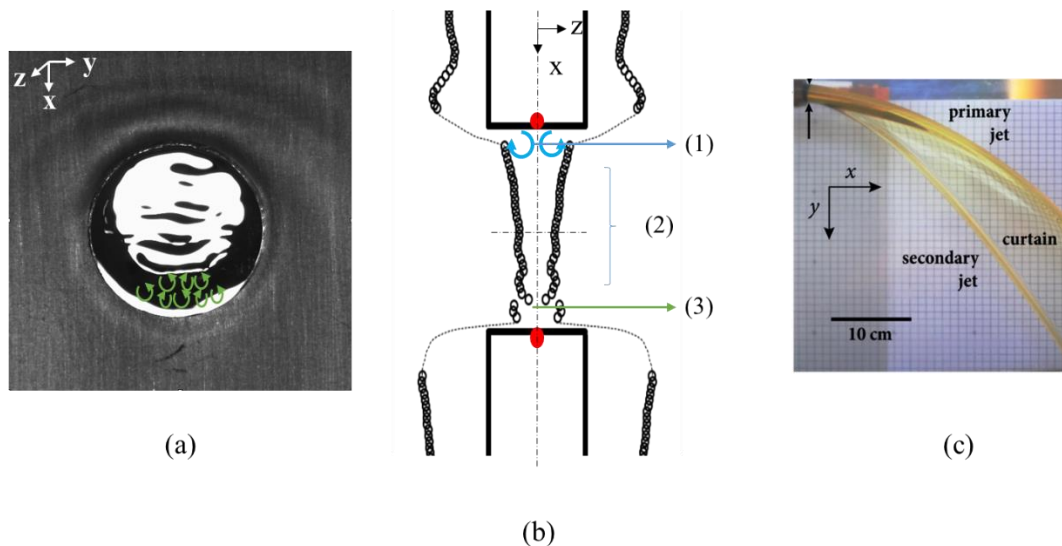


Figure 5-1: Structure of the liquid curtain in a perforation in (a) $x - y$ plane and (b) $x - z$ plane: Deionized water curtain in the perforation of diameter $d = 8$ mm at $Re = \frac{\rho Q}{\mu} = 103$ ($Q = q/W$; $\mu = 0.00105$ Pa.s; $\sigma = 0.073$ N.m⁻¹). (c) Example of the structure of Torricelli's curtain from a horizontally ejected liquid jet from the pipe¹³⁴.

The thin sheet in the region (2) is connected to the relatively thick rim in the inner surface of the perforation entrance and exit. The vertical cross-section of the liquid curtain is similar to the cross-section of Torricelli's curtain formed at the jet exiting the pipe¹³⁴ (see **Figure 5-1c**). Dean vortices^{135,136} (spiral trajectories) is observed flowing down the jets when a dye is injected in the primary and secondary jet. Dean vortices are common in the fully developed curved pipe¹³⁷ and has proved to enhance mass transfer through vigorous mixing at the interface in the liquid-liquid system¹³⁸.

In the recent numerical study, Xie et al⁸⁹ studied the flow structures in the liquid curtain through velocity and vorticity distribution. The liquid film velocity distribution changes drastically in the open window region, as it is no longer influenced by the boundary layer of the solid surface. Eddies or vortices were reported in the stagnation points at the entrance/exit of the window region (see **Figure 5-1ab**) and in the capillary wave crests formed on the suspended liquid film. So far, perforating the structure packing elements was considered advantageous in reducing the packing weight and favoring liquid distribution through the exchange of liquid from one face to another. Only in the recent literature^{20,98,101}, authors have qualitatively assessed the curtain formation in the perforation and relate it to the dynamics that intensify interfacial mass transfer. From the species transport equation (Hu et al¹⁰⁰), the average mass transfer coefficient (k_L)

value for the open window (26.9%) was found to be higher when compared to the wall region (17.4% and 19.2%). The liquid curtain is predicted to increase effective interfacial area^{19,92,98,139,140} due to standing capillary waves. However, physical proof through experiments is necessary to confirm the theories, numerical models prediction or analogies made. To the best of our knowledge, we have not come across any experimental work done on twin liquid film illustrating the velocity distribution or velocity profiles, vorticity maps, etc.

Several studies focus on characterizing the hydrodynamic aspect of mass transfer through spatiotemporal velocity data (PIV/PTV). Experiments have been conducted on the liquid films on vertical, inclined plates (flat⁵⁸/textured⁹⁰) and annular flows⁸⁹ with or without counter-current gas flow. The hydrodynamics of liquid film on these geometries is close to the flow structures in packing elements. In the comparative experimental study, the liquid film with waves has been shown to increase heat and mass transfer rates dramatically (2 to 3 times) compared to the liquid film with no waves (Emmert and Pigford¹⁴¹). Dukler¹⁴³ studied mass transfer in the wavy and non-wavy liquid film. Hydrodynamic data of the liquid films are obtained by solving the convective-diffusion equation with the concentration profiles. Ripples kind of interface is introduced in the model. Mass transfer rates were found to increase by 1.5 to 2.5 times than those predicted for gas absorption in non-wavy films. Their experiments confirm their model results. The waves of various amplitudes^{142,143} and frequencies (imposed or naturally present) like solitary waves, and recirculation regions in wave humps⁶¹ increase mass transfer rates.

Using the Laser Doppler anemometer (LDA) system, interfacial velocities were measured by Yu et al¹⁴⁴ on falling liquid film with the counter-current gas flow. The authors measured three-dimensional velocity component and the film thickness in the liquid phase with counter-current gas flow. Velocity components were decomposed into mean and fluctuating parts. Fluctuating velocity components are extracted to calculate the turbulent intensity in the liquid film. For the mass transfer study, they attempted to use the time-series velocity data to calculate the rate of surface renewal and then to calculate the mass transfer coefficient (using penetration theory for liquid phase).

Most of the experimental studies focus on the measuring velocity profile in the cross-section of the liquid film, specifically in the wave cross-section at different positions on the test surface. The cross-section of the film gives access to the normal velocity component, which is essential when the objective is to relate flow structures to molecular diffusion (direction perpendicular to the film advection).

Aluminum particles were sprinkled on the free surface of the liquid film on complex metallic surfaces⁶⁶ to measure the free surface velocities precisely using the PIV technique. There is a substantial difference in the average film thickness and average velocity on the complex surface compared to Nusselt's flat film at the same liquid load. Higher average film thickness and low average velocity of the liquid film on the complex surfaces have an important consequence in terms of mass transfer. To our knowledge, the above study is the only existing PIV performed on the metallic plates, whereas most optical studies use liquid films on transparent surfaces (glass). Unlike metallic surfaces, transparent surfaces do not suffer parasitic reflections. The camera and the light source can be placed at either side of the region of interest without disturbing the liquid film. However, the surface properties of the transparent surfaces are far different from the surface properties of thin aluminum packing elements. On the other hand, visualizing beneath the microscale film's free surface on opaque metallic surfaces by positioning the light source and camera on the same side of the region of interest without disturbing the free surface could be quite challenging, which explains the limited studies undertaken on the subject.

Optical techniques such as PIV/PTV remains a prime choice for processing image-based flow measurements in any fluid mechanic experiments to extract velocity field or vorticity information. The method often relies on Fast Fourier Transform (FFT) based correlations to obtain displacement vectors and put a constraint on achievable accuracy of the order of 0.1 pixel, yielding a basic limitation of the FFT based technique. Once 2D fields are obtained, the characteristics of the dynamics of the flow can be computed. Despite statistical description such as triple Reynolds decomposition or Proper Orthogonal Decomposition (POD), new technique such as DMD, originally introduced by Schmid¹⁴⁵, is widely used to extract dynamical structures from the experimental/numerical dataset. The method is applied in broad range of dynamical systems because it is purely a data-driven method (only time series data) and it does not require any knowledge of underlying equation of motion. With any numerical or experimental data set, this tool is capable of extracting information about the temporal and spatial structures. The underlying assumption is to find the linear operator that relates data at a given time to the data taken at a previous time. In simple words, the method executes the following steps on a data set: 1. collects spatio-temporal data, 2. reshaping the data set at each time in each column matrix $\mathbf{V}_1^N = \{\mathbf{v}_1, \mathbf{v}_2, \dots, \mathbf{v}_{N-1}\}$. Similarly the second matrix at next consecutive time $\mathbf{V}_2^N = \{\mathbf{v}_2, \mathbf{v}_3, \dots, \mathbf{v}_N\}$ (see Appendix 6 for the detailed description) 3. Then, the DMD essentially extracts eigenvalues or eigenvectors of \mathbf{A} ($\mathbf{V}_2^N = \mathbf{A}\mathbf{V}_1^{N-1} + \mathbf{r}\mathbf{e}_{N-1}^T$; \mathbf{e}_{N-1}^T is a unit vector at $(N - 1)^{\text{th}}$ time and \mathbf{r} is a residual vector), which are known as DMD modes.

The data acquisition time is one of the main parameter of DMD. Schmid¹⁴⁵ specifies that the acquisition frequency must respect the Nyquist-Shannon criterion, i.e. at least twice the frequency of the phenomenon we are interested in studying. Recently Baudoin⁸⁷ applied DMD kind of post processing for 2D time series PIV data to retrieve the dominant modes in the form of frequency. For the frequencies identified, spatial data is reconstructed to observe the characteristic structures. In their case, the authors observe vortex shedding structure associated to the dominant DMD mode. The method have been successfully applied to identify vortex shedding and other large scale features in flow over sphere¹⁴⁶ and in free jet flow¹⁴⁷. In DMD, each mode will have a unique frequency component. The base for the frequency is not regularly distributed as it is the case for a classic FFT decomposition. The mean frequency is same as in FFT.

The question raised here is, how appropriate is the hydrodynamics of twin liquid films, in the prospect of mass transfer, compared to the films on non-perforated elements of structured packing. How can we measure the curtain dynamics to analyse its role in species transport in corrugated and perforated elements of structured packing. Therefore, further attention was given to the subject to obtain new information on the three-component velocity in three dimensions to quantify the complex flow structures.

At present, we developed a novel optical set-up to conduct 3D 3C Particle Tracking Velocimetry with a concept of defocus of tracer particles seeded to the flow. A new variation of non-intrusive optical technique to analyse three components of velocity in three dimensions. The method has been developed by Baudoin et al⁸⁷ and implemented to validate numerical simulation data of the mixing phenomena downstream a spacer grid in the reactor core (nuclear sector). For the first time within falling liquid films, optical flow algorithms (Shi et al.¹⁴⁸) are used instead of classical Fast Fourier Transform (FFT) based PIV to improve the spatial resolution. Optical flow method can detect the movement of even a small change in intensity speck of light. The technique can provide a displacement vector on each pixel of the image and thus known for its potentially high spatial resolution. However, the exact spatial resolution is lower. As optical flow estimation results from the inversion of an ill-posed inverse problem, and some form of regularization is required for closure. This regularization correlates nearby vectors, and therefore reduces the spatial resolution. Traditionally, the method was developed to detect large objects' motion in a real-world scene and applied for robotic vision. However, Quénot et al.¹⁴⁹ applied this technique to the images of flow in a fluid bed and in a wind tunnel with tracer particles and smoke.

The chapter is organized as follows: In the first part, the methodology of the Lagrangian approach based Particle Tracking Velocimetry (PTV) by defocus principle is described. Preliminary 2D measurements of the velocity vectors are performed on liquid film on a flat plate using optical flow algorithm to compute the axial velocity. An attempt is made to obtain the 3rd dimension data by looking at the apparent size of the defocused tracer particles. We qualitatively analyse the hydrodynamics of the liquid curtain using streamline patterns. The liquid curtain is studied using a statistical approach, particle tracking, and DMD spatial modes in the final part.

2. Methodology

2.1. Principle of PTV

The principle of PTV is to detect and track a given particle to obtain information on its evolution in space and time. The method relies on the Lagrangian specification of the flow field. By tracking the evolution of a certain number of particles, trajectories can be reconstructed in 3D space. In addition, fluid velocity is calculated from a differential equation below.

$$\mathbf{u}(x(t), t) = \frac{d\mathbf{x}}{dt} \quad (5.1)$$

The particles are first identified (spatial matching with specific pattern), then individually tracked (temporal tracking), and finally associated two consecutive images. In the present study, we adopt the principle of the PTV based on the concept of particle defocus. To better disseminate the particles and have a higher accuracy, it is important to spread the signal over several pixels. The main difficulty of 3D defocussed PTV is the decrease of signal to noise ratio when particles overlap. In order to overcome the problem, seeding densities are kept low and an annual aperture technique is adopted. Other drawbacks of PTV are the limited number of suitable tracers and the fact that precisely measured 3D positions cannot be prescribed in advance.

2.2. Principle of defocus

The concept of defocus set PTV is based on the ability to detect the particles in space by its apparent size (d_i) when the particle in the image plane is away from the camera focal plane. The further the particle is from the focal plane the bigger is its size on the sensor (see **Figure 5-2**). This methodology is often used to evaluate the depth in the scene based on the difference of blurs in at least two images captured at different focal positions. The concept was first introduced by Pentland et al.¹⁵⁰ and Krotkov¹⁵¹ and widely applied in various fields situations

and a review of various methods is presented in Chaudhuri and Rajagopalan¹⁵². The defocusing of a lens consists in acquiring the image of an object whose position is not at the level of the focal plane but is outside the depth of field of the camera lens. The schematic representation of the system is shown in the **Figure 5-2** with the typical examples (see S5.1) of a real particle taken at different position from the focal plane.

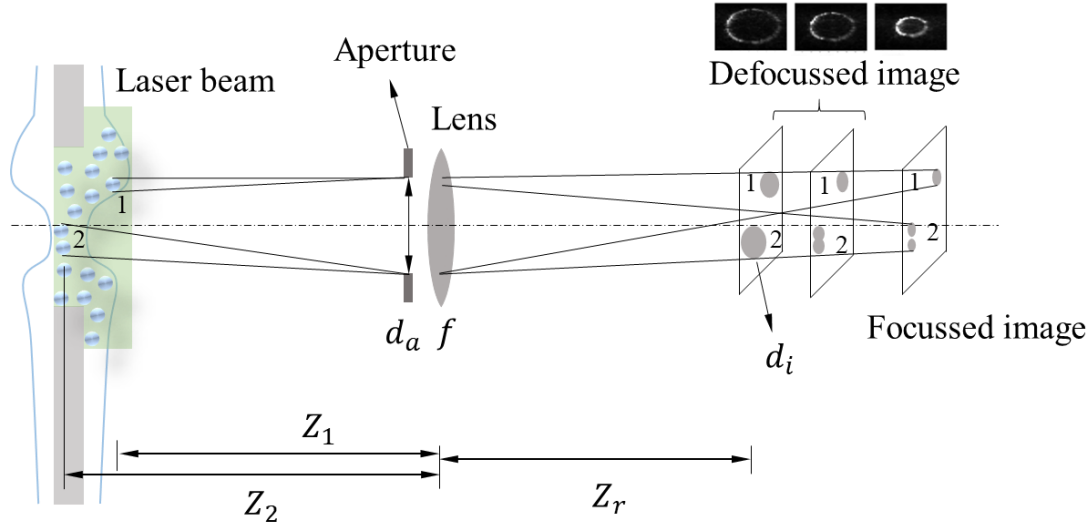


Figure 5-2: Effect of defocuss on the image (adapted from Damaschke et al.¹⁵³) with the examples of the real particle taken at different position from the focal plane.

Using thin lens approximation (see Eq. 5.2), the apparent size of the particle d_i can be estimated. d_i is only a function of aperture size (d_a), focal length (f), the distance from the particle to aperture (z_1 or z_2) (see **Figure 5-3**), and the distance from aperture to sensor (z_r). We apply the principle of defocus to track the particles in a liquid film falling on a vertical plate with a perforation.

$$d_i = d_a * \left| 1 - z_r * \left(\frac{1}{f} - \frac{1}{z_1} \right) \right| \quad (5.2)$$

2.3. Annular aperture technique

Having a more significant size on the image for each particle, overlapping of the signals can occur. It can lead to a decrease in the contrast of the images, which can intervene in determining the velocity vectors. An annular mask of circular disk shape is used to block a part of the lens aperture (see **Figure 5-3**) to limit the overlap of the particles. The mask is inserted between the camera lens and the sensor. The circular disk is held in place by three branch-shaped support. Only the rays passing through the mask (or annular opening) can reach the sensor and leave a luminous contour. This annular-aperture-based defocusing technique was first proposed by Lin

et al.¹⁴⁶ and has been revisited in the recent work by Baudoin et al⁸⁷. They have compared the images from the classic defocus technique and the annular aperture technique (see **Figure 5-3**). They have shown that the amount of particles detected has increased by 30 %, with a size detection accuracy by 13 %.

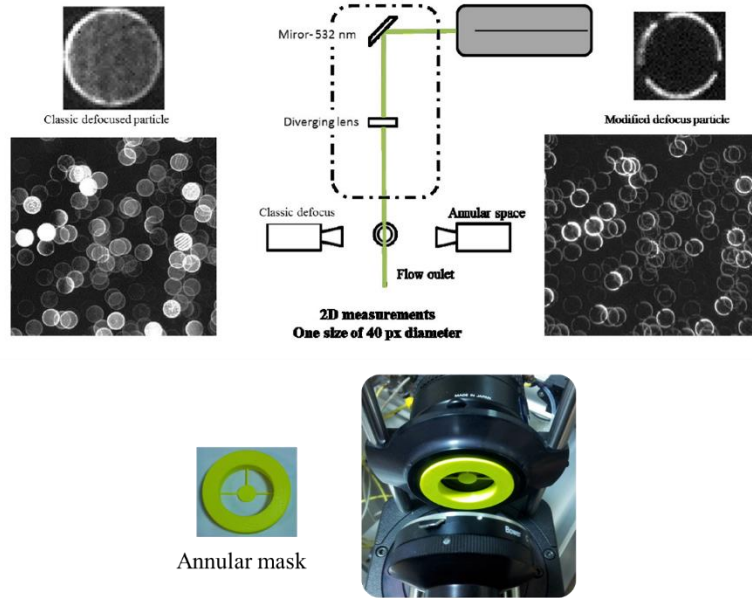


Figure 5-3 : Direct consequence on the appearance of the particles with (right) and without (left) a circular disk or annular space technique¹⁵⁴.

2.4. Velocity measurements

Two different processing techniques are applied to the same images to obtain the velocity of the flow. The first technique is based on an optical flow approach¹⁵⁵, which determines the displacement of the light within two consecutive images for each pixel.

$$\frac{\partial I_t}{\partial x} u + \frac{\partial I_t}{\partial y} v + \frac{\partial I_t}{\partial t} = 0 \quad (5.3)$$

where u , v are streamwise and spanwise velocity components, I_t is the local intensity of the image on each pixel at coordinates x and y and at time t . This approach yields a high-density velocity field but is limited to two dimensions. In order to obtain the third component, a tracking approach is applied, which consists of detecting individual particles and determining their displacement in the three dimensions between two consecutive images. A preliminary prediction is used, based on the optical flow output, to overcome mismatching of association.

Whereas optical flow is a traditional processing technique in computer vision, the three-dimensional tracking technique is less developed, and the different steps are detailed.

2.5. Locating the particles in 3D space

Particle center detection: First, patterns of an individual defocused particle of given sizes are defined (see **Figure 5-4**). Those patterns aim to reproduce the intensity distribution within the annular ring of particles by applying a Gaussian profile to the light distribution along the radial dimension.

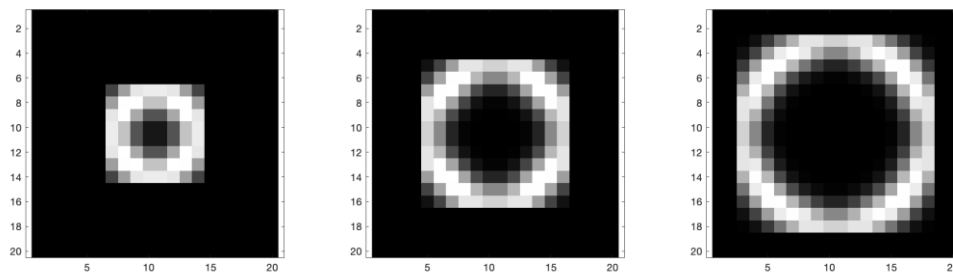


Figure 5-4: Typical patterns created for the detection of particles (respectively 8, 12 and 16 pixels in apparent diameter).

Patterns of size ranging from 8 to 30 px are created with an integer value of apparent size, ranging from the lowest apparent size obtained in the measurements to the bigger one. Normalized cross-correlations between each image and the series of the predefined pattern are computed. A particle is assumed to be detected if the normalized correlation coefficient is above a given threshold. In the current investigations, this level has been set to 0.4. The apparent size is obtained by determining the maximum correlation with respect to the different pattern sizes for a given position. This allows to retain main visible particles. The center of each particle are determined using 3-point Gaussian interpolation in the horizontal and vertical positions. Detections of particles can be run in parallel, and the output is for each instantaneous image, a position of a particle in 2D, together with an apparent size (all values in pixels, interpolated to sub-pixel with a three-point Gaussian fit).

2.6. Association of particles between two images

In parallel to the computation of the location and apparent size of the particles, the image is first processed using optical flow algorithms¹⁵⁵. This allows to recover global 2D maps of instantaneous displacements, which, interpolated to the positions of the particles, will provide an estimation of the planar velocity vector. From this estimated vector, the spatiotemporal

association is sought based on a Particle Tracking Velocimetry method. A probable position in the following image is determined using the displacement predicted through the optical flow algorithm for each particle detected. This algorithm is recursive to ensure that particles are associated with at most one particle only. After this initial step, the real images centered on individual particles alone are kept in the consecutive images. Global optimization is then performed to determine the transformation matrix that maximizes the correlation between the true second image and a second image of the particles interpolated from the first image with a transformation in X , Y , and Z . The third Z coordinate corresponds to the apparent size of the particles. To do so, the image is obtained in a matrix that does not fit the actual pixel, and the transformation aims at projecting the interpolated image to the position of the pixels. Then, the local velocity vectors and subsequent trajectories are deduced from the association of successive particle positions in time and space described in Baudoin *et al*⁸⁷. The particles can be isolated to follow some interesting trajectories that may reveal recirculation zones near stagnation points.

3. Experimental procedure

For a detailed description of experimental set up and test parameters (camera, liquid and geometry), refer to Chapter 2.

4. Quality assessment of the experimental data: Film on vertical flat plate

A sequence of raw images sampled at 800 Hz (exposure time: 1.2 ms) (see **Table 2-6** in Chapter 2) was pre-processed by enhancing the intensity of fluorescent light emitted by the tracer particles and thus increasing the signal-to-noise ratio of individual particles. The raw images were inspected for the tracer particle distribution and density. We observed static tracer particles on the plate at specific regions. These stationary particles serve as a reference for calibration purposes due to their constant size and position. The images were processed with the in-house MATLAB code of optical flow algorithms.

The velocity measurements obtained from the method is first validated by performing measurements of liquid film on a flat plate in steady flow conditions. The light sheet is allowed to pass throughout the entire width of the plate, from left to right (see **Figure 5-5a**). The region of interest is selected based on the shape, size, and visibility of the particles. The intensity of the laser beam reduces from left to right and thus the visibility of the particles. We choose the ROI verifying the particle quality, and therefore ROI is slightly off-centered. We conduct measurements in the liquid film on a flat plate in the same zone where ultimately the

perforations are made. The liquid film is fully developed in ROI. The liquid film is ensured to be flat along streamwise and spanwise of the plate by measuring the film thickness at several points.

4.1. Axial velocity (u_x) distribution in liquid film on flat plate

The time-averaged axial velocity profiles of the liquid film on a flat plate are plotted. The post treatment is performed on the ROI shown in **Figure 5-5a**. 700 - 1000 pre-adjusted images (see **Figure 5-5b**) are processed using an optical flow algorithm. We assess the quality of data through the mean flow field, and the following observations are made:

1. With the increase in supply flow rate, axial velocity globally increase in the measured region. A distinctive patch (deep blue), indicating zero velocity vectors, at the right side of the plate is observed in all flow conditions (see **Figure 5-6(A-D)**). By closely observing the preprocessed images, we noticed an anomaly of signal emitted by too many agglomerated static particles on the plate. The signal from the static particles appears to interfere with the signal from the moving particles. The moving tracer particles suspended in the liquid film are undetected, and the measured velocity is biased towards zero.
2. Overall mean axial velocity appears consistent in most of the ROI. Some blue specs dispersed here and there on the image indicate low or zero velocity.

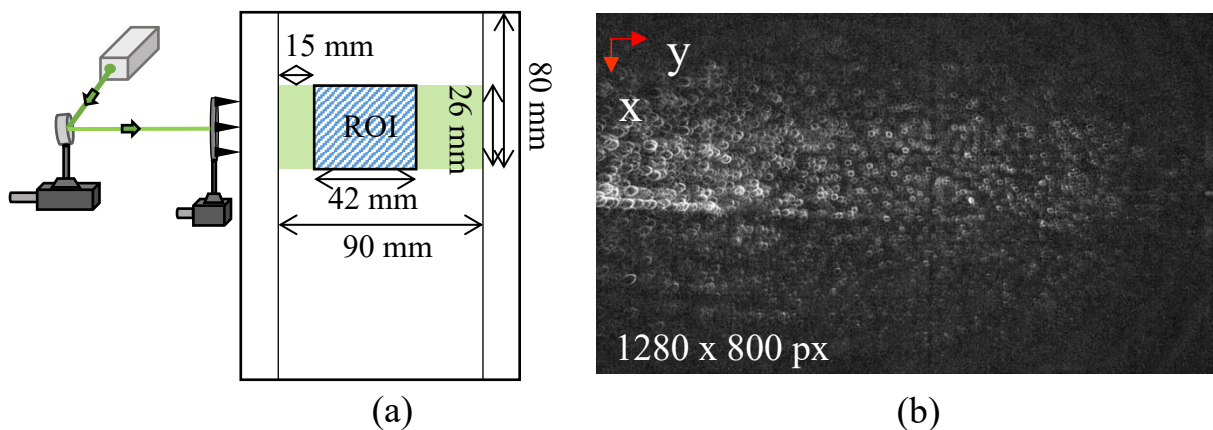


Figure 5-5: (a) Measurement zone on the flat plate with important dimensions (b) An example of pre-processed image with tracer particle when the defocus is set.

The time and space (spanwise) averaged axial velocity profile $\langle u_x \rangle_y$ of the liquid film is plotted in streamwise length (x) of the plate in **Figure 5-6(a-d)**. The top left corner of the y axis (0 mm) corresponds to the top position of ROI and the bottom left position corresponds to bottom position of ROI (26 mm). In ideal laminar film conditions, the velocity in vertical direction is constant for a given flow rate per unit width of the film. The profile of measured $\langle u_x \rangle_y$ is slightly wavy along the length of the plate (see **Figure 5-6(a-d)**).

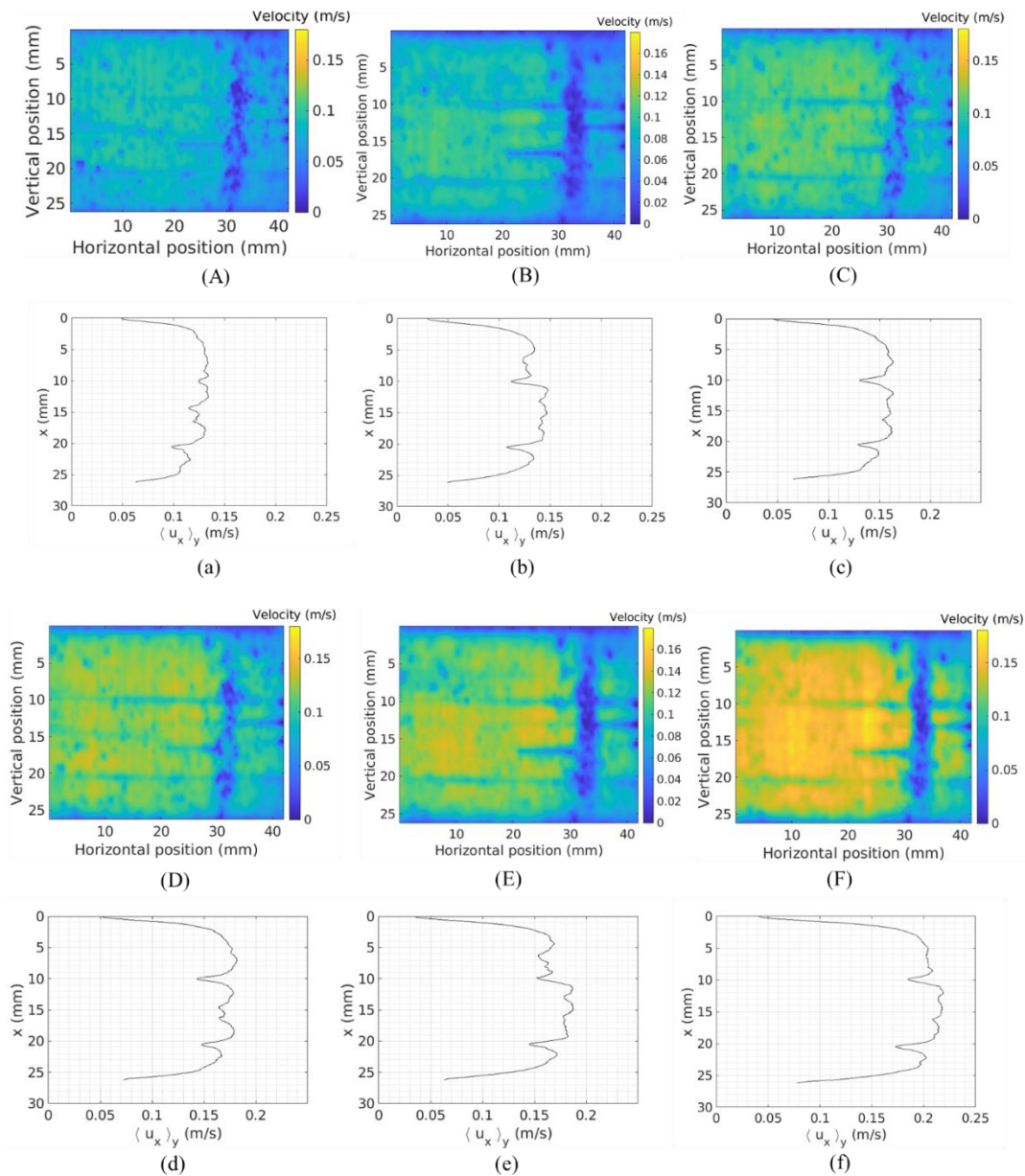


Figure 5-6: (A-D) 2D color map of the time averaged streamwise or axial velocity (u_x) (a-d) Time and space averaged (in spanwise) $\langle u_x \rangle_y$ along the vertical flat plate for $Q = 0.18, 0.22, 0.26, 0.29, 0.31, 0.39 \text{ m}^3/\text{mh}$. Test liquid is propan-2-ol ($Ka = 348$).

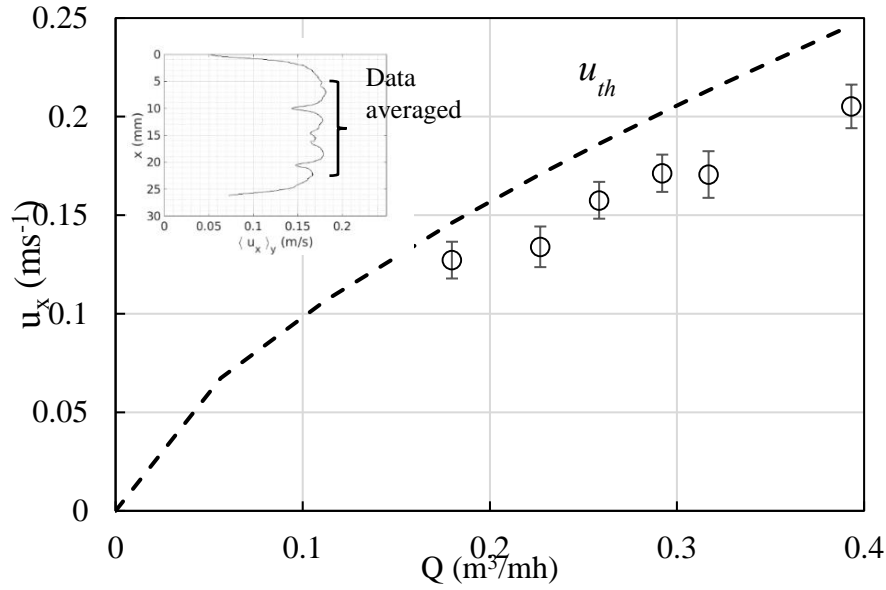


Figure 5-7: Comparison of experimental mean velocity and the theoretical mean velocity for different supply flow rate per width of the film.

The time and space averaged axial velocity values are plotted as a function of supply flow rate. The streamwise velocity profile data is averaged in the central region (see the insert in **Figure 5-7**), where the tracer particles show a low signal-to-noise ratio. The theoretical velocity values are calculated using Nusselt solution for flat liquid film (see Eq. 5.5). The theoretical value is obtained by integrating the velocity profile (see Eq. 5.4) within the film thickness ($z = 0$ to $z = \delta$). Nusselt film thickness is considered to calculate the bulk velocity (see Eq. 5.5).

$$u_x = \frac{g\rho \sin\theta}{\mu} z \left(\delta - \frac{z}{2} \right) \quad (5.4)$$

$$u_x = \frac{g\rho \sin\theta \delta^2}{3\mu} \quad (5.5)$$

The vertical error bars represent the standard deviation of velocity measured for each supply flow condition. We report that the measured values are lower than analytical values by approximately 10-20% for all flow conditions. However, the order of magnitude of the measured value is in good agreement with the theoretical mean velocity. The mean values could be improved by averaging the part of ROI where the distribution of vectors is well represented.

4.2. Relation between apparent size (d_i) of the particle and film thickness (δ)

Ideally, from the concept of defocus, the diameter of the particles decreases or increases based on the defocus adjusted on the camera and their position in the depth of the film. In the present case, the defocus is adjusted so that a particle located on the free surface of the film is relatively smaller in diameter than a particle close to the wall. In other words, the focal plane is in front

of the image plane. The change in apparent size (d_i) of the particle within the focal depth is linked to the position of the tracer particle within the depth of the liquid film. In all six flow conditions, the liquid film thickness is measured in streamwise of the plate, particularly in the ROI using a CCS (see **Table 5-1**). The distance from the plate surface (without film) to the lens is measured (see **Table 2-6**). The size of the stationary tracer particle on the plate surface is used as a reference size for the near-wall particles.

Q ($m^3/m h$)	δ_{Nu} (μm)	δ_{CCS} (<i>Exp</i>) (μm)
0.18	345	381±23
0.23	369	391±18
0.26	386	414±21
0.29	402	426±15
0.32	413	441±18
0.39	443	491±21

Table 5-1: Supply flow rate per unit width of the film, theoretical film thickness and measured film thickness.

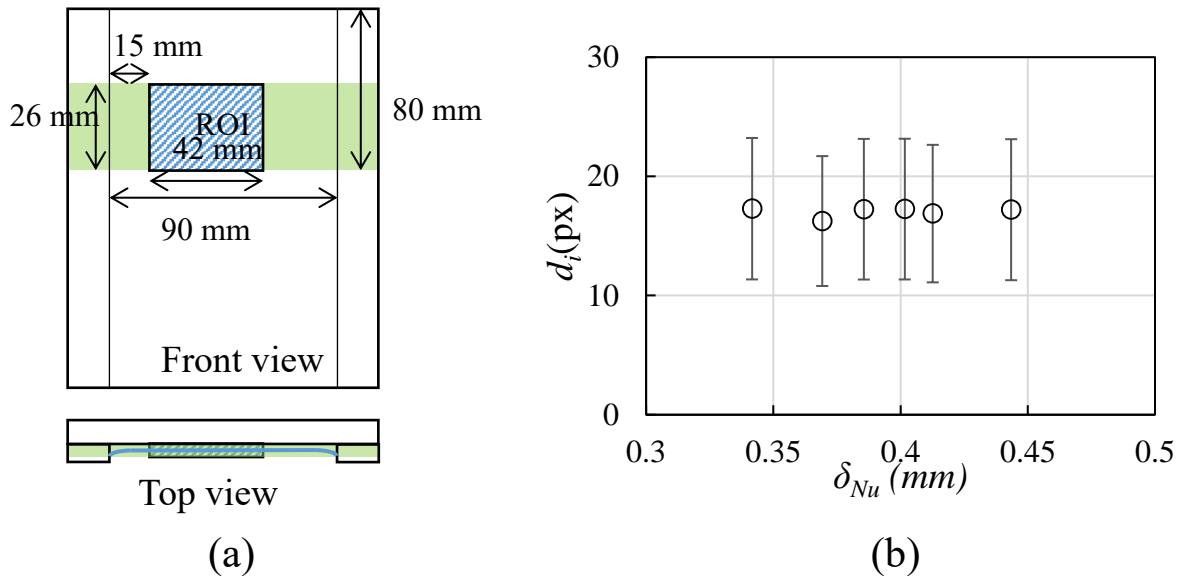


Figure 5-8: (a) Illustration of the region of interest (ROI) on a flat vertical plate. (b) Tracer particle size as a function of Nusselt liquid film thickness (δ_{th})

We create a circular pattern of different dimensions (thickness and diameter of the pattern). The cross-correlation of the pattern with the tracer particle is performed. The pattern presenting a good peak correlation with the raw images (without diffusive filter type Wiener 2) corresponds

to a good match between the pattern and the raw image. We keep only the images whose correlation with the pattern is greater than 0.40. This allows us to keep the main particles only. The centers of the particles are recovered each time and then, the optimum displacement matrix between the pattern and the image centered on the particle is calculated in Δx , Δy and especially the magnification parameter (gives Δz). Our interest is to determine the magnification of the tracer particle in the depth of the film. Particle size statistics are obtained on more than 300,000 particles for each flow condition. Those data are compared with the typical velocity fields obtained using the optical flow approach. **Figure 5-8b** illustrates the apparent size of the particle measured as a function of increasing film thickness (from Nusselt's solution). We report that change in d_i as a function of liquid film thickness is relatively small. Ideally, according to the position of the image plane and focal plane, the size of the fastest particle must decrease with the increase in supply flow rate (as the tracer particle appears closer to the camera). However, in the present case, the small variation of film thickness (ranging between 340 – 440 μm) do not allow us to get a significant change in diameter. The results suggest that the detection limit of the experiments performed is higher than the possible variations of apparent size and thus do not allow us to establish the relationship between the apparent size and depth of the film.

4.3. Partial conclusion

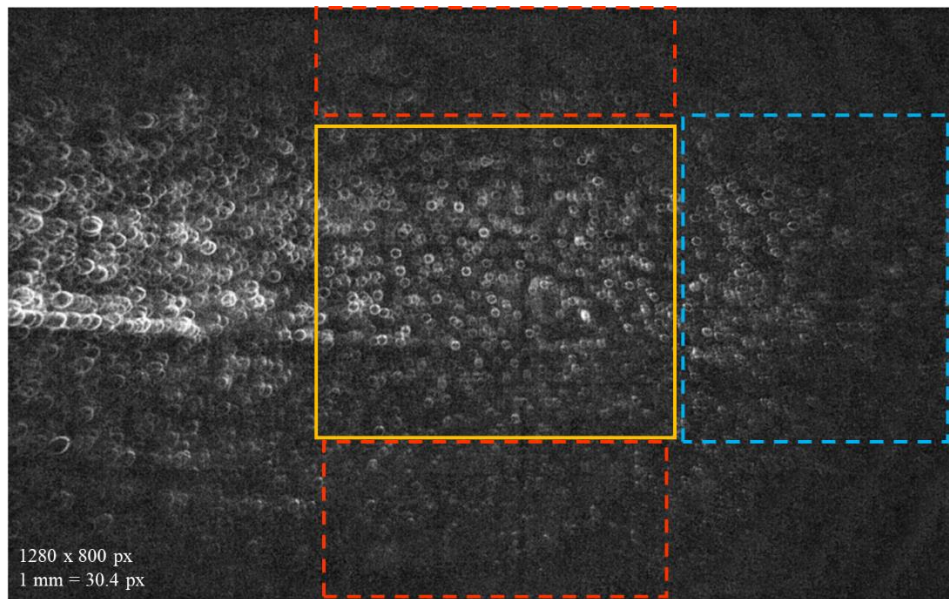
The 2D velocity measurements of the liquid film on a flat plate are in the same order of magnitude as the theoretical values. The method can be applied satisfactorily to extract local 2D 3C velocity vectors and track the particles. However, the information of the apparent size of the tracer particles in the film depth needs refined measurements and further in-depth analysis. The precision in the positioning of the plate and the adjustment of the light sheet in the film depth need further improvement.

We give a few plausible explanations for the errors in detection and association.

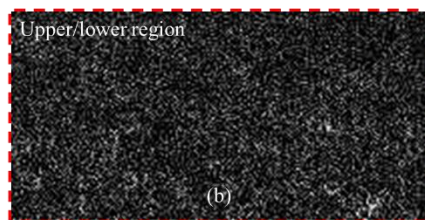
- Inaccurate validation of ghost particles can lead to false temporal associations, and thus incorrect displacement vectors are obtained in some regions. These false associations need to be detected beforehand by identifying the cause. Frequently encountered problems in our experiments, and the possible remedies to rectify these errors are detailed below. Too many static particles are trapped on the plate causing interference with the signal from the tracer particles in motion in the exact location as stationary particles.
- In spite of using a florescent filter and background noise removal, pre-processed images are slightly noisy in certain regions. The signal-to-noise ratio is relatively higher from

the left border to 30 mm in spanwise of the plate (see **Figure 5-9a**) In comparison, upper (5 x 42 mm), lower borders (9 x 42 mm), and the right border (12 x 42 mm) shows a degrading quality of signal from tracer particles. This can cause confusion between the noise and a signal from the tracer particles leading to erroneous particle association. In fact, in the upper and lower region of the ROI (see **Figure 5-6**), the light sheet intensity is not sufficient to view the tracer particles. This explains the strong gradient in 2D maps of mean axial velocity and mean axial profile in the upper and lower border (see **Figure 5-6a-d**).

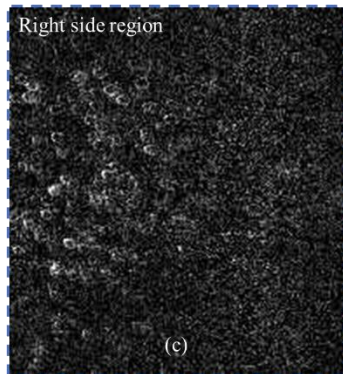
- We also note that the tracer particles are not circular in the region away from the central region (see **Figure 5-9a**). The apparent size of the non-circular tracer particle can misrepresent its position in the depth of the film. The shape of the particle is an important parameter to obtain particle statistics in film depth. However, we can still correctly locate the position of the particle in the x and y-axis. For the particle's location within the film depth, we can only consider the particles in the central region of the ROI (see **Figure 5-9ad**), which preserves a reasonable number of tracer particles whose shape does not vary. The non-circular shape comes from a tiny misalignment between the annular aperture and the exact center of the lens. Furthermore, the perfect circular shape of the aperture cannot be guaranteed, which leads to slightly deformed images.



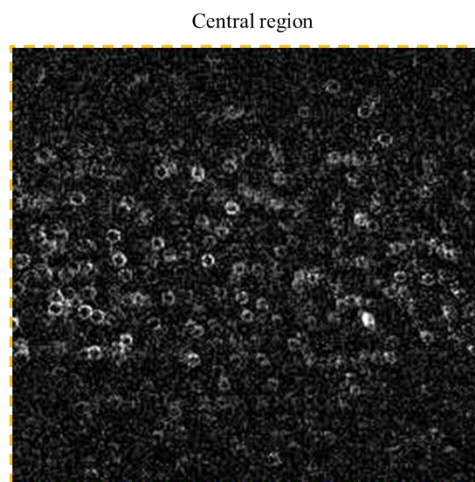
(a)



(b)



(c)



(d)

Figure 5-9: Qualitative view of tracer particles dispersion and their particle density in a (a) complete ROI (b) upper/lower borders, (c) right side and (d) central region of ROI.

5. Applicability of the 3D PTV on the liquid curtain

This section first examines the streamline patterns of the liquid film on a perforated plate in rim and curtain mode for different supply flow conditions. Two test liquids, deionized water ($Ka = 3920$) and propan-2-ol ($Ka = 348$) are used as the test liquid. Diameters of 4 mm and 8 mm on a plate thickness of 0.5 mm are used in the experiments. Based on the flow patterns observed, specific cases are further studied by implementing 2D 3C Lagrangian PTV, subjecting the

particles to defocus mode. We superimposed about 50 images captured at a sampling rate of 800 Hz (exposure time of 1.2 ms) to observe the streamline patterns.

5.1. Recirculation zones prior to curtain mode

At low Reynolds number, $Re < Re_{cr}$ (see **Figure 5-10a**), a stagnation point is formed at the entrance of the perforation, and due to the pinned contact line and lack of inertia, the liquid film flows around the perforation by the sides. The streamlines enabled us to observe the curved trajectories of the particles. In the capillary ridge formed around the perforation, the particles are observed to rotate around the y-axis at first (hole upstream) and then around x-axis (by the hole sides), assuming a helical path within the capillary ridge around a perforation. At small Re (see **Figure 5-10a**), the diameter of the vortices is of the order of magnitude of the height of the capillary ridge. For a slightly higher Re (see **Figure 5-10b**), another curved band of vortices rotating about y-axis and x-axis is observed around the upper half of the perforation. This type of vortex system is similar to vortices formed in jet and cross flow¹⁵⁶ and flow around solid boundaries like cylinders¹⁵⁷. The boundary layer upstream of the perforation overcomes a strong adverse pressure gradient induced by the entrance edge of the perforation in the flow direction resulting in a flow separation near the entrance close to the plate wall. A vortex in the separated region, usually at wave hump, develops and stretches around the perforation profile. This type of vortex, due to its shape, is referred to as a horseshoe vortex. In other words, fast-moving fluid particles away from the wall roll up as it encounters the entrance edge and sweeps around the perforation following a helical path.

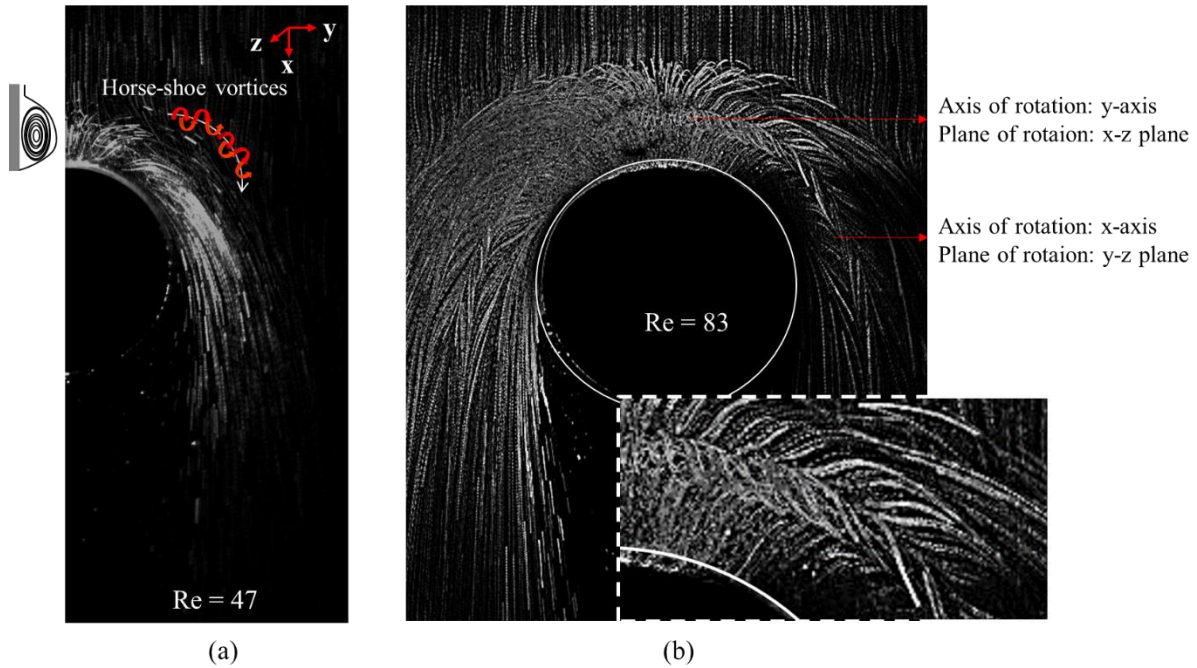


Figure 5-10: 50 super imposed x-y plane images of streamlines patterns of a fluid film falling on a perforated plate prior to curtain mode at (a) $Re = 47$ and (b) $Re = 83$. Diameter of the perforation $d = 8$ mm and thickness of the plate $t = 0.5$ mm is used. Test liquid is deionized water ($Ka = 3920$).

5.2. Recirculation zones in inertial and hysteretic curtain mode

The supply flow rate is increased to curtain Reynolds number ($Re_{cr} = 105$) to force the liquid curtain formation in the perforation. Once the liquid curtain is formed, supply Reynolds number is decreased to $Re = 47$. The curtain is retained in the perforation due to the phenomena of hysteresis. Fifty images are superimposed to observe trajectories of the tracer particles (see **Figure 5-11**). The number of images superimposed is maintained constant to observe the change in the trajectories as a function of film Reynolds number. The liquid curtain can be divided into 3 different regions (see **Figure 5-11ab**):

1. A cylindrical rim in the inner surface at the entrance of perforation,
2. Mid curtain region: thin film with capillary varicose waves,
3. Lower curtain region in the inner surface at the exit of perforation.

The local recirculation in $x - y$ and $x - z$ planes is observed for all supply Reynolds numbers tested here. The stagnation point is on the inner surface at the perforation entrance. Tracer particles entering the perforation rotate in $x - z$ plane (region (1)). The primary flow transports the vortices (1) following a helical path along the radius of curvature of the hole. Part of the fluid film flows along the centerline of the perforation (2) in a way similar to freely falling

liquid film. The trajectories are slightly curved in the liquid curtain, demonstrating the crests and troughs of the stationary capillary waves (see **Figure 5-11**). Under the steady flow assumption, the superimposed trajectories correspond to the streamlines of the flow. The streamlines with high light intensity in the liquid curtain are observed when the particles are on the crest of the capillary wave. The wave amplitude increases with the increase in Reynolds number. Wave troughs are slightly darker due to the particle moving away from the camera's depth of field. In region (3), the mixing of the liquid film from the region (1) and region (2) results in a chaotic region (3). With the increase in Reynolds number, region (3) becomes stochastic as shown in **Figure 5-11ef**.

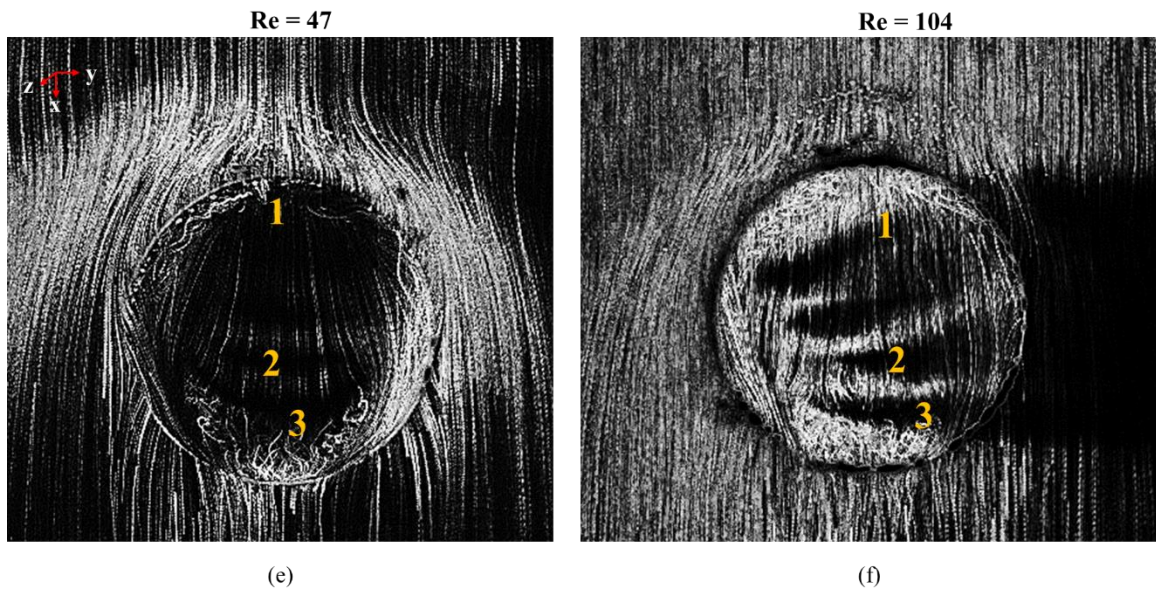
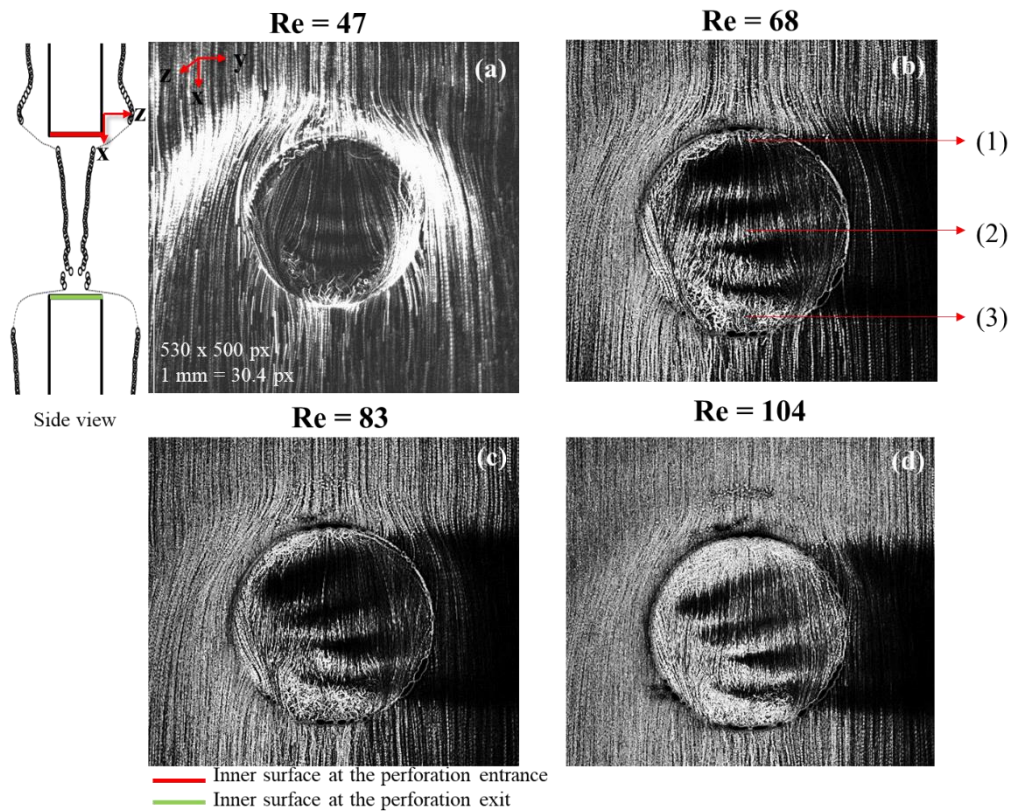


Figure 5-11: 50 superposed images of fluid film with florescent tracer particles showing streamlines in $x - y$ on a perforated plate with hysteresis curtain at (a) $Re = 47$ (b) $Re = 68$ (c) $Re = 83$ and inertial curtain at (d) $Re = 104$ ($Re > Re_{cr}$). Enlarged image of liquid curtain with dominant showing (1) Dean Vortices, (2) Capillary waves (3) recirculation $x-y$ plane. Diameter of the perforation $d = 8$ mm and thickness of the plate $t = 0.5$ mm is used. Test liquid is deionized water ($Ka = 3920$).

In structured packings, perforations are relatively smaller in diameter (2 – 4 mm). We repeat the experiments on a perforated plate with a perforation of diameter 4 mm using two test liquids. The trajectories obtained from 20 superimposed images of the liquid film on a perforation are illustrated in **Figure 5-12**. We also qualitatively investigate the influence of liquid surface tension and viscosity on the flow patterns.

In the case of deionized water: Two distinctive vortices of kidney bean shape have been observed in $x - y$ plane within the liquid curtain (see **Figure 5-12a**).

In case of propan-2-ol: The vortices in $x - y$ plane is localized just above the inner surface of the perforation exit (see **Figure 5-12b**). Due to the relatively high dynamic viscosity of propan-2-ol, the vortex structures are relatively damped.

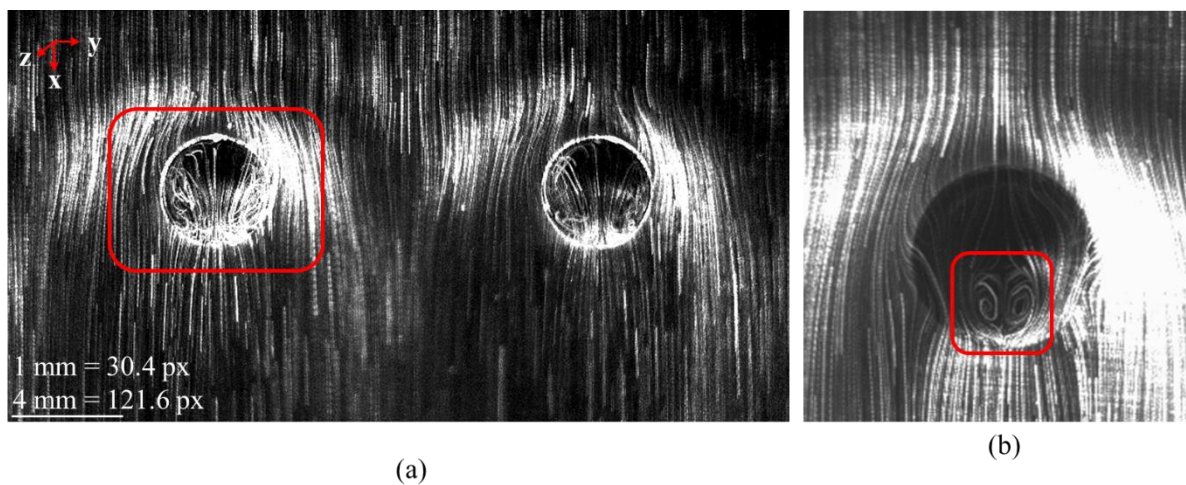


Figure 5-12: 20 superposed images of fluid film with fluorescent tracer particles showing streamlines in $x - y$ on a perforated plate ($d = 4$ mm) with inertial curtain using (a) Deionized water ($\mu = 0,001$ Pa.s, $\sigma = 0.073$ N/m) ($Re = 104$, $Ka = 3920$) (b) propan-2-ol ($\mu = 0.002$ Pa.s, $\sigma = 0.021$ N/m) ($Re = 34$, $Ka = 348$).

5.3. Axial velocity (u_x) on perforated plate

Figure 5-13 compares the experimental mean velocity measured on a perforated plate of two different diameters as a function of supply flow rate. The test plate is supplied on one face with uniform liquid film distribution. The liquid curtain is maintained at all supply Reynolds numbers. The spatiotemporal average of the axial velocity is plotted as a function of supply Reynolds number. The average is done on the complete ROI. We report that the mean axial velocity u_x is 30-40% for $d = 4$ mm and 15-26% for $d = 8$ mm lower than the mean theoretical velocity of the film on a non-perforated plate. The errors are computed for all measured values

except when $Q = 0.23 \text{ m}^3/\text{mh}$ (marked in **Figure 5-13**). In both perforated plate cases, an unusual decrease in measured u_x compared to theoretical value is noted.

The decrease in measured mean velocity can be explained this from the profile of the liquid film around and within the perforation (see **Figure 5-1**). The film thickness drastically changes in the perforation, consequently changing the local axial velocity. Liquid film locally slows down at the entrance of the perforation due to the stagnation point (capillary ridge). Liquid film accelerates in the intermediate curtain region with the free-fall velocity, specifically for large diameters ($d = 8 \text{ mm}$). Finally, liquid film decelerates as it impacts the exit edge of the perforation (inertial ridge).

For small perforation diameter ($d = 4 \text{ mm}$), the intermediate free fall film region is very small. The liquid curtain is constantly under the influence of stagnation points (entrance and exit). Thus, we note a significant decrease in mean axial velocity compared to the mean velocity of liquid film on a flat plate as well as perforated plates with large diameters.

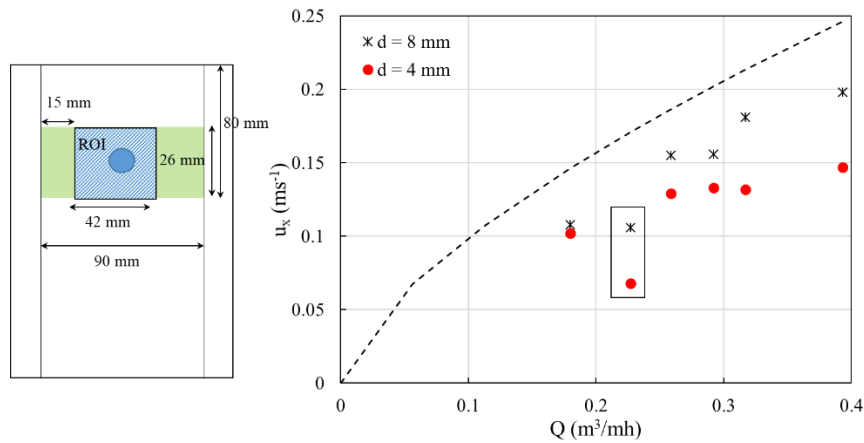


Figure 5-13: ROI of the post processed image. Comparison of the spatio-temporal mean velocity measured on perforated plates with the theoretical mean velocity on non perforated plates. Two unusual measured values are highlighted in black square. Test liquid used is propan-2-ol ($Ka = 348$).

5.4. Probability density distribution of negative velocity

In **Figure 5-14a**, the time series axial velocities measured at the center of the perforation are presented. The velocity results are shown in pixels to address the uncertainty in measured values, approximately of the order of 0.05 px . We observe both positive and negative velocity vectors in the center of the curtain. The negative velocity values correspond to the particles that move in the reverse flow direction. In **Figure 5-14b**, the probability density function of axial velocity vectors found at the center of the perforation is plotted. The flow velocity is globally

positive with a mean value of 0.1. The PDF is slightly skewed towards the positive side. However, the intensity of the events with negative velocities is non-negligible.

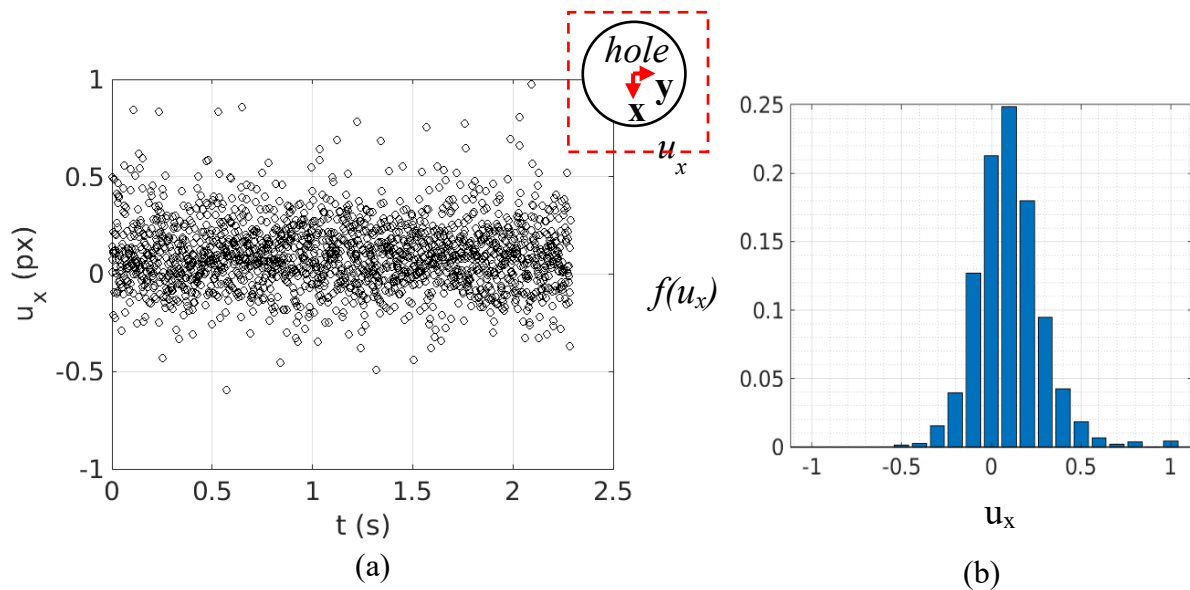
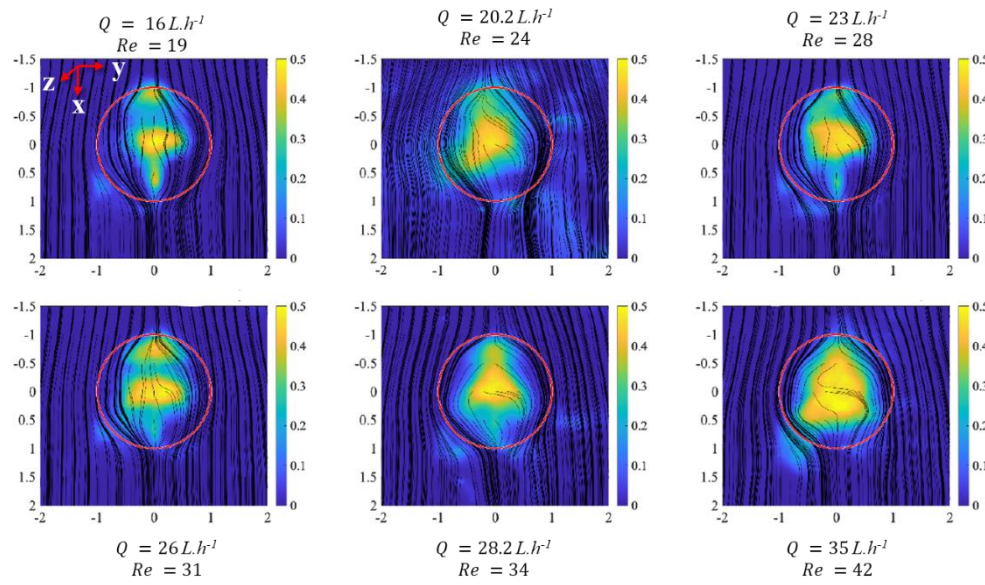


Figure 5-14: (a) Temporal variation of instantaneous axial velocity u_x at the center of the perforation (see insert) and (b) corresponding histogram of the u_x . Supply flow rate is $23 \text{ L}\cdot\text{h}^{-1}$ and mean theoretical velocity is $u_{th} = 0.23 \text{ ms}^{-1}$.

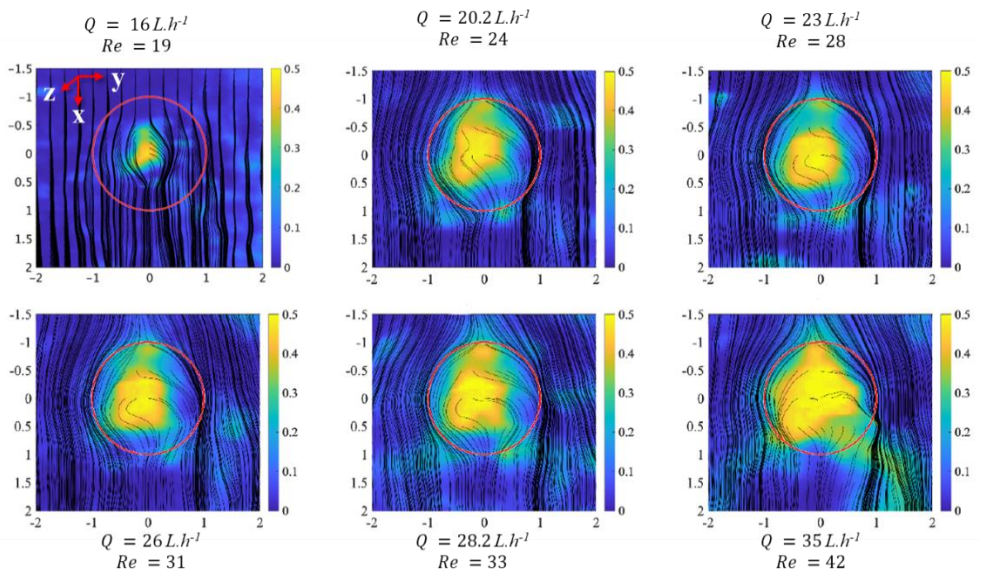
Following the same approach, we examine the PDF of negative velocity in the liquid curtain using 2D color maps (see **Figure 5-15ab** and Figure S5.5).

The color scale ranges between 0 (deep blue) to 0.5 (pale yellow), corresponding to 0% occurrence of negative velocity vectors to almost 50% occurrence. x and y coordinates are centered by considering the center of the perforation as a reference. In this specific case, the plate is supplied on one face (see **Figure 5-15a**) and two faces (see **Figure 5-15b**). The black lines are the steady streamlines, and they represent the mean flow path. For clarity purposes, only a few lines are drawn. We observe the strong intensity of negative velocities in the entrance, center, and exit of the perforation.

We consistently report a localized region at the center of the perforation, where the occurrence of negative velocity is dominant. For the lower Reynolds number, this region is small. With an increase in Reynolds number, the negative velocity dominant region extends radially in the perforation. Some spikes of the intensity of negative velocities are also observed at the entrance and exit of the perforation. For highest supply flow rate, negative velocities represent 60% of the liquid curtain for one face supply and around 80% for two face supply conditions. Overall, for a given supply flow rate, recirculation is relatively intense when the plate is supplied on both faces.



(a)



(b)

Figure 5-15: Probability density map of the negative velocities in and around the perforation in curtain mode for six different volumetric flow rates per unit width of the film (a) one face supply and (b) two-face supply. Diameter of the perforation $d = 4$ mm and plate thickness $t = 0.5$ mm.

5.5. Tracking

A single particle is tracked over 200 images to measure the change in its apparent size (d_i) (see **Figure 5-16b**), horizontal velocity (u_y) (see **Figure 5-16c**) and axial velocity (see **Figure 5-16d**). By convention, a positive vertical velocity corresponds to downwards displacements.

In the wall-bounded liquid film, the size of the particle decreases while it flows down. u_x is approximately constant and u_y is approximately zero or very low. Once the particle enters the perforation ($\tau=165$ ms), it is trapped in the attached rim. The tracer particle follows a helical path rim (vortex in $x - z$ plane) along the radius of curvature of the perforation.

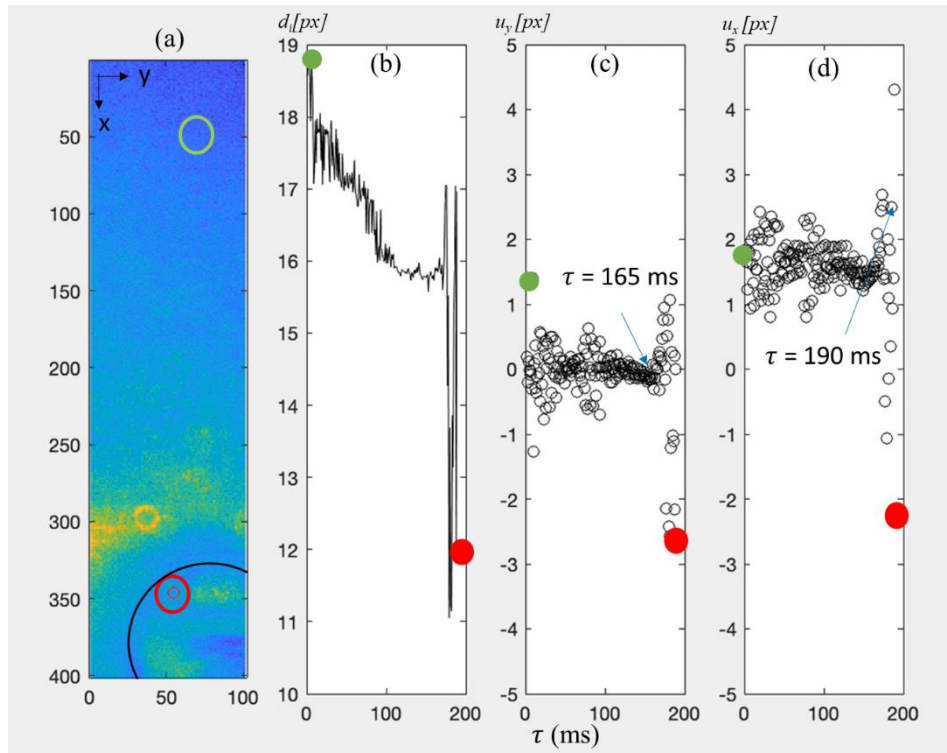


Figure 5-16: Particle tracking spatiotemporal data (sampled at 800 Hz) (a) 2D color map image of the liquid film on a perforated plate (black arc: perforation). Tracer particle position at $\tau = 1$ ms (green circle and dot) and 250 ms (red circle and dot). (b) Time evolution of apparent size of the particles, (b) time evolution of horizontal component of velocity (u_y), (c) time evolution of vertical component of velocity (u_x). Key events are marked by dots and arrows. A perforation of diameter $d = 8$ mm and plate of thickness $t = 0.5$ mm is used. Test liquid used is propan-2-ol ($Ka = 348$).

At the entrance of the perforation, u_x increases dramatically ($\tau = 165$ ms, blue arrow in **Figure 5-16c**) and then decreases to negative values ($\tau = 190$ ms, blue arrow in **Figure 5-16d**). The sudden increase in u_x and u_y is due to the particle being pulled in the rim attached to the inner surface or region (1) of the perforation. The presence of recirculation region is confirmed by a sudden drop in u_x and u_y to negative values at the entrance of the perforation.

5.6. Flow characteristics through DMD post processing

We apply Dynamic Mode Decomposition (DMD) to the liquid curtain to examine the dominant frequency modes. We consider a test case where the perforated plate ($d = 4$ mm) is supplied on one face. The dominant frequency modes are examined for different u_x (or Q) (see **Figure 5-17a**). When examining the spectra of the DMD amplitude, one can notice a sharp peak for the lowest flow rates, with a signal-to-noise ratio of 1.6. This peak is becoming fader as the flow rate increases but is still somehow present. However, an exception is reported for case $u_x = 0.17 \text{ ms}^{-1}$ in which we do not observe any pronounced peak (not presented here). Not taking this particular case into account, **Figure 5-17b** show that the frequency increases linearly ($R^2 = 0.99$) with the increase in axial velocity (theoretical value). We note that the linear fit do not pass through zero when f is zero. It is probably related to a characteristic mean velocity at which the curtain ruptures.

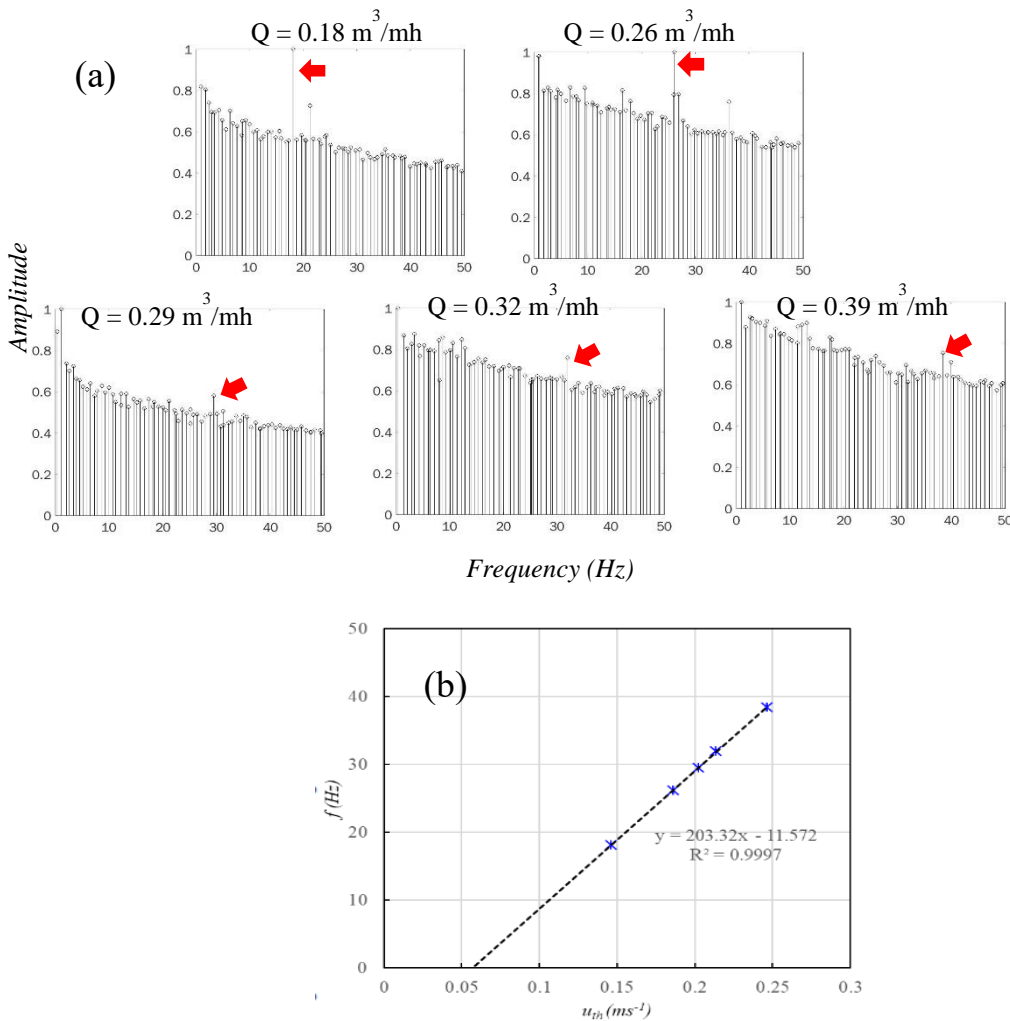


Figure 5-17: (a) Oscillation frequencies obtained from DMD post processing. (b) Dominant frequency modes as a function of mean axial velocity.

6. Discussion

6.1. Vortex structures in liquid curtain on a perforated plate

In the rim of the liquid curtain:

The vortex structure in regions (1) and (3) can be characterized by the axis around which the vortices rotate. The vortices rotating around y-axis (region (1)) are similar to the Dean vortices resulting from a centrifugal instability in curved channels depending upon the magnitude of the wall curvature. These vortices are formed due to high fluid velocity in the center of the curved channel compared to the near-wall fluid particles. The higher velocity fluid particles are subjected to greater centrifugal forces, which direct them outward (towards the concave of the wall). As a result, particles that are already at the concave wall are forced to move inward toward the center of the channel where the velocities are higher. This process is repeated throughout the curved channel, resulting in pairs of counter-rotating vortices, often referred to as Dean vortices. The classic definition of Dean number^{136,158} is

$$De = \frac{\rho u_x l_a}{\mu} \left(\frac{l_a}{R} \right)^{1/2}$$

where l_a is a typical length scale associated with the curved channel cross-section (radius of a circular pipe), R is the radius of curvature of the path of the channel, u_x is the axial velocity. Dean found that this secondary flow would only be present if the dimensionless parameter Dean parameter were greater than 36.6.

The rim region of the liquid curtain behaves like a curved channel. We redefine Dean number using the length scales of the rim and perforation diameter. The expression becomes:

$$De = Re \sqrt{\frac{d_R}{R_1}}$$

Where d_R is the diameter and R_1 is the radius of the curvature of the convex surface of the curved channel).

We measured d_R and R_1 from the images of streamline patterns (see **Figure 5-18a**). The value d_R is 0.63 ± 0.09 mm for a perforation of diameter $d = 8$ mm and $t = 0.5$ mm. The order of magnitude of d_R is slightly higher than the thickness of the plate.

Dean number is plotted as a function of supply flow rate per unit width of the film (see **Figure 5-18b**). De increases with the supply flow rate. Dean criteria is satisfied when the supply flow rate is greater than $0.3 \text{ m}^3/\text{mh}$ (28 L.h^{-1}). However, Dean vortices are observed regardless of

Dean criteria ($De < 36.6$). This difference is probably due to the adaptation of length scales to redefine the Dean number, initially defined for solid boundary channels. Unlike curved channels, there is no continuous solid boundary all around the liquid rim. The part of the rim attached to the inner surface of the perforation is in contact with the solid boundary. The other part of the rim is a free surface film.

Xie et al¹⁰¹, in their numerical study, reported that vortices in the rim occur as rotating cells.

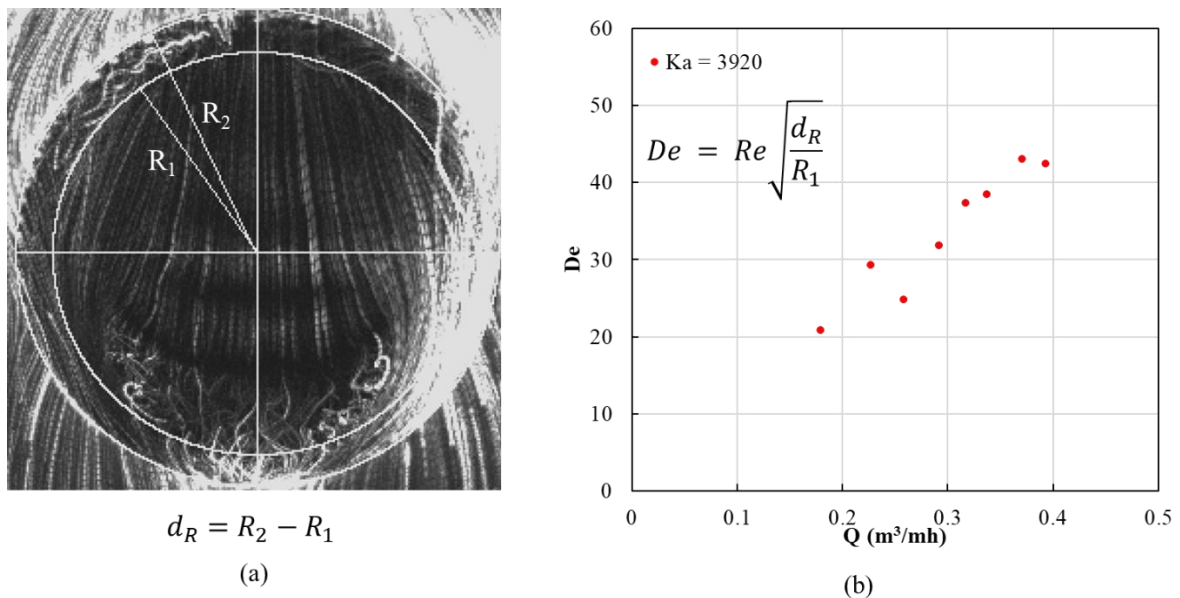


Figure 5-18:(a) 20 superimposed images to measure R_1 and d_R (b) Dean number (De) calculated for the measured values of R_1 and d_R for a liquid curtain in the perforation for eight different supply flow rate per width of the film.

At the exit of the perforation

The descending freely falling film and the liquid film conducted through the rim impinges the solid boundary of the perforation edge. As a result of this action, liquid film rebounds and rolls up into counter-rotating vortex rings and begins to oscillate at a fixed position. These rebounding counter-rotating vortex rings in the liquid curtain are observed even at low flow rates per unit width. In small diameter perforation, these vortex rings occur in pairs, also known as kidney-pair vortex (see **Figure 5-12**). The characteristic length of the vortex is observed to vary with the diameter of perforation and liquid viscosity. The vortex structures are chaotic in large diameters. (see **Figure 5-11**).

6.2. DMD spatial modes

In DMD, a frequency is associated with a spatial mode, and the typical streamlines associated with those modes are shown in **Figure 5-19** and **Figure 5-20** together with the typical vertical

velocity that directs them outward (induces an outward motion). Spatial modes corresponding to the dominant frequencies are reconstructed and plotted at three different time periods and phase angles for two different supply conditions (see Figure S5.6). The red color on the 2D map corresponds to high axial velocity (greater than mean velocity), and conversely, the blue color represents negative axial velocity. For the sake of illustration, actual negative axial velocity vectors are added to the positive average velocity. The onset of the instability occurs at the entrance, slightly on either side of the hole. Overall, the velocity is positive. However, the velocity vectors change sign primarily in the curtain region and downstream. In **Figure 5-19b**, both positive and negative velocity distribution is observed. The spatial modes are some kind of low-frequency oscillation associated with the DMD modes rather than the expected recirculation observed earlier (see **Figure 5-11**, **Figure 5-12**). With the increase in supply flow rate (see **Figure 5-20**), the intensity of the negative and positive velocity vectors is damped. When inertia forces are dominant in the flow, the amplitude and wavelength of capillary waves are small.

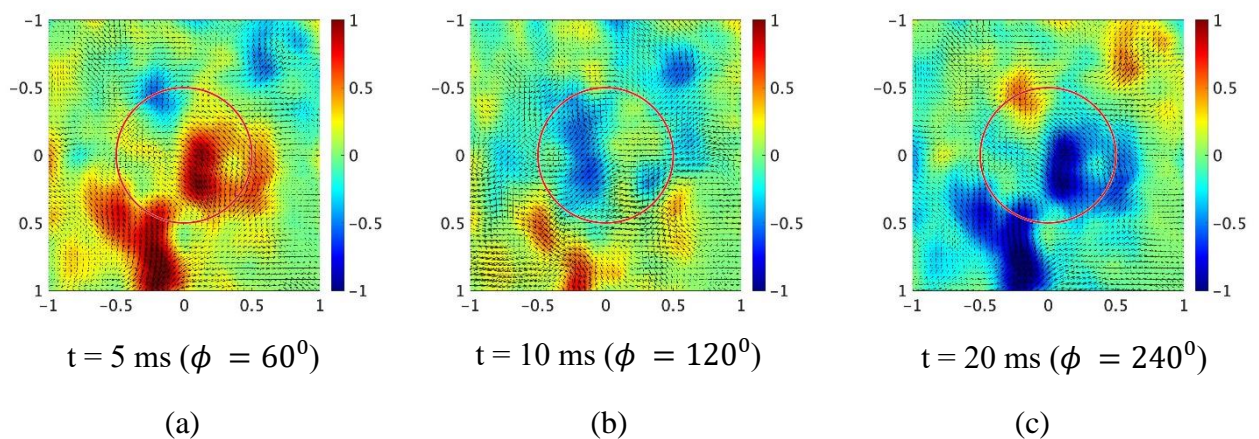


Figure 5-19: DMD Relative spatial axial velocities in the liquid curtain at 18.2 Hz with supply flow rate of $Q = 0.18 \text{ m}^3/\text{mh}$; $Re = 19$.

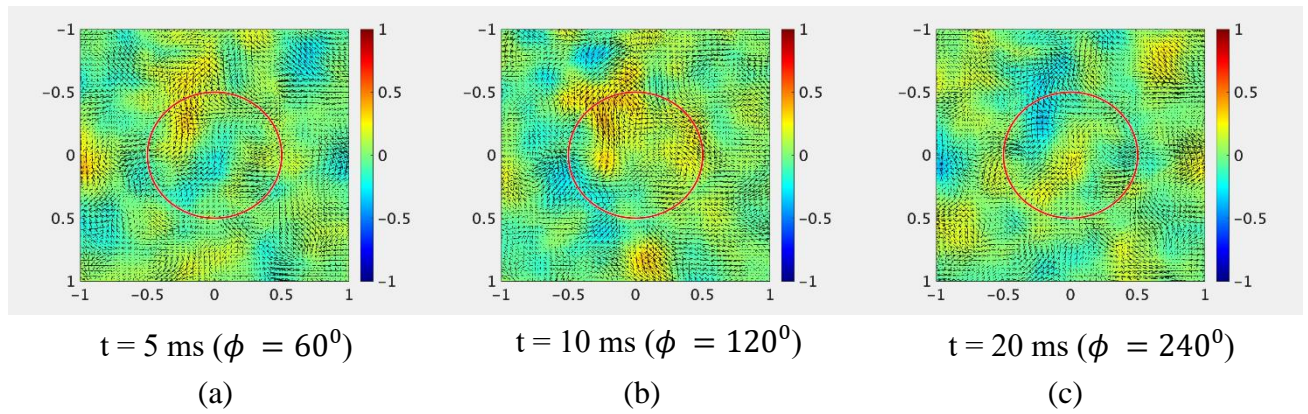


Figure 5-20: DMD Relative spatial axial velocities in the liquid curtain at 38.4 Hz with supply flow rate of $Q = 0.39 \text{ m}^3/\text{mh}$; $Re = 42$.

7. Conclusions

For the first time, a new non-intrusive optical technique, 3D 3C PTV with the concept of defocus was implemented for characterization of liquid film on a “metallic” vertical flat plate and a vertical perforated plate. By adding an opaque disk (annular aperture) between the camera lens and the sensor, a significant improvement in the global noise reduction and the detection capacity is observed. A new type of image processing technique by optical flow algorithm is used to measure 2D velocity. The method’s application is validated with 2D velocity measurements of a falling liquid film over a flat at first and then extended to the liquid films on a perforated plate.

Liquid film on flat plate

Measured mean axial velocities obtained were approximately 10-20% lower than the theoretical mean velocity from Nusselt’s solution. We attempted to measure the evolution of the apparent size of the particle in the film depth. The particle's apparent size does not vary significantly enough to obtain a relation with the depth of the film. However, the method permits to measure all 3C velocity vectors.

Local streamline variations were measured in the twin liquid films on perforated plate for different supply Reynolds number, diameter of the perforation (d) and liquid properties (Ka). The liquid film recirculation is predominantly observed in the liquid curtain at stagnation points. This is an important difference between wall-bounded and twin films. The vortex structures become chaotic with the increase in Reynolds number.

For large perforation, the vortex structures in the curved rim are characterized using Dean number, originally applied in curved channels. These vortex structures satisfy Dean’s criteria ($De > 36.6$).

Impingement of the curtain on the exit edge of the perforation results in a pair of counter rotating vortices ($d = 4 \text{ mm}$, kidney-pair vortices) and small-scale eddies ($d = 8 \text{ mm}$).

The mean axial velocities on the perforated plate are 30-40% for $d = 4 \text{ mm}$ and 15-26% for $d = 8 \text{ mm}$ lower than theoretical values. Interestingly, these mean values are also lower than the mean velocity measured on a non-perforated plate.

At low Reynolds number, the intensity of negative axial velocity is localized in the center of the liquid curtain. Such zones extend radially, which covers almost 80% of the liquid curtain.

DMD analysis is applied to extract the dynamic information of the liquid curtain. The spatial modes are extracted corresponding to the dominant frequencies. The flow patterns in the liquid curtain resemble low-frequency oscillations type of flow. These oscillations are initiated at the entrance of the perforation. It is observed to develop in the liquid curtain and propagates downstream the perforation.

In this study, we explored new techniques that paved the way for understanding complex flow structures in the liquid curtain. A rigorous interpretation of the results is necessary to confirm their impact in mass transfer intensification in corrugated and perforated structured packing. Vortex structures in the flow are known to transport the liquid phase toward the interface in counter-current flow, producing steeper concentration gradients at the interfaces. As a result, the mass fluxes through the interface increase, and then mass transfer intensifies. The stagnation points may reduce the liquid film velocity locally, increasing the local residence time, leading to a longer gas-liquid contact time.

8. Supplementary Material

A1. Difference between focussed and defocussed tracer particles

In Figure S5.1a, we present an example of the fluorescent tracer particles observed when the camera is set to focus (Figure S5.1b) and defocus (Figure S5.1b).

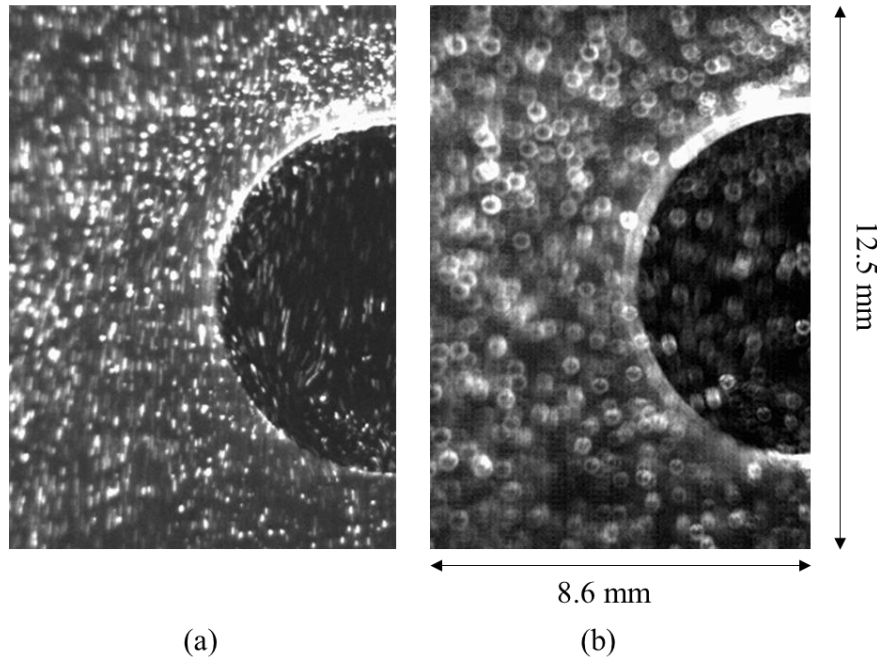


Figure S5.1: (a) Focussed fluorescent tracer particle (b) Defocussed fluorescent tracer particles in the liquid film (deionised water) in curtain mode.

A2. Optical flow for motion detection: relative magnification of the particle

This approach has been detailed in the doctoral thesis work of Baudoin¹⁵⁹. We, however, present main idea of the capacity of optical flow algorithm to measure displacements perpendicular to the focal plane; that is to say to quantify the magnification (positive or negative) of the particle between two images. To determine the accuracy of this approach, a fundamental experiment is set up (see Baudoin¹⁵⁹ (Annexe C.1)). It consists in the acquisition of images of the block illuminated by a laser beam. A pinhole is used to set the initial beam size to a minimum of about 250 m. In order to limit the problems of light diffraction by the particles contained in the block, only a region close to the block is used. This region covers 2 cm wide. The camera is moved by a micrometric positioner, controlled remotely by computer (Figure S5.2).

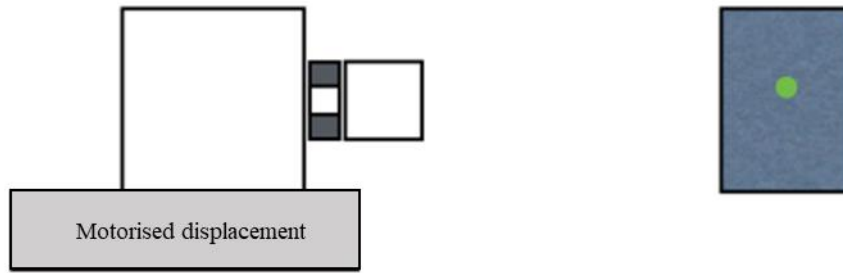


Figure S5.2 : Schematic presentation of the volume measurement using direct beam (Baudoin¹⁵⁹).

The experiments were performed by moving the camera in steps of 100 μm . It is thus possible to determine the average magnification measured for different relative displacements of the camera and for all the particles contained in the image. The process is continued by moving to distances up to 800 μm for a 100 μm of increment. For 200 μm , the result will be divided by 2. The average results obtained for displacements between two images from 100 to 800 m are presented in Figure S5.3.

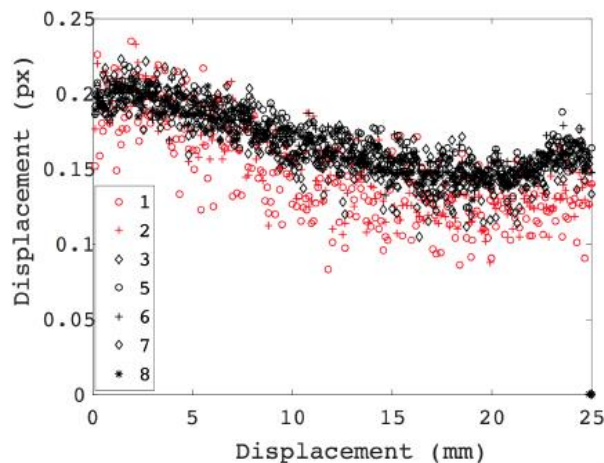
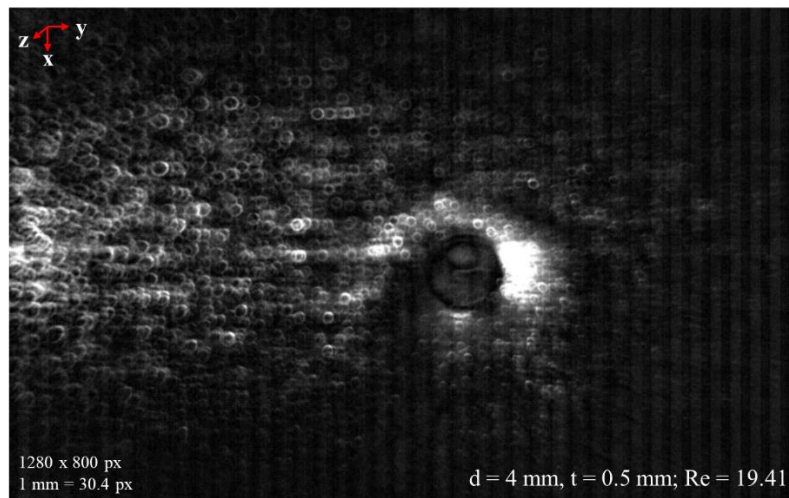


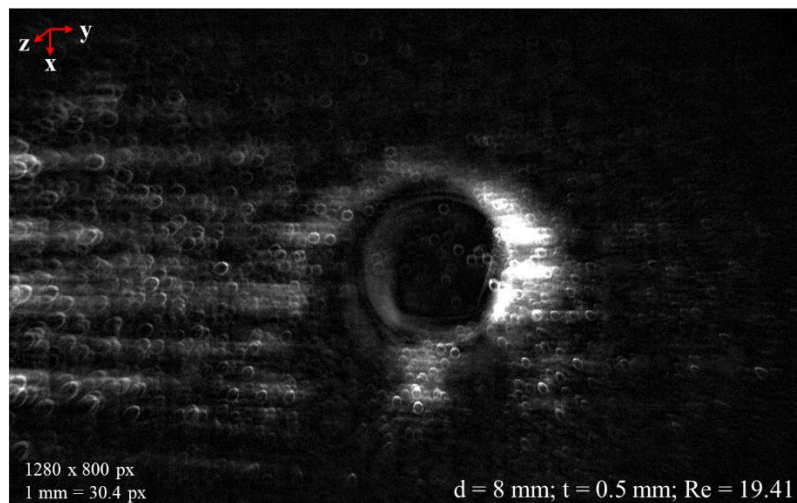
Figure S5.3: Relative displacement of the particles measured by moving camera up to 800 μm in 100 μm increments

It is interesting to note that the displacement of the particles has a very small variation. The measured displacements present a small variation between the different positions of the camera. This means that a relative magnification of 0.2 px is perfectly measured because it corresponds to $1/8^{\text{th}}$ of magnification obtained in addition to the displacement in the sense of depth which is eight times higher.

A3. Probability distribution of negative axial velocities



(a)



(b)

Figure S5.4: Example of a pre-processed raw images of a perforated plate

Some examples of pre-processed raw images, obtained by denoising and adjusting the contrast, are presented in Figure S5.4. This enhancement procedure is applied to all the images before applying post processing techniques.

A4. Probability distribution of negative axial velocities

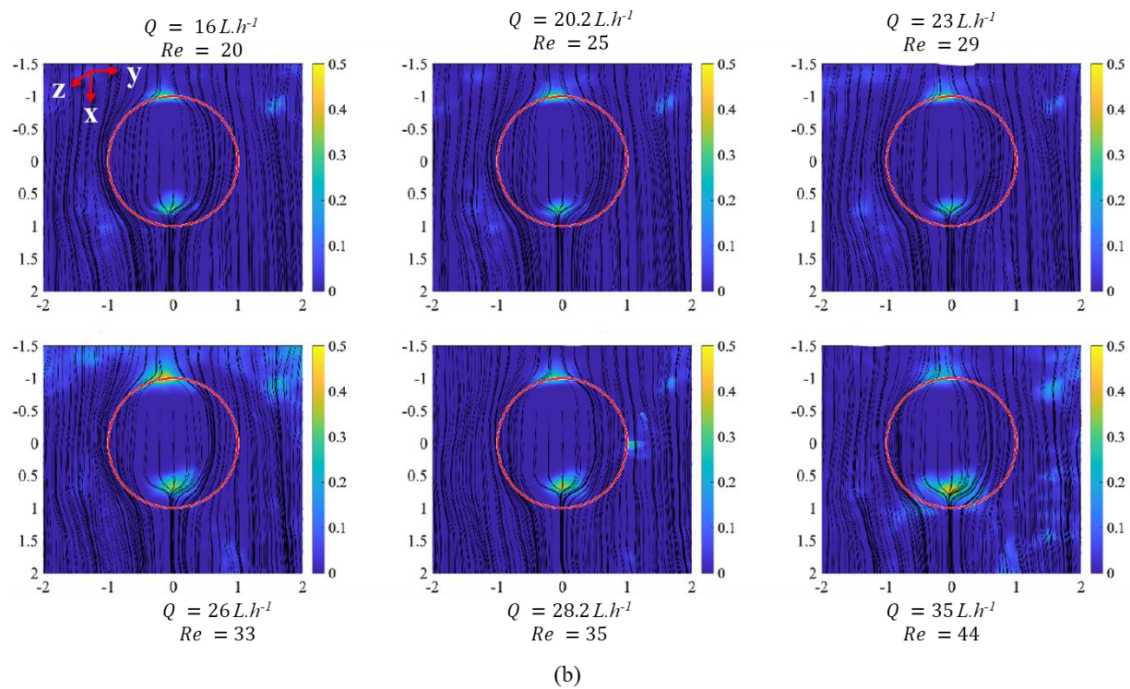
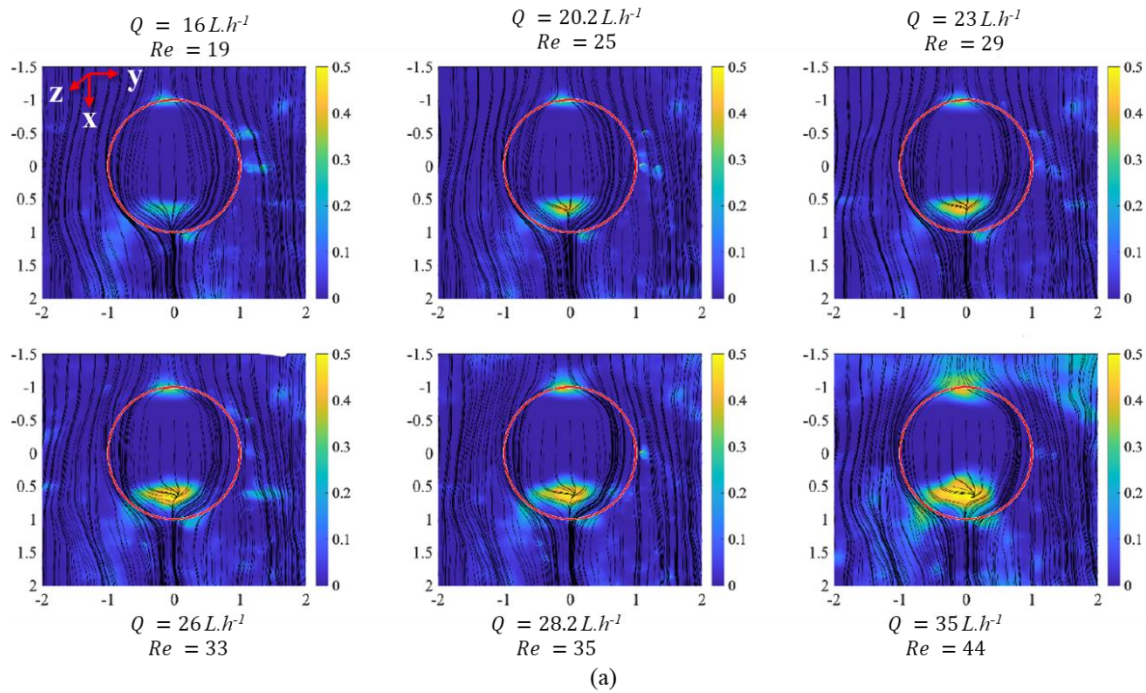


Figure S5.5: Probability density map of the negative velocities in and around the perforation in curtain mode for six different volumetric flow rate per width of the film in (a) on face supply and (b) two-face supply. Diameter of the perforation $d = 8$ mm and plate thickness $t = 0.5$ mm.

The intensity of negative velocities is predominantly high at the entrance and exit of the perforation. In the presence of stagnation points, the liquid film slightly rebound in the reverse flow direction. An increase in supply flow rate per unit width tends to slightly increase the spreading of the recirculation zones. The test liquid is propan-2-ol. The test liquid's high viscous and low surface tension property relatively dampens the vorticity regions compared to high surface tension liquids such as water. The freely falling liquid curtain in the mid region shows no reverse flow.

A5. DMD spatial modes

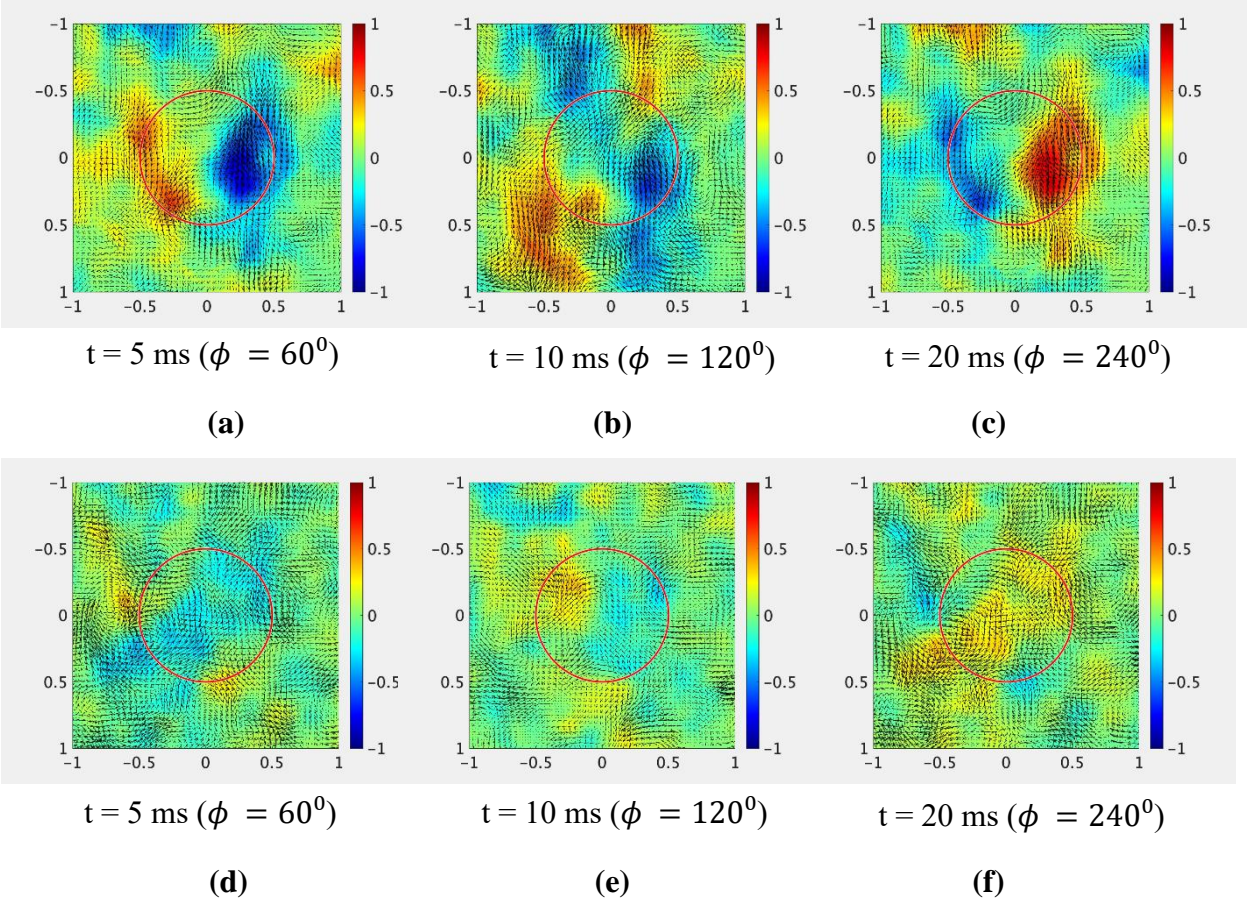


Figure S5.6: DMD Relative spatial axial velocities in the liquid curtain (a, b, c) 29.49 Hz ($Q = 0.29 \text{ m}^3/\text{mh}$) (d, e, f) 32.02 Hz ($Q = 0.32 \text{ m}^3/\text{mh}$).

6 Conclusions and Perspectives

The thesis work is a part of a CIFRE contract between LGPM laboratory and Air Liquide Research & Development. The work aims to understand the local hydrodynamics of a liquid film flowing over perforations which are identified to contribute to liquid phase redistribution and mass transfer on a corrugated and perforated metallic sheet of structured packing. In a structured packing column, liquid spreads itself at various scales. Pavlenko (2018) observed that the hydrodynamics of the liquid film on local geometry (microtextures and holes) of the structured packing element has a significant effect on the way liquid spreads. However, we have noted that the fundamental mechanisms of the liquid film on complex surfaces are not very clearly known.

At LGPM, an experimental test bench is newly constructed to study the hydrodynamics of liquid film on single element of structured packing. The test plate is equipped with liquid distributors, specifically designed to supply both sides of the plate as in industrial conditions. The test bench is adapted to incorporate supplementary devices and apparatuses to perform measurements such as shadowgraph techniques, spatiotemporal liquid film thickness (using CCS), and velocity measurements (PIV/PTV).

As a first step, we experimentally explored different transition mechanisms of liquid film flowing over a single perforation on a flat vertical plate. Quite often, structured packing elements are perforated to aid in liquid phase redistribution and thereby mass-transfer enhancement. We used shadowgraph techniques to qualitatively observe the liquid film transition in the perforation. As a function of Reynolds number, we observed rim, drop/column, and pendant sheet modes of transition of the liquid film in the perforations for increasing Reynolds number. When inertia completely takes over surface tension forces, the liquid film fills the hole. This state occurs at a critical value of Reynolds number referred to as curtain Reynolds number (Re_{cr}). We measured curtain Reynolds number for a wide range of geometrical parameters and liquid properties. Increase in Re_{cr} is noted with the increase in perforation diameter and plate thickness up to a certain value. A plateau is attained at higher diameters. The curtain was observed to exhibit teapot phenomenon at the entrance of the perforation for thicker plates. Liquid properties are characterised using Kapitza number. A scaling of $Re_{cr} \propto (Ka)^{3/5}$ is retrieved for large perforation diameters (plateau region). We established a criterion for curtain formation by writing a momentum balance equation at the stagnation point (entrance of the perforation). The model agreed well with the experiments especially in the case of high-viscosity liquids. The profile of the curtain highlighted a stretched

region and a region of stationary varicose waves. The varicose waves are expected to enhance mass-transfer through the liquid curtain. We also highlighted the most striking phenomenon, namely the hysteresis of the liquid curtain. This hysteretic behaviour of the curtain may be favourable in structured packing as it increases the liquid retention at low flow rates.

Small diameter perforations (up to 4 mm) irrigate the other face (back) of the plate mainly through rim and curtain modes of transition. At low Reynolds number, the liquid film follows the perforation structure instead of flowing through them. With the increase in Reynolds number, it shifts to rim mode and a part of the liquid passes to the other face (back of the plate). At curtain Reynolds number and beyond, the transfer of liquid is through curtain mode. Thanks to hysteresis, the liquid curtain, once formed, stays maintained even after reducing the supply flow rate. We experimentally quantified the liquid flow rate transferred through the perforation(s) in curtain mode. The volume flow rate transferred (per diameter) varies linearly with the supply flow rate (per unit width).

The transferred volume flow rate is examined below each row of perforations. The volume flow rate flowing on the back of the plate increases and relaxes towards an asymptotic value as the number of the perforation rows increases. Starting from the third row of perforations, the volume flow rate on the back of the plate already reaches 65% to 90% (7th row) of its asymptotic value. Inertia forces accelerate this relaxation as the supply flow rate increases. A simple recurrence model is proposed to estimate the volume flow rate per unit width on the back of the plate below each row of perforations. Our model well estimates the experimental trend of volume flow rate transferred through the perforations at low supply flow rates.

The liquid transferred through the perforations leaks as a rivulet. We selected a standard perforation diameter to study the evolution of the rivulet in streamwise and spanwise directions of the plate as a function of supply Reynolds number when the perforation operates in curtain mode. The rivulet flowing from the perforation widens as the 0.25 power of the rescaled streamwise distance and flattens as the -0.075 power of this distance.

In the case of a row of perforations, adjacent rivulets merge to form a continuous wavy film at a traveled distance which scales as the 4.58 power of the perforation spacing. The scaling exponents obtained in our study are in close agreement with the theoretical exponents derived by Shetty & Cerro (1995) and Duffy & Moffatt (1997) for a rivulet spreading in the capillary-dominant regime.

The continuous wavy surface after the merging relaxes downstream to a flat film (spanwise). The theoretical relaxation length scales as the $13/3$ power of the spacing between the perforations.

As a final part of the study, we implemented a new 3D 3C Particle tracking Velocimetry with the concept of defocus to measure local instantaneous velocity in the thin falling liquid films on a non-perforated plate and a perforated plate. We capture spatiotemporal images by adjusting defocus of the lens on tracer particles. Using optical flow algorithms, we obtain global 2D velocity vectors. The spatiotemporal association of these vectors is then performed based on a Particle Tracking Velocimetry method. The apparent size of the defocused particles dispersed in the 3D space is computed to locate their position. An attempt has been made to obtain their size in the film depth using a thin lens approximation (Damaschke (2002)).

We first implement the method to the liquid film on a flat vertical plate to validate its feasibility. 2D velocity vectors are computed as a function of Reynolds number. The measured mean axial component velocity is 10 – 20 % lower than the Nusselt theory. An attempt has been made to locate the tracer particles in 3D space. The change in the particle size is too small to estimate its precise position. The feasibility test concludes that the results obtained are not far from the theoretical values, however, further refinement is necessary to gain in precision.

We first analysed the streamline patterns on a perforated plate to identify specific regions where the flow structures are complex and may contribute to mass transfer intensification. Localized areas (capillary ridge and liquid curtain) in the liquid film have been identified with vortical structures (Horseshoe Vortex, Dean Vortex, and Counter-rotating Kidney-pair Vortex). The vortex structures are observed to be a function of perforation diameter and liquid viscosity.

Finally, quantitative measurements are performed using 3D 3C PTV in curtain mode of transition. The mean axial velocity of the liquid film on the perforated plate consistently measures a value up to 20% lower than the theory.

We then assessed the recirculation zones in the liquid curtain by measuring (i) 2D maps of the probability distribution of negative axial velocity in the liquid curtain (ii) particle trajectory of a single particle (iii) dominant frequency modes via DMD post-processing.

We observed a complex flow pattern on both faces of the plate in the liquid curtain. In addition, the liquid curtain is highly hysteretic at low irrigation densities. With these observations, we expect that maximizing the number of perforations in an actual structured packing should promote curtain formation and should significantly enhance the liquid redistribution and mass transfer. We proposed a new design of structured packing elements, which will be tested in the cryogenic distillation column at Air Liquide.

Perspectives

This work delivers diverse viewpoints to explore further the complex surfaces of the elements of structured packings. Even though many macroscopic studies have indicated the importance of optimizing surface features on the packed elements, very little research has been undertaken on microscale. We have identified a few directions in the interest of continuity of our research in both experimentation and modeling perspectives:

- Influence of plate inclination angle on transition mechanisms of liquid film in perforations, liquid transfer from one side to other and rivulet spreading.
- Investigation of rivulet spreading by varying liquid properties to validate the Gaussian approximation of rivulet spanwise profiles along the plate.
- Investigating liquid transfer on horizontally corrugated and perforated plates and an extension to industrial corrugated and perforated plates. Modification to the linear model proposed in case of liquid transfer by including other packing element parameters such as: corrugation geometry, angle parameters.
- Improving the resolution of velocity measurements in all three dimensions. Use of pulsed laser of higher intensity, better adjustment of the laser sheet with respect to the film, validating the velocity measurements with thick films preferably high viscous fluids.

Appendix 1 : Construction of McCabe-Thiele diagram

We consider to address the basic concept of separation using McCabe-Thiele chart or $x - y$ diagram. By considering a simple form of pressure column with just one feed F . The location above and below the feed is called the rectification column and the stripping column. The condenser returns a liquid flow L to the column (reflux), the remaining liquid flow D is called distillate. In the same way, at the level of the boiler, a part is collected in liquid form B , the other is reinjected in vapour form L' . To simplify further, we will assume that the liquid and vapour flow rates are constant in both rectification and stripping sections of the column (i.e. Constant Molar Overflow (CMO) assumption). Now if mass balance is applied to condenser, reboiler and the column:

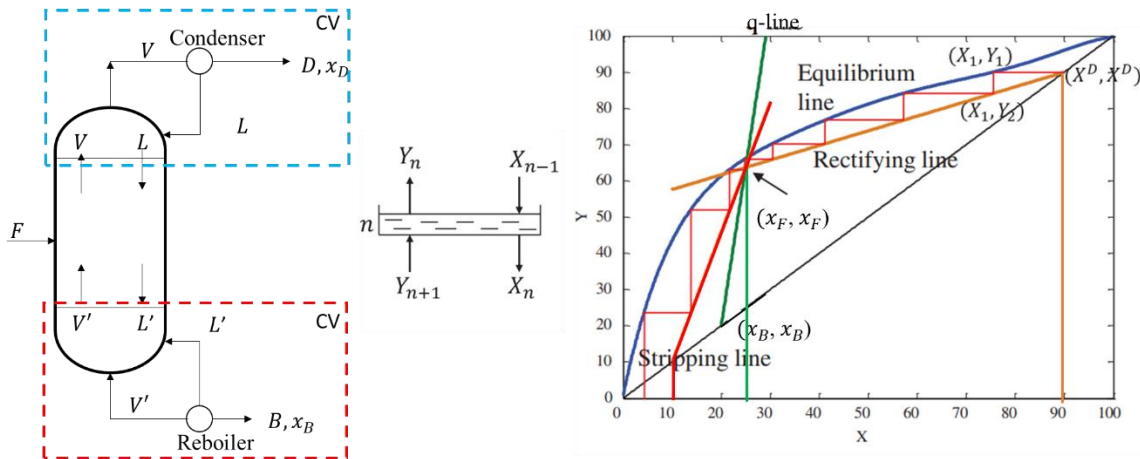


Figure A1.1: Simple representation of a separation column and a typical McCabe-Thiele diagram of theoretical stages¹⁶⁰

Mass balance of the condenser:

$$Vy = D x_d + L x \quad (1.1)$$

x , y are liquid and vapour fraction of the component respectively and x_d is a column specification.

$$y = \frac{L}{V}x + \frac{D}{V}x_d \quad (1.2)$$

By rearranging and introducing reflux ratio $R = L/D$ in the above equation, we get

$$y = \frac{R}{R+1}x + \frac{1}{R+1}x_d \quad (1.3)$$

Similarly, by mass balance of reboiler, we obtain:

$$y = \frac{L'}{V}x + \left(1 - \frac{L'}{V}\right)x_b \quad (1.4)$$

Finally, at the intersection of the rectifying and stripping sections, the feed is introduced, corresponding liquid and vapour compositions are determined via material balances.

By the mass balance of the column:

$$x_F F = x_D D + x_B B \quad (1.5)$$

$$q = 1 - \frac{x_F - x_B}{x_D - x_B} \quad (1.6)$$

With these 3 equations (Eq 1.1, 1.3 and 1.6) McCabe-Thiele diagram can be constructed by plotting operating lines. Detailed derivation is described in McCabe et al¹⁶¹. In the analysis of binary distillation systems, there are numerous ways of calculating the number of stages using computational software such as HYSYS, Aspen, or gPROMS. However, McCabe-Thiele graphical method is still very popular and widely used to determine the number of equilibrium stages needed to achieve a specified separation in a distillation column.

Diagram construction

The x-axis of the graph (see Figure A1.1) corresponds to the fraction of nitrogen in liquid phase and y-axis corresponds to the fraction of nitrogen in the vapour phase. The diagram consists of the vapour liquid equilibrium curve, the diagonal $y = x$, the rectification and stripping lines. Upper operating line for the rectifying section is plotted with the known value x_D . Draw a vertical line from x_D up to $y = x$ line (orange). In a similar way, locate lower operating point (x_B) (red) and the feed point (x_F) (green) on the x axis and draw a vertical line (see Figure A1.1) to intersect on $y = x$ line. Starting at the intersection of x_D on $y = x$ line, draw a rectifying operating line at a downward slope $R/(R + 1)$ (orange slope line). Draw a slope or q line, starting from the intersection of x_F and $y = x$. The slope of the q-line is $q/(q - 1)$ (green slope line).

- Slope of the q line is 1: If the feed is saturated liquid and has no vapour,
- Slope of the q line is ∞ : the line is vertical,
- Slope of the q line is 0: If the feed is saturated vapour, which means that the line is horizontal.

From the intersection of the x_F and the $y = x$ line, the slope of the lower or stripping operating line (red slope line) up to the point where the green q-line intersects the orange upper operating line.

Starting from the point, where x_D meets $y = x$ line, a horizontal line is drawn until it intersects the VLE curve. A vertical line is then drawn down from this point until it meets one of the

two operating lines. This process is repeated until the last vertical line falls to the left of the bottom product line. The number of theoretical trays can now be determined by counting the number of times the horizontal 'steps' touch the VLE curve (include the line that passes the bottoms product line). These trays are counted starting at the top right and moving to the bottom left.

Appendix 2: CAD model of the test bench

The CAD model of the test bench is illustrated here. The schematic representation of the principal test bench showed in chapter 3, 4, and 5 corresponds to the CAD model. However, additional measuring equipment used in chapters 4 and 5 is not presented here. The CAD model is designed by Joel Casalinho.

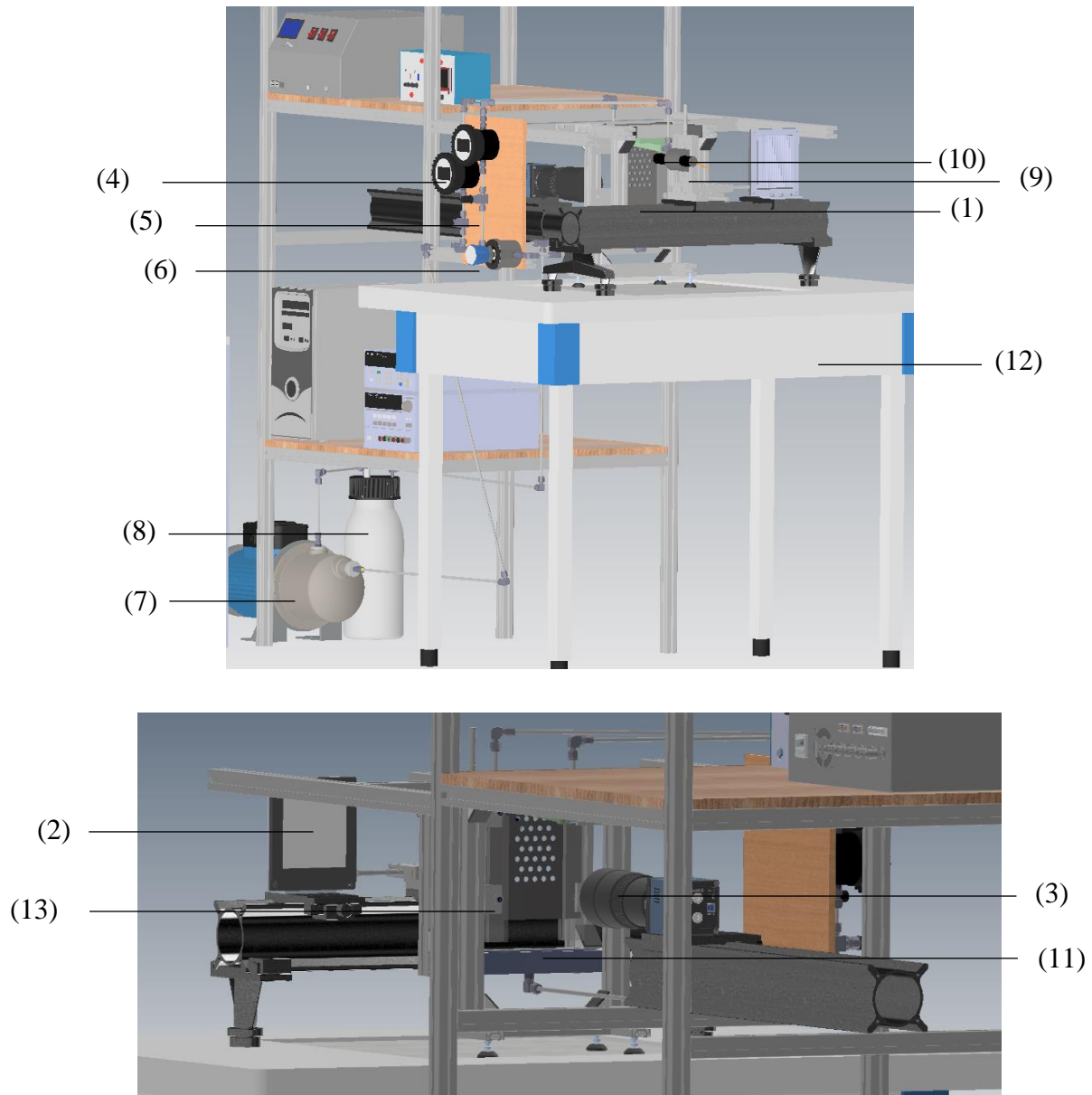


Figure A2.1: CAD model of the complete setup: 1. Test plate 2. LED panel 3. High speed camera 4. Volumetric flow meters 5. Needle control valve 6. Spillway 7. Gear pump 8. Reservoir 9. CCI sensor 10. Distributor 11. Liquid Collector 12. Anti-vibration mount 13. Frame that holds the plate.

Appendix 3 : Complementary information related to test setup construction

1.1. Evolution of distributor

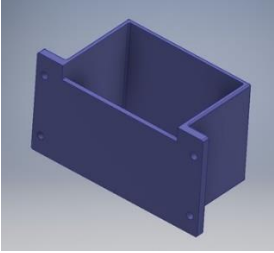

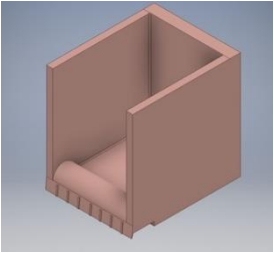
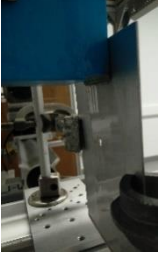
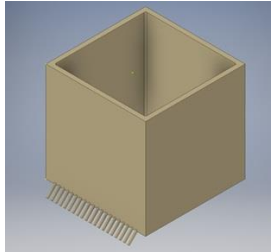
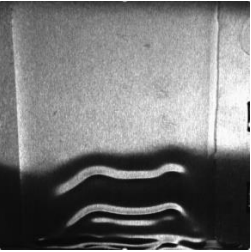
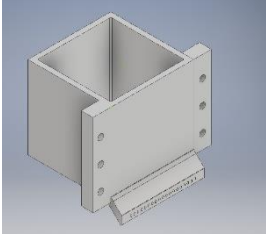

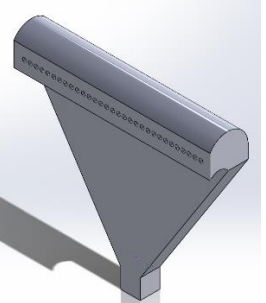

Designs	Test results	Pros and Cons
		<p>Advantages:</p> <ul style="list-style-type: none"> • Good uniform distribution • Simple and easy to fabricate <p>Disadvantages:</p> <ul style="list-style-type: none"> • Difficult distribution on both sides • Loss of precision in measurements • Traces of liquid found on the other face
		<p>Advantages:</p> <ul style="list-style-type: none"> • Good uniform distribution <p>Disadvantages:</p> <ul style="list-style-type: none"> • Difficult flow rate control • Cannot operate on wide range of Re • Distance between plate and flow exit may have some effect on film thickness
		<p>Advantages:</p> <ul style="list-style-type: none"> • Good uniform distribution • Easy to fabricate • Easy measurements and calculations • Reservoir borders – no effect on the flow <p>Disadvantages:</p> <ul style="list-style-type: none"> • Insufficient hydrostatic head, can result in dripping
		<p>Advantages:</p> <ul style="list-style-type: none"> • Good uniform distribution <p>Disadvantages:</p> <ul style="list-style-type: none"> • Air bubbles are likely to form at the exit • Flow at the borders induces disturbances
		<p>Advantages:</p> <ul style="list-style-type: none"> • Good uniform distribution • Easy measurements and calculations • Reservoir borders – slight perturbation <p>Disadvantages:</p> <ul style="list-style-type: none"> • Can block a part of the plate

Table A1.1: Different conceptions of distributors fabricated and tested during the conceptualization phase of the test bench

Good and reliable results are directly related to how well the liquid is distributed on the plate. Early designs of distributor included the idea of overflow of the liquid (Kofman et al.¹⁶²) on the sample plate. The results of their experiments conform uniform distribution of liquid on the sample. Based on the same principle, we have designed the first prototype. The results from the tests are shown in the first row in the table. These first tests are used as a basis of defining the criteria necessary to have an improved design. The criteria of improved design in our case include quick flow detachment at the exit, no air bubbles in the flow, uniform film thickness in streamwise and spanwise direction, less interference from the edge of the distributor to the flow on the sample and finally easy to fabricate and install. Refer to the table A1 for the list of distributors that were designed and tested to integrate to our test module before choosing the final design.

1.2. Roughness measurements

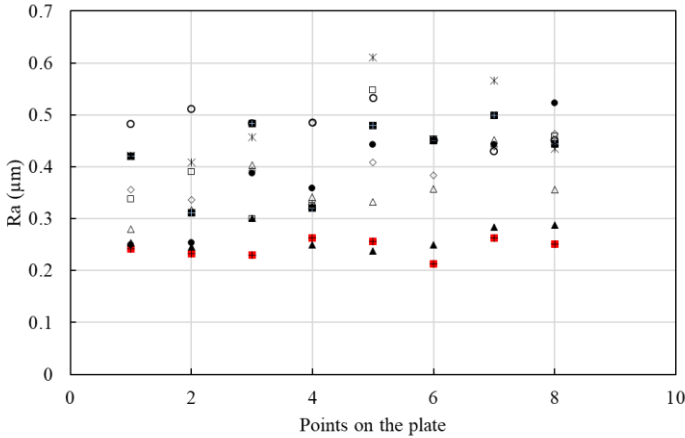


Figure A2.2 : Roughness coefficient measured on several points on different test plates used in the experiments

Initially, the samples had a shiny surface that was manually polished with fine grit sand paper to eliminate the reflective aspect of the test plates. On each face of a sample, eight points were selected to perform 2D roughness measurements (Microtopograph STIL CHR150, F3 probe, 0-80μm). The points selected are mostly in the vicinity of the perforation. The tests are repeated on eight plates (single/multiple perforations). Roughness parameter measured for all eith plates is shown in the Figure A2.2.

1.3. Preparation of aqueous glycerol mixture

From the compilation of aqueous glycerol mixtures^{82,163}, a priori estimation of the physical properties such as ρ, μ, σ are made. For a given temperature, volume of pure glycerin and volume of deionized water, physical properties (ρ, μ, σ) and then the values of Ka are calculated. With a certain number of water, glycerin weight ratios, we considered 25 wt% and 55 wt% aqueous glycerol mixtures in the present study.

The mixture is prepared by slowly adding pure glycerin to water under constant agitation (using magnetic agitator). The mixtures are prepared at a room temperature of 25 °C in a clean environment. The density of the mixture is measured using a volumetric pipette. The measurement of density is repeated after the mixture has been used in the experiments. We note slight decrease (up to 4%) in the values of density previously (before experiments) measured.

1.4. Particles selection and Annual aperture

Silver coated particles

In the first step, the test liquid was seeded with silver coated glass hollow particles of $d_p = 20$ to $50 \mu m$. Images are sampled at a sampling rate of 800 fps. In the resulting image, we observed a high background noise due to the reflective aluminum surface. The reflection of the aluminum surface interferes with particle detection and thus distorts the calculation of trajectories. The particles disappear in consecutive frames and reappear after a certain number of frames. Due to the small thickness of the film, it is challenging to adjust the light sheet in the liquid film without having the plate in contact. The laser beam reflects light when in contact with the aluminum plate. Reflection can be catastrophic for the sensor of the camera and can lead to erroneous measurements. Undoubtedly, we could prevent the reflection by using anti-reflective paint or black color matte finish paint. However, surface treatments modify the surface properties of aluminum and thus the contact angle. We considered using fluorescent seeding particles to avoid secondary reflection while not altering the surface property of plates (see Figure A2.3).

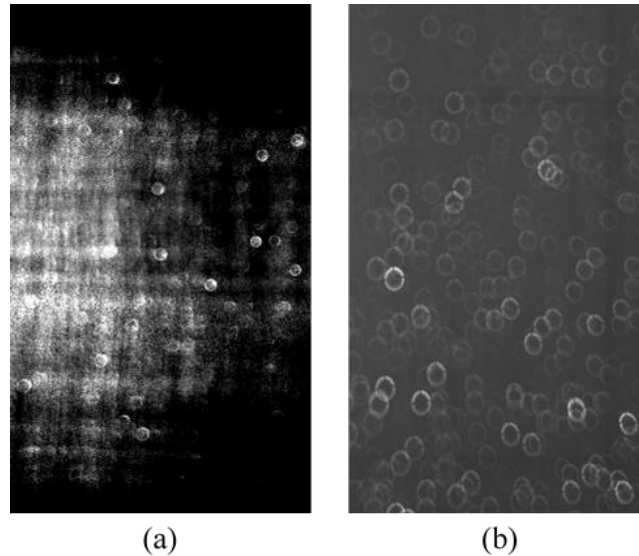


Figure A2.3: An example of a defocused image of a falling liquid film on the flat plate seeded with (a) silver coated glass hollow particles and (b) fluorescent particles.

Several tests are performed to ensure the appropriate seeding density in the liquid film. Due to the deformed free surface, a slightly incorrect adjustment creates secondary reflections that interfere with the particle reflection. With the same acquisition and camera parameters, we adjusted the focus of the camera on the particles to find a correct position of the laser sheet with respect to the liquid film. We used two different liquids (deionized water and propan-2-ol) on a sample plate of thickness $t = 1$ mm with a perforation diameter of $d = 4$ mm. As the technique is digital, typical measurements and uncertainties are first presented in pixel. Fluid displacement between two frames is around 3-15 pixels at the free surface of the film and around 1 – 5 pixels near the wall. We observed that for the same conditions, the overall visibility of tracer particles was better when deionized water was used as the test liquid (see Figure A2.4). The curtain in the perforation was slightly darker when the test liquid was propan-2-ol. The secondary reflections originating from surface deformation were kept to minimum.

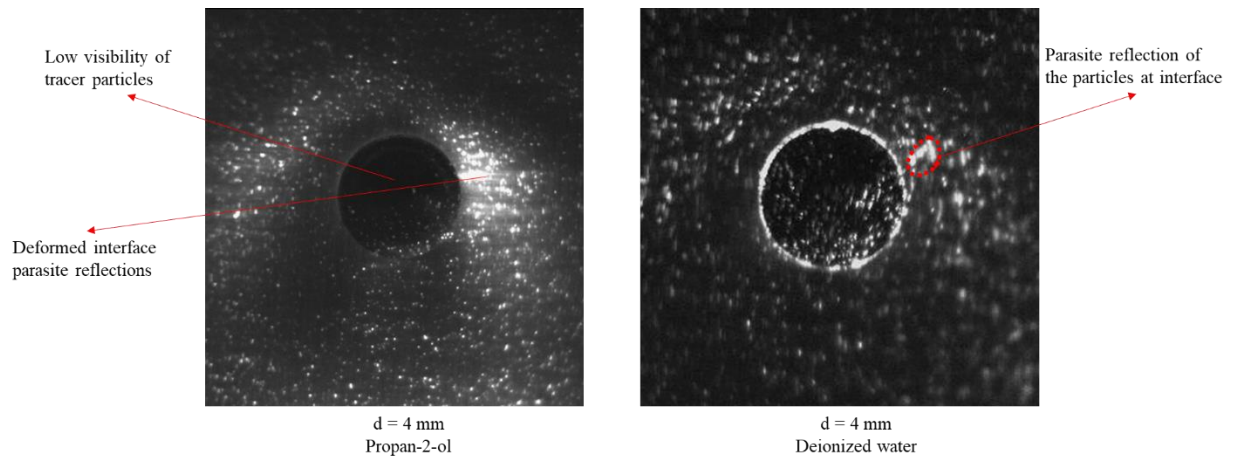


Figure A2.4: Two images (camera focused on particles) of concentration and distribution of particles seeded in the liquid film on a perforated plate.

Appendix 4 : Model derivation predicting curtain Reynolds number (Re_{cr})

1. Derivation of the model

We consider that the film profile is flat on both sides of the plate and axisymmetric with respect to the perforation axis (see Figure 3-10). We denote R the radius of the hole surrounded by the rim. The energy required to vary the hole radius from R to $R + dR$ reads:

$$dE = -4\pi\sigma R dR + (t + \delta_{Nu}(Q_1) + \delta_{Nu}(Q_2))2\pi\sigma dR$$

Then, the surface tension force per unit circumference of the rim acting in the radial direction (f_σ) is given by:

$$f_\sigma = \sigma \left(2 - \frac{t}{R} - \frac{\delta_{Nu}(Q_1)}{R} - \frac{\delta_{Nu}(Q_2)}{R} \right)$$

f_σ is an increasing function of R and is maximal when $R = d/2$. As a first approximation, let us consider that $f_\sigma = f_\sigma(R/2)$ at the curtain transition:

$$f_\sigma = 2\sigma \left(1 - \frac{t}{d} - \frac{\delta_{Nu}(Q_1)}{d} - \frac{\delta_{Nu}(Q_2)}{d} \right) \quad (A3.1)$$

We keep in mind that this assumption tends to overestimate the capillary force. Therefore, the inertial force required to drive the curtain transition should be overrated as well.

f_σ cancels for $d = t + \delta_{Nu}(Q_1) + \delta_{Nu}(Q_2)$. Spontaneous curtain formation is expected for perforation diameter $d \leq t + \delta_{Nu}(Q_1) + \delta_{Nu}(Q_2)$. f_σ opposes the formation of the liquid curtain for $d \geq t + \delta_{Nu}(Q_1) + \delta_{Nu}(Q_2)$.

The x-component of the momentum net flux entering the rim close to the stagnation point reads (per unit length of rim):

$$f_u = \int_0^{\delta_{Nu}(Q_1)} \rho u_x^2(y) dy + \int_0^{\delta_{Nu}(Q_2)} \rho u_x^2(y) dy \quad (A3.2)$$

$u_x(y)$ is the Nusselt velocity profile given by

$$u_x(y) = \frac{g}{\nu} \left(\delta_{Nu} - \frac{y}{2} \right) y \quad (A3.3)$$

After substitution of Eq. (A3.3) in Eq. (A3.2) and integration of Eq. (A3.2)

$$f_u = \frac{2}{15} \times \frac{\rho g^2}{\nu^2} \left((\delta_{Nu}(Q_1))^5 + (\delta_{Nu}(Q_2))^5 \right) \quad (A3.4)$$

Curtain forms when the momentum flux balances the surface tension force:

$$f_u = f_\sigma \quad (A3.5)$$

By combining Eq. (3.4), (S7), (S8), we get the following criterion for the curtain formation, expressed with the dimensionless parameters determined in the problem description.

$$\text{Re}_{cr} = \frac{1}{3} \left(\frac{15 \text{Ka}}{1 + \left(\frac{Q_2}{Q_1}\right)^{5/3}} \left(1 - \frac{t}{d} - 3^{1/3} \text{Ka}^{-1/2} \left(\frac{d}{l_c}\right)^{-1} \text{Re}_{cr}^{1/3} \left(1 + \left(\frac{Q_2}{Q_1}\right)^{1/3} \right) \right) \right)^{3/5} \quad (\text{A3.6})$$

Eq. (A3.6) simplifies in the case of one face and two face supply with equal flow rates and gives, respectively,

$$\text{Re}_{cr} = \frac{1}{3} \left(15 \text{Ka} \left(1 - \frac{t}{d} - 3^{1/3} \text{Ka}^{-1/2} \left(\frac{d}{l_c}\right)^{-1} \text{Re}_{cr}^{1/3} \right) \right)^{3/5} \quad (\text{A3.7})$$

$$\text{Re}_{cr} = \frac{1}{3} \left(\frac{15 \text{Ka}}{2} \left(1 - \frac{t}{d} - 2 \times 3^{1/3} \text{Ka}^{-1/2} \left(\frac{d}{l_c}\right)^{-1} \text{Re}_{cr}^{1/3} \right) \right)^{3/5} \quad (\text{A3.8})$$

Appendix 5 : Theoretical expression for length scale of onset of rivulet merging

1. Onset of rivulet merging: Derivation

Liquid film falling from a point source (in our case perforations on a vertical flat plate), the profile of the rivulet when it merges with the adjacent rivulet is not always homogenous. Some sort of adjustment of the merged rivulet happens for a certain distance of the plate. Smith¹²⁵ has studied this adjustment on incline plates without considering surface tension. In vertical plate, we cannot neglect surface tension and we revisit the form of liquid film equation used in Duffy and Moffatt¹²⁶ to derive the length at which rivulet merging begins:

$$\delta \delta_{yyyy} + 3 \delta_y \delta_{yyy} + \frac{3\rho g \sin\alpha}{\sigma} \delta_x = 0 \quad \text{A4.1}$$

We study the relaxation of the free surface when the upstream of the film is in the form of a sine wave. We perform a calculation of first order. We search a solution of the form:

$$\delta(x, y) = \delta_\infty \left(1 + \varepsilon(x) \cos\left(\frac{2\pi y}{s}\right) \right) \quad \text{A4.2}$$

$$\frac{\partial \delta}{\partial x} = \delta_\infty \varepsilon'(x) \cos\left(\frac{2\pi y}{s}\right) \quad \text{A4.3}$$

$$\frac{\partial \delta}{\partial y} = \delta_\infty \varepsilon(x) \left(-\frac{2\pi}{s}\right) \sin\left(\frac{2\pi y}{s}\right) \quad \text{A4.4}$$

$$\frac{\partial^2 \delta}{\partial y^2} = \left(-\frac{2\pi}{s}\right)^2 \delta_\infty \varepsilon(x) \cos\left(\frac{2\pi y}{s}\right) \quad \text{A4.5}$$

$$\frac{\partial^3 \delta}{\partial y^3} = \left(\frac{2\pi}{s}\right)^3 \delta_\infty \varepsilon(x) \sin\left(\frac{2\pi y}{s}\right) \quad \text{A4.6}$$

$$\frac{\partial^4 \delta}{\partial y^4} = \left(\frac{2\pi}{s}\right)^4 \delta_\infty \varepsilon(x) \cos\left(\frac{2\pi y}{s}\right) \quad \text{A4.7}$$

$$\begin{aligned} & \left(\frac{2\pi}{s}\right)^4 \delta_\infty \varepsilon(x) \cos\left(\frac{2\pi y}{s}\right) \delta_\infty \varepsilon(x) \cos\left(\frac{2\pi y}{s}\right) \\ & + 3\delta_\infty \varepsilon(x) \left(-\frac{2\pi}{s}\right) \sin\left(\frac{2\pi y}{s}\right) \left(\frac{2\pi}{s}\right)^3 \delta_\infty \varepsilon(x) \sin\left(\frac{2\pi y}{s}\right) \\ & + \frac{3\rho g}{\sigma} \delta_\infty \varepsilon'(x) \left(\frac{2\pi y}{s}\right) = 0 \end{aligned} \quad \text{A4.8}$$

We substitute in the liquid film equation A4.1:

$$\delta_\infty^2 \left(\frac{2\pi}{s}\right)^4 \varepsilon(x) \cos\left(\frac{2\pi y}{s}\right) + \frac{3\rho g}{\sigma} \delta_\infty \varepsilon'(x) \cos\left(\frac{2\pi y}{s}\right) = 0 \quad \text{A4.9}$$

$$\frac{\varepsilon'(x)}{\varepsilon(x)} = \left(\frac{2\pi}{s}\right)^4 \frac{\delta_\infty \sigma}{3\rho g} \quad \text{A4.10}$$

$$\frac{\partial \varepsilon}{\varepsilon} = \Theta \frac{dx}{\mathcal{L}} \quad \text{A4.11}$$

$$\text{Where } \mathcal{L} = \frac{3s^4}{(2\pi)^4 l_c^2 \delta_\infty} \quad \text{A4.12}$$

Integrating equation A4.11, we have:

$$\ln \frac{\varepsilon}{\varepsilon_0} = \Theta \frac{x - x_0}{\mathcal{L}} \quad \text{A4.13}$$

$$\varepsilon = \varepsilon_0 \exp^{\Theta \left(\frac{x - x_0}{\mathcal{L}}\right)}$$

$$\delta(x, y) = \delta_\infty \left(1 + \varepsilon_0 \exp\left[-\left(\frac{x - x_0}{\mathcal{L}}\right)\right]\right)$$

$$\frac{\delta(x, y) - \delta_\infty}{\delta_\infty} = \left(\varepsilon_0 \exp\left[-\left(\frac{x - x_0}{\mathcal{L}}\right)\right]\right) \quad \text{A4.14}$$

Appendix 6 : Dynamic Mode Decomposition

1. Definition

Originally, the DMD algorithm was formulated in terms of a companion matrix, which highlights its connections to the Arnoldi algorithm and to Koopman operator theory. The SVD-based algorithm presented in [8] is more numerically stable, and is now generally accepted as the defining DMD algorithm; we describe this algorithm below

Preprocessed experimental data shall be represented in the form of a sequence of snapshots, represented by a matrix \mathbf{V}_1^N ,

$$\mathbf{V}_1^N = \{\mathbf{v}_1, \mathbf{v}_2, \mathbf{v}_3 \dots, \mathbf{v}_N\} \quad (\text{A5.1})$$

where \mathbf{v}_i is the i^{th} flow field, \mathbf{v}_1 denotes first member of the sequence and \mathbf{v}_N denotes the last member of the sequence.

First step is to assume that an operator \mathbf{A} connects the flow field \mathbf{v}_i to the subsequent flow field \mathbf{v}_{i+1} , that is,

$$\mathbf{V}_1^N = \{\mathbf{v}_1, \mathbf{A}\mathbf{v}_1, \mathbf{A}^2\mathbf{v}_1 \dots, \mathbf{A}^{N-1}\mathbf{v}_1\} \quad (\text{A5.2})$$

The DMD seeks to extract the dynamic characteristics (eigenvalues, eigenvectors, pseudo eigenvalues, resonance behaviour, etc.) of the dynamical process described by \mathbf{A} based on the sequence, \mathbf{V}_1^N . In the second step, it is assumed that beyond a critical number of acquisitions, the vector in equation 6.1 becomes linearly dependent. The vector \mathbf{v}_N can therefore be written as a linear combination of the previous fields.

$$\mathbf{v}_n = \{a_1\mathbf{v}_1 + a_2\mathbf{v}_2 + \dots + a_{N-1}\mathbf{v}_{N-1} + \mathbf{r}\} \quad (\text{A5.3})$$

$$\text{Or } \mathbf{v}_n = \mathbf{V}_1^{N-1}\mathbf{a} + \mathbf{r} \quad (\text{A5.4})$$

where $\mathbf{a}_T = \{a_1, a_2, \dots, a_{N-1}\}$ and \mathbf{r} is a residual vector. From equation 6.4, and by considering it is possible to write:

$$\mathbf{A}\mathbf{v}_1^{n-1} = \mathbf{v}_2^n \quad (\text{A5.5})$$

$$\mathbf{A}\{\mathbf{v}_1, \mathbf{v}_2, \mathbf{v}_3, \dots, \mathbf{v}_{N-1}\} = \{\mathbf{v}_2, \mathbf{v}_3, \mathbf{v}_4, \dots, \mathbf{v}_N\} = \{\mathbf{v}_2, \mathbf{v}_3, \mathbf{v}_4, \dots, \mathbf{v}_1^{N-1}\mathbf{a}\} + \mathbf{r}\mathbf{e}_{N-1}^T \quad (\text{A5.6})$$

where \mathbf{e}_{N-1}^T is $(N - 1)^{th}$ unit vector.

Or equation 6.6 can be written in matrix form:

$$\mathbf{A}\mathbf{V}_1^{N-1} = \mathbf{V}_2^N = \mathbf{V}_1^{N-1}\mathbf{S} + \mathbf{r}\mathbf{e}_{N-1}^T \quad (\text{A5.7})$$

where \mathbf{S} is the companion matrix defined as:

$$\mathbf{S} = \begin{pmatrix} 0 & & & a_1 \\ 1 & 0 & & a_2 \\ & & \dots & \\ & & \dots & \\ & & & 1 & 0 & a_{N-2} \\ & & & 1 & a_{N-1} \end{pmatrix} \quad (\text{A5.8})$$

To compute \mathbf{S} , the last element of a given data sequence v_N is expressed as a linear combination of the previous elements of the sequence as stated in (6.4) whose least-squares solution, for a full-rank matrix \mathbf{V}_1^{N-1} , is given by :

$$a = \mathbf{R}^{-1} \mathbf{Q}^H v_N \quad (\text{A5.9})$$

with $\mathbf{QR} = \mathbf{V}_1^{N-1}$, as the economy-size QR-decomposition of the data sequence \mathbf{V}_1^{N-1} . The $(N - 1)$ -component vector a then forms the last column of the companion matrix \mathbf{S} . The following expression is used to extract dynamic modes Φ_i :

$$\Phi_i = \mathbf{U} \mathbf{y}_i \quad (\text{A5.10})$$

with \mathbf{y}_i as the i th eigenvector of $\tilde{\mathbf{S}}$, i.e. $\tilde{\mathbf{S}} \mathbf{y}_i = \boldsymbol{\mu}_i \mathbf{y}_i$, and \mathbf{U} as the right singular vectors of the snapshot sequence \mathbf{V}_1^{N-1} .

Bibliography

1. Timmerhaus, K. D., & Reed RP. *Cryogenic Engineering: Fifty Years of Progress*. Springer Science & Business Media,; 2007.
2. Moll A. *Air Distillation*. Elsevier Inc.; 2014.
3. Smith AR, Klosek J. A review of air separation technologies and their integration with energy conversion processes. *Fuel Process Technol.* 2001;70(2):115-134.
4. Banaszkiwicz T, Chorowski M, Gizicki W. Comparative analysis of cryogenic and PTSA technologies for systems of oxygen production. *AIP Conf Proc.* 2014;1573:1373-1378.
5. Banaszkiwicz T, Chorowski M, Gizicki W. Comparative analysis of oxygen production for oxy-combustion application. *Energy Procedia.* 2014;51(June 2015):127-134.
6. Agrawal R, Yee TF. Heat Pumps for Thermally Linked Distillation Columns: An Exercise for Argon Production from Air. *Industrial & engineering chemistry research*, 33(11), 2717-2730; 1994.
7. Mandler JA, Vinson DR, Chatterjee N. Dynamic Modelling and Control of Cryogenic AIR Separation Plants. *IFAC Proceedings Volumes* 22, no. 8 (1989): 267-273.
8. Castle WF. Air separation and liquefaction: Recent developments and prospects for the beginning of the new millennium. *International Journal of Refrigeration* 25, no. 1 (2002): 158-172.
9. Agrawal R, Woodward DW, Ludwig KA, Bennett DL. Impact of low pressure drop structure packing on air distillation. *Inst Chem Eng Symp Ser.* 1993;128:A125-A138.
10. Górak A, Schoenmakers H. *Distillation: Operation and Applications.*; 2014.
11. Mackowiak J. Fluid Dynamics of Packed Columns. *Chemische Technik. Verfahrenstechnik.* Springer-Verlag Berlin Heidelberg (2010).
12. Lassauce A, Alix P, Raynal L, Royon-Lebeaud A, Haroun Y. Pertes de charge, Capacité et aires de transfert de matière requises pour le captage du CO₂ en post-combustion par solvants. *Oil Gas Sci Technol.* 2014;69(6):1021-1034.
13. Spiegel L, Meier W. Generalized pressure drop model for structured packings. In: *Institution of Chemical Engineers Symposium Series.* ; 1992:B85.
14. Spiegel L, Meier W. Distillation columns with structured packings in the next decade. *Chem Eng Res Des.* 2003;81(1):39-47.
15. Olujic Z, Jansen H, Kaibel B, Rietfort T, Zich E. Stretching the capacity of structured

- packings. *Industrial & engineering chemistry research* 40, no. 26 (2001): 6172-6180.
16. Yu D, Cao D, Li Z, Li Q. Experimental and CFD studies on the effects of surface texture on liquid thickness, wetted area and mass transfer in wave-like structured packings. *Chem Eng Res Des.* 2018;129(1998):170-181.
 17. Bessou V, Rouzineau D, Prévost M, et al. Performance characteristics of a new structured packing. *Chem Eng Sci.* 2010;65(16):4855-4865.
 18. Pavlenko AN, Volodin OA, Surtaev AS. Hydrodynamics in falling liquid films on surfaces with complex geometry. *Appl Therm Eng.* 2017;114:1265-1274.
 19. Li X, Liu Q, Li H, Gao X. Experimental study on liquid flow behavior in the holes of SiC structured corrugated sheets. *J Taiwan Inst Chem Eng.* 2016;64:39-46.
 20. Yao Y, Pavlenko AN, Volodin OA. Effects of layers and holes on performance of wire mesh packing. *J Eng Thermophys.* 2015;24(3):222-236.
 21. Shi MG interfacial area in packed columns., Mersmann A. Effective interfacial area in packed columns. *German chemical engineering*, 8(2), 87-96;1985.
 22. Puranik SS, Vogelpohl A. Effective interfacial area in irrigated packed columns. *Chemical Engineering Science* 29, no. 2 (1974): 501-507.
 23. Karimi G, Kawaji M. Flow characteristics and circulatory motion in wavy falling films with and without counter-current gas flow. *Int J Multiph Flow.* 1999;25(6-7):1305-1319.
 24. André B. IN. Mass transfer in structured packing: A wetted-wall study. *Ind Eng Chem Res.* 2001;40(10):2310-2321.
 25. Erasmus, André Brink. "Mass transfer in structured packing." PhD diss., Stellenbosch: University of Stellenbosch, 2004.
 26. Fair JR, Seibert AF, Behrens M, Saraber PP, Olujic Z. Structured packing performance - Experimental evaluation of two predictive models. *Ind Eng Chem Res.* 2000;39(6):1788-1796.
 27. Chilton, T. H., & Colburn AP. Distillation and Absorption in Packed Columns. *Ind Eng Chem.* 1935;27(8):977-978.
 28. Górak, A, & Olujic Z. *Distillation: Equipment and Processes.* Academic Press, 2014.; 2010.
 29. Wallis GB. *One-Dimensional Two-Phase Flow,*. McGraw Hil.; 1969.
 30. Ataki A. Wetting of Structured Packing Elements - CFD and Experiment (2006).
 31. Wang GQ, Yuan XG, Yu KT. A method for calculating effective interfacial area of structured packed distillation columns under elevated pressures. *Chem Eng Process*

- Process Intensif.* 2006;45(8):691-697.
32. Olujić Ž. Development of a Complete Simulation Model for Predicting the Hydraulic and Separation Performance of Distillation Columns Equipped with Structured Packings. *Chemical and biochemical engineering quarterly* 11, no. 1 (1997): 31-46.
 33. Rocha JA, Bravo JL, Fair JR. Distillation columns containing structured packings: A comprehensive model for their performance. 2. Mass-transfer model. *Ind Eng Chem Res.* 1996;35(5):1660-1667.
 34. Olujić Ž, Kamerbeek AB, De Graauw J. A corrugation geometry based model for efficiency of structured distillation packing. *Chem Eng Process Process Intensif.* 38, no. 4-6 (1999): 683-695.
 35. Billet R, Schultes M. Prediction of mass transfer columns with dumped and arranged packings: Updated summary of the calculation method of Billet and Schultes. *Chem Eng Res Des.* 1999;77(6):498-504.
 36. Suess P, Spiegel L. Hold-up of Mellapak structured packings. *Chemical Engineering and Processing: Process Intensification* 31, no. 2 (1992): 119-124.
 37. Olujić Ž, Seibert AF, Fair JR. Influence of corrugation geometry on the performance of structured packings: An experimental study. *Chemical Engineering and Processing: Process Intensification* 39, no. 4 (2000): 335-342.
 38. Olujić Ž, Behrens M, Spiegel L. Experimental characterization and modeling of the performance of a large-specific-area high-capacity structured packing. *Industrial & engineering chemistry research* 46, no. 3 (2007): 883-893.
 39. Olujić Ž, Kaibel B, Jansen H, Rietfort T, Zich E, Frey G. Distillation column internals/configurations for process intensification. *Chem. Biochem. Eng. Q* 17 (2003): 301.
 40. Pavlenko AN, Pecherkin NI, Chekhovich VY, et al. Separation of mixtures and distribution of a liquid on a structured packing in a large-scale model of a distillation column. *Theor Found Chem Eng.* 2006;40(4):329-338.
 41. Hoffmann R, Boden S, Schubert M, Hampel U. Measuring liquid flow in structured packings using gamma and x-ray tomography: (2016).
 42. Schug S, Arlt W. Imaging of Fluid Dynamics in a Structured Packing Using X-ray Computed Tomography. *Chem Eng Technol.* 2016;39(8):1561-1569.
 43. Marchot P, Toye D, Pelsser A, Crine M, Homme GL. Liquid Distribution Images on Structured Packing by X-Ray Computed Tomography. 2001;47(6):1471-1476.
 44. Janzen A, Steube J, Aferka S, et al. Investigation of liquid flow morphology inside a

- structured packing using X-ray tomography. *Chem Eng Sci.* 2013;102:451-460.
45. Bolenz L, Fischer F, Toye D, Kenig EY. Determination of local fluid dynamic parameters in structured packings through X-ray tomography: Overcoming image resolution restrictions. *Chem Eng Sci.* 2021;229:115997.
 46. Aferka S, Viva A, Brunazzi E, Marchot P, Crine M, Toye D. Tomographic measurement of liquid hold up and effective interfacial area distributions in a column packed with high performance structured packings. *Chem Eng Sci.* 2011;66(14):3413-3422.
 47. Fourati M, Roig V, Raynal L. Experimental study of liquid spreading in structured packings. *Chem Eng Sci.* 2012;80:1-15.
 48. Tsai RE, Schultheiss P, Kettner A, et al. Influence of surface tension on effective packing area. *Ind Eng Chem Res.* 2008;47(4):1253-1260.
 49. Alekseenko S V., Markovich DM, Evseev AR, Bobylev A V., Tarasov B V., Karsten VM. Experimental study of liquid distribution in a column with a structured packing. *Theor Found Chem Eng.* 2007;41(4):417-423.
 50. Kalliadasis, S., & Homsy GM. Stability of free-surface thin-film flows over topography. *J Fluid Mech.* 2001;448:387-410.
 51. Nusselt W. *Die Oberflächenkondensation Des Wasserdampfes.* Zeitschrift des Vereines Deutscher Ingenieure. 1916;60:541-546.
 52. Kapitza PL. *Wave Flow of Thin Layers of a Viscous Fluid, Collected Papers of P.L. Kapitza (1965), Pages 662–689.* Pergamon (Oxford); 1948.
 53. Ishigai, S., Nakanisi, S., Koizumi, T., Oyabu Z. Hydrodynamics and Heat Transfer of Vertical Falling Liquid Films : Part 1, Classification of Flow Regimes. *Bull JSME 15,* 594–602.
 54. Chang HC. Wave evolution on a falling film. *Annu Rev Fluid Mech.* 1994;26(1):103-136.
 55. Tselodub OY, Trifonov YY. Nonlinear waves on the surface of a falling liquid film. Part 2. Bifurcations of the first-family waves and other types of nonlinear waves. *J Fluid Mech.* 1992;244(5):149-169.
 56. Kharlamov SM, Guzanov V V., Bobylev A V., Alekseenko S V., Markovich DM. The transition from two-dimensional to three-dimensional waves in falling liquid films: Wave patterns and transverse redistribution of local flow rates. *Phys Fluids.* 2015;27(11).
 57. Dietze GF, Rohlfs W, Nährich K, Kneer R, Scheid B. Three-dimensional flow

- structures in laminar falling liquid films. *J Fluid Mech.* 2014;743:75-123.
58. Charogiannis A, An JS, Markides CN. A simultaneous planar laser-induced fluorescence, particle image velocimetry and particle tracking velocimetry technique for the investigation of thin liquid-film flows. *Exp Therm Fluid Sci.* 2015;68(November):516-536.
59. Brauner N. Department of Fluid Mechanics and Heat Transfer, Faculty of Engineering, Tel-Aviv University, Ramat Aviv, Tel-Aviv 69978, Israel. *Chem Eng Sci.* 1987;42(2):265-273.
60. Nosoko T, Yoshimura PN, Nagata T, Oyakawa K. Characteristics of two-dimensional waves on a falling liquid film. *Chem Eng Sci.* 1996;51(5):725-732.
61. Park CD, Nosoko T. Three-Dimensional Wave Dynamics on a Falling Film and Associated Mass Transfer. *AIChE J.* 2003;49(11):2715-2727.
62. Kofman N, Ruyer-Quil C, Mergui S. Selection of solitary waves in vertically falling liquid films. *Int J Multiph Flow.* 2016;84:75-85.
63. Kofman N. "Films liquides tombants avec ou sans contre-écoulement de gaz: application au problème de l'engorgement dans les colonnes de distillation." PhD diss., Université Pierre et Marie Curie-Paris VI, 2014.
64. Transport phenomena, R. B. Bird, W. E. Stewart, and E. N. Lightfoot, John Wiley and Sons, Inc., New York(1960). *AIChE J.* 1961.
65. Yoshimura PN, Nosoko T, Nagata T. Enhancement of mass transfer into a falling laminar liquid film by two-dimensional surface waves-some experimental observations and modeling. *Chemical Engineering Science* 51, no. 8 (1996): 1231-1240.
66. Zhao L, Cerro RL. Experimental characterization of viscous film flows over complex surfaces. *Int J Multiph Flow.* 1992;18(4):495-516.
67. Vlachogiannis M, Bontozoglou V. Experiments on laminar film flow along a periodic wall. *J Fluid Mech.* 2002;457:133-156.
68. Kofman N, Mergui S, Ruyer-Quil C. Characteristics of solitary waves on a falling liquid film sheared by a turbulent counter-current gas flow. *Int J Multiph Flow.* 2017;95:22-34.
69. Pozrikidis C. The flow of a liquid film along a periodic wall. *J Fluid Mech.* 1988;188:275-300.
70. Pollak T, Aksel N. Crucial flow stabilization and multiple instability branches of gravity-driven films over topography. *Phys Fluids.* 2013;25(2).
71. Schörner M, Reck D, Aksel N. Does the topography's specific shape matter in general

- for the stability of film flows? *Phys Fluids*. 2015;27(4).
72. Reck D, Aksel N. Experimental study on the evolution of traveling waves over an undulated incline. *Phys Fluids*. 2013;25(10).
 73. Popovich AT, Hummel RL. A new method for non-disturbing turbulent flow measurements very close to a wall. *Chem Eng Sci*. 1967;22(1):21-25.
 74. Popovich AT, Hummel RL. Experimental study of the viscous sublayer in turbulent pipe flow. *AIChE J*. 1967;13(5):854-860.
 75. Kawaji M, Ahmad W, DeJesus JM, Sutharshan B, Lorencez C, Ojha M. Flow visualization of two-phase flows using photochromic dye activation method. *Nucl Eng Des*. 1993;141(1-2):343-355.
 76. Karimi G, Kawaji M. Flooding in vertical counter-current annular flow. *Nucl Eng Des*. 2000;200(1):95-105.
 77. Mendez MA, Scheid B, Buchlin J. Low Kapitza Falling Liquid Films. *Chem Eng Sci*. 2017;170:122-138.
 78. Decré MMJ, Baret JC. Gravity-driven flows of viscous liquids over two-dimensional topographies. *J Fluid Mech*. 2003;487(487):147-166.
 79. Malacara, D., Servin, M. and Malacara, Z., 2018. Interferogram analysis for optical testing. CRC press.
 80. *Design and Development of a Prototype Static Cryogenic Heat Transfer System.*; 1971.
 81. Vazquez G, Alvarez E, Navaza JM. Surface Tension of Alcohol + Water from 20 to 50 °C. *J Chem Eng Data*. 1995;40(3):611-614.
 82. Segur J. Physical properties of glycerol and its solutions. *AciscienceOrg*. Published online 1953:1-27.
 83. Paez S, Contreras M. Densities and Viscosities of Binary Mixtures of 1-Propanol and 2-Propanol with Acetonitrile. *J Chem Eng Data*. 1989;34(4):455-459.
 84. Korson L, Drost-Hansen W, Millero FJ. Viscosity of water at various temperatures. *J Phys Chem*. 1969;73(1):34-39.
 85. Kapłonek, W., Sutowska, M., Ungureanu, M., & Çetinkaya K. Optical profilometer with confocal chromatic sensor for high-accuracy 3D measurements of the uncirculated and circulated coins. *J Mech Energy Eng*. 2018;2.
 86. Dietze GF, Al-Sibai F, Kneer R. Experimental study of flow separation in laminar falling liquid films. *J Fluid Mech*. 2009;637:73-104.
 87. Baudoin R, Zimmer L, Muller T. Development and application of a time resolved dual camera 3D PTV technique around obstacles using defocus concept downstream a

- spacer grid. In 17th International Symposium on Applications of Laser Techniques to Fluid Mechanics, Lisbon, Portugal, pp. 07-10. 2014.
88. Charogiannis A, Denner F, Van Wachem BGM, Kalliadasis S, Markides CN. Detailed hydrodynamic characterization of harmonically excited falling-film flows: A combined experimental and computational study. *Phys Rev Fluids*. 2017;2(1):1-37.
 89. Zadrazil I, Markides CN. An experimental characterization of liquid films in downwards co-current gas – liquid annular flow by particle image and tracking velocimetry. *Int J Multiph Flow*. 2014;67:42-53.
 90. Gerke SJ, Leuner H, Repke J. Experimental Investigation of Local Film Thickness and Velocity Distribution Inside Falling Liquid Films on Corrugated Structured Packings. *Chemie Ingenieur Technik* 2018;69:1-6.
 91. Hampel U, Schubert M, Döb A, et al. Recent Advances in Experimental Techniques for Flow and Mass Transfer Analyses in Thermal Separation Systems. *Chemie Ingenieur Technik* 2020;(7):1-24.
 92. Pavlenko AN, Pecherkin NI, Zhukov VE, Meski G, Houghton P. Overview of methods to control the liquid distribution in distillation columns with structured packing: Improving separation efficiency. *Renew Sustain Energy Rev*. 2020;132(110092).
 93. Shetty S, Cerro RL. Flow of a thin film over a periodic surface. *Int J Multiph Flow*. 1993;19(6):1013-1027.
 94. Trifonov YY. Stability of a viscous liquid film flowing down a periodic surface. *Int J Multiph Flow*. 2007;33(11):1186-1204.
 95. Cao Z, Vlachogiannis M, Bontozoglou V. Experimental evidence for a short-wave global mode in film flow along periodic corrugations. *J Fluid Mech*. 2013;718:304-320.
 96. Dietze GF. Effect of wall corrugations on scalar transfer to a wavy falling liquid film. *Journal of Fluid Mechanics* 859 (2019): 1098-1128.
 97. Negny S, Meyer M, Prevost M. Study of a laminar falling film flowing over a wavy wall column: Part II. Experimental validation of hydrodynamic model. *Int J Heat Mass Transf*. 2001;44(11):2147-2154.
 98. Xie H, Hu J, Wang C, Dai G. Liquid flow transition and confined free film formation on a vertical plate with an open window. *Exp Therm Fluid Sci*. 2018;92(July 2017):174-183.
 99. Hu J, Liu J, Yu J, Dai G. CO₂ absorption into highly concentrated DEA solution flowing over a vertical plate with rectangular windows. *Int J Greenh Gas Control*.

- 2013;19:13-18.
100. Hu J, Yang X, Yu J, Dai G. Carbon dioxide (CO₂) absorption and interfacial mass transfer across vertically confined free liquid film—a numerical investigation. *Chem Eng Process Process Intensif.* 2017;111:46-56.
 101. Xie H, Hu J, Dai G. Numerical simulation on flow behavior of twin-liquid films over a vertical plate with an open window. *AIChE J.* 2018;64(4):1458-1468.
 102. Hu X, Jacobi AM. The intertube falling film: Part 1—flow characteristics, mode transitions, and hysteresis. *J Heat Transfer.* 1996;118(3):616-625.
 103. Aksel N, Schörner M. Films over topography: from creeping flow to linear stability, theory, and experiments, a review. *Acta Mech.* 2018;229(4):1453-1482.
 104. Stillwagon LE, Larson RG. Leveling of thin films over uneven substrates during spin coating. *Phys Fluids A.* 1990;2(11):1937-1944.
 105. Mazouchi A, Homsy GM. Free surfaces stokes flow over topography. *Phys Fluids.* 2001;13(10):2751-2761.
 106. Bontozoglou V, Serifi K. Falling film flow along steep two-dimensional topography: The effect of inertia. *Int J Multiph Flow.* 2008;34(8):734-747.
 107. Brown DR. A study of the behaviour of a thin sheet of moving liquid. *J Fluid Mech.* 1961;10(2):297-305.
 108. Culick FEC. Comments on a ruptured soap film. *J Appl Phys.* 1960;31(6):1128-1129.
 109. Hu X, Jacobi AM. Departure-site spacing for liquid droplets and jets falling between horizontal circular tubes. *Exp Therm Fluid Sci.* 1998;16(4):322-331.
 110. Yung D, Lorenz, J J, Ganic EN. Vapor/Liquid Interaction and Entrapment in Falling Film. *J Heat Transf Asme.* 2016;102(78):20-25.
 111. Taylor G. The Dynamics of Thin Sheets of Fluid. II. *Proc R Soc A Math Phys Eng Sci.* 1959;253(1274):313-321.
 112. Lin SP. Stability of a viscous liquid curtain. *J Fluid Mech.* 1981;104:111-118.
 113. Le Grand-Piteira N, Brunet P, Lebon L, Limat L. Propagating wave pattern on a falling liquid curtain. *Phys Rev E - Stat Nonlinear, Soft Matter Phys.* 2006;74(2):1-8.
 114. Kistler SF, Scriven LE. The Teapot Effect: Sheet-Forming Flows With Deflection, Wetting and Hysteresis. *J Fluid Mech.* 1994;263:19-62.
 115. Hartley DE, Murgatroyd W. Criteria for the break-up of thin liquid layers flowing isothermally over solid surfaces. *Int J Heat Mass Transf.* 1964;7(9):1003-1015.
 116. Shilkin A, Kenig EY. A new approach to fluid separation modelling in the columns equipped with structured packings. *Chem Eng J.* 2005;110(1-3):87-100.

117. Gorodilov AA, Berengarten MG, Pushnov AS. Features of fluid film falling on the corrugated surface of structured packings with perforations. *Theor Found Chem Eng.* 2016;50(3):325-334.
118. Spiegel L. The maldistribution story - An industrial perspective. *Chem Eng Trans.* 2018;69(1957):715-720.
119. Singh RK, Galvin JE, Sun X. Hydrodynamics of the rivulet flow over corrugated sheet used in structured packings. *Int J Greenh Gas Control.* 2017;64:87-98.
120. Singh RK, Galvin JE, Sun X. Three-dimensional simulation of rivulet and film flows over an inclined plate: Effects of solvent properties and contact angle. *Chem Eng Sci.* 2016;142:244-257.
121. Edwards DP, Krishnamurthy KR, Potthoff RW. Development of an improved method to quantify maldistribution and its effect on structured packing column performance. *Chem Eng Res Des.* 1999;77(7):656-662.
122. Wehrli M, Kögl T, Linder T, Arlt W. An unobstructed view of liquid flow in structured packing. *Chem Eng Trans.* 2018;69(2016):775-780.
123. Iyer M, Duval H, Casalinho J, Seiwert J, Wattiau M. Experimental study of a liquid film flowing over a perforation. *AIChE J.* 2021;67(11):e17363.
124. Shetty SA, Cerro RL. Spreading of Liquid Point Sources over Inclined Solid Surfaces. *Ind Eng Chem Res.* 1995;34(11):4078-4086.
125. Smith BPC. A similarity solution for slow viscous flow down an inclined plane. *J Fluid Mech.* 1973;58:275-288.
126. Duffy BR, Moffatt HK. A similarity solution for viscous source flow on a vertical plane. *Eur J Appl Math.* 1997;8(1):37-47.
127. Wilson SK, Duffy BR, Davis SH. On a slender dry patch in a liquid film draining under gravity down an inclined plane. *Eur J Appl Math.* 2001;12(3):233-252.
128. Hoffmann A, Ausner I, Repke JU WG. Detailed investigation of multiphase (gas-liquid and gas-liquid-liquid) flow behaviour on inclined plates. *Chem Eng Res Des.* 2006;84:147-154.
129. Hoffmann A, Ausner I, Repke JU WG. Fluid dynamics in multiphase distillation processes in packed towers. *Comput Chem Eng.* 2005;29:1433-1437.
130. Xu Y, Yuan J, Repke JU WG. CFD Study on liquid flow behavior on inclined flat plate focusing on effect of flow rate. *Eng Appl Comput Fluid Mech.* 2012;6:186-194.
131. Le Grand-Piteira N, Daerr A, Limat L. Meandering rivulets on a plane: A simple balance between inertia and capillarity. *Phys Rev Lett.* 2006;96(25).

132. Sellier M, Lee YC, Thompson HM, Gaskell PH. Thin film flow on surfaces containing arbitrary occlusions. *Comput Fluids*. 2009;38(1):171-182.
133. Baxter SJ, Power H, Cliffe KA, Hibberd S. Three-dimensional thin film flow over and around an obstacle on an inclined plane. *Phys Fluids*. 2009;21(3).
134. Tramis, O., Merlin-Anglade, E., Paternoster, G., Rabaud, M., & Ribe NM. Torricelli's Curtain: Morphology of Horizontal Laminar Jets Under Gravity. *Phys Fluids*. 2021;062116:1-33.
135. Dean WR. LXXII. The stream-line motion of fluid in a curved pipe (Second paper). *London, Edinburgh, Dublin Philos Mag J Sci*. 1928;5(30):673-695.
136. Dean, W. R. and JMH. Note on the motion of fluid in a curved pipe. *MATHEMATIKA*. 1959;6(1):77-85.
137. S A Berger, L Talbot LSY. Flow in Curved Pipes. *Annu Rev Fluid Mech*. 15(1):461.
138. Gelfgat AY, Yarin AL, Bar-Yoseph PZ. Dean vortices-induced enhancement of mass transfer through an interface separating two immiscible liquids. *Phys Fluids*. 2003;15(2):330-347.
139. Xie H, Zong Y, Shen L, Dai G. Interfacial mass transfer intensification with highly viscous mixture. *Chemical Engineering Science* 2021;236.
140. Fair JR, Seibert AF, Behrens M, Saraber PP, Olujić Z. Structured Packing Performance - experimental evaluation of two predictive models. *Ind Eng Chem Res*. 2000;39(6):1788-1796.
141. Emmert, R. E.; Pigford RLA. Study of Gas Absorption in Falling Liquid Films. *Chem Eng Prog*. 1954;50(2):93.
142. Nieuwoudt I, Crause JC. Mass transfer in a short wetted-wall column. 2. Binary systems. *Ind Eng Chem Res*. 1999;38(12):4933-4937.
143. Dukler AE. A Numerical Study of Mass Transfer in Free Falling Wavy Films. 1990;36(9):1379-1390.
144. Yu L, Zeng A, Yu KT. Effect of Interfacial Velocity Fluctuations on the Enhancement of the Mass-Transfer Process in Falling-Film Flow. *Ind Eng Chem Res*. 2006;45(3):1201-1210.
145. Schmid PJ. Dynamic mode decomposition of numerical and experimental data. *J Fluid Mech*. 2010;656:5-28.
146. Nidhan S, Tarin JLO, Chongsiripinyo K, Sarkar S, Schmid PJ. Dynamic mode decomposition of stratified sphere wakes. *AIAA Aviat 2019 Forum*. 2019;(June):1-15.
147. Johansson S, Westerberg LG. Vortex shedding interaction with a free jet. (2017).

148. Shi B, Wei J, Pang M. A modified optical flow algorithm based on bilateral-filter and multi-resolution analysis for PIV image processing. *Flow Meas Instrum.* 2014;38:121-130.
149. Quénot G, Pakleza J, Kowalewski T. Particle image velocimetry using optical flow for image analysis. 8th Int. Symposium on Flow Visualization, pp. 47-1. 1998.
150. Pentland AP. New Sense for Depth of Field. 1987;(4):523-531.
151. Krotkov E. Focusing. *Int J Comput Vis.* 1988;1(3):223-237.
152. Chaudhuri S and ANR. *Depth From Defocus : A Real Aperture Imaging Approach.* Springer Science & Business Media, 1999.
153. Damaschke N, Nobach H, Tropea C. Optical limits of particle concentration for multi-dimensional particle sizing techniques in fluid mechanics. *Experiments in fluids* 32, no. 2 (2002): 143-152.
154. Lin D, Angarita-Jaimes NC, Chen S, Greenaway AH, Towers CE, Towers DP. Three-dimensional particle imaging by defocusing method with an annular aperture. *Opt Lett.* 2008;33(9):905-907.
155. Sun D, Roth S, Black MJ. A quantitative analysis of current practices in optical flow estimation and the principles behind them. *Int J Comput Vis.* 2014;106(2):115-137.
156. Kelso RM, Smits AJ. Horseshoe vortex systems resulting from the interaction between a laminar boundary layer and a transverse jet. *Phys Fluids.* 1995;7(1):153-158.
157. Lin C, Ho TC, Dey S. Characteristics of Steady Horseshoe Vortex System near Junction of Square Cylinder and Base Plate. *J Eng Mech.* 2008;134(2):184-197.
158. Dean WR. The stream-line motion of fluid in a curved pipe. *London, Edinburgh, Dublin Philos Mag J Sci.* 1928;5(30):673-695.
159. Baudoin MR. Développement d'une technique de vélocimétrie laser en trois dimensions par suivi basée sur le principe de défocalisation et son application autour d'obstacles en aval d'une grille. PhD diss., Université Paris-Saclay (ComUE), 2015.
160. Kong L, Maravelias CT. From graphical to model-based distillation column design: A McCabe-Thiele-inspired mathematical programming approach. *AIChE J.* 2019;65(11).
161. McCabe WL, Thiele EW. Graphical Design of Fractionating Columns. *Ind Eng Chem.* 1925;17(6):605-611.
162. Ruyer-Quil C, Kofman N, Chasseur D, Mergui S. Dynamics of falling liquid films. *Eur Phys J E.* 2014;37(4).
163. Volk A, Kähler CJ. Density model for aqueous glycerol solutions. *Exp Fluids.* 2018;59(5):1-4.

List of Figures

Figure 1-1 : Time evolution of energy demand for oxygen separation	14
Figure 1-2: Flow diagram ¹⁰ of a particular Air Separation Unit (ASU) process for the production of pure N ₂ , O ₂ and Ar.	15
Figure 1-3: Different components in the distillation column.	18
Figure 1-4: Inside of a tray column with an illustration of sieve, bubble cap and valve trays (respectively from left to right)	19
Figure 1-5: Types of random packing ¹¹	20
Figure 1-6: Comparison of the pressure drop of structured packings (Mellapak series) and random packings ¹² (IMTP series, I-ring) for different effective interfacial area (<i>ae</i>).	21
Figure 1-7: Historical timeline of structured packing ¹⁴ (above). Photographs of some of the widely used structured packing (below).	22
Figure 1-8: (a) Structured packing (b) Placing of the plates and flow paths through the channels (c) Sketch of a corrugated-perforated metallic sheet.	23
Figure 1-9 : (ab) Example of surface features on structured packing ¹⁶ , (c) Average liquid film thickness ¹⁶ without counter-current gas flow	24
Figure 1-10: Wallis diagram of capacity for different structured packing material ¹²	28
Figure 1-11 : Liquid flow patterns for different liquid systems ³⁰ with a wide range of physical properties.	29
Figure 1-12: Liquid flow pattern for chlorobenzene – ethylbenzene 50% (16.9 ml/min.plate) with capillaries or irrigation points 10 mm distance apart from the plates surfaces ³⁰	30
Figure 1-13: Experimental liquid holdup data ³⁶ in different regions of operation for Sulzer Melapak 250X data, air/water, 1 bar.	32
Figure 1-14: From structured packing scale to thin film scale.	33
Figure 1-15: Flow patterns identified by X-ray CT. Green rectangles: film flow, blue circles: contact point liquid, red dotted circles: flooded regions ⁴⁴	34
Figure 1-16: (a) Schematic representation of the experimental setup with a 400 mm diameter block of Mellapak 250.X, (b) Liquid holdup maps ⁴⁷ , at different positions (Z_2 , Z_j and Z_3) of the column; $QL = 16 \text{ m}^3/\text{m}^2\text{h}$, $FC = 0.74 \text{ Pa}^{0.5}$, (20% <i>FG</i>).	35
Figure 1-17: Sessile drop on a wettable (left) and non-wettable (right) solid.	36
Figure 1-18 : Fractional area measurements ⁴⁸ for Mellapak 250Y (left) and 500Y (right) series packings for two different surface tension values.	37
Figure 1-19: Sketch of 2D laminar liquid film on an inclined surface	38
Figure 1-20: Naturally occurring waves on vertically falling film at $Re = 32.7$ without controlled perturbations imposed on film flow ⁶¹ .	40
Figure 1-21: Waves on vertically falling liquid film without counter-current gas for different liquid Reynolds number	41
Figure 1-22: Visualizations of different wave forms for moderate gas backflow velocities ($Re_L = 56$; $Re_G = 11200$) : U-shaped waves (left) and pocket waves (right).	41
Figure 1-23: Mass-transfer enhancement by surface waves and two breaks of mass-transfer curve ⁶⁴ .	42
Figure 1-24: Linear stability chart of liquid films flowing over sinusoidal corrugations. ω (dimensionless frequency of the neutral disturbance) versus Re for different steepness $\xi = a/\delta$ of the topography. a is the amplitude of the topography and δ is the Nusselt film thickness.	43
Figure 1-25: Free surface and streamlines of the steady film flow (a) the sinusoidal topography and (b) the rectangular topography ⁷¹ .	44
Figure 1-26: Flow of liquid nitrogen over a microtextured sheet at $Re_L = 860$ ($4QL/\nu L$) and hole diameter of 4 mm ¹⁸ . Onset of droplet formation in the perforation.	45

Figure 1-27: The flow of liquid nitrogen on the face (a and b) and back (c and d) sides of the sheets without microtexture at $Re = 860$ ($4QL/\nu L$). Hole diameter - 10 mm ¹⁸ .	45
Figure 1-28: Simplified representation of Light Absorption (LABs) test section ⁷⁷ : LEDs (1), screen (2) to back-light the test section (3) with diffuse, monochromatic light. A CMOS camera (4), to measure the attenuation of light produced by the liquid film absorbance.	47
Figure 1-29: Schematic representation of basic Twyman–Green interferometer ⁷⁹	48
Figure 2-1: (a) Schematic representation of the experimental setup. (b) CAD (Computer Aided Design) model of the distributor. (c) Photograph of the setup. 1. Test plate 2. LED panel 3. High-speed camera 4. Volumetric flow meters 5. Needle control valve 6. Spillway 7. Gear pump 8. Reservoir 9. CCI sensor 10. Distributor 11. Liquid Collector 12. Anti-vibration mount 13. Frame that holds the plate.	53
Figure 2-2: Image of a distributor with its section view	55
Figure 2-3: Flowmeter reading vs measured flow rate for flowmeter 1 and 2 when tested simultaneously with demineralized water.	56
Figure 2-4: Demonstration of liquid retrieval system added to the initial set-up to study liquid transfer through perforations.	57
Figure 2-5: Visualization of the liquid film flow on a corrugated and perforated metallic sheet. An enlarged image showing the fluid film deformation around perforations.	59
Figure 2-6: Front view of the plate and perforation dimensions along with x, y and z coordinate system in case of (a) single perforation (b) multiple perforations (c) two examples, widely spread and tightly packed perforations, to illustrate the notion of arrangement of perforations as a function of spacing.	60
Figure 2-7: Side view of the perforated plate when plate is irrigated on (a) one face (b) both faces with equal volumetric flow rate.	61
Figure 2-8: Comparison of the values of density measured before and after its use in the experiments for 25 wt% of aqueous glycerin mixture at 25 °C.	64
Figure 2-9: An image of the Tracker device (Teclis)	66
Figure 2-10 : Visualization of free surface deformation of the fluid film at low volume flow rate per width (W) of the film	68
Figure 2-11: Visualization of rim, drop, column and full and partial curtain at moderate volume flow rate per width (W)	68
Figure 2-12: (a) Shadowgraph images of the suspended rim at different time intervals ($d = 6$ mm; $t = 1$ mm; $Q2/Q1 = 1$) (b) Zone of interest selected for image analysis	70
Figure 2-13: Periodic time variation of centroid and corresponding FFT of the signal in (a,b) horizontal (y) direction (c,d) vertical (x) direction (e,f) surface area of the shape.	70
Figure 2-14: Demonstration of the principal of confocal chromatic imaging	72
Figure 2-15: Comparison of the film thickness measured using needle contact probe for 3 different volumetric flow rate per unit width with the analytical Nusselt film thickness	73
Figure 2-16: Comparison of film thickness measured in line in spanwise direction (y direction) by needle contact method and CCI with the theoretical estimation.	74
Figure 2-17: Demonstration of the light sheet optics: orientation of the laser sheet and collection optics from the front side.	75
Figure 2-18: An image of the test setup: 1. Yag laser (532 nm) 2. Mirror 3. Cylindrical lens (75 mm) 4. Micrometer positioner 5. Test plate 6. Plexiglas support.	76
Figure 2-19 : (a) Schematic of the test section showing the orientation of the laser sheet and collection optics (top view). (b) Velocity vector maps of the film cross-section from PIV and PTV ⁵⁸ .	78
Figure 2-20: Microtextured corrugated surface inclined at 45 ^{o90} . A static recirculating eddy in the zoomed image.	79

Figure 2-21: Images of the closed transparent packing channel: (a) with minimal static liquid hold-up (no liquid load) and (b) static holdup for $QL = 40 \text{ m}^3 \text{m}^2 \text{h}^{-1}$ (green arc) (c) measured velocity vectors. 90

Figure 3-1 : (a) Schematic representation of the experimental setup. (b) CAD (Computer Aided Design) model of the distributor. (c) Photograph of the setup. 1. Test plate 2. LED panel 3. High speed camera 4. Volumetric flow meters 5. Needle control valve 6. Spillway 7. Gear pump 8. Reservoir 9. CCI sensor 10. Distributor 11. Liquid Collector 12. Anti-vibration mount 13. Frame that holds the plate. 91

Figure 3-2: Perforated plate front view and cross-section along x-z plane: (a) dimensions, coordinate system and definitions of perforation top edge, bottom edge and inner surface, (b) One face supply ($Q2Q1 = 0$), (c) two face supply with equal flow rates ($Q2Q1 = 1$). Arrows indicate the flow path followed by the fluid film before the curtain transition. 91

Figure 3-3: Film thickness profile in the $y=0$ plane far below the curtain transition: CCI measurements for perforation diameter $d = 8 \text{ mm}$, plate thickness $t = 1 \text{ mm}$, propan-2-ol, $Ka = 348$, $Re = 23$, supply conditions $Q2Q1 = 0$ and $Q2Q1 = 1$. The thick black segments on the x-axis correspond to the plate surface and the gap between them to the perforation. The origin of the coordinate frame coincides with the center of the perforation. The streamwise direction (x) is rescaled by the capillary length (lc), and the current film thickness (δ) by the Nusselt flat film thickness (δNu) measured far upstream of the perforation. Insert: Image of the flow pattern far below the curtain transition, same experimental conditions, $Q2Q1 = 1$. 94

Figure 3-4: Rim dynamics and transition to the curtain mode as a function of perforation diameter and $Q2Q1$: observations for plate thickness $t = 1 \text{ mm}$, propan-2-ol, $Ka = 348$. Re values are different since $Recr$ depends on d . (a) Oscillating rim with circular hole ($d = 4 \text{ mm}$, $Q2Q1 = 1$, $Re = 28$) ; (b) Oscillating rim with bean-shaped hole ($d = 8 \text{ mm}$, $Q2Q1 = 1$, $Re = 34$) ; (c) Drops or liquid columns ($d = 12 \text{ mm}$, $Q2Q1 = 0$, $Re = 29$) ; (d) Pendant sheet ($d = 12 \text{ mm}$, $Q2Q1 = 1$, $Re = 32$). 97

Figure 3-5: Curtain images just beyond the transition: $t = 1 \text{ mm}$, $Q2Q1 = 1$; (a) $d = 4 \text{ mm}$, propan-2-ol ($Ka = 348$), $Recr = 31$; (b) $d = 8 \text{ mm}$, propan-2-ol, $Recr = 37$; (c) $d = 12 \text{ mm}$, propan-2-ol, $Recr = 35$; (d) $d = 12 \text{ mm}$, pure water ($Ka = 3920$), $Recr = 125$. The curtain exhibits parallel stationary waves in (b) and a rugged wave pattern in (c) and (d). 98

Figure 3-6: Free surface profile in the $y=0$ plane (streamwise direction) just beyond the curtain transition: CCI measurements (circles) for perforation diameter $d = 8 \text{ mm}$, plate thickness $t = 1 \text{ mm}$, propan-2-ol, $Ka = 348$, $Re = 36$, $Q2Q1 = 1$. The thick black segments correspond to the plate surface. The origin of the coordinate frame coincides with the perforation center. The thin grey dotted lines are drawn to indicate the probable shape taken by the free surface of the film (data are missing because the local slope of the free surface is too steep for the CCI to capture the film thickness). 99

Figure 3-7: Variations of the curtain Reynolds number as a function of the perforation diameter rescaled by the capillary length (d/lc) for three plate thickness values ($t = 0.5, 1, 1.5 \text{ mm}$). The tested liquid is propan-2-ol ($Ka = 348$). (a) One face supply. (b) Two face supply with equal volume flow rates. 101

Figure 3-8: Variations of the curtain Reynolds number as a function of $Q1Q2$ for two different values of the perforation diameter ($d = 4 \text{ mm}$ and $d = 8 \text{ mm}$). The plate thickness is equal to $t = 1 \text{ mm}$. The tested liquid is propan-2-ol. $Recr$ is calculated from $Q1cr$, the volume flow rate on the front side that induces curtain transition at given $Q2$. 102

Figure 3-9: Variations of the curtain Reynolds number as a function of the perforation diameter rescaled by the capillary length for four different liquids, i.e. propan-2-ol ($Ka = 348$), 55 wt% glycerin aqueous solution ($Ka = 245$), 25 wt% glycerin aqueous solution ($Ka = 1470$) and pure water ($Ka = 3920$). The plate thickness is equal to $t = 1 \text{ mm}$. (a) One face supply. (b) Two face supply with equal volume flow rates. 103

Figure 3-10: Section along the plane $y=0$: idealized flat film profile on the perforated plate before the curtain transition. The red dotted lines represent the idealized curtain free surface.

104

Figure 3-11: Comparison between prediction of Eq. (3.4) (solid lines) and the experimental results (points) obtained with propan-2-ol ($Ka = 348$) and perforated plates of thickness $t = 1$ mm. (a) variations of Re_{cr} as a function of the perforation diameter rescaled by the capillary length for $Q_2Q_1 = 0$ and $Q_2Q_1 = 1$. (b) variation of Re_{cr} as a function of the ratio Q_1Q_2 for perforation diameter $d = 4$ mm.

105

Figure 3-12: (a) Measured half thickness profile of the curtain (squares) and calculated profile assuming free fall and omitting varicose waves (red solid line). (b) Predicted wavelength values along the liquid curtain (dashed line) and wavelength values measured on the waves that stand on the real curtain (crosses), same experimental conditions as **Figure 3-6**.

108

Figure 4-1: Perforated plate front view and cross-section along x - z plane: (a) geometric parameters and coordinate system (b) Scheme of the film flow on the front and on the back of the plate (the plate is supplied solely on its front, the film flows in the curtain mode). The arrows indicate the flow path followed by the fluid. We define the top edges of the perforation on the front and on the back of the plate (red squares), the bottom edges (blue squares) and the perforation inner surface (in green).

127

Figure 4-2: (a) Schematic representation of the experimental set-up. (b) Photograph of the front of the plate (with a single perforation). (c) Photograph of the rear side (with a staggered array of perforations). 1. Test plate 2. LED panel 3. High-speed camera 4. Volumetric flow meter 5. Needle control valve 6. Spillway 7. Gear pump 8. Reservoir 9. CCI sensor 10. Distributor 11. Liquid Collector 12. Anti-vibration mount, 13. Removable collector, 14. Measuring beaker. 15. Frame that holds the plate to ensure plate flatness.

129

Figure 4-3: Single isolated perforation: transferred volume flow rate per unit diameter of perforation (Qt) as a function of the supply flow rate (on the front of plate) per unit width (Q). The diameter is $d = 4$ mm, the plate thickness $t = 1$ mm. The straight lines linking the dots are intended to guide the eye along the data points. Arrows indicate how Qt evolves as Q is swept up and down. Rim mode (green), inertial curtain (red), hysteretic curtain (blue).

132

Figure 4-4: Transferred volume flow rate per unit diameter of perforation (Qt) as a function of the supply flow rate (on the front of plate) per unit width (Q): effect of plate thickness. Single perforation with $d = 4$ mm (circle), 6 mm (square), 8 mm (triangle), plate thickness $t = 0.5$ mm (filled), 1 mm (empty). Curtain mode (hysteretic in blue, inertial in red). Linear fit for $d = 4$ mm and $t = 0.5$ mm (dotted line), for $d = 4$ mm and $t = 1$ mm (dashed line).

133

Figure 4-5: Spanwise rivulet profile on the rear side of the plate at $x = 2, 20, 60, 100$ mm from the bottom edge of the perforation. Plate thickness $t = 1$ mm, perforation diameter $d = 4$ mm. Curtain mode. (a) $Re = 29$; (b) $Re = 42$. The lines linking the dots are intended to guide the eye along the data points.

134

Figure 4-6: Average volume flow rate transferred per unit diameter of perforation (Qt) as a function of the supply flow rate (on the front of plate) per unit width (Q): effect of perforation spacing (s). Perforation diameter $d = 4$ mm, perforation spacing $s = 6$ mm (\times), 8 mm (\diamond), 10 mm (\triangle), 12 mm (\circ), 14 mm (\square), single isolated perforation or $s = \infty$ ($+$). Plate thickness $t = 1$ mm. Rim mode (green), inertial curtain mode (red), hysteretic curtain mode (blue). Linear fit on the curtain mode data for $s = 6$ mm (dashdotted line), $s = 8$ mm (dotted line), and $s = 14$ mm (dashed line).

135

Figure 4-7: Streamwise film profile along $y = 0$ and $y = s/2$ (see the inset in the graph) for spacing $s = 6, 10$ mm. Single spanwise row of perforations, perforation diameter $d = 4$ mm, plate thickness $t = 1$ mm, and Reynolds number $Re = 38$ (curtain mode).

136

243

- Figure 4-8:** Film spanwise profiles for different streamwise locations (x), supply Reynolds numbers (Re) and perforation spacings (s). Single spanwise row of perforations, diameter $d = 4$ mm, plate thickness $t = 1$ mm, curtain mode. The lines linking the dots are intended to guide the eye along the data points. 137
- Figure 4-9:** Liquid film pattern on a staggered array of perforations at $Re = 23$ when rim mode (in odd rows) and curtain mode (in even rows) coexist. Plate thickness $t = 1$ mm, perforation diameter $d = 4$ mm and spacing $s = 14$ mm. (Top) front of the plate, (bottom) back of the plate. Some holes without curtain appear completely black because they are not adequately lit. 139
- Figure 4-10:** Volume flow rate per unit width (Qb) on the back of the plate beneath the 1st, 2nd, 3rd and 10th row as a function of the supply flow rate per unit width on the front (Q). Plate thickness $t = 1$ mm, perforation diameter $d = 4$ mm, and spacing $s = 14$ mm. Curtain mode. The solid black line represents the asymptotic value of Qb , i.e., after a large number of perforation rows. The beam of colored straight lines corresponds to the model predictions of Qb flowing on the back of the plate after $k = 1$ to $k = 10$ rows of perforations. 140
- Figure 4-11:** Collapse of the rivulet spanwise profiles with appropriate rescaling. Supply Reynolds number $Re = 42$ (inertial curtain mode). Data are well described by the Gaussian law (solid line). 144
- Figure 4-12:** Rescaled peak film thickness and width as a function of the rescaled streamwise coordinate. Data (except the point (1;1)) are fitted with a power-law using the least-squares method. 146
- Figure 4-13:** Rescaled perturbation amplitude of the liquid film flowing on the back of the plate as a function of the rescaled streamwise coordinate. Single row of perforations, perforation diameter $d = 4$ mm, plate thickness $t = 1$ mm, and Reynolds number $Re = 38$ (curtain mode). The data points with red dots are fitted with an exponential law using the least-squares method (red solid line extended with dashes). 148
- Figure 5-1:** Structure of the liquid curtain in a perforation in (a) $x - y$ plane and (b) $x - z$ plane: Deionized water curtain in the perforation of diameter $d = 8$ mm at $Re = \rho Q \mu = 103$ ($Q = q/W$; $\mu = 0.00105$ Pa.s; $\sigma = 0.073$ N.m⁻¹). (c) Example of the structure of Torricelli's curtain from a horizontally ejected liquid jet from the pipe¹³⁴. 173
- Figure 5-2:** Effect of defocuss on the image (adapted from Damaschke et al.¹⁵³) with the examples of the real particle taken at different position from the focal plane. 178
- Figure 5-3 :** Direct consequence on the appearance of the particles with (right) and without (left) a circular disk or annular space technique¹⁵⁴. 179
- Figure 5-4:** Typical patterns created for the detection of particles (respectively 8, 12 and 16 pixels in apparent diameter). 180
- Figure 5-5:** (a) Measurement zone on the flat plate with important dimensions (b) An example of pre-processed image with tracer particle when the defocus is set. 182
- Figure 5-6:** (A-D) 2D color map of the time averaged streamwise or axial velocity (ux) (a-d) Time and space averaged (in spanwise) uxy along the vertical flat plate for $Q = 0.18, 0.22, 0.26, 0.29, 0.31, 0.39$ m³/mh. Test liquid is propan-2-ol ($Ka = 348$). 183
- Figure 5-7:** Comparison of experimental mean velocity and the theoretical mean velocity for different supply flow rate per width of the film. 184
- Figure 5-8:** (a) Illustration of the region of interest (ROI) on a flat vertical plate. (b) Tracer particle size as a function of Nusselt liquid film thickness (δ_{th}) 185
- Figure 5-9:** Qualitative view of tracer particles dispersion and their particle density in a (a) complete ROI (b) upper/lower borders, (c) right side and (d) central region of ROI. 188
- Figure 5-10:** 50 super imposed x-y plane images of streamlines patterns of a fluid film falling on a perforated plate prior to curtain mode at (a) $Re = 47$ and (b) $Re = 83$. Diameter of the

- perforation $d = 8$ mm and thickness of the plate $t = 0.5$ mm is used. Test liquid is deionized water ($Ka = 3920$). 190
- Figure 5-11:** 50 superposed images of fluid film with florescent tracer particles showing streamlines in $x - y$ on a perforated plate with hysteresis curtain at (a) $Re = 47$ (b) $Re = 68$ (c) $Re = 83$ and inertial curtain at (d) $Re = 104$ ($Re > Re_{cr}$). Enlarged image of liquid curtain with dominant showing (1) Dean Vortices, (2) Capillary waves (3) recirculation $x-y$ plane. Diameter of the perforation $d = 8$ mm and thickness of the plate $t = 0.5$ mm is used. Test liquid is deionized water ($Ka = 3920$). 192
- Figure 5-12:** 20 superposed images of fluid film with florescent tracer particles showing streamlines in $x - y$ on a perforated plate ($d = 4$ mm) with inertial curtain using (a) Deionized water ($\mu = 0,001$ Pa.s, $\sigma = 0.073$ N/m) ($Re = 104$, $Ka = 3920$) (b) propan-2-ol ($\mu = 0.002$ Pa.s, $\sigma = 0.021$ N/m) ($Re = 34$, $Ka = 348$). 193
- Figure 5-13:** ROI of the post processed image. Comparison of the spatio-temporal mean velocity measured on perforated plates with the theoretical mean velocity on non perforated plates. Two unusual measured values are highlighted in black square. Test liquid used is propan-2-ol ($Ka = 348$). 194
- Figure 5-14:** (a) Temporal variation of instantaneous axial velocity ux at the center of the perforation (see insert) and (b) corresponding histogram of the ux . Supply flow rate is $23 \text{ L}\cdot\text{h}^{-1}$ and mean theoretical velocity is $uth = 0.23 \text{ ms}^{-1}$. 195
- Figure 5-15:** Probability density map of the negative velocities in and around the perforation in curtain mode for six different volumetric flow rates per unit width of the film (a) one face supply and (b) two-face supply. Diameter of the perforation $d = 4$ mm and plate thickness $t = 0.5$ mm. 196
- Figure 5-16:** Particle tracking spatiotemporal data (sampled at 800 Hz) (a) 2D color map image of the liquid film on a perforated plate (black arc: perforation). Tracer particle position at $\tau = 1$ ms (green circle and dot) and 250 ms (red circle and dot). (b) Time evolution of apparent size of the particles, (b) time evolution of horizontal component of velocity (uy), (c) time evolution of vertical component of velocity (ux). Key events are marked by dots and arrows. A perforation of diameter $d = 8$ mm and plate of thickness $t = 0.5$ mm is used. Test liquid used is propan-2-ol ($Ka = 348$). 197
- Figure 5-17:** (a) Oscillation frequencies obtained from DMD post processing. (b) Dominant frequency modes as a function of mean axial velocity. 198
- Figure 5-18:** (a) 20 superimposed images to measure $R1$ and dR (b) Dean number (De) calculated for the measured values of $R1$ and dR for a liquid curtain in the perforation for eight different supply flow rate per width of the film. 200
- Figure 5-19:** DMD Relative spatial axial velocities in the liquid curtain at 18.2 Hz with supply flow rate of $Q = 0.18 \text{ m}^3/\text{mh}$; $Re = 19$. 201
- Figure 5-20:** DMD Relative spatial axial velocities in the liquid curtain at 38.4 Hz with supply flow rate of $Q = 0.39 \text{ m}^3/\text{mh}$; $Re = 42$. 202

List of tables

Table 1-1 : Modern industrial air separation technologies listing its performance and energy demands	12
Table 1-2 : Correlations proposed based on the experimental data ²⁵	26
Table 2-1 : List of test plate parameters used in the experiments of transition of liquid film and liquid transfer and spreading through perforations	63
Table 2-2 : Specifications of the Ubbelohde type viscosimeter to measure viscosities of propan-2-ol and 25% aqueous glycerin mixture	64
Table 2-3 : Physical properties (at 25°C) of the liquids used in the experiments and range of Reynolds number investigated.	66
Table 2-4 : Flow and test plate parameters used in oscillation frequency measurements	69
Table 2-5 : List of frequencies detected corresponding to the highest amplitudes	71
Table 2-6 : List of test plate, liquid, camera and optical parameters used in the study	77
Table 3-1 . Physical properties (at 25°C) of the liquids used in the experiments and range of Reynolds number investigated. The bounds of the contact angle (θ) interval correspond to the receding contact angle and to the advancing contact angle, respectively. The equilibrium contact angle (θE) lies in-between.	89
Table 5-1 : Supply flow rate per unit width of the film, theoretical film thickness and measured film thickness.	185

French summary (résumé français)

Contexte

Les unités de séparation de l'air (ASU) sont des systèmes industriels majeurs permettant la production industrielle d'oxygène, d'azote et d'argon à partir de l'air. Bien qu'il existe différentes approches de la séparation de l'air, comme l'adsorption et les membranes, la distillation cryogénique est le seul procédé qui combine les avantages d'une grande pureté du produit (95-99,98%) et d'une grande capacité de production (plus de 5000 tonnes d'oxygène/jour par ASU). Cependant, les taux de production et les puretés élevées se font au prix d'une forte consommation d'énergie. Le principal défi de ce procédé est d'obtenir des performances de séparation élevées et, en même temps, de maintenir la hauteur des colonnes et les coûts d'investissement et d'exploitation à un niveau bas. Des progrès significatifs en termes de performance ont été réalisés dans les années 1970, lorsque des garnissages structurés en feuilles ondulées-croisées ont été introduits. Depuis lors, ces garnissages sont largement utilisés dans les colonnes de distillation et d'absorption. Ils sont composés de feuilles minces, verticales et ondulées, disposées parallèlement les unes aux autres. Dans la séparation cryogénique de l'air, les feuilles sont généralement en aluminium. Ces garnissages structurés combinent une fraction de vide et une surface interfaciale élevées. Cela permet d'obtenir une perte de charge plus faible, un rendement plus élevé et une capacité supérieure par rapport aux plateaux. Pourtant, les garnissages structurés sont très sensibles à la répartition et à l'étalement du liquide, cela a un impact sur la surface interfaciale liquide-vapeur, et donc sur le transfert de masse et l'efficacité de séparation de la colonne. Dans un garnissage de feuilles ondulées, trois types de motifs géométriques contribuent à la distribution du liquide : les ondulations, les perforations et éventuellement la micro-texture, dont l'échelle de longueur caractéristique est généralement inférieure d'un à plusieurs ordres de grandeur à celle des ondulations. Les perforations permettent au liquide de s'écouler d'un côté de la feuille vers l'autre côté. Par conséquent, elles favorisent l'échange de liquide entre les deux côtés d'une même feuille et réduisent l'accumulation de liquide dans le creux des ondulations évitant ainsi le phénomène de « channeling ».

Pour que les garnissages structurés fonctionnent à leur capacité maximale, il est important de disposer d'une bonne répartition du liquide sur toute la surface du garnissage. La distribution et l'étalement des liquides sur des garnissages structurés (en feuilles ondulées) ont été étudiés à

différentes échelles : l'échelle de la colonne (pilote), l'échelle de la feuille et l'échelle des motifs géométriques (ondulations, perforations). Après avoir visualisé l'intérieur de la colonne à l'aide de techniques optiques modernes telles que la tomographie par ordinateur (CT), les chercheurs ont souligné l'importance de la géométrie des motifs de surface et la nécessité d'une optimisation pour éviter une mauvaise distribution locale à l'intérieur du garnissage, en particulier loin des sorties du distributeur ou sur les extrémités du garnissage. Fourati et al (2012) ont utilisé la tomographie à rayons gamma pour étudier la distribution du liquide dans une colonne gaz-liquide à contre-courant équipée d'un garnissage Mellapak 250.X et alimentée par un jet de liquide central et situé au sommet. Ils ont obtenu des cartes de rétention (exprimées en fraction volumique de liquide) à différentes positions axiales dans la colonne. Ils ont constaté que la rétention globale du liquide augmente avec le débit d'alimentation et la viscosité du liquide. La phase liquide se disperse radialement avec une longueur caractéristique appelée facteur d'étalement (spread factor) de l'ordre de quelques millimètres. Comme le facteur d'étalement ne varie pas significativement avec la charge de liquide, la charge de gaz et la viscosité du liquide, ils en ont conclu que la distribution du liquide est principalement contrôlée par la géométrie du garnissage.

Une étude approfondie est donc nécessaire pour comprendre et quantifier les structures d'écoulement sur la géométrie des feuilles métalliques de garnissage afin de maîtriser le comportement de la phase liquide sur la surface. Très peu d'études ont été réalisées sur ce sujet. Parmi celles-ci, citons celle de Pavlenko et al. (2017). Ces auteurs ont examiné l'effet des perforations sur la répartition du liquide pour une seule feuille verticale perforée-ondulée. Deux diamètres de perforation ont été étudiés : 4 mm et 10 mm, en utilisant de l'azote liquide à des températures cryogéniques. En fonction du nombre de Reynolds, différents régimes de mouillage de la surface de la feuille ont été identifiés. Des ondes 3D de grande amplitude se propagent sur la surface libre de liquide, sauf dans les régions situées sous les trous. Ces zones calmes sans ondes deviennent plus étroites et plus courtes lorsque le débit augmente. Pour le trou de 10 mm, des gouttes et des jets se détachent périodiquement du bord supérieur du trou. Le détachement des gouttes et des jets du bord du trou (à l'entrée de la perforation) arrose les zones en aval du trou et la face arrière à travers le trou.

Plus récemment, Xie et al (2017 et 2018) ont étudiés expérimentalement et numériquement des écoulements de films liquides autour de perforations de différentes formes (dans le cas d'une plaque plane verticale en aluminium). Ils ont examiné l'influence du nombre de Reynolds d'alimentation, du nombre de Kapitza (52 jusqu'à 2930) pour un film liquide s'écoulant autour d'une seule grande

perforation (rectangulaire ou circulaire). Ils ont observé plusieurs régimes : goutte, jet, nappe liquide pendante dans la perforation pour des valeurs faibles à modérées du nombre de Reynolds. Pour des valeurs plus élevées du nombre de Reynolds, un rideau liquide remplit complètement la perforation. Ce rideau présente un motif d'ondes capillaires. Lorsque le liquide "traverse" la perforation (sous forme de goutte, de colonne, de nappe liquide pendante ou de rideau), une partie du liquide s'écoule de la face avant vers la face arrière de la plaque. Xie et al (2018) proposent également une corrélation empirique pour le nombre de Reynolds du film à la transition du rideau liquide. Ils notent une hystérésis : le nombre de Reynolds du film, correspondant à la rupture du rideau liquide, est plusieurs fois inférieur à celui de la formation du rideau. Dans leurs simulations numériques de dynamique des fluides (CFD), le régime rideau est appelé « twin film » en raison de la coexistence d'un film s'écoulant sur la plaque et d'un film suspendu dans la perforation. Le film liquide en suspension présente des ondes capillaires variqueuses stationnaires. De plus, les simulations numériques mettent en évidence une forte génération de vortex à la fois à l'intérieur du film suspendu ondulé et sur sa surface libre. Ces phénomènes contribuent à l'intensification du transfert de masse, qui est observée pour la plaque perforée (par rapport à la plaque non perforée).

L'écoulement du film sur une perforation présente également certaines ressemblances avec l'écoulement sur des topographies telles que celles de type step-in, step-out, tranchée ou trou borgne (non traversant). Il existe une littérature abondante sur ce sujet. Il apparaît qu'une topographie est précédée d'une onde capillaire stationnaire : une ride capillaire avant un step-in, ou une dépression de la surface libre avant un step-out. Lorsque le nombre de Reynolds du film augmente, une ride d'origine inertielle apparaît après un step-out. Les mêmes caractéristiques ont été observées par Xie et al. (2017 et 2018) à l'entrée et à la sortie d'une perforation rectangulaire.

D'après la revue de littérature, nous constatons que les connaissances existantes sur le sujet de l'hydrodynamique des films liquides sur les surfaces de garnissage sont limitées, une grande partie de recherche est consacrée à l'étude des films liquides sur des surfaces planes (inclinées ou verticales). Cependant, peu d'études ont examiné finement l'effet des motifs de surface sur la redistribution du liquide. Certaines études ont évalué de manière visuelle et qualitative la structure du film liquide sur des éléments ondulés et perforés de garnissages structurés. Les obstacles dans la géométrie des garnissages, comme les trous ou les points de contact entre plaques, génèrent également des ondes, favorisant aussi le transfert de matière dans la phase

liquide (Hu et al. (2017)). Certains chercheurs se sont concentrés sur les ondulations, sans ajouter de perforations, et ont mesuré l'épaisseur locale du film liquide.

Toutefois, aucune étude ne nous permet de quantifier et modéliser a priori les mécanismes locaux associés aux perforations sur la surface complexe du garnissage structuré.

Si on suppose que les perforations favorisent la redistribution liquide, alors il est nécessaire de déterminer quels sont les mécanismes fondamentaux, et comment il est possible de les quantifier. Cela exige de mener une recherche expérimentale permettant d'établir des corrélations et des modèles physiques à un niveau plus fondamental.

Dans cette thèse, nous cherchons à examiner l'hydrodynamique du film liquide pour comprendre les mécanismes de redistribution de la phase liquide sur la forme simplifiée d'une feuille métallique ondulée et perforée. Les ondulations ajoutant plusieurs paramètres (angle de sertissage, inclinaison, etc.), le processus de quantification devient difficile à contrôler. Les résultats sont donc généralement bruyants et non reproductibles. La simplification du garnissage industriel est alors essentielle pour comprendre le comportement du film liquide sur la forme géométrique identifiée, en régime permanent, afin de pouvoir dériver des modèles analytiques.

Montage expérimental et Méthodologie

La première configuration du dispositif expérimental permet d'étudier les différents mécanismes de transition du film liquide dans la perforation pour une large gamme de paramètres géométriques (diamètre du trou d et épaisseur de la plaque t) et de propriété du film (Re & Ka). Dans un deuxième temps, pour les mesures du transfert de liquide à travers la ou les perforations, le montage a été légèrement modifié. Nous avons également ajouté un collecteur pour récupérer le liquide transféré via les perforations.

Des dispositifs optiques ont été utilisés pour les mesures par ombroscopie et pour les mesures d'épaisseur de film en utilisant un capteur confocal chromatique.

Pour la mesure de vitesse du film liquide, la boucle d'écoulement principale est conservée. Une configuration optique est ajoutée pour réaliser une vélocimétrie par suivi de particules 3D 3C. Cette méthode est appliquée au film s'écoulant sur la paroi et au film suspendu dans la perforation.

Par la suite, nous considérons une plaque ou une feuille plane verticale avec une seule perforation circulaire. La plaque est alimentée en liquide sur une seule face et/ou ses deux faces d'une manière homogène avec un distributeur de liquide conçu dans cet objectif.

Principaux résultats et conclusions

Etude hydrodynamique du film liquide au voisinage d'une perforation

Dans un premier temps, nous avons examiné expérimentalement les différentes structures d'écoulement d'un film liquide autour d'une perforation unique sur une plaque plane verticale. Nous avons utilisé la technique d'ombroscopie pour observer qualitativement ces structures. En augmentant le nombre de Reynolds, nous avons observé successivement les modes suivants : bourrelet liquide qui cerne la perforation, goutte/colonne liquide entre les bords supérieur et inférieur de la perforation, nappe liquide pendant du bord supérieur de la perforation et la fermant partiellement.

Lorsque la force d'inertie domine complètement les forces de tension superficielle, le film liquide remplit le trou. Cet effet se produit à partir d'une valeur critique du nombre de Reynolds appelée « nombre de Reynolds de rideau » (Re_{cr}). Nous avons mesuré ce nombre de Reynolds de rideau pour une large gamme de paramètres géométriques. Re_{cr} augmente en fonction du diamètre de perforation et de l'épaisseur de la plaque jusqu'à une certaine valeur de diamètre ($d > 8 \text{ mm}$) et atteint ensuite un plateau.

En fonction de l'épaisseur de la plaque, et notamment pour les plaques épaisses, le rideau présente un phénomène de "teapot" à l'entrée de la perforation.

Nous avons ensuite étudié l'effet du nombre de Kapitza (Ka) sur Re_{cr} en variant les propriétés du liquide. Le seuil de franchissement du trou augmente avec Ka . Pour de grands diamètres de trou ($d > 8 \text{ mm}$), on retrouve expérimentalement la loi d'échelle $Re_{cr} \propto Ka^{3/5}$ établie de manière théorique.

Nous avons construit un modèle simple pour le critère de formation du rideau. Ce critère est dérivé d'un bilan de quantité de mouvement macroscopique sur le bourrelet qui cerne la perforation, près du point d'arrêt (bord supérieur de la perforation). Cette approche revisite un modèle proposé pour la première fois par Hartley et Murgatroyd (1964) pour la rupture de films liquides minces s'écoulant sur la surface solide (critère pour la formation de zones sèches). Au début de la formation du rideau dans une perforation, nous nous attendons à ce que le bourrelet soit essentiellement soumis à deux forces : la force de tension superficielle qui résiste à la formation du rideau et l'inertie du fluide qui conduit à cette transition. Afin d'exprimer la force de tension superficielle, nous considérons que le profil du film sur les deux côtés de la plaque

est plat et axisymétrique par rapport à l'axe de la perforation. On écrit l'énergie de la surface avant franchissement du trou et ensuite on calcule la force de tension superficielle par unité de longueur du bourrelet liquide. Nous considérons l'expression du profil de vitesse de Nusselt (semi-parabolique) pour exprimer le flux net de quantité de mouvement entrant dans le bourrelet, près du point d'arrêt. Le modèle met en relation le nombre de Reynolds de rideau (critère de formation du rideau) avec le diamètre de la perforation, l'épaisseur de la plaque, les propriétés du liquide, exprimés sous forme non dimensionnelle. En comparant les résultats expérimentaux avec le modèle, nous trouvons que le modèle décrit de façon pertinente l'effet de la géométrie de la perforation et des propriétés de l'écoulement sur le nombre de Reynolds de rideau.

Enfin, nous avons montré que la dynamique d'un rideau au sein d'une perforation était le résultat de deux phénomènes superposés : l'étirement du rideau sous l'effet de l'accélération de la gravité et l'excitation d'ondes variqueuses par l'impact du rideau sur le bord inférieur de la perforation. L'étirement est bien décrit par un modèle de chute libre. Nous avons constaté que la longueur d'onde de l'onde variqueuse est fixée de façon à ce que la vitesse des ondes satisfasse à la fois la relation de dispersion de Taylor et corresponde aussi à la vitesse locale du rideau. Nous avons également mis en évidence le phénomène d'hystérésis du rideau liquide. Ce comportement hystérétique du rideau peut être favorable dans un garnissage structuré dans la mesure où il augmente la rétention du liquide à de faibles débits.

Etude du transfert et de la redistribution du liquide à travers les perforations

Avec la même configuration du banc d'essai, le transfert et la redistribution du liquide ont été étudiés pour (i) une perforation unique, (ii) une ligne de perforation et (iii) un réseau de perforations (jusqu'à 10 lignes, rangées en quinconce). Dans cette partie, la plaque est alimentée sur une seule de ses faces. En deçà d'un certain débit, il n'y a pas de transfert de liquide entre la face alimentée et la face non alimentée : la ligne triple reste ancrée à l'entrée de la perforation. Au-delà de ce débit, la perforation arrose l'arrière de la plaque. Dans le cas d'une perforation de petit diamètre (jusqu'à 4 mm), on distingue deux modes d'arrosage : en mode bourrelet puis en mode rideau au-delà du nombre de Reynolds de rideau. Du fait de l'hystérésis, l'arrosage en mode rideau, une fois amorcé, peut être maintenu pour des nombres de significativement inférieurs à Re_{cr} .

Perforation unique

Nous avons quantifié expérimentalement le débit de liquide transféré à travers la perforation en mode rideau pour plusieurs diamètres de perforation et plusieurs épaisseurs de la plaque en régime inertiel ($Re \geq Re_{cr}$) et en régime hystérétique ($Re < Re_{cr}$). On trouve que le débit volumique transféré (par unité de diamètre de perforation) varie linéairement avec le débit linéique d'alimentation (débit par unité de largeur de plaque). L'effet « teapot » augmente de façon significative le débit transféré à travers les perforations, dans le cas de plaques plus épaisses.

Un modèle linéaire a été proposé pour prédire le débit volumique transféré par une perforation d'une taille donnée.

Un réseau de perforations

Nous avons mesuré le débit de liquide s'écoulant sur le dos de la plaque et provenant du transfert cumulé à travers les perforations. On note que le débit de liquide au dos de la plaque augmente avec le nombre de rangées et converge vers une valeur asymptotique correspondant à 50% du débit d'alimentation de la face avant. Un modèle de récurrence simple a été proposé. Il a pour but de mettre en relation le débit volumique à l'arrière de la plaque, juste en aval d'une rangée de perforations, avec le débit volumique sur la face d'alimentation. On suppose que le rideau liquide au sein des perforations se divise de façon égale entre les deux faces. De manière itérative, on peut déterminer le débit de liquide s'écoulant en aval de chaque rangée de trous pour chacune des faces.

Dans l'ensemble, le modèle décrit bien les tendances expérimentales du débit volumique transféré à travers les perforations, notamment dans la gamme de faibles débits d'alimentation. Il prévoit que le débit volumique au dos de la plaque atteint 65% de sa valeur asymptotique à partir de la troisième rangée de perforations. Cette valeur atteint 90% à partir de la 7ème rangée. Le modèle ne rend pas compte de la relaxation plus rapide du débit vers sa valeur asymptotique lorsque le débit d'alimentation augmente (conséquence du « teapot » effect).

Comment le liquide transféré s'étale-t-il au dos de la plaque lorsque la perforation fonctionne en mode rideau ?

Le liquide transféré à travers une perforation s'écoule sous la forme d'un ruisseau le long de la face arrière de la plaque. Nous avons ici choisi un diamètre de perforation constant pour étudier l'évolution du ruisseau, dans le sens du courant et de la largeur de la plaque, en fonction du nombre de Reynolds d'alimentation. Nous avons mesuré avec le capteur confocal chromatique

les variations d'épaisseur du ruisseau suivant la largeur de la plaque à différentes hauteurs le long de la plaque.

Nous observons que le ruisseau s'élargit et s'aplatit dans le sens de l'écoulement. L'épaisseur du film est maximale près de la perforation. En suivant Shetty et Cerro (1994), la forme du ruisseau a été approximée par une distribution gaussienne. Il apparaît que la largeur du ruisseau varie comme la puissance 0,2 de la distance à la perforation, son épaisseur comme la puissance $-0,075$ de cette même distance, en accord avec les exposants théoriques $-1/13$ et $3/13$ obtenus par Shetty & Cerro (1995) et Duffy & Moffatt (1997) pour l'étalement d'un ruisseau sous l'effet de la pression capillaire.

Nous avons également analysé la forme des ruisseaux dans le cas d'une rangée de perforations. On note que les ruisseaux (adjacents) fusionnent à une certaine distance en aval d'une rangée. Cette « distance de fusion » est une fonction de l'espacement entre les perforations. Nous observons expérimentalement que la distance de fusion varie comme la puissance 4,58 de l'espace entre les perforations. Cet exposant est en bon accord avec l'exposant théorique $13/3$ que l'on peut dériver des modèles de Shetty & Cerro (1995) et Duffy & Moffatt (1997).

A l'issue de la fusion des ruisseaux, le film continu formé a une forme ondulée. Il apparaît que l'amplitude des crêtes et des creux de cette surface ondulée décroît exponentiellement dans le sens de l'écoulement. La longueur de relaxation théorique est égale à la puissance $13/3$ de l'espacement entre les perforations.

Etude des structures de l'écoulement : vélocimétrie 3D3C par suivi de particules

Dans la dernière partie de l'étude, nous avons mis en place un système optique pour réaliser une nouvelle technique de vélocimétrie de suivi de particules 3D3C avec le concept de défocalisation. Cela permet de mesurer la vitesse locale dans les films liquides minces tombants, sur une plaque non perforée et une plaque perforée (perforation unique). Elle est fondée sur la détection, la correspondance et le suivi de particules individuelles dans la zone visualisée. Les informations sur la vitesse de l'écoulement du fluide sont rendues accessibles par la localisation en 3D des particules traceuses. Celles-ci sont préalablement injectées dans le fluide et sélectionnées pour suivre parfaitement son évolution.

Le concept de défocalisation en vélocimétrie laser consiste à supposer que la taille apparente d'une particule défocalisée sur l'image ne dépend pas de sa taille physique, mais seulement de son éloignement par rapport au plan focal. En se défocalisant, l'image des particules prend la forme de l'ouverture. Après une phase de calibration, il devient possible de relier une taille

apparente à une profondeur par une expression fondée sur l'approximation des lentilles minces (Damaschke (2002)).

Nous enregistrons des images spatio-temporelles en réglant la défocalisation de l'objectif sur des particules traceuses. En utilisant des algorithmes de flot optique, nous obtenons des vecteurs de vitesse 2D globaux. L'association spatio-temporelle de ces vecteurs est ensuite réalisée selon une méthode de vélocimétrie par suivi de particules.

Sachant que la technique de mesure n'avait jamais été appliquée à des films minces, nous avons fait un test de faisabilité en mesurant la vitesse axiale d'un film laminaire sur une plaque plane verticale. Les images sont enregistrées à un taux d'échantillonnage de 1200 Hz dans le régime du film laminaire. En fonction du débit d'alimentation, les mesures montrent que la vitesse axiale est plus ou moins uniforme dans la direction du flux et dans le sens de la largeur de la plaque. En outre, les mesures de la vitesse axiale moyenne pour différents débits d'alimentation ont été comparées à la vitesse axiale moyenne théorique en 1D à partir de la solution de Nusselt. Comme la théorie le prédit, la vitesse augmente en fonction du débit d'alimentation. Cependant, les valeurs expérimentales sont inférieures d'environ 10-20% à la valeur théorique.

Nous avons également visualisé les trajectoires des particules d'un film sur une plaque perforée afin d'identifier des structures d'écoulement, essentiellement des zones de recirculation qui contribuent à l'intensification du transfert de masse. Le rideau liquide révèle des tourbillons bien localisés. Nous les identifions qualitativement sur la base de l'axe de rotation et des forces qui provoquent leur apparition. Dans les grandes perforations ($d \geq 6mm$), on constate la présence de tourbillons de Dean, souvent observés dans les conduites courbées, et de tourbillons induits par l'impact du film liquide sur le bord de la perforation. Ensuite, dans les petites perforations ($d \leq 4mm$), notamment de taille industrielle, on observe une paire de tourbillons contrarotatifs.

On constate que ces vortex varient en fonction du diamètre de la perforation et de la viscosité du liquide.

Nous anticipons que les zones de recirculation locales peuvent réduire localement la vitesse du film liquide. Par conséquent le temps de séjour augmente, ainsi que la rétention liquide dans les garnissages ondulés.

Ensuite les zones de recirculation dans le rideau liquide ont été évaluées en traçant :

- (i) la fonction de densité de probabilité de la composante axiale du vecteur vitesse en un point, au centre de la perforation,

- (ii) les cartes 2D de la distribution de probabilité de la vitesse axiale négative en fonction du débit d'alimentation
- (iii) la trajectoire d'une seule particule
- (iv) les modes de fréquence dominants via le post-traitement décomposition en mode dynamique (DMD).

La fonction de densité de probabilité des vecteurs vitesse en un point a la forme d'une gaussienne décalée. La valeur moyenne est positive. Cependant, 1/3 des vecteurs vitesse sont négatifs. Les cartes 2D de la distribution de probabilité montrent également explicitement les zones dans le rideau liquide où la vitesse négative est dominante (jusqu'à 50%).

Pour conclure, on constate que le schéma d'écoulement sur les deux faces de la plaque est complexe surtout lorsque le film liquide se présente dans deux états : s'écoulant sur la paroi et suspendu dans la perforation (mode rideau liquide). Les tourbillons observés localement peuvent avoir un effet positif sur le transfert de masse interfacial. De plus, le rideau liquide est fortement hystérétique à de faibles débits d'alimentation. Ces résultats nous ont montré une possibilité d'amélioration du transfert de masse interfacial si la plupart des perforations d'un garnissage ondulé fonctionnent en mode rideau. Suite à ces observations, nous avons proposé un nouveau design d'éléments de garnissage structuré, qui sera testé dans la colonne de distillation cryogénique chez Air Liquide.

Ce travail nous a permis d'améliorer les connaissances de la contribution des perforations dans la redistribution du film liquide, à échelle microscopique, dans un garnissage ondulé et perforé.

Perspectives

Ce travail offre de nouvelles perspectives pour explorer plus profondément les phénomènes se produisant sur les surfaces complexes des garnissages structurés. Bien que de nombreuses études macroscopiques aient montré l'importance de l'optimisation des motifs de surface des éléments de garnissage, très peu de recherches ont été réellement menées à l'échelle microscopique. Nous avons identifié quelques pistes d'intérêt, dans la continuité de nos recherches, avec des perspectives d'expérimentation et de modélisation :

- Impact de l'angle d'inclinaison de la plaque sur les modes du film liquide dans les perforations, le transfert du liquide d'un côté à l'autre et l'écoulement/étalement des ruisselets.

- Étude de l'étalement des ruisselets en faisant varier les propriétés du liquide, pour valider l'approximation gaussienne des profils des ruisselets le long de la plaque.
- Etude du transfert de liquide sur des plaques perforées et ondulées dans le sens horizontal ainsi que sur des plaques de configuration industrielle. Modification du modèle linéaire proposé dans le cas du transfert de liquide en prenant en compte d'autres paramètres de l'élément de garnissage tels que : la géométrie de l'ondulation, les paramètres d'angle.
- Amélioration de la résolution des mesures de vitesse dans les trois dimensions. Utilisation d'un laser pulsé de plus forte intensité, meilleur ajustement de la nappe laser par rapport au film, validation des mesures de vitesse avec des films épais (pour des fluides de forte viscosité).